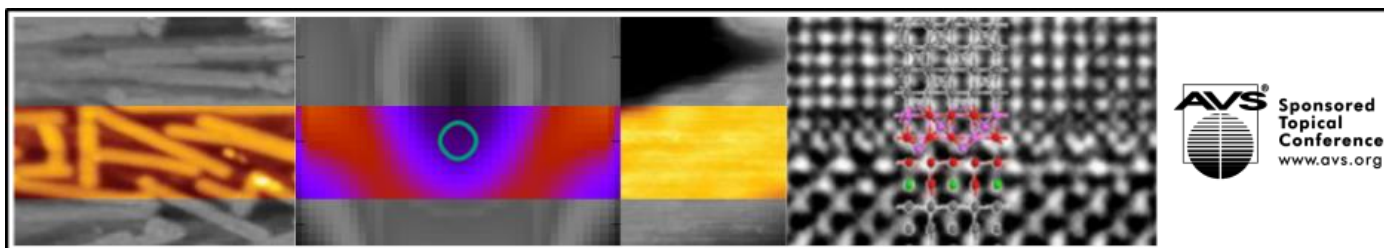


**2018 Workshop on
Innovative Nanoscale Devices and Systems**

WINDS
Book of Abstracts



November 25 - 30, 2018, The Westin Hapuna Beach Resort, Kohala Coast, Hawaii, USA

Edited by

Josef Weinbub

Berend T. Jonker

Henning Riechert

Tomoki Machida

Stephen Goodnick

Siegfried Selberherr

The Workshop on Innovative Nanoscale Devices and Systems (WINDS) is a week-long, international, and interactive workshop designed to explore the fundamental properties of nanoscale devices and applications thereof. In particular, WINDS provides a forum for material, device, and characterization as well as experimental and modeling researchers to interact.

The program consists of invited talks, regular talks, and poster presentations. All contributions have been peer-reviewed by the program committee.

This workshop is composed of morning and evening sessions, with afternoons free for ad hoc meetings to encourage extended interaction and discussion among participants. It is the successor of the original WINDS and the International Symposium on Advanced Nanodevices and Nanotechnology (ISANN), which were held on alternate years. WINDS itself began as an outgrowth of the successful Advanced Heterostructures Workshop, which has a long history dating from the 1980s.

WINDS 2018 was supported by the American Vacuum Society (AVS). We greatly appreciate their support.



ISBN 978-3-901578-32-8

© 2018 Society for Micro- and Nanoelectronics
c/o Technische Universität Wien
Gußhausstraße 27-29, 1040 Wien, Austria

Conference Chairs

General Chair

Josef Weinbub, TU Wien, Austria, Josef.Weinbub@TUWien.ac.at

US Co-Chair

Berend T. Jonker, Naval Research Laboratories, USA, Berry.Jonker@nrl.navy.mil

Europe Co-Chair

Henning Riechert, Paul Drude Institute, Germany, Riechert@pdi-berlin.de

Japan Co-Chair

Tomoki Machida, University of Tokyo, Japan, TMachida@iis.u-tokyo.ac.jp

Local Arrangements

Stephen Goodnick, Arizona State University, USA, Stephen.Goodnick@asu.edu

Publications Chair

Siegfried Selberherr, TU Wien, Austria, Siegfried.Selberherr@TUWien.ac.at

Program Committee

Alexander Balandin, University California Riverside, USA

John F. Conley, Oregon State University, USA

Jaroslav Fabian, University of Regensburg, Germany

David K. Ferry, Arizona State University, USA

Matthew Gilbert, Stanford University, USA

Koji Ishibashi, RIKEN, Japan

David Janes, Purdue University, USA

Akinobu Kanda, Tsukuba University, Japan

Victor Klimov, Los Alamos National Laboratory, USA

Saulius Marcinkevicius, KTH, Sweden

Kazuhiko Matsumoto, Osaka University, Japan

Wolfgang Porod, University of Notre Dame, USA

Viktor Sverdlov, TU Wien, Austria

Sunday, November 25

15:00-18:00 Registration

18:00 Gala Reception

Monday, November 26

09:00 General Welcome, Stephen Goodnick and Josef Weinbub

Session 1 **The Hall Effect at 40**

Chair: David K. Ferry

09:15-10:00 Klaus von Klitzing, MPI für Festkörperphysik, Germany,
“Quantum Hall Effect and the New SI System: The Biggest Revolution in
Metrology Since the French Revolution” (invited) 1

10:00-10:30 A. Seredlinski, A. Draelos, M.-T. Wei, L. Zhao, E. Arnault, C.-T. Ke, and
Gleb Finkelstein, Duke University, USA, T. Fleming, Y. Mehta, E. Mancil, H. Li,
and F. Amet, Appalachian State University, USA, T. Taniguchi and K. Watanabe,
NIMS, Japan, S. Tarucha and M. Yamamoto, University of Tokyo and RIKEN,
Japan, and I. Borzenets, City University of Hong Kong, Hong Kong,
“Superconductivity in the Quantum Hall Regime” (invited) 2

10:30-11:00 Coffee Break

Session 2 **Spintronics**

Chair: Tomoki Machida

11:00-11:30 Eiji Saitoh, JST, University of Tokyo, Tohoku University, JAEA, Japan,
“Various Spin Current Phenomena in Condensed Matter” (invited) 3

11:30-11:45 Alexander Khitun, University of California - Riverside, USA,
“Spin Wave Devices: Progress Update” 4

11:45-12:00	<u>Viktor Sverdlov</u> and S. Selberherr, TU Wien, Austria, “Shot Noise Enhancement at Spin-Dependent Hopping”	6
12:00-12:30	<u>Patrick M. Lenahan</u> , Pennsylvania State University, USA, “Electrically Detected Magnetic Resonance in SiC Metal-Oxide-Semiconductor Field Effect Transistors” (invited)	8
12:30-	Lunch and ad hoc sessions	
Session 3	Nanoscale and High Frequency Devices Chair: Robert Wolkow	
19:00-19:30	<u>Akira Fujiwara</u> , NTT, Japan, “Ultimate Electronics with Silicon Nanowire MOSFETs” (invited)	11
19:30-19:45	<u>Asen Asenov</u> , T. Al-Ameri, and V. Gerorgiev, University of Glasgow, UK, “Performance Evaluation of Multi-Channel Silicon Nanowire Transistors”	12
19:45-20:00	<u>Denis Mamaluy</u> and X. Gao, Sandia National Laboratories, USA, “Fully-Coupled Electronic-Ionic and Thermal Transport Simulation of Metal Oxide Memristors”	14
20:00-20:15	<u>Maarten L. Van de Put</u> , M. V. Fischetti, and W. G. Vandenberghe, University of Texas at Dallas, USA, “Quantum Transport Modeling Using a Bloch Basis Expansion”	18
20:15-20:30	M. Mensi, R. Ivanov, and <u>Saulius Marcinkevičius</u> , KTH Royal Institute of Technology, Sweden, K. M. Kelchner, S. P. DenBaars, S. Nakamura, and J. S. Speck, University of California Santa Barbara, USA, “Nanoscale Mapping of Carrier Diffusion: Application for InGaN Quantum Wells”	20
20:30-20:45	G. P. Szakmany, A. O. Orlov, G. H. Bernstein, and <u>Wolfgang Porod</u> , University of Notre Dame, USA, “Suspended Antenna-Coupled Nanothermocouples for Infrared Detection”	22

20:45-21:00 Kouichi Semba, NICT, Japan,
“Light-Matter Interaction ‘Beyond’ Strong-Coupling Regime in
Superconducting Circuit Quantum Electrodynamics” 24

21:00-21:15 Goran Rasic, B. Vlahovic, and Y. Tang, North Carolina Central University, USA,
“Controlling the Properties of Multiferroic Heterostructures via Nanoscale
Topographic Design” 26

Tuesday, November 27

Session 4 Oxides

Chair: Berend T. Jonker

09:00-09:30 J. Wisser, L. Riddiford, M. Veit, P. Li, S. Emori, and Yuri Suzuki,
Stanford University, USA, K. Mahalingam, B. Urwin, B. Howe,
Air Force Research Laboratory, USA, O.van t'Erve, B.T. Jonker,
Naval Research Laboratory, USA, C. Klewe, P. Shafer, A. N'Diaye, E. Arenholz,
Lawrence Berkeley National Laboratory, USA,
“A New Class of Low Loss Spinel Ferrite Films for Spin Current Based
Applications” (invited) 28

09:30-09:45 Henning Riechert, P. Vogt, and O. Bierwagen,
Paul-Drude-Institut für Festkörperelektronik, Germany,
“Growth of Semiconducting Oxides – Challenges and Surprises” 30

09:45-10:00 M. A. Jenkins, J. M. McGlone, J. F. Wager, and John F. Conley, Jr.,
Oregon State University, USA,
“Internal Photoemission Spectroscopy Measurements of Energy Barriers
Between Amorphous Metal/Insulator Heterostructures” 32

10:00-10:30 Satoshi Iwamoto, T. Yamaguchi, Y. Ota, and Y. Arakawa, University of Tokyo,
Japan,
“Valley-Protected Edge State in Semiconductor Photonic Crystal Slab”
(invited) 34

10:30-11:00 Coffee Break

12:30-12:45	<u>Kazuhiko Matsumoto</u> , T. Kawata, K. Yamamoto, T. Ono, Y. Kanai, and K. Inoue, Osaka University, Japan, “Sugar Chain Functionalized Graphene FET for Detection of Virus”	46
12:45-	Lunch and ad hoc sessions	
Session 7 Solar Cells and Novel Devices		
Chair: Wolfgang Porod		
19:00-19:30	H. Esmailpour, V. R. Whiteside, J. Tang, M. B. Santos, and <u>Ian R. Sellers</u> , University of Oklahoma, USA, “Inhibited Hot Carrier Thermalization in Type-II Quantum Wells: A Practical Route to Hot Carrier Solar Cells” (invited)	47
19:30-19:45	<u>David K. Ferry</u> , Arizona State University, USA, “In Search of a True Hot Carrier Solar Cell”	48
19:45-20:00	<u>Stephen Goodnick</u> , Y. Zou, and R. Hathwar, Arizona State University, USA, “Ultrafast Relaxation Processes in Advanced Concept Solar Cell Structures”	49
20:00-20:15	M. Buchhold, California Institute of Technology, USA, S. Diehl and <u>Alexander Altland</u> , Universität zu Köln, Germany, “Nodal Points in Weyl Semimetals Survive the Presence of Weak Disorder”	50
20:15-20:30	<u>Dmitry Pikulin</u> , Microsoft Research, USA, “Quantum Oscillations in Inhomogeneous Weyl Semimetals”	51
20:30-20:45	<u>Josef Weinbub</u> , M. Ballicchia, and M. Nadjalkov, TU Wien, Austria, “Electron Interference in a Double-Dopant Potential Structure”	52
20:45-21:00	<u>Mohammad Al-Mamun</u> , M. Altaf, A. Edrees, and Marius Orlowski, Virginia Tech, USA, “Neuromorphic Semi-Organic Devices on Flexible Substrates”	54

Wednesday, November 28

Session 8 *Quantum Information Systems*

Chair: Victor I. Klimov

- 09:00-09:30 Andrew Sachrajda, National Research Council, Canada,
“Few-Hole Quantum Dots” (invited) 57
- 09:30-9:45 Robert Wolkow, University of Alberta and Quantum Silicon, Canada,
“Atomic Computational Elements Composed of
Silicon Dangling Bonds” 58
- 9:45-10:00 A. Hida and Koji Ishibashi, RIKEN, Japan,
“Formation of Coupled Quantum Dots and Optically Operated Conditional
Gates with Single Wall Carbon Nanotubes” 60
- 10:00-10:30 Mark A. Eriksson, University of Wisconsin - Madison, USA,
“Quantum Control of Silicon Quantum Dot Spin Qubits” (invited) 61
- 10:30-11:00 *Coffee Break*
- 11:00-11:15 Shiro Kawabata, AIST, Japan,
“Integration Technology for Scalable Superconducting
Quantum Annealer” 62
- 11:15-11:30 Aruna N. Ramanayaka, K. Tang, J. A. Haggmann, H.-S. Kim, C. A. Richter, and
J. M. Pomeroy, NIST, USA,
“Magnetotransport in Highly Enriched ^{28}Si for Quantum Information
Processing Devices” 64

Session 9 Van Der Waals 2D Materials I

Chair: Koji Ishibashi

- 11:30-12:00 *D. Yadav and A. Dubinov, Russian Academy of Sciences, Russia, S. Boubanga-Tombet, G. Tamamushi, T. Watanbe, A. Satou, V. Ryzhii, and Taiichi Otsuji, Tohoku University, Japan, M. Rizhii, University of Aizu, Japan, “Terahertz Current-Driven Plasmonic Lasing and Amplification” (invited) 66*
- 12:00-12:30 *Kosuke Nagashio, University of Tokyo, Japan, “Electrically Inert Interface in 2D Heterostructure FETs” (invited) 69*
- 12:30-12:45 *Slava V. Rotkin, Pennsylvania State University, USA, M. Blades, H. Wang, and X. Xu, Lehigh University, USA, H. Q. Ta and M. H. Rummeli, Soochow University, China and Polish Academy of Sciences, Poland, “Near-Field Hyperspectral Imaging of Hybrid Plasmonics in Twisted Graphene” 72*
- 12:45-13:00 *Tomoki Machida, K. Kinoshita, Y. Wakafuji, M. Onodera, M. Arai, S. Masubuchi, and R. Moriya, University of Tokyo, Japan, K. Watanabe and T. Taniguchi, National Institute for Materials Science, Japan, “Cyclotron Resonance Absorption of Mid-Infrared Light in Graphene/h-BN van der Waals Heterostructures” 74*
- 13:00-13:15 *J. Kwon and David B. Janes, Purdue University, USA, S. Das, Kansas State University, USA, C. J. Delker, C. T. Harris, and B. Swartzentruber, Sandia National Laboratories, USA, “Mobility and 1/f Noise in MoS₂ and MoSe₂ Field-Effect Transistors – Understanding the Intrinsic Device” 76*
- 13:15- *Lunch and ad hoc sessions*
- 18:00 *Reception and Banquet*

Thursday, November 29

Session 10 Topological States II

Chair: Henning Riechert

- 09:00-09:30 Joel E. Moore,
University of California and Lawrence Berkeley National Laboratory, USA,
“Novel Optical and Electrical Responses in Topological Materials”
(invited) 79
- 09:30-09:45 M. Kayyalha, A. Kazakov, I. Miotkowski, S. Khlebnikov, Leonid P. Rokhinson,
Y. P. Chen, Purdue University, USA, M. Kargarian, V. M. Galitski, and
V. M. Yakovenko, University of Maryland, USA,
“Induced Superconductivity in Topological-Insulator BiSbTeSe₂
Nanoribbons” 81
- 09:45-10:00 Y. Kim, University of Illinois Urbana-Champaign, USA and Matthew J. Gilbert,
Stanford University, USA,
“Impact of Thermal Fluctuations on Transport in Antiferromagnetic Topological
Dirac Semimetals” 82
- 10:00-10:15 M. Hirsbrunner and T. M. Philip, University of Illinois at Urbana-Champaign,
USA, and Matthew J. Gilbert, Stanford University, USA,
“Topology of the Non-Hermitian Chern Insulator” 84
- 10:15-10:30 Valeria Lauter, Oak Ridge National Laboratory, USA, F. Katmis and
J. S. Moodera, Massachusetts Institute of Technology, USA,
D. Heiman, Northeastern University, USA,
“High-Temperature Magnetic Order in Topological Insulator –
Ferromagnetic Insulator Heterostructures” 86
- 10:30-11:00 Coffee Break
- 11:00-11:15 Tonica Valla, I. K. Drozdov, G. Gu, and I. Bozovic,
Brookhaven National Laboratory, USA,
“Superconducting ‘Glue’ in Cuprates: Disappearance of Superconductivity Due
to Diminishing Coupling in Overdoped Bi₂Sr₂CaCu₂O_{8+δ}” 87

Session 11 *Nanowires and Dots*

Chair: David Janes

- 11:15-11:45 *Daniel Vanmaekelbergh, M. Slot, T. Gardenier, S. Freaney, I. Swart, S. Kempkes, J. vand Broeke, and C. Morais Smith, University of Utrecht, Netherlands, and C. Delerue, IEMN, France,*
“*Honeycomb Semiconductors and Their Artificial Analogs*” (invited) 88
- 11:45-12:00 *A. Geremew and Alexander A. Balandin, University of California Riverside, USA, T. T. Salguero, University of Georgia, USA, S. Rumyantsev, Ioffe Physical-Technical Institute, Russia,*
“*Electron Transport in Quasi-1D ZrTe₃ van der Waals Nanoribbons: Extraordinary High Current Density and Unique Noise Characteristics*” 90
- 12:00-12:15 *Cody Hayashi, T. Yamauchi, Carlos Torres Jr., and R. Ordonez, Space and Naval Warfare Systems Center Pacific, USA, D. Buzzell and S. Das, Pennsylvania State University, USA,*
“*Tunneling-Assisted Relaxation in Hybrid Graphene Quantum-Dot Photodetectors*” 92
- 12:15-12:30 *Heedae Kim, Northeast Normal University China and University of Oxford, UK, J. Kim, Yeungnam University, Republic of Korea, and J. Song, KIST, Republic of Korea,*
“*Optical Studies of Exciton/Biexciton States on a Single Coupled Quantum Dot*” 94
- 12:30-12:45 *Y.-S. Park, J. Lim, and Victor I. Klimov, Los Alamos National Laboratory, USA,*
“*Asymmetrically Strained Quantum Dots with Ultrastable Single-Dot Emission Spectra and Subthermal Room-Temperature Linewidths*” 96
- 12:45- *Lunch and ad hoc sessions*

Session 12 Posters

19:00-21:00

- P1 *F. Kargar, E. Aytan, J. S. Lewis, and Alexander A. Balandin,
University of California Riverside, USA, E. H. Penilla and J. E. Garay,
University of California San Diego, USA,
“Acoustic Phonon Spectrum Engineering in Bulk Crystals via Incorporation of
the Size-Dissimilar Dopant Atoms”* 98
- P2 *Gautam Gaddemane, M. L. Van de Put, and M. V. Fischetti,
University of Texas at Dallas, USA,
“Performance Analysis of a 10 nm Phosphorene
Double-Gate MOSFET”* 100
- P3 *Jubin Nathawat, M. Zhao, C.-P. Kwan, H. Ramamoorthy, J. E. Han, and
J. P. Bird, State University of New York at Buffalo, USA,
G.-H. Kim, Chinese Academy of Sciences, China,
N. Matsumoto, M. Matsunaga, and N. Aoki, Chiba University, Japan,
K. Watanabe and T. Taniguchi, National Institute for Materials Science, Japan,
“Transient Investigation of Hot-Carrier Transport in BN-Encapsulated
Graphene FETs”* 102
- P4 *Bilal Barut, E. Einarsson, J. M. Jornet, and J. P. Bird,
State University of New York at Buffalo, USA,
G. R. Aizin, Kingsborough Community College, USA, and T. Sugaya, AIST,
Japan,
“Realizing Asymmetric Boundary Conditions for Plasmonic THz Wave
Generation in HEMTs”* 104
- P5 *Seong Hyeok Jeon, Y. H. Chang, J. Seo, and M. Shin,
Korea Advanced Institute of Science and Technology, Republic of Korea,
“DFT Hamiltonian Based Simulation of GaSb UTB-FET with
Spin Orbit Coupling Effect”* 106
- P6 *Yasuyuki Miyamoto, N. Kise, and R. Aonuma,
Tokyo Institute of Technology, Japan,
“GaAsSb/InGaAs Double Gate Tunnel FET Operating Below 60 mV/Decade
and Temperature Dependence of Band-Edge Decay Parameters”* 108

- P7 *Michael D. Randle, A. Kumar, K. He, C.-P. Kwan, J. Nathawat, R. Dixit, S. Yin, N. Arabchigavkani, U. Singiseti, and J. P. Bird, State University of New York at Buffalo, USA, A. Lipatov, P. A. Dowben, and A. Sinitskii, University of Nebraska-Lincoln, USA, “Electrical Characterization of Thin, Quasi-1D Titanium Trisulfide (TiS₃) Field Effect Transistors” 110*
- P8 *Z.-T. Ao, F. Shan, H.-S. Kim, H.-B. Guo, J.-Y. Lee, and Sung-Jin Kim, Chungbuk National University, Republic of Korea, “Solution Processed Indium Zinc Oxide Thin-Film Transistors with Nanoscale Multi Stacking Channel Layer” 112*
- P9 *F. Shan, Z.-T. Ao, H.-S. Kim, H.-B. Guo, J.-Y. Lee and Sung-Jin Kim, Chungbuk National University, Republic of Korea, “Enhanced Electrical Properties of TiO₂-Based Oxide Thin Film Transistor by a Femtosecond Laser Irradiation” 114*
- P10 *Futo Hashimoto and N. Mori, Osaka University, Japan, “Impact of Lattice Matching Condition on the Simulation of Band-to-Band Tunneling in MoS₂/Ge van der Waals Heterojunctions” 116*
- P11 *Takaya Mishima, F. Hashimoto, and N. Mori, Osaka University, Japan, “Modeling of Inter-Layer Tunneling Between Semiconductor Nanoribbons” 118*
- P12 *N. Nishizawa, T. Takahashi, and Hiro Munekata, Tokyo Institute of Technology, Japan, T. Kuchimaru, Jichi Medical University, Japan, “Preparation of a Phantom: A Step Toward Application of a Spin-LED for Unstained and Non-Invasive Cancer Detection” 120*
- P13 *Junbeom Seo, S. H. Jeon, and M. Shin, Korea Advanced Institute of Science and Technology, Republic of Korea, “A Variability Study of Ferroelectric Tunnel Junction” 122*
- P14 *V. Sverdlov, A. Makarov, and Siegfried Selberherr, TU Wien, Austria, “Fast, Reliable and Field-Free Perpendicular Magnetization Reversal in Advanced Spin-Orbit Torque MRAM by Two-Pulse Switching” 124*

- P15 Zhu Diao, K. Yang, and D. G. Cahill,
University of Illinois at Urbana-Champaign, USA,
“Magnetic Anisotropy of KNiF₃ Single Crystals Investigated by
Torque Magnetometry” 126
- P16 Shintaro Makihira and N. Mori, Osaka University, Japan,
“Zero-Eigenvalue Method for Solving the Barker-Ferry Equation in One-
Dimensional Systems” 128

Friday, November 30

Session 13 Van Der Waals 2D Materials II

Chair: John F. Conley, Jr.

- 08:30-09:00 Christopher L. Hinkle, University of Notre Dame, USA,
“Low-Temperature Growth for 3D Integration of 2D Materials”
(invited) 130
- 09:00-09:15 Curt A. Richter, S. T. Le, and A. Balijepalli,
National Institute of Standards and Technology, USA, and N. D. Amin and
H. C. Pant, National Institutes of Health, USA,
“Quantum-Limited Monolayer MoS₂ pH and Biosensors” 132
- 09:15-09:30 A. T. Hanbicki, H.-J. Chuang, M. R. Rosenberger, C. S. Hellberg, S. V. Sivaram,
K. M. McCreary, I. I. Mazin, and Berend T. Jonker,
Naval Research Laboratory, USA,
“Double Indirect Interlayer Exciton in a MoSe₂/WSe₂
van der Waals Heterostructure” 134
- 09:30-09:45 Masashi Kawasaki, K. S. Takahashi, K. Maruhashi, M. S. Baharamy, H. Ishizuka,
R. Kurihara, A. Miyake, S. Shimizu, T. Murata, Q. Y. Wang, M. Tokunaga,
Y. Tokura, and N. Nagaosa, RIKEN and University of Tokyo, Japan,
“Quantum Transport in a Magnetic Semiconductor Oxide” 136

- 09:45-10:15 *M. Bonilla, P. Coelho Neto, S. Kolekar, V. Kalappattil, M.-H. Phan and Matthias Batzill, University of South Florida, USA, “Magnetism in Monolayer Transition Metal Dichalcogenides” (invited)* 138
- 10:15-10:45 *Coffee Break*
- Session 15** **Spin Photonics**
Chair: Viktor Sverdlov
- 10:45-11:15 *Hayk Harutyunyan, Emory University, USA, A. Govorov, Ohio University, USA, S. K. Gray and G. Wiederrecht, Argonne National Laboratory, USA, “Enabling Optically Forbidden Transitions by Extreme Localization of Light” (invited)* 140
- 11:15-11:45 *Igor Zutic, State University of New York at Buffalo, USA, “Spintronics Beyond Magnetoresistance: From Spin-LEDs to Spin-Lasers” (invited)* 142
- 11:45-12:00 *Hiro Munekata and N. Nishizawa, Tokyo Institute of Technology, Japan, “Realization of Pure Circular Polarization Electroluminescence at Room Temperature with Spin-LEDs”* 144
- 12:00-12:15 *Mehdi Alouini, J. Frougier, and J. M. George, CNRS, France, A. Joly, G. Baili and D. Dolfi, Thales Research & Technology, France, “Modelling Framework for Predicting Polarization Behavior of Spin-Controlled VCSELs and its Experimental Validation”* 146
- 12:15-12:30 *M. Lindemann, M. R. Hofmann, and Nils Gerhardt, Ruhr-University Bochum, Germany, T. Pusch, and R. Michalzik, Ulm University, Germany, G. Xu and I. Zutic, State University of New York at Buffalo, USA, “Ultrafast Birefringent Spin-Lasers”* 148
- 12:30** **Closing Session**
Stephen Goodnick
Josef Weinbub

**Quantum Hall Effect and the New SI System:
The Biggest Revolution in Metrology since the French Revolution**

Klaus v. Klitzing¹

*¹Max-Planck-Institut für Festkörperforschung, D-70569 Stuttgart
K.Klitzing@fkf.mpg.de*

It is expected that at the time of the WINDS Workshop the General Conference on Weights and Measures (CGPM) has decided at their meeting on 16.11.2018 to introduce on 20.5.2019 a new international system of units based on constants of nature. The Quantum Hall Effect played an important role in this development and the talk will summarize the development.

Superconductivity in the Quantum Hall Regime

Andrew Seredinski¹, Anne Draelos¹, Ming-Tso Wei¹, Lingfei Zhao¹, Ethan Arnault¹, Chung-Ting Ke¹, Tate Fleming², Yash Mehta², Ethan Mancil², Hengming Li², Takashi Taniguchi³, Kenji Watanabe³, Seigo Tarucha^{4,5}, Michihisa Yamamoto^{4,5}, Ivan Borzenets⁶, François Amet², and Gleb Finkelstein¹

¹*Department of Physics, Duke University, Durham, NC 27708, USA*

²*Department of Physics, Appalachian State University, Boone, NC 28607, USA*

³*Advanced Materials Laboratory, NIMS, Tsukuba 305-0044, Japan*

⁴*Department of Applied Physics, University of Tokyo, Bunkyo-ku, Tokyo 1-8656, Japan*

⁵*Center for Emergent Matter Science (CEMS), RIKEN, Wako-shi, Saitama 351-0198, Japan*

⁶*Department of Physics, City University of Hong Kong, Kowloon, Hong Kong SAR*
gleb@duke.edu

One of the promising routes towards creating novel topological states and excitations is to combine superconductivity with quantum Hall (QH) effect. However, signatures of superconductivity in the QH regime remain scarce, and a superconducting current through a QH weak link has until recently eluded experimental observation. Here, we explore high mobility graphene/boron nitride heterostructures contacted by type II superconducting electrodes that could withstand magnetic fields of a few Tesla. At low magnetic fields, our devices demonstrate the Fraunhofer pattern and Fabri-Perot oscillations, confirming their uniformity and ballisticity [1]. At fields of 1-2 Tesla, when Landau quantization is fully developed, regions of superconductivity can be observed on top of the conventional QH fan diagram [2]. The measured supercurrent is very small, on a few nA scale, and periodic in magnetic field. Additional measurements on side- and top-gated samples shed light on the alternative mechanisms that mediate supercurrent along the QH edge states [3-5]. Finally, we demonstrate the evidence of the “Andreev edge states” – single particle electron-hole hybrid states propagating along the QH-superconductor boundary [6].

[1] I.V. Borzenets et al., Phys. Rev. Lett. **117**, 237002 (2016)

[2] F. Amet et al., Science **352**, 966 (2016)

[3] A.W. Draelos et al., J. Low Temp. Phys. **191**, 288 (2018)

[4] A. Seredinski et al., MRS Adv. **3** (2018)

[5] A. Seredinski et al., preprint (2018)

[6] L. Zhao et al., preprint (2018)

Various Spin Current Phenomena in Condensed Matter

Eiji Saitoh¹⁻⁵

¹*ERATO-SQR, JST, Tokyo 102-0076, Japan*

²*Department of Applied Physics, The University of Tokyo, Tokyo 113-8656, Japan*

³*WPI- AIMR, Tohoku University, Sendai, Miyagi 980-8577, Japan*

⁴*IMR, Tohoku University, Sendai, Miyagi 980-8577, Japan*

⁵*ASRC, JAEA, Tokai, Ibaraki 319-1195, Japan*

eizi@ap.t.u-tokyo.ac.jp

Various types of spin current have been found in condensed matter. Such currents give rise to various functions of matter, and they have led the recent progress of spintronics. The firstly discovered spin current is so called conduction-electron spin current, detected in terms of the inverse spin Hall effect [1]. Secondly, we found spin-wave spin current in ferromagnetic materials, in which spin waves carry angular momentum when their population is antisymmetric in the momentum space. Spin-wave spin current can also be created by heat current, which we named the spin Seebeck effect. The concept of spin-wave spin current was expanded to other magnetically ordered phases such as antiferromagnets. Thirdly, we recently found that spin current can also be carried by spinons [2]; excitation from quantum spin liquid states. I will give an introduction to spin-wave spin current phenomena in antiferromagnets [3,4] with a well-defined Neel vector, spinon-spin injection into 1D quantum spin liquids, spin induced phenomena in antiferromagnets with DM interaction, and some related spin-current effects in antiferromagnets. Spin current generation from micromechanical motion will also be mentioned [5] in my talk.

Acknowledgments: I would like to thank Dr. D. Hou, Dr. Z. Qiu, Dr. D. Hirobe, Dr. T. Kikkawa, Dr. Y. Shiomi, Dr. K. Yamamoto, Prof. Y. Tserkovnyak, O. Gomonay, and G.E.W. Bauer for the fruitful collaboration.

[1] E. Saitoh et al., Appl. Phys. Lett. **88**, 182509 (2006)

[2] D. Hirobe et al., Nat. Phys. **13**, 30 (2017)

[3] Z. Qiu et al., Nat. Comm. **7**, 12670 (2016)

[4] Z. Qiu et al., Nat. Mater. **17**, 577 (2018)

[5] R. Takahashi et al., Nat. Phys. **12**, 52 (2015)

Spin Wave Devices: Progress Update

Alexander Khitun¹

¹*Department of Electrical and Computer Engineering, University of California -Riverside,
Riverside, California, USA 92521
akhitun@engr.ucr.edu*

We provide a comprehensive progress update on spin wave devices. Spin wave propagation does not involve electric current but a collective oscillation of spins. First, we will present experimental data showing a pure spin current control using spin wave interference. The data are collected in the $Y_3Fe_2(FeO_4)_3$ waveguide using Brillouin-Mandelstam spectroscopy. It was observed the oscillation of the scattered light intensity depending on the relative phase of the interfering spin waves as far as 7.5 mm away from the spin-wave generating antennas at room temperature. Second, we will present a spin wave modulator based on synthetic multiferroic structure comprising piezoelectric and magnetostrictive materials. We present experimental data on a prototype consisting of a piezoelectric $[Pb(Mg_{1/3}Nb_{2/3})O_3]_{(1-x)}-[PbTiO_3]_x$ substrate, and 30 nm layer of magnetostrictive Ni film, where the film is attached to a 30 nm thick $Ni_{81}Fe_{19}$ spin wave bus. The modulation of the spin wave signal in $Ni_{81}Fe_{19}$ is obtained by ± 0.3 MV/m electric field applied across the piezoelectric layer. The On/Off ratio exceeds 300% at 80 μm away from the excitation port at room temperature. Finally, we will present experimental data on the spin wave magnetometer in the active ring configuration. The response to the magnetic field variation exceeds 0.5 V per 1 Oe. The measured noise power is about 1 nV/ \sqrt{Hz} . All measurements are done at room temperature.

Acknowledgments: This was supported in part by the Spins and Heat in Nanoscale Electronic Systems (SHINES), an Energy Frontier Research Center (Center Director: Dr. Jing Shi) funded by the U.S. Department of Energy, Office of Science, Basic Energy Sciences (BES) under Award # SC0012670. The work on spin wave magnetometer was supported by the National Science Foundation under the SBIR Award #1819705 (Program Director: Dr. Murali Nair).

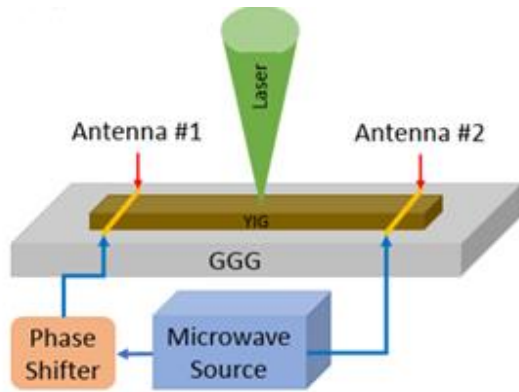


Fig.1: Schematics of the experimental setup. The test structure consists of a YIG waveguide with two micro-antennas fabricated on top. The length of the channel is 16 mm, the width is 2 mm.

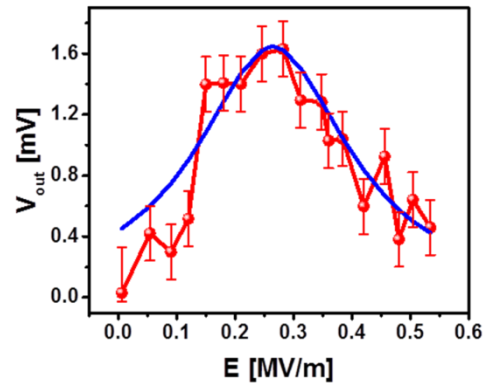


Fig.4: Experimental data showing the output characteristics of the spin wave modulator. Red markers and red curve show the inductive voltage in mV produced by the propagating spin-waves.

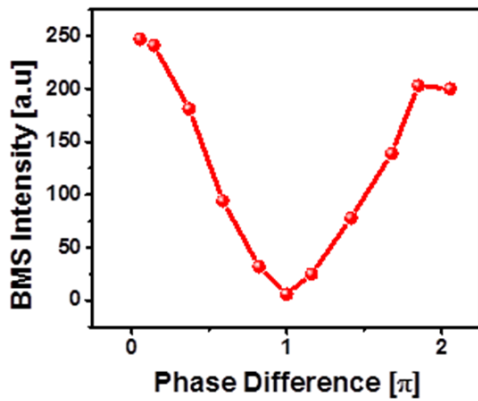


Fig.2: Experimental data showing the oscillation of the BMS intensity as a function of the phase difference between the spin waves excited by antennas #1 and #2.

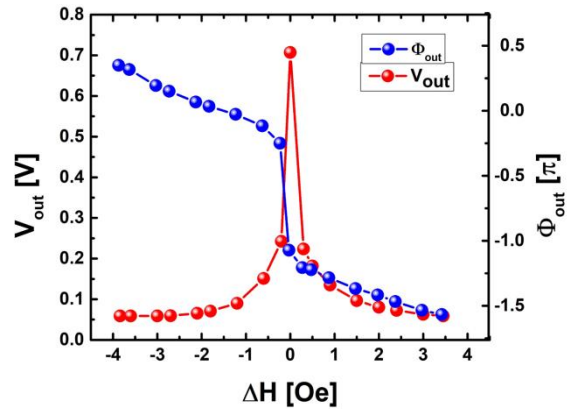


Fig.5 Experimental data showing the response of the spin wave magnetometer. The red and the blue markers correspond to the amplitude and the phase of the output inductive voltage.

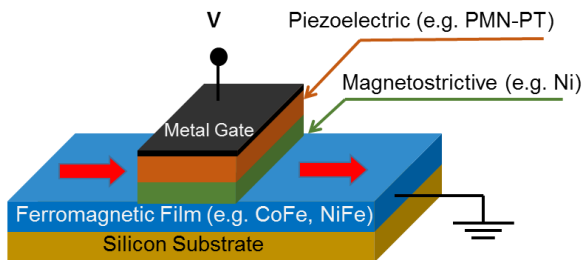


Fig.3: Schematics of the spin-wave modulator. It consists of a semiconductor substrate (e.g. silicon), a piezoelectric layer (e.g. PMN-PT), and a spin wave bus (e.g. CoFe, NiFe).

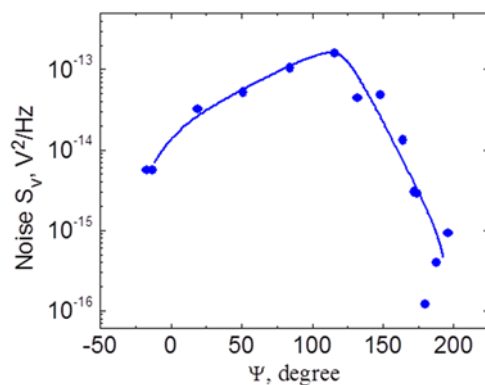


Fig.6: Experimental data: noise power as a function of the phase difference between the interfering spin waves. All measurements are done at room temperature.

Shot Noise Enhancement at Spin-dependent Hopping

Viktor Sverdlov¹ and Siegfried Selberherr²

¹*Christian Doppler Laboratory for Nonvolatile Magnetoresistive Memory and Logic at the*

²*Institute for Microelectronics, TU Wien, Gußhausstraße 27-29, 1040 Vienna, Austria*

Viktor.Sverdlov@TUWien.ac.at

Coulomb repulsion induces correlations between electrons and makes charge transport at hopping in one-dimensional chains more “continuous” [1] by preventing two electrons from occupying the same site and maintaining a certain average distance between the carriers in the chain. The Fano factor $F = S(\omega = 0)/(2eI)$ defined as the ratio of the spectral current density fluctuations at low frequency $S(\omega = 0)$ to the stationary current I (times 2 the electron charge e) is a useful measure characterizing the smoothness of the transport process: The smaller the Fano factor, the more regular the charge transport. For a single-trap assisted hopping between two normal metal electrodes the Fano factor is reduced from 1 and takes the minimum value of $\frac{1}{2}$ at equal tunneling rates to/from the trap.

The Pauli exclusion principle results in spin-driven correlations [2] as it forbids two electrons with the same spin projection to occupy the same trap state. At trap-assisted hopping from a normal metal source electrode ($\mathbf{p}_s=0$) to a ferromagnetic (FM) drain electrode, Fig.1, the finite spin on a trap leads to large magnetoresistance [3], [4] (Fig.2). We analyze the shot noise/Fano factor.

Fig.3 shows that, in contrast to spin-independent hopping, the shot noise is significantly enhanced to $F=3$, where the current is small. It implies that the electrons are transferred in bunches of three electrons in average separated by longer waiting times. At spin-dependent tunneling between two FM electrodes (Fig.1) the shot noise can be enhanced (Fig.4) at the current maximum as well (Fig.5). Although the correlations between the current and the noise are opposite to the case of tunneling from a normal metal to a FM electrode, in both cases the noise enhancement is due to spin correlations. Strong spin dephasing reduces the shot noise at some angles between the magnetic field and the drain FM below unity, however, dephasing does not reduce the Fano factor at the maximum (Fig.6).

[1] A.N. Korotkov and K.K. Likharev, Phys. Rev. B **61**, 15975 (2000)

[2] Y. Wang et al., Phys. Rev. X, **6**, 011011 (2016)

[3] Y. Song and H. Dery, Phys. Rev. Lett. **113**, 047205 (2014)

[4] V. Sverdlov et al., WINDS 2017; Solid-State Electron., submitted (2018)

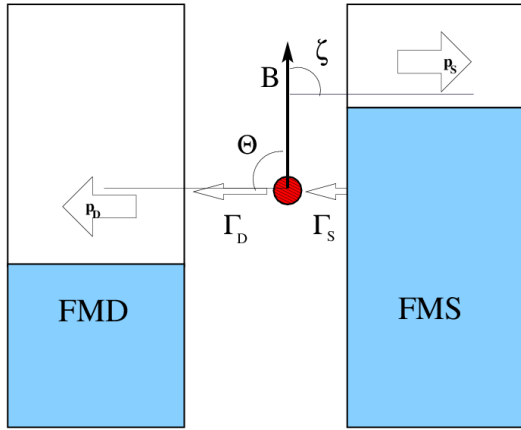


Fig.1: The ferromagnetic source (FMS)/drain(FMD) polarizations $\mathbf{p}_{S,D}$ form angles Θ and ζ, φ with respect to the magnetic field \mathbf{B} . The trap is coupled by the rates $\Gamma_{S(D)}$ to FMS (FMD).

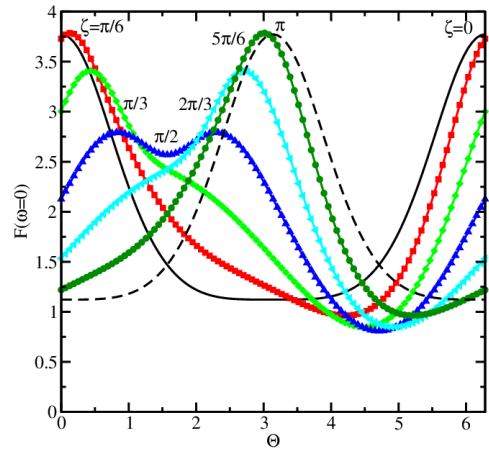


Fig.4: Shot noise at hopping between the source and drain ferromagnetic electrode as a function of Θ for several ζ . $\Gamma_S=5\Gamma_D$, $\omega_L=\Gamma_D$, $p_S=p_D=0.8$. There is no spin relaxation nor dephasing.

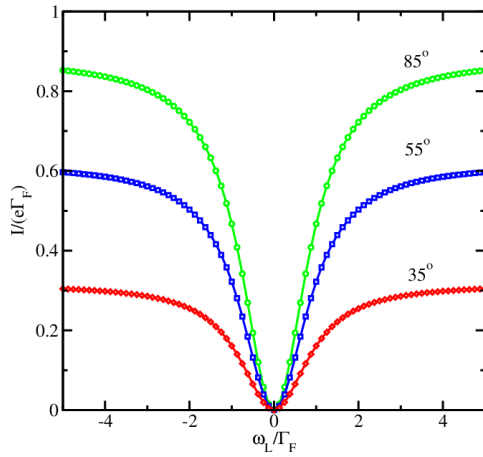


Fig.2: Trap-assisted tunneling magnetoresistance at tunneling from a normal metal to a ferromagnetic electrode, for several angles between the field \mathbf{B} and \mathbf{p}_D , for $p_S=0$. $\Gamma_F = \omega_L$, $|\mathbf{p}|=1$, $\Gamma_N = 8\Gamma_F$.

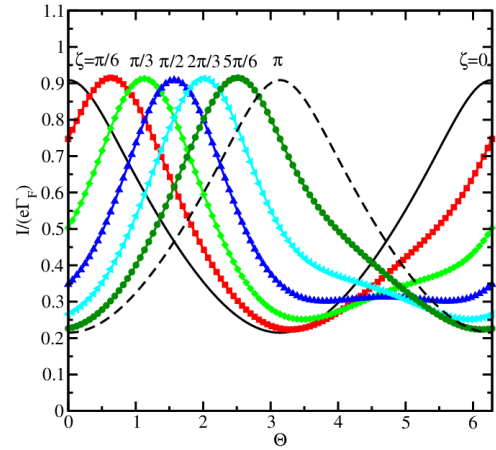


Fig.5 Trap-assisted tunneling current between the source and drain ferromagnetic electrode as a function of Θ for several ζ . $\Gamma_S=5\Gamma_D$, $\omega_L=\Gamma_D/2$, $p_S=p_D=0.8$. There is no spin relaxation nor dephasing.

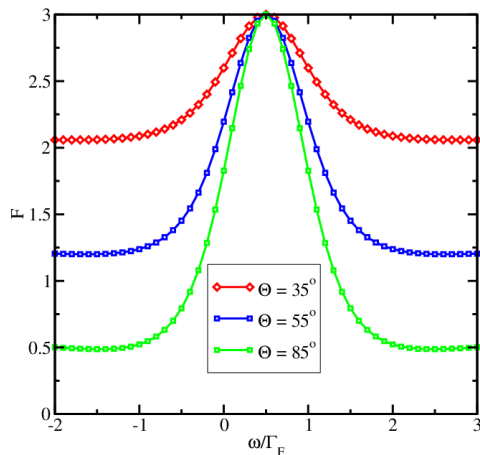


Fig.3: Fano factor at spin-dependent hopping as a function of the Larmor frequency, for several angles between the magnetization and the magnetic field.

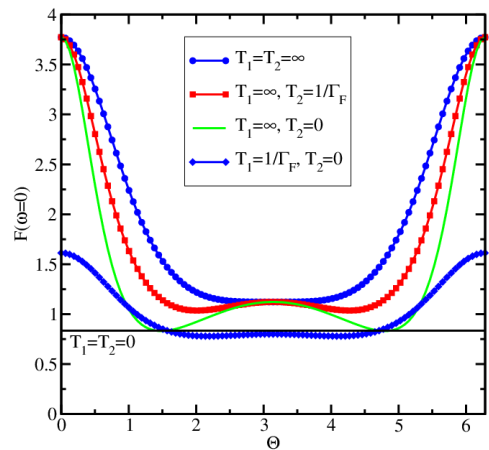


Fig.6: Effect of spin relaxation and dephasing on shot noise as a function of Θ for $\zeta, \varphi = 0$. The parameters are: $\Gamma_S=5\Gamma_D$, $\omega_L=\Gamma_D/2$, $p_S=p_D=0.8$.

Electrically Detected Magnetic Resonance in SiC Metal Oxide Semiconductor Field Effect Transistors

Patrick M. Lenahan¹

¹*The Pennsylvania State University, Engineering Science and Mechanics,
University Park, Pennsylvania, USA
pmlesm@engr.psu.edu*

Silicon carbide is among the most promising materials for electron spin-based quantum computing and other spintronic applications [1,2]. This is so for several reasons. Long decoherence times are key features in choosing systems suitable for such applications. Spin-orbit coupling and electron-nuclear hyperfine interactions are the most important factors in determining these decoherence times. Since both silicon and carbon nuclei have relatively small spin-orbit coupling effects due to the relatively small nuclei, and since only 1.1% of carbon nuclei and 4.7% of silicon nuclei have nuclear magnetic moments, SiC is an exceptionally strong candidate for these applications. Also, since carbon and silicon are both relatively small atoms, it is relatively easy to greatly reduce the percentage of magnetic nuclei. At the present time, spin-based quantum computing and some other aspects of spintronic research have focused primarily upon defect centers in diamond. Diamond, like SiC, can be home to multiple long decoherence time defects. However, it has been difficult to make high quality electrical measurements in diamond-based devices. Thus, it is difficult to envision a diamond-based device in which spin states are accessed via a purely “electronic” measurement. An additional difficulty for diamond-based devices is very high cost. Silicon carbide is far more attractive as an “electronic” material. It is one of only two materials in which high quality native oxides can be grown which are suitable for the construction of metal oxide semiconductor field effect transistors (MOSFETs). SiC devices, MOSFETs in particular, are exceptionally well-suited for electrically detected magnetic resonance (EDMR) detection. The existence of relatively high quality SiC MOSFETs provides the opportunity for potentially useful detection in which paramagnetic defects, in effect, may be turned “on” or “off” with the application of a gate voltage. We have explored electrically detected magnetic resonance (EDMR) of various point defects in 4-H SiC MOSFETs via multiple techniques.[3,4] Of greatest potential interest to spin based quantum computing and other spintronic applications is EDMR through the application of a periodic low to relatively high frequency (Hz to MHz) trapezoidal gate voltage waveforms, spin dependent charge pumping (SDCP). Utilizing SDCP, we detect multiple paramagnetic centers in 4H SiC MOSFETs with high sensitivity, including the silicon vacancy, which has been proposed as a strong candidate for spintronic and quantum computing applications.

The paramagnetism of these defects can be turned on or off rapidly, over a period of a microsecond or less. The EDMR detection offers several additional advantages, among them, a nearly field and frequency independent sensitivity.

- [1] M. Widmann et al., Nat. Mater. **14**, 164 (2015)
- [2] P.G. Baranov et al., Phys. Rev. B **83**, 125203 (2011)
- [3] C. J. Cochrane et al., Appl. Phys. Lett. **100**, 023509 (2012)
- [4] M. A. Anders et al., J. Appl. Phys. **122**, 234503 (2017)

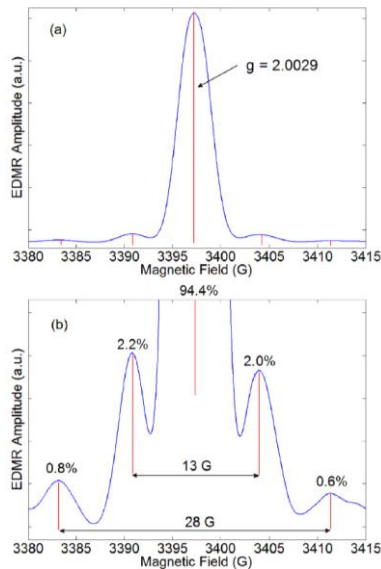


Fig.1: EDMR results on a 4H SiC MOSFET at (a) low and (b) high gain. The traces were taken at X-band with the magnetic field oriented along the SiC crystal c-axis. Although broadening of the EDMR response completely obscures the ^{29}Si hyperfine interactions, the ^{13}C hyperfine peaks are clearly visible.

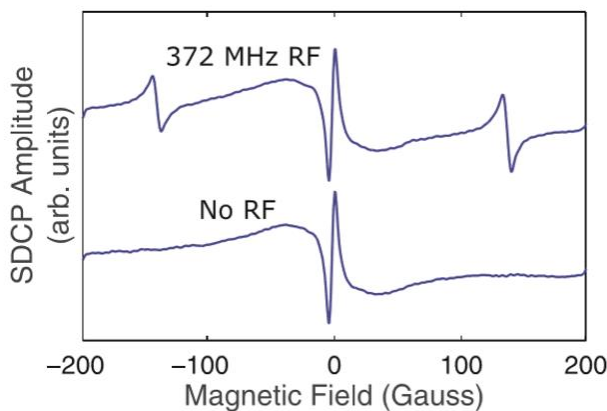


Fig.3: This figure illustrates: (above) the very high EDMR sensitivity obtained from a 4H-SiC MOSFET in an SDCP EDMR measurement at a very low magnetic resonance frequency, 372 MHz. Note also the near zero field SDCP response at a magnetic field around zero. (The trace below, with the RF magnetic field turned off shows that the near zero field response is not affected by the presence or absence of the RF field.

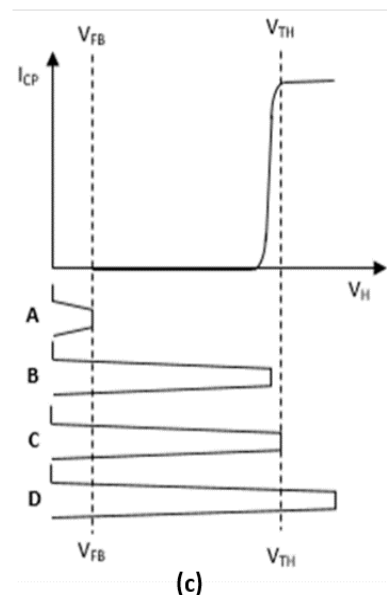
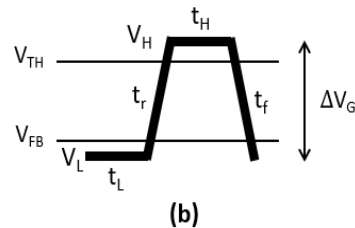
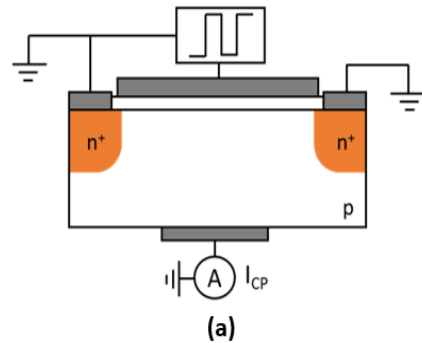


Fig.2: (a) shows the charge pumping biasing scheme, the pulse waveform is shown in (b) and an idealized charge pumping current vs. pulse height is illustrated in fig. (c).

Ultimate Electronics With Silicon Nanowire MOSFETs

Akira Fujiwara¹

¹*NTT Basic Research Laboratories, NTT Corporation 3-1, Morinosato Wakamiya,
Atsugi, Kanagawa 243-0198, Japan
fujiwara.akira@lab.ntt.co.jp*

Scaling of silicon MOSFETs has been predicted to stop around 10 nm and there have been an increasing number of researches for developing beyond CMOS devices using other materials. On the other hands, silicon nanoscale MOSFETs fabricated by the mature device technology show excellent stability and gate control with tiny leakage current, which would be promising for electronic devices requiring high precision and high sensitivity.

We have been developing tunable-barrier single-electron pumps using silicon nanowire MOSFETs for future quantum current standards in metrology. We have so far reported a quantum dot pump with the transfer accuracy better than 0.92 ppm at 1 GHz [1] and a single-trap electron pump [2] using a localized trap state in silicon, which operated up to 6.5 GHz with 20 ppm accuracy [3].

We have also developed feedback control schemes of single electrons with a charge sensor to demonstrate thermal noise suppression [4] and current/power generation by Maxwell demon [5] in silicon nanowire MOSFETs, thereby providing a platform for studying the statistical physics and thermodynamics of nanoscale systems.

Recently, our nanoscale transistors have been successfully applied to blood serum ionogram where the SiO₂ surface of the channel exhibits an anomalous response to multiple cations in liquid [6].

We believe that all these achievements will open up the possibility of diverse applications of silicon nanowire MOSFETs. In the presentation I will talk about some of our recent work based on the charge manipulation and sensing capabilities towards realizing future ultimate electronics.

[1] G. Yamahata et al., Appl. Phys. Lett. **109**, 013101(2016)

[2] G. Yamahata et al., Nat. Comm. **5**, 5038 (2014)

[3] G. Yamahata et al., Sci. Rep. **7**, 45137 (2017)

[4] K. Chida et al., Appl. Phys. Lett. **107**, 073110 (2015)

[5] K. Chida et al., Nat. Comm. **8**, 15310 (2017)

[6] R. Sivakumarasamy et al., Nat. Mater. **17**, 464 (2018)

Performance Evaluation of Multichannel Silicon Nanowire Transistors

Asen Asenov¹, Talib Al-Ameri¹, and Vihar Georgiev¹

¹*The University of Glasgow, Glasgow, UK*

Asen.Asenov@glasgow.ac.uk

All Gate Around (AGA) silicon (Si) Nanowire Transistors (NWTs) have the ultimate electrostatic integrity and are considered as suitable candidates for 5nm CMOS technology and beyond [1]. Their operation is governed by strong quantum confinement effects and non-equilibrium quasi-ballistic transport. Therefore the Ensemble Monte Carlo transport simulations are the best vehicle for studying of their performance. Here we report a comprehensive EMC simulation study of NWTs suitable for 5nm CMOS technology generation. The quantum confinement effects are properly taken into account in the MC simulations using the effective quantum potential approach based both on the solution of the Poisson-Schrodinger (PS) equation and on the Density Gradient (DG) algorithm. The impact of the NWT cross sectional shape, channel orientation and strain are taken into consideration. The simulations are carried out with GARAND (Synopsys). Due to the heavy computational requirements only single NWT are simulated using the EMC approach. Multi-channel NWTs with complex contact arrangements are simulated using the Drift Diffusion (DD) approach meticulously calibrated to the EMC simulations. The study concludes with the optimal NWT design, meeting the requirements for the 5nm CMOS technology and beyond. The DD simulations are also used to evaluate the statistical variability in the multichannel NWTs.

The cross section of the single channel Si NWT used in the EMC simulations is illustrated in Fig.1. The quantum mechanical charge distribution in the cross section of the simulated NWTs with different shape is illustrated in Fig. 2. Fig. 3 presents the dependence of the mobile charge in the NWT channel as a function of the gate bias. A very interesting observation is that the largest amount of mobile charge is available in NWTs with elliptical cross section obeying the Golden Rule (GR) ratio as illustrated in Fig. 4. The EMC simulations also confirm that the GR NWT has the best drive current performance as illustrated in Fig. 5. The simulation domain for the multi-channel Si NWTs used in the DD simulations calibrated in respect of the EMC simulations are illustrated in Fig. 6. Results for the performance of the multi-channels NWTs will be presented at the conferences together with a comprehensive study of the corresponding variability.

[1] J.-P. Colinge, FinFETs and Other Multi-Gate Transistors (Springer, 2008)

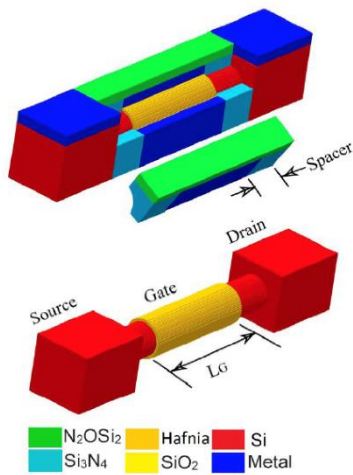


Fig.1: Cross section of the single channel Si NWT used in the EMC simulations.

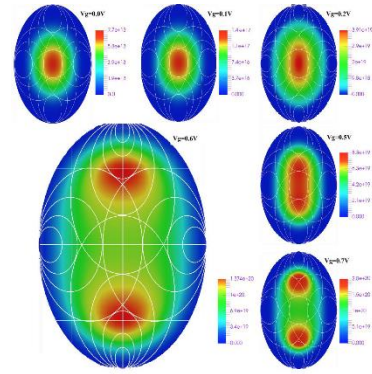


Fig.4: Normalized current as a function of the position x relative to silicon, for $p=1$, $\Gamma_N=\Gamma_0 \exp(-x/d)$, $\Gamma_F=\Gamma_0 \exp(-(d-x)/d)$, $T_2=T_1$, $\omega_L T_2 = \Gamma_0 T_2 = 10$,

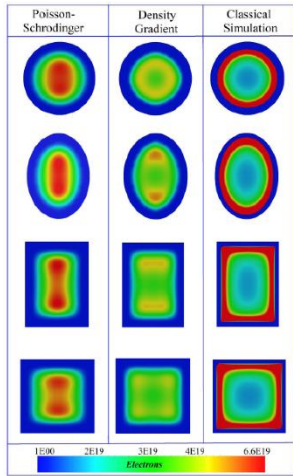


Fig.2: Quantum mechanical charge distribution in the cross section of the simulated NWTs with different shape.

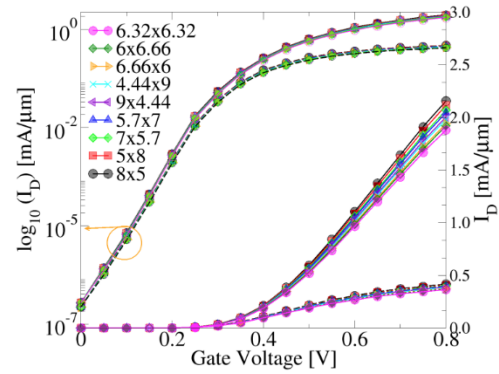


Fig.5 Current as a function the gate voltage for NWT with different cross section obtained from the EMC simulations.

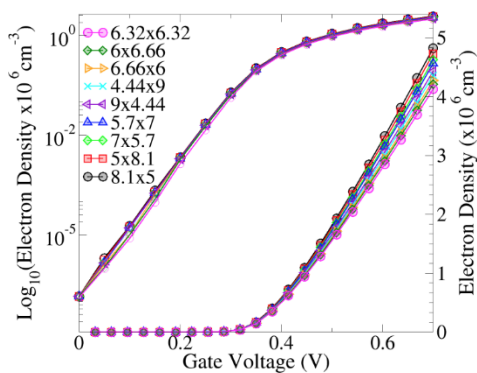


Fig.3: Dependence of the mobile charge in the NWT channel as a function of the gate bias.

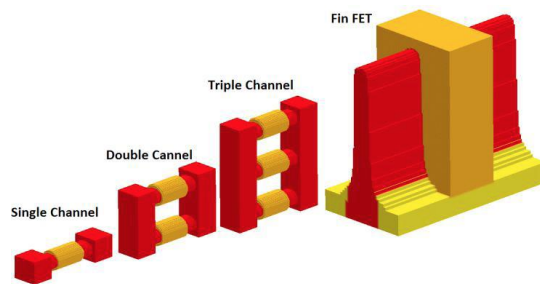


Fig.6: DD simulation domain for evaluating the performance of multichannel NWTs.

Fully-Coupled Electronic-Ionic and Thermal Transport Simulation of Metal Oxide Memristors

Denis Mamaluy¹ and Xujiao Gao¹

¹*Sandia National Laboratories, Albuquerque, New Mexico, USA*

mamaluy@sandia.gov

As modern field effect transistors (FETs) scale down into the sub-10-nm regime, the approaching end of CMOS scaling becomes evident. Thus, recently, we have performed [1] a series of fully quantum-mechanical three-dimensional charge-self-consistent transport simulations and optimizations to show that all FETs, irrespective of their channel material, will reach a fundamental downscaling limit around 4-5 nm technology node, due to unacceptably high levels of thermally induced errors. To investigate alternatives to FET/CMOS scaling, many emerging devices and technologies have been under active research in recent years. Among them, transition metal oxide-based memristors have become one of the strongest candidates to replace flash, and possibly DRAM and SRAM in the near future [2]. Moreover, memristors have a high potential to enable beyond-CMOS technology advances in novel architectures for high performance computing [3]. However, despite the spectacular progress in experimental demonstration and fabrication of oxide memristors, their microscopic transport theory and even some key operational principles, essential to advance experimental progress, remain uncertain [4].

To facilitate the understanding of physical switching mechanisms and accelerate experimental development in oxide memristors, we have developed a 3D fully-coupled electrical and thermal transport model [5] that solves simultaneously the time-dependent continuity equations for electrons, holes, and oxygen vacancies, the time-dependent heat equation including Joule heating sources, and the Poisson equation for all the charged species. The model captures the most of the important processes that drive memristive switching, including field-drift due to the electrochemical potential gradient, Fick diffusion due to the concentration gradient, and the Soret effect due to the temperature gradient. To properly simulate the movement of oxygen vacancies, the rigid point ion model [5] is used, in which the vacancy velocity exponentially depends on the temperature and the electric field when the field exceeds a critical value. The fully-coupled equations and relevant physical models are implemented in CHARON, a multi-dimensional parallel TCAD code developed at Sandia National Labs. CHARON is built upon the open-source Trilinos packages [6], which support finite element and finite volume discretization methods, state-of-the-art nonlinear and linear solvers, MPI parallel capability, and many more.

It can simulate arbitrary device geometry and supports multi-physics capability (i.e., allowing for solving different equations in different regions).

The coupled model described above has been applied to simulate the switching process in a 3D filamentary tantalum oxide memristor shown in Fig. 1(a). The layer material and thickness come from an experimental device published in Ref. [7].

Making use of the multi-physics capability in CHARON, we solve the coupled Poisson, electron, oxygen vacancy, and heat equations in the active Ta and conduction filament (CF) regions, with vacancies confined in Ta and CF regions, while in the Pt and Ta₂O₅ regions, due to absence of mobile vacancies, the coupled Poisson, electron, and heat equations are solved, with Pt treated as a highly doped n-type semiconductor using immobile dopants, and Ta₂O₅ as an undoped semiconductor. Holes are excluded here due to the n-type nature of TaOx memristors. Extensive simulations show that both field drift and thermal processes play crucial roles in determining the switching dynamics of the bipolar TaOx device. Specifically, (i) during OFF switching, when a sufficient negative voltage is applied to the top Pt electrode, Joule heating causes the increase of temperature with the hottest spot located in the CF, and consequently, oxygen vacancies move away from CF into Ta under the influence of both heating and field, which leads to a vacancy density gap and possible depletion of vacancies in the entire CF at high negative voltage, resulting in the OFF state; (ii) during ON switching, a sufficient positive voltage causes Joule heating and the increase of temperature, and increased temperature causes vacancies moving from Ta into CF to refill the vacancy gap, resulting in the ON state. Interestingly, we show that the thermally activated field-switching in the considered devices can lead to up to three orders of magnitude speed-up in switching, with only 50% voltage/current increase. Simulated resistances during OFF and ON switching as a function of time and voltage show very good qualitative agreement with experimental measurement in Ref. [7]. Furthermore, under a triangular voltage sweep, the simulated current-voltage hysteresis curve is shown in Fig. 1(b), which also shows good qualitative agreement with the measured data in Ref. [8]. The generality of the proposed model allows to simulate and investigate the underlying physical switching mechanisms in a wide spectrum of oxide memristors ranging from field-dominant, field-thermal-driven to thermal-dominant memristive devices.

- [1] D. Mamaluy and X. Gao, Appl. Phys. Lett. **106**, 193503 (2015)
- [2] P.R. Mickel et al., Mod. Phys. Lett. B **28** (2014)
- [3] K.H. Kim et al., Nano Lett. **12**, 389 (2012)
- [4] N. Hashem and S. Das, Appl. Phys. Lett. **100**, 262106 (2012)
- [5] X. Gao et al., ECS Trans., accepted, October 2015
- [6] <https://trilinos.org/>
- [7] P.R. Mickel et al., Appl. Phys. Lett. **102**, 223502 (2013)
- [8] P.R. Mickel et al., Adv. Mat. **26**, 4486 (2014)

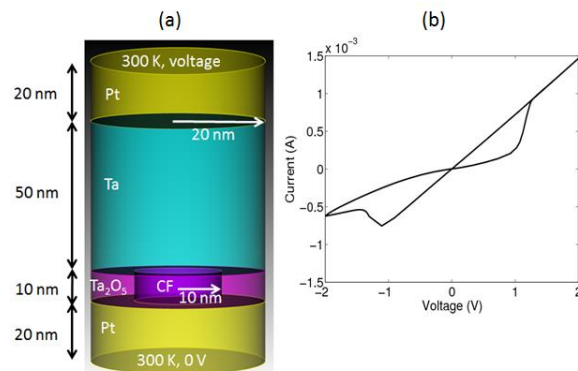


Fig.1: (a) Structure of a 3D filamentary TaOx memristor, with the layer material and thickness from an experimental device. (b) Simulated current-voltage hysteresis for a triangular voltage sweep.

Quantum Transport Modeling Using a Bloch Basis Expansion

Maarten L. Van de Put¹, Massimo V. Fischetti¹, and William G. Vandenberghe¹

¹*Department of Material Science and Engineering, The University of Texas at Dallas,
Richardson, Texas, USA
maarten.vandepuut@utdallas.edu*

We have developed a technique to efficiently calculate ballistic electron transport through atomic structures using plane-wave based pseudopotential methods, either empirical or from first-principles. In our technique, we approximate the wavefunction in the whole device using a partition-of-unity [1], constructed using traditional linear finite-element (FE) shape functions, centered on nodes, which are enhanced with the Bloch waves. Specifically, we use enhancement Bloch-waves that are taken at the gamma-point and the Brillouin zone edge, where all valence bands and a few (approx. 10) conduction bands are included. Thanks to the compact support of the FE shape functions in space, the expansion results in a tight-binding like Hamiltonian with nearest neighbors coupling between adjacent nodes. With the Galerkin method, we transform the Schrödinger equation into a sparse generalized eigenvalue problem in the FE coefficients. To study transport between open contacts, we use the quantum transmitting boundary method (QTBM) [2], and calculate the extended wavefunctions self-consistently with the Poisson equation. To demonstrate the capabilities of our solver, we simulate a highly scaled graphene nanoribbon (GNR) field-effect transistor (FET) containing 960 atoms (shown in Fig. 1). As a Bloch basis, we use 42 valence bands and 20 conduction bands, at the center and edge of the Brillouin zone, calculated using plane-wave empirical pseudopotentials [3]. Our method accurately reproduces the reference plane-wave band structure throughout the entire Brillouin zone without introducing spurious solutions in the spectrum (Fig. 2). A self-consistent solution for the GNR FET at a particular bias is obtained in 20 minutes on a single CPU core, two orders of magnitude faster than direct use of plane waves. In Fig. 3, we show the three-dimensional density, the potential energy and electric field in the off-state, resolved to well below the atomic scale. In Fig 4, we show the device transfer characteristics. Finally, we will discuss our progress on extending our technique to use Bloch waves calculated using density functional theory, particularly using the projector-augmented wave (PAW) method [4].

[1] I. Babuska and J.M. Melenk, *Int. J. Numer. Meth. Eng.* **40**, 727 (1998)

[2] C.S. Lent and D.J. Kirkner, *J. Appl. Phys.* **67**, 6353 (1990)

[3] M.L. Van de Put et al., *J. Appl. Phys.* **119**, 214306 (2016)

[4] G. Kresse and J. Furthmüller, *Comput. Mat. Sci.* **6**, 15, (1996)

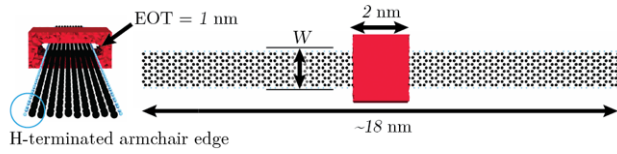


Fig. 1: 3D cartoon of the graphene nanoribbon field-effect transistor (GNRFET) with a gate-all-around configuration. The GNR has an armchair-edge and is 10 atom layers wide. Carbon (black) and hydrogen (blue) atom positions are indicated with balls.

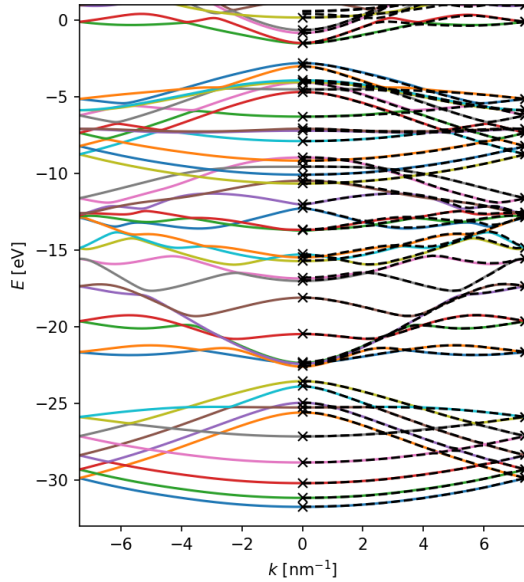


Fig. 2: The electronic band structure of the GNR ribbon shown in Fig. 1. From a full empirical pseudopotential calculation in dashed black lines. Reconstructed using a Bloch wave basis at points indicated with a cross in solid, colored lines.

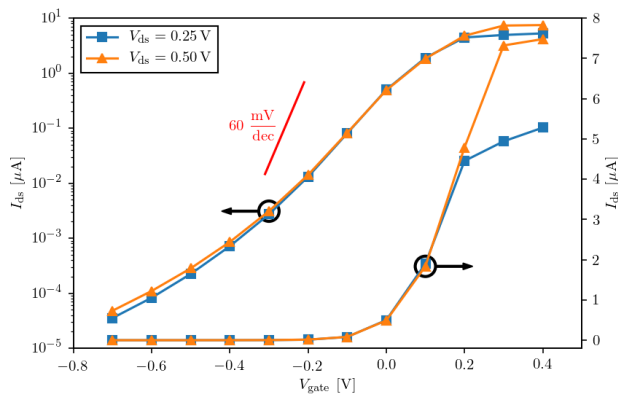


Fig. 3: The transfer characteristics of the device shown in Fig. 1. The sub-threshold performance of GNRFETs is highly degraded by source-to-drain tunneling in the off-state due to the short gate length, even with excellent gate control.

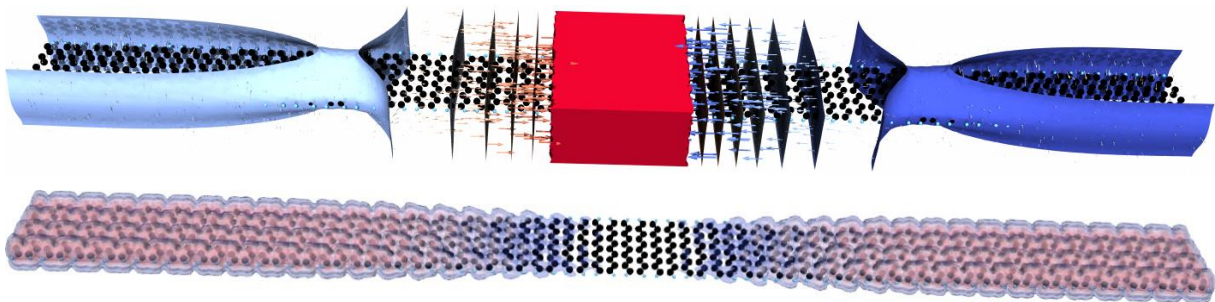


Fig. 4: 3D rendering of the device in the off-state. Top: The self-consistent potential as equi-potential surfaces, with the gate-all-around in red. Bottom: Equi-density surfaces of the free electron density. Carbon (black) and hydrogen (blue) atom positions are indicated with balls.

Nanoscale Mapping of Carrier Diffusion: Application for InGaN Quantum Wells

Mounir Mensi¹, Ruslan Ivanov¹, Kathryn M. Kelchner², Steven P. DenBaars²,
Shuji Nakamura², James S. Speck², and Saulius Marcinkevičius¹

¹*Department of Applied Physics, KTH Royal Institute of Technology, Electrum 229,
16440 Kista, Sweden*

²*Materials Department, University of California, Santa Barbara, California 93106, USA
sm@kth.se*

Carrier transport in wide band gap semiconductor alloys (e.g. $\text{In}_x\text{Ga}_{1-x}\text{N}$) and their nanostructures is strongly affected by nm-scale band potential fluctuations. The nonuniform cation distribution forms deep potential minima [1] and may cause strong localization [2], which has a large impact on carrier recombination and diffusion, especially that of holes. As a result, the hole diffusion length may be <100 nm, which can hardly be measured by electrical techniques. In this work, we present a method that allows measuring such small diffusion lengths, their anisotropy and spatial variation. The method is based on photoluminescence (PL) mapping performed with the help of scanning near-field optical microscopy (SNOM) simultaneously in several modes [3]. These modes include time-integrated and time-resolved PL in illumination-collection (IC, PL excitation and collection through a probe) and illumination (I, probe excitation, far-field collection) modes. In the IC mode, the PL intensity is determined by the carrier recombination and out-diffusion from under the probe, in the I mode - just by the recombination. Comparing PL intensity maps taken in both modes allows evaluating the diffusion parameters. The crucial point for a correct evaluation is the knowledge of the spatial variation of the radiative and nonradiative recombination times.

The method has been demonstrated on an example of a nonpolar m -plane 8 nm $\text{In}_{0.15}\text{Ga}_{0.85}\text{N}$ quantum well grown on GaN substrate. The recombination times were evaluated from mapped PL transients. The lifetime maps were used to calculate PL intensity maps. Diffusion parameters were extracted by minimizing the difference between the calculated and measured IC and I mode maps. Ambipolar diffusion coefficients $D_c = 0.21$ cm²/s and $D_a = 0.84$ cm²/s for directions parallel and perpendicular to the wurtzite \mathbf{c} axis were obtained. The strong diffusion anisotropy is assigned to the anisotropy of the top-most valence band.

[1] R. Ivanov et al., Phys. Rev. Appl. **7**, 064033 (2017)

[2] W. Hahn et al., Phys. Rev. B **98**, 045305 (2018)

[3] M. Mensi et al., ACS Photonics **5**, 528 (2018)

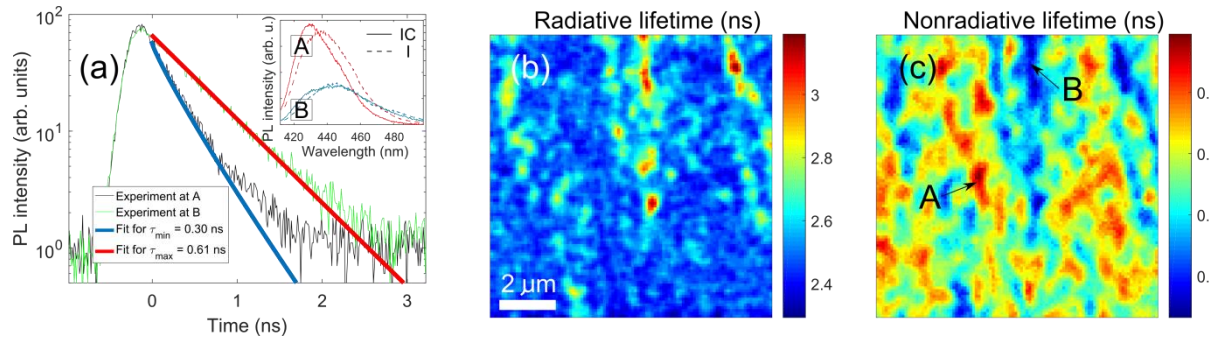


Fig.1: (a): Room-temperature near-field PL transients and spectra (inset) measured at points A and B indicated in part (c). (b and c): Maps of the radiative and nonradiative lifetimes, respectively.

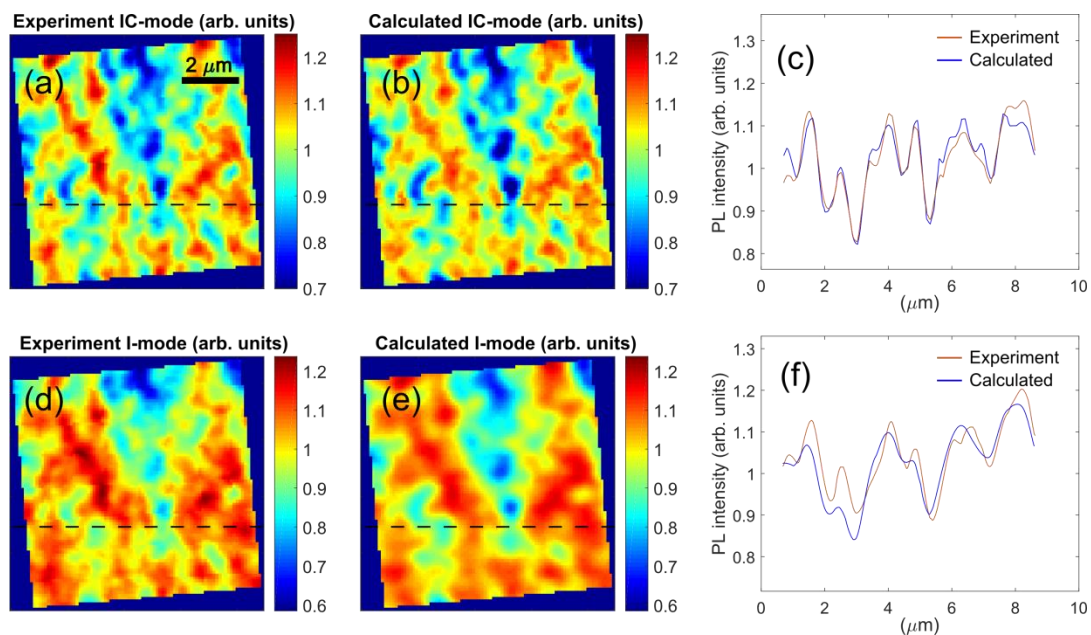


Fig.2: Experimental (left column) and calculated PL intensity maps for IC (top row) and I (bottom row) modes, as well as PL intensity profiles along the lines shown in the maps.

Suspended Antenna-Coupled Nanothermocouples for Infrared Detection

Gergo P. Szakmany¹, Alexei O. Orlov¹, Gary H. Bernstein¹, and Wolfgang Porod¹

¹*Center for Nano Science and Technology, Department of Electrical Engineering,
University of Notre Dame, Notre Dame, Indiana 46556, USA
gszakman@nd.edu*

Antenna-coupled nanothermocouples (ACNTCs) for long-wave infrared radiation (IR) and THz wave detection have been studied [1-2]. The operating principle of these devices is based on the wave nature of the IR radiation, Joule heating, and the Seebeck effect. A nanoantenna, tuned for the operating frequency receives the incident radiation, and the radiation-induced antenna currents heat the hot junction of a NTC, placed at the center of the antenna, by Joule heating. The NTC converts the heat to electrical signals by the Seebeck effect. The heat loss to the air, lead lines, and most significantly to the substrate, as shown in Fig. 1, limits the open-circuit voltage (V_{OC}) response of these devices. Therefore, thermally insulating the hot junction from the substrate significantly increases the V_{OC} response of ACNTCs and increases their sensitivity.

In this paper, we study suspended single-metal ACNTCs [3] for IR (10.6 μm) detection. The thermal conductivity of air is about 100 times less than that of SiO_2 ; therefore, the antenna and the hot junction are thermally insulated from the SiO_2/Si substrate by suspending above a cavity. The ACNTCs, as previously discussed in [2], are fabricated on top of a highly-resistive Si wafer from Pd using electron-beam lithography (EBL), electron beam evaporation, and lift-off. Then, a $6 \times 6 \mu\text{m}^2$ window is exposed with EBL around the antenna and the hot junction (Fig. 2), and the Si substrate is etched by XeF_2 . A completed suspended ACNTC is shown in Figs. 2 and 3. The 8- μm -deep cavity under the device is hemispherical due to the isotropic etch properties of the XeF_2 , as shown in Fig. 4.

The finished devices were illuminated by a CO_2 laser, operating at 10.6 μm , for IR testing. Polarization-dependent responses of a suspended device and a nominally identical device without thermal insulation (on a SiO_2/Si substrate) are shown in Fig. 5. The V_{OC} response of the thermally insulated device is increased by about 20-fold compared to devices on a SiO_2/Si substrate. Figure 6 compares the suspended device to various ACNTCs on substrates.

In our talk, we will discuss the fabrication and measurement results in detail, and present the cavity-depth-dependent responses of ACNTCs.

[1] G. P. Szakmany et al., IEEE T. Terahertz Sci. Technol. **7**, 582 (2017)

[2] G. P. Szakmany et al., IEEE T. Nanotechnol. **12**, 163 (2013)

[3] G. P. Szakmany et al., IEEE T. Nanotechnol. **13**, 1234 (2014)

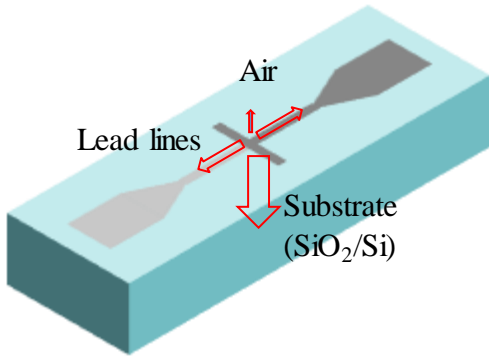


Fig.1: Heat loss of the antenna by air, lead lines, and substrate. The substrate effect is the strongest, and can be reduced by thermal insulation.

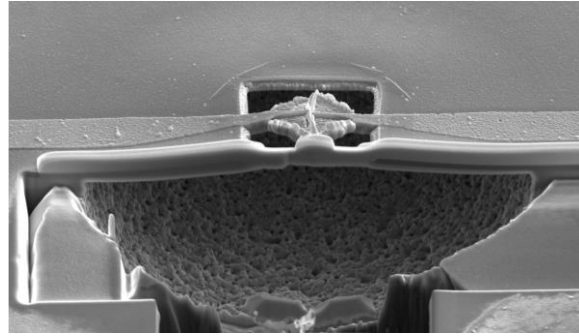


Fig.4: Cross section of the cavity with an ACNTC.

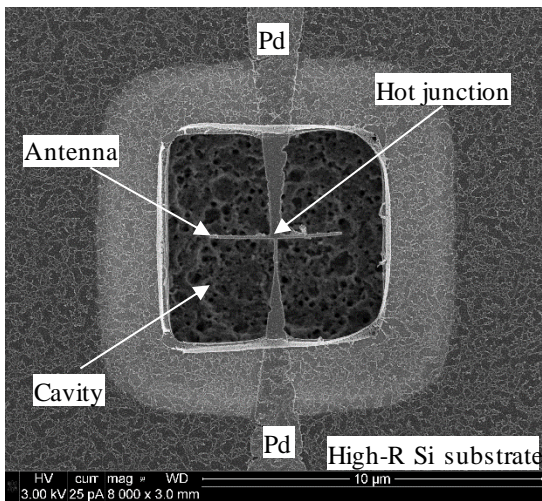


Fig.2: SEM image of a suspended ACNTC, top view.

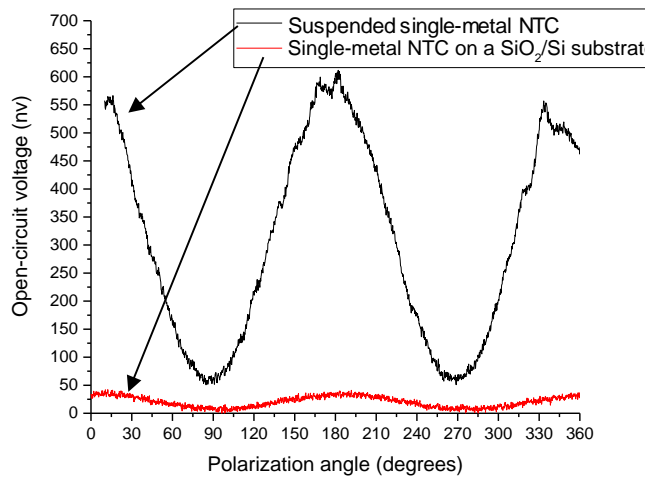


Fig.5: Polarization-dependent response of a suspended single-metal ACNTC and a nominally identical ACNTC on a SiO₂/Si substrate.

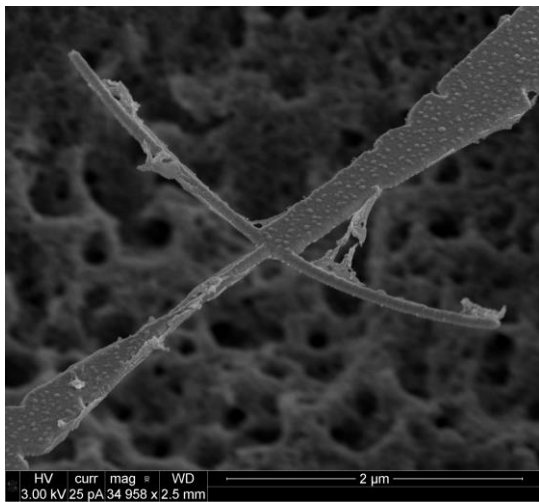


Fig.3: Tilted SEM image of a suspended ACNTC.

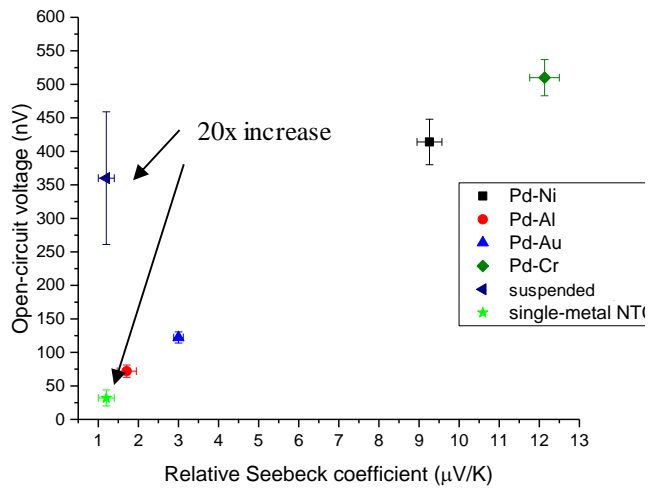


Fig.6: Comparison of various ACNTCs. Thermal insulation increases the response by 20 fold over a single-metal ACNTC.

Light-Matter Interaction ‘Beyond’ Strong-Coupling Regime in the Superconducting Circuit Quantum Electrodynamics

Kouichi Semba¹

¹*National Institute of Information and Communications Technology,
4-2-1, Nukuikitamachi, Koganei, Tokyo 184-8795, Japan
semba@nict.go.jp*

The superconducting qubit-oscillator system is an ideal physical system for studying the interaction of a very strong light-matter interaction. The flux qubit-oscillator circuit is well described by the generalized quantum Rabi-model Hamiltonian shown in Eq. (1). The first, second and third terms respectively represent the energy of the qubit, the energy of the harmonic oscillator, and the interaction energy. If the coupling strength g becomes as large as the atomic and cavity frequencies (Δ and ω , respectively), the energy eigenstates including the ground state

$$\hat{H} = -\frac{\hbar}{2}(\Delta\hat{\sigma}_x + \varepsilon\hat{\sigma}_z) + \hbar\omega\hat{a}^\dagger\hat{a} + \hbar g\hat{\sigma}_z(\hat{a} + \hat{a}^\dagger). \quad (1)$$

are predicted to be highly entangled [1]. We have experimentally achieved this deep strong coupling using a superconducting-flux-qubit LC-oscillator system [2]. By carefully designing a superconducting persistent-current qubit interacting with an LC harmonic oscillator that has a large zero-point fluctuation current via a large shared Josephson inductance, we have realized circuits with g/ω ranging from 0.72 to 1.34 and $g/\Delta \gg 1$. From the transmission spectroscopy, we have observed unconventional transition spectra which can be interpreted using predicted energy levels which are well described by Schrödinger-cat like entangled states between persistent-current states and displaced vacuum or Fock states of the oscillator [2]. By using two-tone spectroscopy, the energies of the six lowest levels of each circuit have been determined. We have observed huge Lamb shifts that exceed 90% of the bare qubit frequencies and inversions of the qubits’ ground and excited states when there are a finite number of photons in the oscillator[3]. We have also observed collective coupling between an engineered 4300 ensemble of flux-qubits and a superconducting resonator [4], and considered the condition for observing generation of superradiant ground state in the presence of parameter fluctuations [5].

[1] S. Ashhab and Franco Nori, Phys. Rev. A **81**, 042311 (2010)

[2] F. Yoshihara et al., Nat. Phys. **13**, 44 (2017)

[3] F. Yoshihara et al., Phys. Rev. Lett. **120**, 183601 (2018)

[4] K. Kakuyanagi et al., Phys. Rev. Lett. **117**, 210503 (2016)

[5] S. Ashhab and K. Semba, Phys. Rev. A **95**, 053833 (2017)

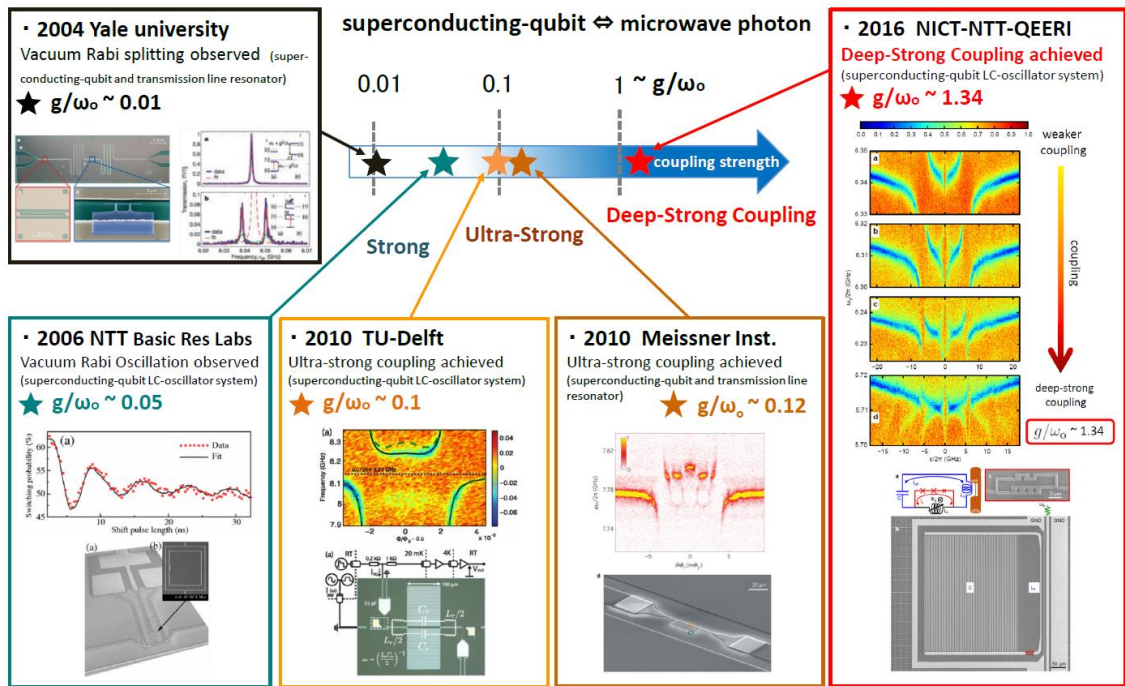


Fig.1: Evolution in circuit-QED from a viewpoint of normalized coupling strength g/ω_0 with ω_0 the oscillator-circuit frequency (equivalent to resonator frequency in cavity-QED).

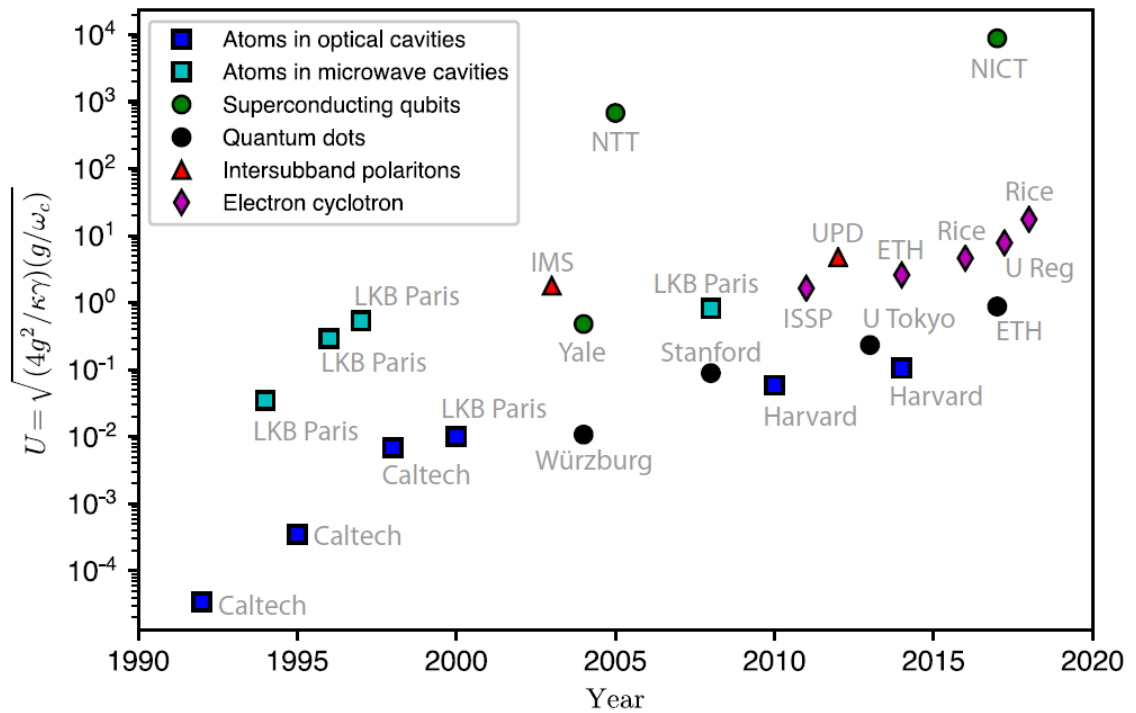


Fig.2: Evolution in time in cavity QED of the highest value of the parameter $U = \sqrt{(4g^2 / \kappa\gamma)}(g/\omega_c)$ for different physical platforms, where $C = 4g^2 / \kappa\gamma$ is the cooperativity, with κ and γ being the cavity and qubit loss rates, respectively. From Fig.2 of arXiv:1804.09275v2 [quant-ph] by P. Forn-Diaz et al.

Controlling the Properties of Multiferroic Heterostructures via Nanoscale Topography Design

Goran Rasic¹, Branislav Vlahovic¹, and Yongan Tang¹

¹*Department of Physics, North Carolina Central University, Durham, NC 27707, USA*
grasic@ncsu.edu

Traditionally, magnetic properties have been considered intrinsic and material dependent. Recently, another approach was reported where control over one of the key magnetic properties, coercivity, is possible through proper nanostructuring of the thin film surface [1-4]. By changing the surface topography we can control the domain wall movement and domain formation in the thin film. With proper selection of the surface pattern, the domain size and distribution can be altered through modification of energetically favorable domain configuration which in turn reduces the coercivity. This allows us to change a material's magnetic properties without changing its composition. In combination with traditional methods of altering magnetic properties, such as doping and alloying, this greatly adds to the tunability of magnetic properties. More importantly, it allows us to select materials based on a critical property and then tailor the magnetic properties for optimal performance.

Here we report on the origin of the coercivity reduction as well as the effects of varying the feature size on topography, crystallography, and magnetic properties. Surface patterned NiFe₂O₄ films were deposited on c-plane sapphire substrates using chemical solution deposition. Films with pattern sizes ranging from 500 nm to 1300 nm were made. X-ray diffraction images showed all samples to be pure single phase inverse spinel nickel ferrite and to have similar texture. Magnetic measurements showed patterning did not affect the magnetic response of the samples. The dependence of feature size was shown to have opposite trends for the in-plane and out-of-plane magnetized samples.

These results extend beyond magnetic thin films. Applying the same principles to heterostructures we can improve the coupling coefficients in exchange bias and magnetoelectric composites thus improving the device performance.

Acknowledgments: This work has been supported by ARDEC W911SR-14-2-0001-0024.

- [1] G. Rasic et al., MRS Comm. **6**, 397 (2016)
- [2] G. Rasic et al., Phys. Status Solidi A **212**, 449 (2015)
- [3] G. Rasic et al., IEEE Mag. Lett. **5**, 1 (2014)
- [4] G. Rasic et al., MRS Comm. **3**, 207 (2013)

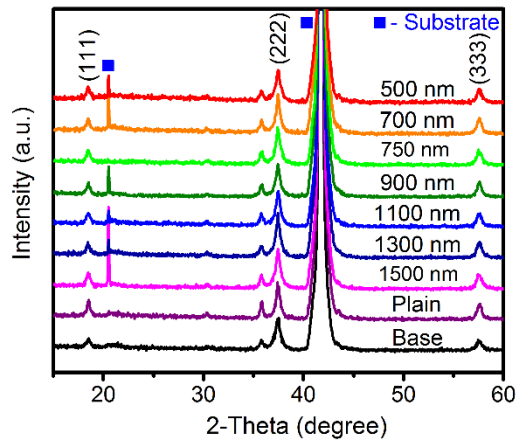


Fig.1: Θ - 2Θ X-ray diffraction of NiFe₂O₄ thin films with a range of pattern sizes.

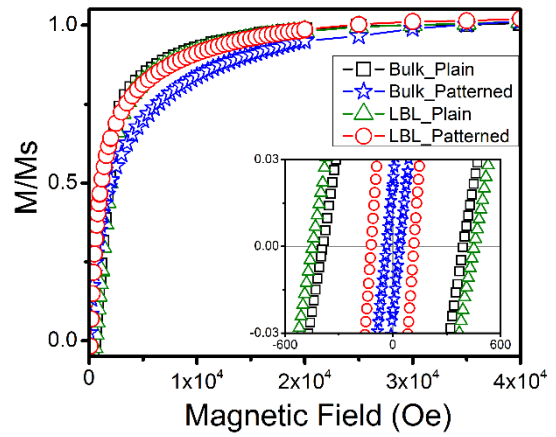


Fig.3: Magnetic hysteresis measurements of NiFe₂O₄ thin films. Higher magnification image of the coercivity values is shown in inset.

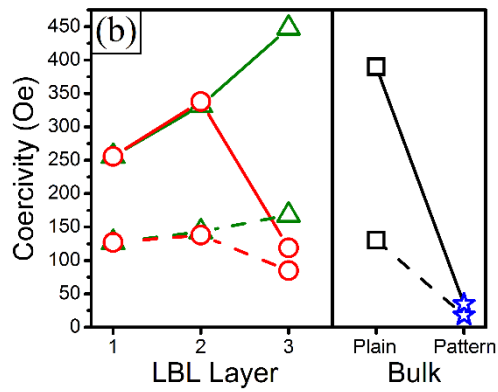


Fig.2: Comparison of in-plane (dashed) and out-of-plane coercivity values for bulk and layer-by-layer made samples.

A New Class of Low Loss Spinel Ferrite Films for Spin Current Based Applications

Jake Wisser^{1,2}, Lauren Riddiford^{1,2}, Peng Li¹, Mike Veit^{1,2}, Satoru Emori¹,
Krishnamurthy Mahalingam³, Brittany Urwin³, Brandon Howe³, Olaf Van t'Erve⁴,
Christoph Klewe⁵, Padraic Shafer⁵, Alpha N'Diaye⁵, Elke Arenholz⁵, Berend T. Jonker⁴,
and Yuri Suzuki^{1,2}

¹*Geballe Laboratory for Advanced Materials, Stanford University, Stanford, CA 94305 USA*

²*Department of Applied Physics, Stanford University, Stanford, CA 94305 USA*

³*Air Force Research Laboratory, WPAFB, Dayton, OH 45433 USA*

⁴*Naval Research Laboratory, Washington, D.C. 45555 USA*

⁵*Advanced Light Source, Lawrence Berkeley National Laboratory, Berkeley, CA 94720 USA*

e-mail: ysuzuki1@stanford.edu

Electronics that is based on the manipulation of electron spin has the potential to improve energy efficiency if spin information can be propagated in the form of a spin current without an accompanying charge current. The generation, manipulation and detection of such pure spin currents have been the focus of many recent studies. Thin film magnetic insulators have been identified as promising materials for spin-current technology because they are thought to exhibit lower damping compared with their metallic counterparts. However, insulating behavior is not a sufficient requirement for low damping, as shown by the very limited options for low-damping insulators [1,2]. We have developed a new class of low loss spin ferrite thin films that exhibit ultra-low Gilbert damping parameter ($\alpha \sim 0.001$) and negligible inhomogeneous linewidth broadening, resulting in narrow half-width half-maximum linewidths (see Figure 1) [3]. The most promising spinel ferrite films are of the composition $\text{Mg}(\text{Al,Fe})_2\text{O}_4$. We have also demonstrated efficient spin pumping from these spinel ferrites into an adjacent heavy metal layer through measurement of the spin-mixing conductance, Gilbert damping enhancement (see Figure 2) and electrical voltage peaks that appear at ferromagnetic resonance. The reversal of the measured voltage signal between spinel/Pt and spinel/W samples, is consistent with the opposite signs of the respective spin Hall angles and indicates that the signal is indeed dominated by the inverse spin Hall effect and not by proximity-induced anisotropic magnetoresistance. Spin-torque ferromagnetic resonance measurements indicate that we can indeed achieve significant charge-to-spin conversion. These materials are promising for future low-power electronics such as spin-wave logic devices and voltage controlled magnetic memory.

- [1] S. Emori et al., Adv. Mater. **9** 064039 (2017)
- [2] M.T. Gray et al., Phys. Rev. Appl. **9** 064039 (2018)
- [3] S. Emori et al., Nano Lett. **18** 4273 (2018)

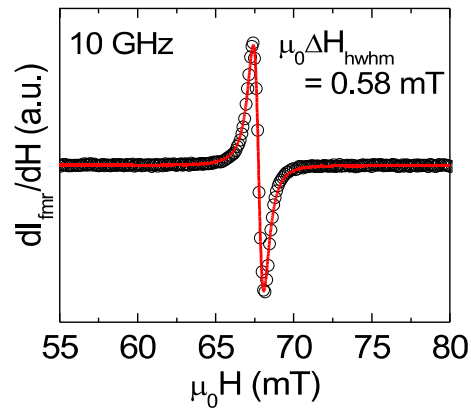


Fig.1: Ferromagnetic resonance of a $\text{MgAl}_{0.5}\text{Fe}_{1.5}\text{O}_4$ thin film on MgAl_2O_4 with typical linewidths on the order of 0.5mT.

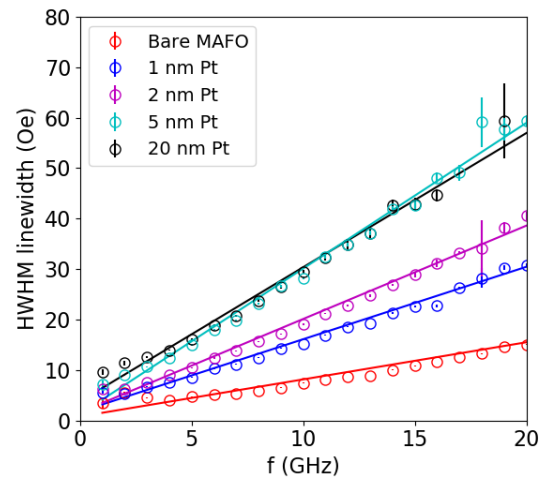


Fig.2: Frequency dependence of the ferromagnetic linewidth shows a Gilbert damping parameter on the order of ~ 0.001 for bare $\text{MgAl}_{0.5}\text{Fe}_{1.5}\text{O}_4$ thin films and increased damping parameter due to the spin pumping into an adjacent Pt layer.

Growth of Semiconducting Oxides – Challenges and Surprises

Henning Riechert¹, Patrick Vogt¹, and Oliver Bierwagen¹

¹*Paul-Drude-Institut für Festkörperelektronik,
Leibniz-Institut im Forschungsverbund Berlin
Hausvogteiplatz 5-7, 10179 Berlin, Germany
riechert@pdi-berlin.de*

In₂O₃ and Ga₂O₃ are wide band gap n-type semiconducting “sesquioxides” with band gaps of 2.7 and 4.5 eV, respectively. While In₂O₃ has been used for decades as a transparent contact material or in gas sensors, Ga₂O₃ has recently been recognized as a promising material for power electronics applications with the potential to outperform GaN or SiC. Due to the different crystal structures of In₂O₃ and Ga₂O₃, the typical efforts for band-gap engineering by forming alloys as well as heterostructures is quite challenging and remains largely unresolved.

This contribution presents a comprehensive study of the growth kinetics and thermodynamics of Ga₂O₃, In₂O₃, and (In_xGa_{1-x})₂O₃, also comparing it to the well-established nitride growth. The aim lies in establishing a growth regime allowing for high growth rates at sufficiently high growth temperatures. We employ plasma-assisted molecular beam epitaxy (MBE) to synthesize binary and ternary materials, where a plasma source is employed to generate sufficiently reactive oxygen species from O₂.

In studies of the growth kinetics we have shown that the growth rate of In₂O₃ and Ga₂O₃ is flux-stoichiometrically and thermally limited by the formation and desorption of their respective suboxides In₂O and Ga₂O [1, 2]. This limitation is much stronger for Ga₂O₃ than for In₂O₃, leading to severely limited Ga₂O₃ growth rates at substrate temperatures that are sufficiently high to ensure high material quality. The underlying reason is the higher vapor pressure of Ga₂O with respect to In₂O as well as the lower oxidation efficiency of Ga with respect to In. [1, 3]. On the other hand, we have found that thermodynamics largely rules the formation of (In_xGa_{1-x})₂O₃ alloys, where the incorporation of Ga is thermodynamically favored over that of In due to the stronger Ga–O bonds compared to the In–O bonds [4].

In a most striking contrast to nitride growth, we find that the presence of In on the growing surface can drastically affect the growth rate of Ga₂O₃. We demonstrate how the kinetic advantage of In to be oxidized to In₂O₃ and the thermodynamic preference of Ga to be incorporated into (In_xGa_{1-x})₂O₃ collaboratively lead to a strongly enhanced growth rate of Ga₂O₃ under an additional In-flux, even at high growth temperatures. This enhancement is based on metal-exchange catalysis through sequential oxidation of In to In₂O₃ followed by an exchange of Ga with the oxidized In [5].

A possibly very beneficial side effect of this growth scheme is the formation of ϵ -Ga₂O₃. Unlike the typically formed β -Ga₂O₃, this polytype is structurally compatible with the one of In₂O₃. We expect that this will ease the formation of heterostructures between the two materials.

- [1] P. Vogt and O. Bierwagen, Appl. Phys. Lett. **106**, 081910 (2015)
- [2] P. Vogt and O. Bierwagen, Appl. Phys. Lett. **108**, 072101 (2016)
- [3] P. Vogt and O. Bierwagen, Appl. Phys. Lett. **109**, 062103 (2016)
- [4] P. Vogt and O. Bierwagen, APL Mat. **4**, 086122 (2016)
- [5] P. Vogt et al., Phys. Rev. Lett. **119**, 196001 (2017)

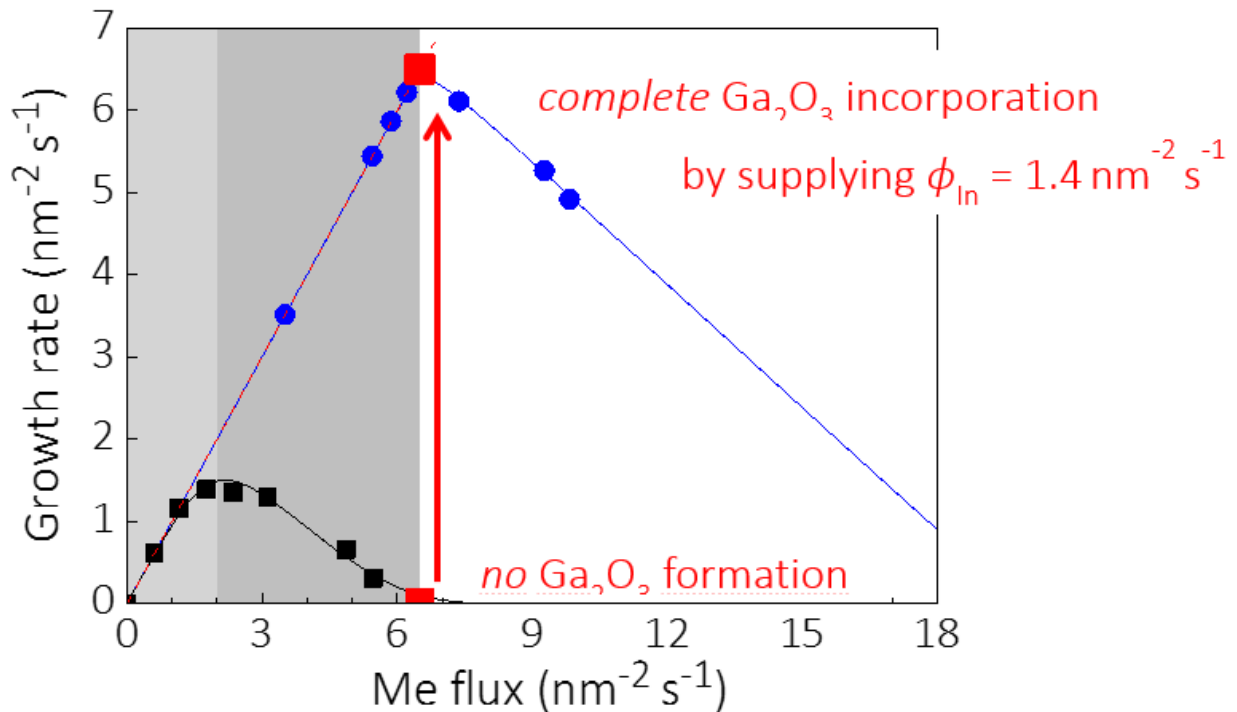


Fig.1: Growth rates of Ga₂O₃ (black symbols) and In₂O₃ (blue symbols) for the same oxygen flux, plotted over the respective metal fluxes. The decrease in growth rates for higher metal fluxes (i.e. in the metal-rich regime) is due to the formation and desorption of suboxides. Symbols in red show the effect of adding a flux of In during growth of Ga₂O₃.

Internal Photoemission Spectroscopy Measurements of Energy Barriers between Amorphous Metal / Insulators Heterostructures

Melanie A. Jenkins¹, John M. McGlone¹, John F. Wager¹, and John F. Conley, Jr.¹

¹*School of EECS, Oregon State University, Corvallis, Oregon, USA*
John.Conley@oregonstate.edu

Metal/insulator/metal (MIM) heterostructures are used as high speed diodes for rectenna based energy harvesting, capacitors, resistive memory, and hot-electron transistors [1-6]. To better control electric fields and improve the performance of these devices, there is growing interest in integrating amorphous thin films as smooth and uniform work function electrodes [6,7]. Precise knowledge of metal/insulator barrier heights, ϕ_{Bn} , is critical for predicting, understanding, and optimizing MIM device charge transport and operation [8]. In the simplest model, with charge transfer across the interface neglected, ϕ_{Bn} should vary with the vacuum work function of the metal, $\Phi_{M,vac}$, so that $\phi_{Bn} = \Phi_{M,vac} - \chi_i$ where χ_i is the insulator electron affinity. However, this is not usually the case. In induced gap state theory, charge transfer at intrinsic interface traps creates an interfacial dipole that drives the metal Fermi level, E_{FM} , towards the charge neutral level of the insulator, $E_{CNL,i}$, the energy at which the dominant character of the interface states switches from donor-like to acceptor-like. Thus, the metal behaves as if it has an effective work function, $\Phi_{M,eff}$, different from $\Phi_{M,vac}$, where $\Phi_{M,eff} = E_{CNL,i} + S(\Phi_{M,vac} - E_{CNL,i})$ and $S = 1 / (1 + 0.1(\epsilon_{hf} - 1)^2)$ is the slope that describes how much for a given insulator, $\Phi_{M,eff}$ actually changes in response to changing $\Phi_{M,vac}$ [9]. As the high frequency dielectric constant of the insulator, ϵ_{hf} , increases, S decreases and the insulator more effectively "pins" E_{FM} at $E_{CNL,i}$. Finally, it is often observed that ϕ_{Bn} 's also depend on deposition method and can deviate substantially from either model due to *extrinsic* interface traps. It is therefore necessary to directly measure ϕ_{Bn} for each metal/insulator combination.

In this work, we use internal photoemission (IPE) spectroscopy to measure ϕ_{Bn} of the thin film glassy metals TaWSi, TaNiSi, and ZrCuAlNi in MIM stacks with various insulators deposited via atomic layer deposition (ALD). Results are compared to ϕ_{Bn-TaN} , ϕ_{Bn-Al} , and ϕ_{Bn-Au} . To date, there have been few reports of IPE measurements of MIM structures [8] and only two on amorphous metals [10,11].

For the Ta-based metal bottom electrodes with Al_2O_3 , we find that ϕ_{Bn} decreases with decreasing $\Phi_{M,vac}$ ($\phi_{Bn,TaNiSi} > \phi_{Bn,TaWSi} > \phi_{Bn,TaN}$), whereas for HfO_2 , ϕ_{Bn} remains relatively constant ($\phi_{Bn,TaNiSi} \approx \phi_{Bn,TaWSi} \approx \phi_{Bn,TaN}$). The difference between HfO_2 and Al_2O_3 is attributed to enhanced interface pinning, which is quantified through determination of S . Barrier heights for the Al and Au top electrodes are near the predicted values ($\phi_{Bn} = \Phi_M - \chi_I$) for each insulator.

In devices with a TaWSi bottom electrode, use of a Au top electrode led to significantly lower TaWSi/insulator ϕ_{Bn} 's than were obtained with an Al top electrode, likely due to the migration of Au^+ ions toward the opposite electrode interface where the positive charge reduces ϕ_{Bn} . The presence of switching behavior in TaWSi/SiO₂/Au devices provides evidence for Au^+ migration [11]. IPE determined ϕ_{Bn} are qualitatively consistent with the asymmetry in the I-V response. TaWSi and TaNiSi electrodes showed consistently higher ϕ_{Bn} 's than ZCAN electrodes and comparable performance to TaN. With low roughness and thermal stability approaching 900 °C, TaWSi is a promising bottom electrode for MIM diodes.

Acknowledgments: This work was support by the NSF Center for Sustainable Materials Chemistry, CHE-1606982.

- [1] M. Bareib et al., IEEE T. Microw. Theory Tech. **59**, 2751 (2011)
- [2] A. Sharma et al., Nat. Nanotechnol. **10**, 1027 (2015)
- [3] G. Karbasian et al., Appl. Sci. **7**, 246 (2017)
- [4] D.Z. Austin et al., Appl. Phys. Lett. **110**, 263503 (2017)
- [5] N. Alimardani et al., J. Appl. Phys. **116**, 024508 (2014)
- [6] N. Alimardani et al., J. Vac. Sci. Technol. A **30**, 01A113 (2012)
- [7] J.M. McGlone et al., MRS Commun. **7**, 715 (2017)
- [8] V. V. Afanas'ev et al., Phys. Status Solidi A **215**, 1700865 (2017)
- [9] Y.C. Yeo et al., J. Appl. Phys. **92**, 7266 (2002)
- [10] M.A. Jenkins et al., Phys. Status Solidi RRL **12**, 1700437 (2018)
- [11] M.A. Jenkins et al., ECS Trans. **85**, 729 (2018)

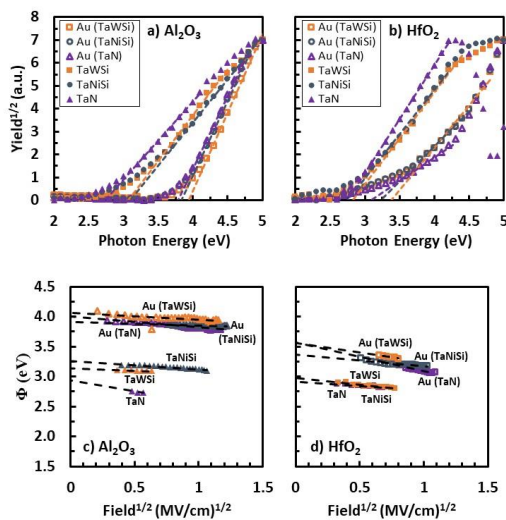


Fig.1: Representative plots of IPE yield $Y^{1/2}$ vs. $h\nu$ for (a) Al₂O₃ and (b) HfO₂ in MIM devices with Au top electrodes and either TaN, TaWSi, or TaNiSi bottom electrodes. The dashed lines show the linear ϕ_{thres} extraction for each interface. Shown plots were taken at an applied field in the range of 0.4 to 1.2 [MV²/cm²]. (c) and (d) show Schottky plots of ϕ_{thres} vs. $\text{field}^{1/2}$ used to extrapolate the zero-field barrier heights.

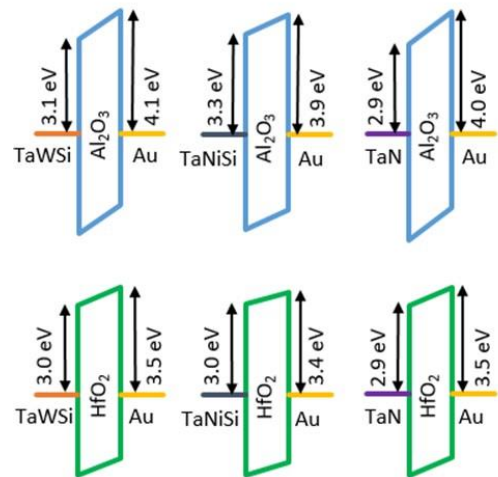


Fig.2: Energy band diagrams for Al₂O₃ and HfO₂ MIM devices with Au top electrodes and TaWSi, TaNiSi, or TaN bottom electrodes based on IPE determined zero field barrier height.

Valley-Protected Edge State in Semiconductor Photonic Crystal Slab

Satoshi Iwamoto¹, Takuto Yamaguchi¹, Yasutomo Ota², and Yasuhiko Arakawa²

¹*Nanoscience Center for Photonics, Electronics, and Materials Engineering,
Institute of Industrial Science, The University of Tokyo, Komaba Meguro-ku,
Tokyo 153-8505, Japan*

²*Institute for Nano Quantum Information Electronics, The University of Tokyo, Japan
iwamoto@iis.u-tokyo.ac.jp*

Photonic crystal (PhC), an artificial optical material with a wavelength-scale periodic structure of refractive index, is now an important tool for controlling not only the propagation but also the localization of light. Various kinds of photonics devices using PhCs have been demonstrated so far. Recently, a new paradigm of PhC research has been explored by introducing the concept of band topology developed in condensed matter physics. As in electronic systems, topologically-protected photonic edge states appear at interfaces with two PhCs possessing topologically distinct common bandgap. Such states are capable to guide the light with suppressed backscattering even under the presence of sharp bends or structural imperfections, leading further developments of photonic integrated circuits.

Here, we discuss the efficient light guiding via valley-protected edge state in semiconductor valley PhC (VPhC) slabs [1]. Our VPhC consist of a staggered honeycomb lattice with two different-sized equilateral-triangle air holes [2] formed in a 200-nm-thick GaAs slab suspended in air. The unit cells for two VPhC structures, A and B. Both structures have the same photonic band diagram and a common bandgap for TE-like mode, but different valley topology. Thus a valley-protected edge state exists at an interface between the two types of VPhCs. We fabricated a VPhC slab with a Z-shaped interface. Utilizing the photoluminescence (PL) from quantum dots (QDs) embedded in the slab, we demonstrated efficient light propagation even through sharp bends of the interface. PL images were taken through a band pass filter with different center wavelength λ_c . The QDs were photo-excited at a grating coupler. As expected, no output was observed in the case λ_c is set outside the bandwidth of the edge state. Once λ_c is set inside the bandwidth, clear emission from the output port was observed. Importantly, no significant scattering at the corners was observed. This robustness against sharp bends in VPhCs is applicable to low-loss optical delay line with a small foot print. The latest results including the comparison with a conventional W1-type PhC waveguide will be also discussed in the presentation.

[1] T. Yamaguchi et al., 23rd Microoptics Conference, C-2 (2018)

[2] S. Iwamoto and Y. Arakawa, ICO-24, F1E-03 (2017)

Signatures of Majorana Zero Models in scalable, IN-SITU fabricated $(\text{Bi}_x\text{Sb}_{1-x})_2\text{Te}_3/\text{Nb}$ Josephson junctions

Detlev Grützmacher^{1,2}, Peter Schüffelgen^{1,2}, Daniel Rosenbach^{1,2}, Mussler Gregor^{1,2}, Thomas Schaeppers^{1,2}, Jonas Koelzer^{1,2}, Tobias Schmitt^{2,4}, Sarah Schmitt^{1,2}, Chuan Li³, and Alexander Brinkmann³

¹*Peter Grünberg Institute 9, Institute for Semiconductor Nanoelectronics, Forschungszentrum Jülich, Jülich, Germany*

²*JARA-FIT, Forschungszentrum Jülich and RWTH Aachen University, Germany*

³*Universiteit Twente, MESA+ Institute for Nanotechnology, Twente, Netherlands*

⁴*JARA Institute for Green-IT, RWTH Aachen University, Aachen, Germany*
d.gruetzmacher@fz-juelich.de

Topologically protected Majorana Zero Modes (MZMs) promise to obey non-Abelian exchange statistics, thus have the potential to facilitate fault-tolerant quantum computing [1]. Josephson Junctions were fabricated using a s-wave superconductor (Nb) and 3-dimensional topological insulators, namely $(\text{Bi}^x\text{Sb}_{1-x})_2\text{Te}_3$ alloys, as test vehicles on the search for Majorana modes. Induced superconductivity in Josephson junctions with weak links of 3D TI films is expected to be mediated partly by Majorana bound states. In $(\text{Bi}_x\text{Sb}_{1-x})_2\text{Te}_3$ alloys the band gap and the position of the Fermi level at the sample surface can be controlled by the composition. However, a serious problem is the large bulk carrier concentration and the high sensitivity towards surface oxidation. Thus, in-situ fabrication of the TI/SC interface as well as TI surface passivation is required to obtain a high contact transparency and a high mobility in the surface layer, respectively. The Molecular beam epitaxy process presented in this work combining selective growth and stencil lithography [2] assures these necessities. The in-situ prepared Josephson junctions show a record high interface transparency of 95% and large $I_c R_N$ products of 325 μV , indicating a strong proximity effect and a large superconductive gap. The Shapiro response of radio frequency measurements indicates the presence of gapless Andreev bound states, the so called Majorana bound states. The in-situ fabrication process can be adapted to complex layouts, first experiments for the in-situ processing of nanowire devices and qubit structures will be presented. Thus the process paves the way towards networks of in-situ grown Majorana devices for the proposed topological qubit layouts.

[1] F. Hassler, Lecture Notes of the 44th IFF Spring School Quantum Information Processing (Verlag des Forschungszentrums Jülich, 2013)

[2] P. Schüffelgen et al., arXiv:1711.01665 (2017)

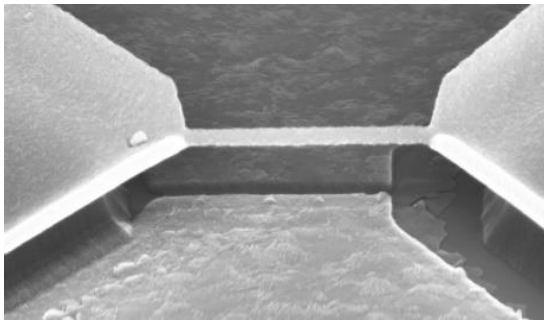


Fig.1: SEM image of an in-situ fabricated Josephson Junction composed of a selectively grown $(\text{Bi}_x\text{Sb}_{1-x})_2\text{Te}_3$ alloy, Nb contacts aligned by the stencil mask and an Al_2O_3 passivation layer.

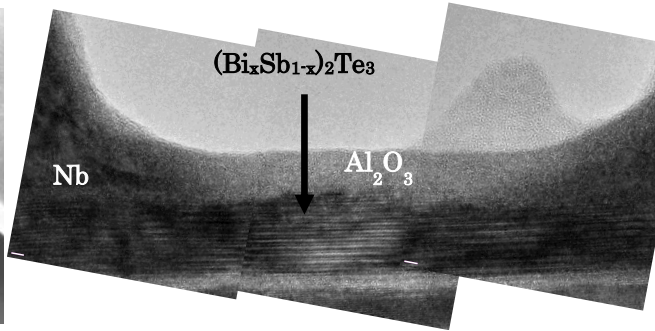


Fig.2: High resolution TEM image of an Nb/Ti/Nb Josephson Junction passivated by Al_2O_3 completely in-situ prepared by advanced MBE processing.

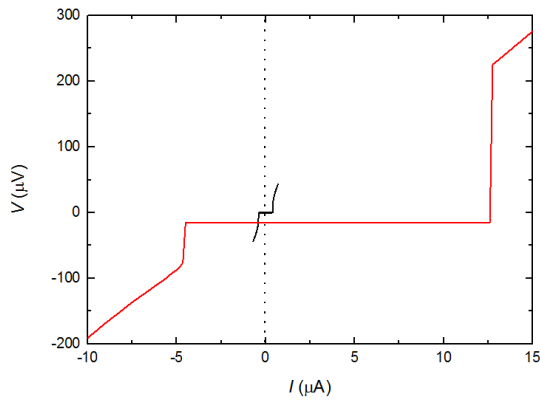


Fig.3: Comparison of the I/V characteristic of an ex-situ (black line) and an in-situ (red line) prepared Josephson Junction, demonstrating impressively the superiority of the in-situ prepared junction by an 20-fold increased superconducting gap.

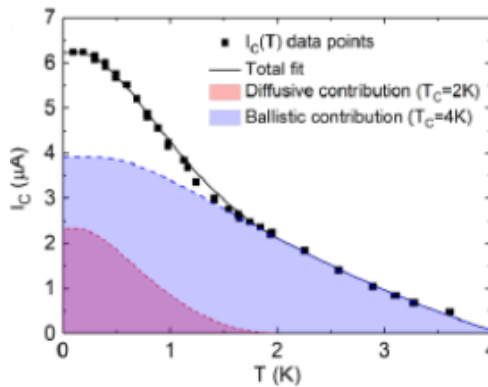


Fig.4: $I_c(T)$ of a Nb/Ti/Nb Josephson Junction, which is comprised of ballistic and diffusive contributions. For temperatures above 2.2K the transport is solely carried by ballistic contributions. By fitting the ballistic contribution to the Eilenberger formalism, an interface transparency of 95% is obtained

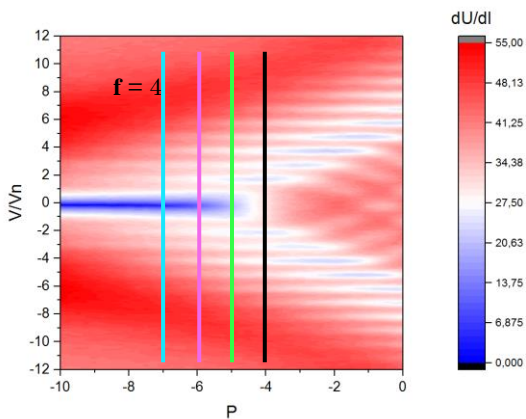


Fig.5: Colour plot of dV/dI characteristics under hf-radiation (4 GHz, $T=3.2\text{K}$) showing Shapiro steps with the first step completely missing. Profiles along the coloured lines are presented in Fig.6

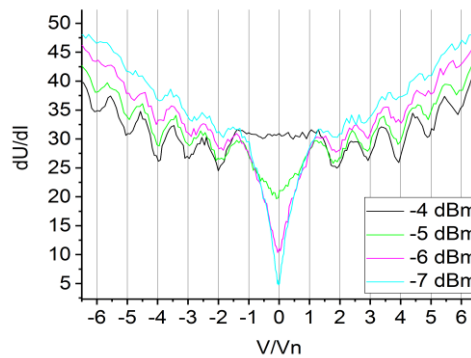


Fig. 6: Derivative of the I/V characteristics under hf-radiation (4 GHz, $T=3.2\text{K}$) showing Shapiro steps with the first step completely missing indicating Majorana Zero Modes

Effects of Gate-Induced Electric Fields on Semiconductor Majorana Nanowires

Andrey E Antipov¹, Arno Bargerbos^{1,2}, Georg W Winkler¹,
Bela Bauer¹, Enrico Rossi^{3,1}, and Roman M Lutchyn¹

¹*Station Q, Microsoft Research, Santa Barbara, California 93106-6105, USA*

²*QuTech, Delft University of Technology, 2600 GA Delft, Netherlands and
Kavli Institute of Nanoscience, Delft University of Technology, 2600 GA Delft, Netherlands*

³*Department of Physics, William & Mary, Williamsburg, Virginia 23187, USA*
andrey.antipov@microsoft.com

We study the effect of gate-induced electric fields on the properties of semiconductor-superconductor hybrid nanowires which represent a promising platform for realizing topological superconductivity and Majorana zero modes. Using a self-consistent Schrödinger-Poisson approach that describes the semiconductor and the superconductor on equal footing, we are able to access the strong tunneling regime and identify the impact of an applied gate voltage on the coupling between semiconductor and superconductor. We discuss how physical parameters such as the induced superconducting gap and Landé g factor in the semiconductor are modified by redistributing the density of states across the interface upon application of an external gate voltage. Finally, we map out the topological phase diagram as a function of magnetic field and gate voltage for InAs/Al nanowires.

[1] A.E. Antipov et al., Phys. Rev. X **8**, 031041 (2018)

High Temperature Majorana Fermions in RuCl₃

Yiping Wang¹, Gavin B. Osterhoudt¹, Yao Tian², Paige Lampen-Kelley^{3,4}, Arnab Banerjee⁴,
Thomas Goldstein⁵, Jun Yan⁵, Johannes Knolle⁶, Joji Nasu⁷, Yukitoshi Motome⁸,
Stephen Nagler⁴, David Mandrus³, and Kenneth S. Burch¹

¹*Department of Physics, Boston College, 140 Commonwealth Avenue, Chestnut Hill, MA
02467, USA*

²*SICK Product Center Asia Pte. Ltd., 8 Admiralty Street, Singapore 757438*

³*Department of Materials Science and Engineering, University of Tennessee, Knoxville, TN
37821, USA*

⁴*Materials Science and Technology Division, Oak Ridge National Laboratory,
Oak Ridge, TN 37821, USA*

⁵*Department of Physics, University of Massachusetts, Amherst, Massachusetts 01003, USA*

⁶*Blackett Laboratory, Imperial College London, London SW7 2AZ, United Kingdom*

⁷*Department of Physics, Tokyo Institute of Technology, Meguro, Tokyo 152-8551, Japan*

⁸*Department of Applied Physics, University of Tokyo, Bunkyo, Tokyo 113-8656, Japan
ks.burch@bc.edu*

Majorana fermions, particles that are their own anti-particles, can emerge in insulating magnets as excitations with fractions of the constituent's quantum numbers. Interest in Majoranas is driven by their potential for quantum computation, and as evidence of novel topological states. Observations have been limited to liquid helium temperatures as edge modes in topological superconductors and quantum spin liquids (QSL) without combined evidence of particle-hole symmetry, Fermi statistics, and presence in the bulk. In this talk I will report the observation of all three in α -RuCl₃, at temperatures exceeding liquid nitrogen via new energy gain as well as loss Raman spectra and a unique framework to identify the statistical properties of the Kitaev QSL. α -RuCl₃ is van-der-Waals material amenable to future novel device architectures and close to the Kitaev QSL, where bond-dependent Ising interactions produce excitations that are non-local in terms of spin flips. Consistent with particle-hole symmetric excitations obeying Pauli-exclusion, the sum of the energy loss and gain responses are nearly temperature and energy independent. This is in excellent agreement with new quantum Monte Carlo (QMC) calculations of the Kitaev QSL. The new data allow unambiguous separation of the bosonic thermal fluctuations from the continuum due to the Majoranas, further establishing their presence above liquid nitrogen. Our new method can be used to identify the unique properties of QSLs, and demonstrates the promise of α -RuCl₃ for efforts in topological phases and quantum computation.

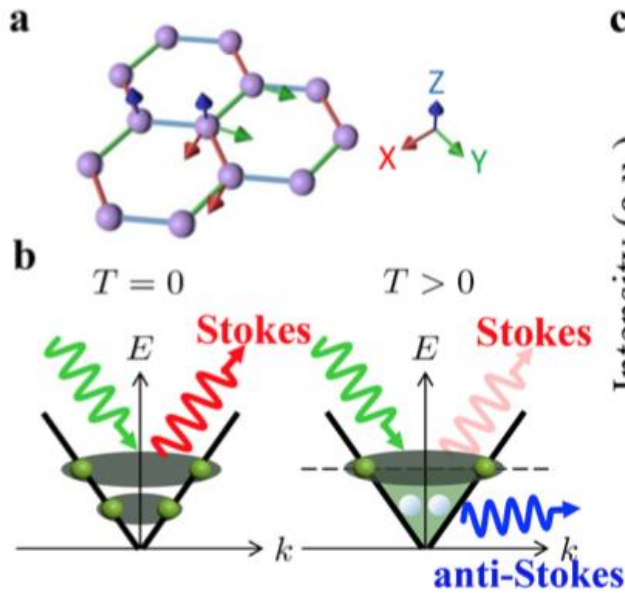


Fig.1: (a) Bond dependent exchange of the Kitaev model. (b) For fermionic particles obeying Pauli exclusion, at zero temperature only pairs can be created giving a strong Stokes response. For higher temperatures the states become filled, enhancing anti- Stokes at the cost of Stokes.

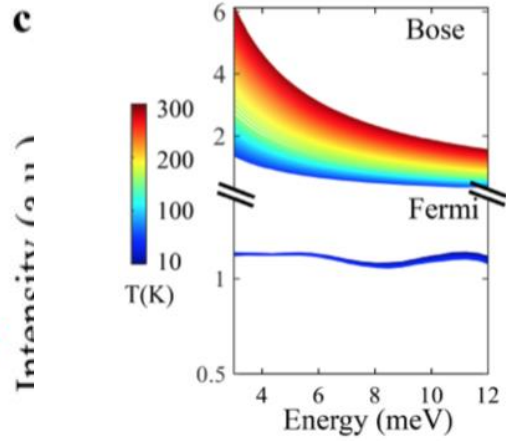


Fig.3: Theoretical calculation of Isum. Lower panel shows the quantum monte-carlo for the Kitaev lattice reveal excellent agreement with the data. The nearly energy and temperature independence results from pairs of Majorana fermions where particle-hole symmetry and Pauli-exclusion conserve the total loss and gain intensity The top portion shows the result of a constant Raman susceptibility, revealing a strong temperature dependence expected for Bosonic particles.

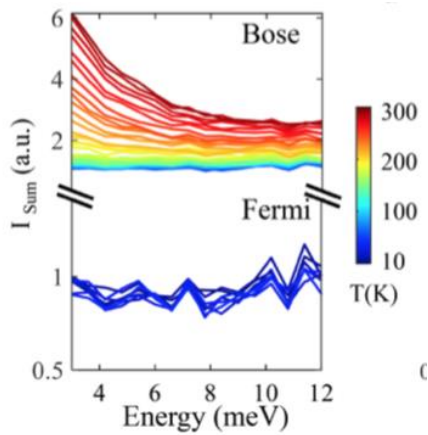


Fig.2: Isum, the sum of the loss and gain intensity, is nearly temperature independent in low temperature range ($T < 75$ K, expanded on the bottom). For the full temperature range, Isum reveals an upturn from thermal fluctuations.

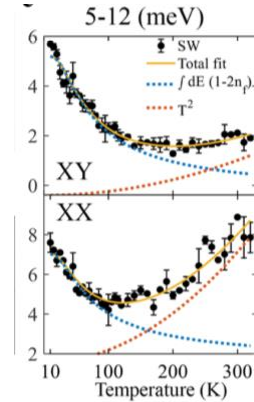


Fig. 4 Difference of the SW $\Delta SW^{XY}(T) = I^{XY}(T) - I^{XY}(T)$ (top panel) and $\Delta SW^{XX}(T)$ (bottom panel) for the indicated energy range. A single fit of the fermionic response ($\alpha(1 - 2nf) d\omega$) is used for both symmetry channels (blue). The high temperature data is well described by the QES amplitude βT^2 (red), with the whole range fit by the sum (yellow).

Status of the Search for Majorana Fermions in Semiconductor Nanowires

Sergey Frolov¹

¹*Department of Physics and Astronomy, University of Pittsburgh, PA 15206, USA*
frolovsm@pitt.edu

Majorana fermions are non-trivial quantum excitations that have remarkable topological properties and can be used to protect quantum information against decoherence. Tunneling spectroscopy measurements on one-dimensional superconducting hybrid materials have revealed signatures of Majorana fermions which are the edge states of a bulk topological superconducting phase. We couple strong spin-orbit semiconductor InSb nanowires to conventional superconductors (NbTiN, Al) to obtain additional signatures of Majorana fermions and to explore the topological phase transition. A potent alternative explanation for many of the recent experimental Majorana reports is that a non-topological Andreev state localizes near the end of a nanowire. We compare Andreev and Majorana modes and investigate ways to clearly distinguish the two phenomena. We are also exploring how Andreev states can be chained together along the nanowire to realize the one-dimensional Kitaev model, a discrete way of generating Majorana modes.

Developing SWCNT Nano-Sensors for C17.2 Neural Stem Cells

Tetyana Ignatova¹, Slava V. Rotkin², and Sabrina S. Jedlicka³

¹*Nanoscience Department, Joint School of Nanoscience and Nanoengineering, University of North Carolina at Greensboro, Greensboro, NC, 27401, USA*

²*Materials Research Institute, Department of Engineering Science and Mechanics, The Pennsylvania State University, University Park, PA, USA*

³*Department of Bioengineering, Department of Materials Science and Engineering, Lehigh University, Bethlehem, PA, 18015, USA*

t_ignato@uncg.edu

Reliable intra-cellular tracking of nanocarbon material at ultra-low concentrations is required to enable a new generation of biosensor and drug delivery vectors. In this work^[1], hyperspectral imaging of DNA-functionalized single-wall carbon nanotubes inside neural stem cells was demonstrated, over several mitosis cycles, also in 3D z-stacking mode.

CoMoCAT SWCNTs wrapped by ssDNA GT(20) were introduced to C17.2 neural stem cells with concentrations ranged from 50 ng/mL to 5 ng/mL (up to 10⁶ times smaller than in some earlier works). The absorption spectra of a typical SWCNT solution is shown in Fig. 1b. We used resonant Raman imaging of DNA-wrapped SWCNTs for single-particle detection. Three dominant SWCNT Raman features correspond to the radial breathing mode (RBM) in low frequency range (Fig. 1a,c), the tangential (G band, ~1590 cm⁻¹), and double resonance (G' band, ~2610 cm⁻¹) at higher frequencies (Fig. 1d). These modes (as well as other weaker features, such as the disorder induced D band and a few overtone modes) can be used for (1) imaging of the SWCNTs, (2) identifying individual SWCNTs, and (3) extracting detailed information about their structure and their environment.

The high spatial resolution of confocal Raman microscopy allows one to localize the SWCNT position in 3D. In Fig. 2a fast mapping of the cell area allowed us to identify position of a nanotube (inside light blue rectangle area) as being close to the cell membrane. Panel b shows the high-resolution G-band image of the individual (11,0) SWCNT. Fig. 2d-g presents a sequence of Raman maps taken at varying z-location. It is clearly seen that a center of hotspot associated with the nanotube moves, coming in and out of focus at different depths inside the cell. Similar images were produced for several samples with cells incubated with SWCNTs maintained for at least one (and up to 4) division cycles.

Acknowledgments: SVR has been supported by NSF (ECCS-1509786); SSJ has been supported by NSF:CBET (IDR-1014957).

[1] T. Ignatova et al., J. Mater. Chem. B **5**, 6536 (2017)

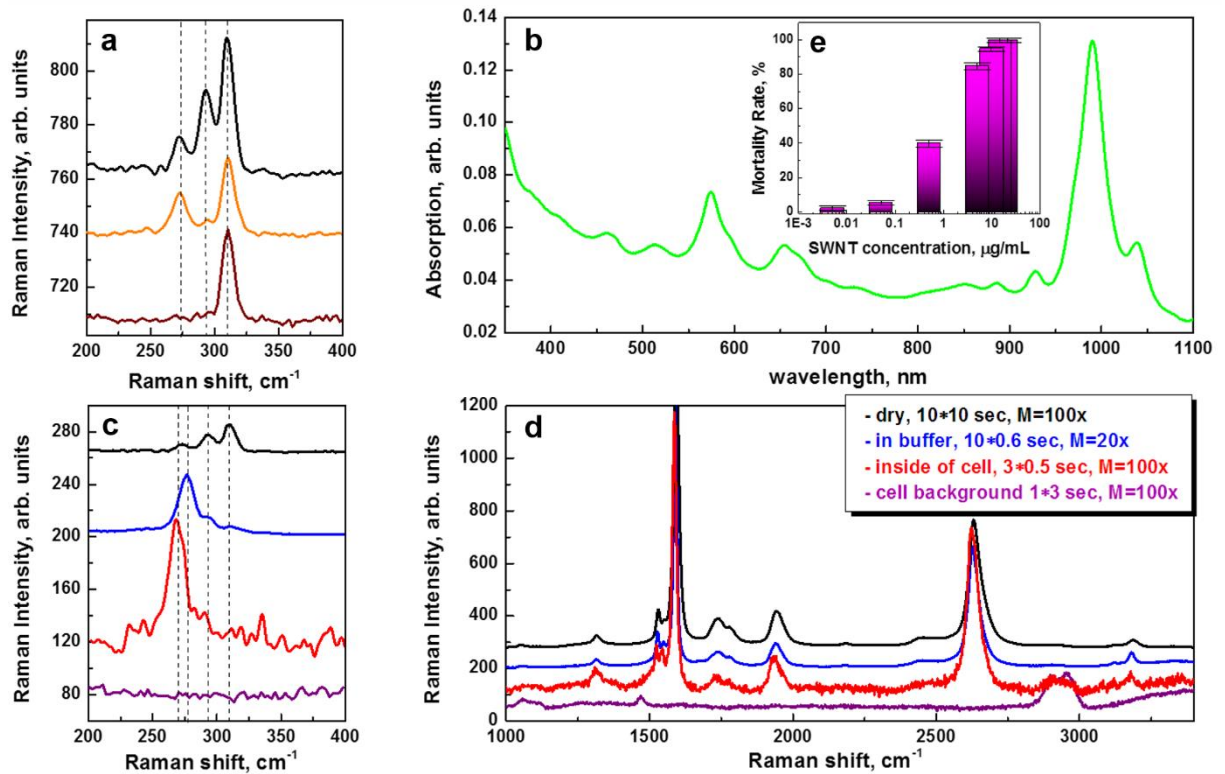


Fig.1: (a) SWCNT Raman RBM modes (dry sample) resolving 3, 2 and single chirality tubes within a focal volume; (b) absorption spectrum of typical SWCNT solution, arrows show available laser lines matching resonance absorption peaks (for multiple chirality species); Inset (e) shows cell mortality rate vs. SWCNT concentration. (c) RBM and (d) high-frequency bands of SWCNT Raman spectrum inside the cell (red line). (Reproduced from [1].)

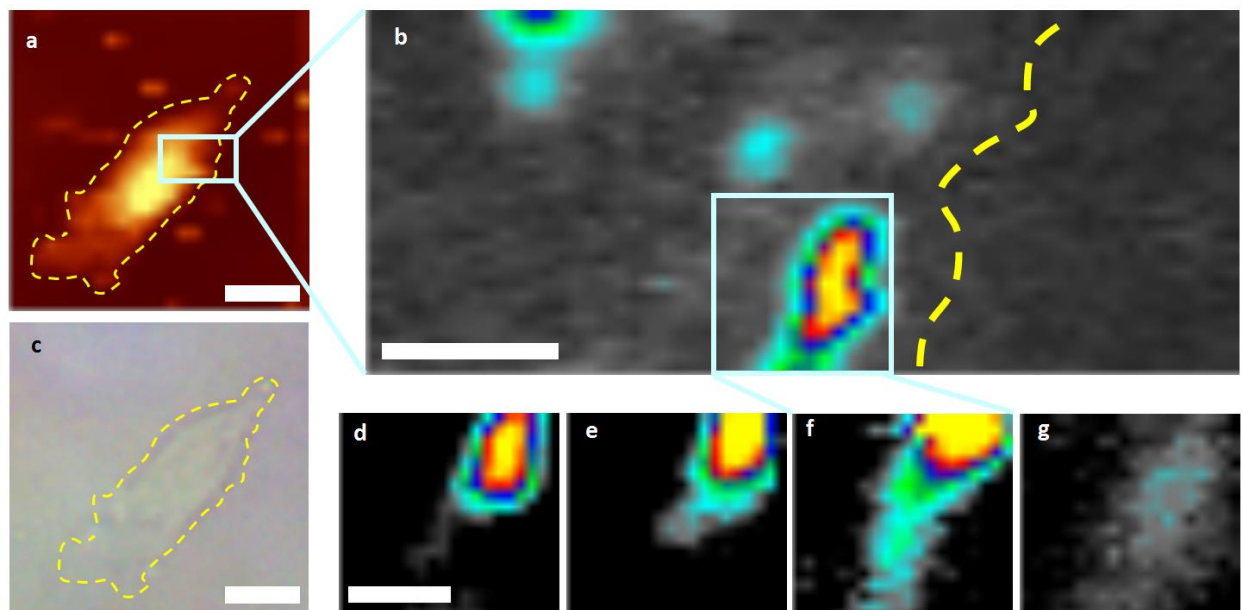


Fig.2 3D localization of SWCNT by confocal Raman imaging. (a) Cell autofluorescence and (c) optical image. (b) SWCNT G band image (the full spectrum is presented in Fig. 1cd, red curve). (d-g) High-resolution G band maps taken at 1, 1.5, 2 and 7 μm depth inside the cell. Scale bars: 10 μm in (a,c), 2 μm in (b) and 1 μm in (d-g). (Reproduced from [1].)

Sugar Chain Functionalized Graphene FET for Detection of Virus

Kazuhiko Matsumoto¹, Takuya Kawata¹, Kaori Yamamoto¹, Takao Ono¹,
Yasushi Kanai¹, and Koichi Inoue¹

¹*Institute of Scientific & Industrial Research, Osaka University
8-1 Mihogaoka, Ibaraki-shi, Osaka-fu, 567-004, Japan
k-matsumoto@sanken.osaka-u.ac.jp*

This abstract is not printed due to the authors' request.

Inhibited Hot Carrier Thermalization in Type-II Quantum Wells: A Practical Route to Hot Carrier Solar Cells?

Hamidreza Esmailpour¹, Vincent R. Whiteside¹, Jinfeng Tang¹,
Michael B. Santos¹, and Ian R. Sellers¹

¹*Department of Physics & Astronomy, University of Oklahoma, Norman, OK 73019
sellers@ou.edu*

Recently, there has been a great deal of interest in the design of hot carrier absorbers with large hot carrier lifetimes. Understanding the dynamics of hot carriers, as well as their relaxation mechanisms, provides a number of potential opportunities for hot carrier based optoelectronic devices. In polar semiconductors (group III-V), the coupling between electrons and longitudinal optical (LO) phonons (Fröhlich interaction) is the major source of hot carrier relaxation. These systems lose their excess energy via the emission of LO phonons, which are then dissipated through multiple longitudinal acoustic (LA) phonon processes (Klemens mechanism); or through the emission of a transverse optical (TO) and an LA phonon (Ridley mechanism). To reduce thermalization loss, it is required to inhibit the Fröhlich interaction or to provide a condition to reabsorb the transferred energy back into the system before its dissipation through either the Klemens or Ridley mechanism.

In this presentation, it will be shown that in type-II quantum wells (QWs) robust non-equilibrium carrier distributions can be produced [1] apparently, independently of the presence and dispersion of phonons in the constituent materials (InAs and AlAsSb) comprising the quantum wells [2, 3]. Specifically, it will be shown that it is the increased radiative lifetime of the photogenerated carriers in type-II QWs - due to the reduced overlap between electron and hole wavefunctions - which play a critical role in hot carrier thermalization in these systems, rather than electron-phonon interactions. Current-voltage characterization of associated p-i-n structures show an increase in extracted photocurrent at higher excitation powers. This indicates the presence of a hot carrier population that contributes to device operation under more intense illumination, when one also considers the suppression of “cooler” less energetic carriers between 0.3V-0.5V (due to the confinement of the photogenerated electrons within the deep QWs).

[1] J. Tang et al., *Appl. Phys. Lett.* **106**, 061902, (2015)

[2] H. Esmailpour et al., *Prog. Photovolt. Res. Appl.* **25**, 591 (2016)

[3] H. Esmailpour et al., *Sci, Rep.* **8**, 12473 (2018)

In Search of a True Hot Carrier Solar Cell

David K. Ferry¹

¹*Arizona State University, Tempe, AZ 85287, USA*

ferry@asu.edu

In the years since the solar industry began and expanded to its current state, no single junction solar cell has yet reached the so-called Shockley-Quiesser limit in efficiency. In 1982, Ross and Nozik proposed that a hot-carrier solar cell (HCSC) could conceivably produce an efficiency near 85% [1]. In order to reach this dreamed of efficiency, one must do two things: (1) prevent the photo-generated carriers from thermalizing to the band edges by optical phonon emission, and (2) extract only the hot carriers into the contacts through an energy-selective contact. Since that time, a great deal of effort has been expended on phononic engineering to try to reduce the emission of optical phonons by the carriers [2]. An additional extensive effort has been expended on fancy multi-layer heterostructures to create the energy-selective contact, which is required to have a narrow band of energies allowed into the contact [3]. The efficacy of such an approach has been questioned by detailed simulations of HCSC which indicate that the energy-selective contact approach may well be limited to <2% efficiency [4]. In spite of such demonstrated limitations, work on the HCSC continues unabated. The problem, however, lies not in the concepts but clearly in the limited views of most of the practitioners. In fact, they continue to draw their concepts in terms of semiconductor band diagrams with only the central, single conduction band minimum and/or the single valence band maximum. In short, the development of the HCSC is extremely limited by the inability of the community to examine the proper condensed matter physics and band structure that can be brought to the problem. In this talk, I will describe how the use of the entire band structure, particularly the use of a meta-stable valley, for the absorber material can be used to give realistic, and conservative, estimates of achieving efficiencies above 50% for HCSC.

[1] R. T. Ross and A. J. Nozik, *J. Appl. Phys.* **53**, 3813 (1982)

[2] See, e.g., H. Esmalelour et al., *Prog. Photovolt. Res. Appl.* **24**, 591 (2016)

[3] See, e.g., J. A. R. Dimmock et al., *J. Opt.* **18**, 074003 (2016)

[4] A. P. Kirk and M. V. Fischetti, *Phys. Rev. B* **86**, 165206 (2012)

Ultrafast Relaxation Processes in Advanced Concept Solar Cell Structures

Stephen Goodnick¹, Yongjie Zou¹, and Raghuraj Hathwar¹

¹*School of Electrical Computer and Energy Engineering, Arizona State University
Tempe, AZ 85287, USA
stephen.goodnick@asu.edu*

Advanced concept solar cells depend on ultrafast dynamics of electrons and phonons in order to maximize the work performed by photoexcited carriers, and minimize thermalization losses to the environment, in order to circumvent the efficiency limitations of single bandgap converters. Nanostructured systems offer advantages in terms of reduced channels for energy relaxation in reduced dimensional systems, as well as enhancing processes such as multiple carrier generation. Here we use ensemble Monte Carlo simulation of electrons and holes and energy balance approaches to investigate the role of ultrafast carrier processes in the advanced concept architectures. The simulation approaches includes the electron-phonon scattering in quantum wells and nanowires, intercarrier scattering such as electron-electron and electron-hole, including impact ionization processes, and nonequilibrium phonon effects. While the bare electron-phonon scattering rates in reduced dimensional systems vary with respect to the bulk energy loss rates, the buildup of nonequilibrium optical phonons under high intensity photoexcitation lead to phonon bottleneck effects where energy is retained in the coupled electron-phonon system. The role of nonequilibrium acoustic phonons is also investigated, and their coupling back to the electron-optical phonon system. We also report on real space transfer effects during relaxation, which lead to long relaxation times due to carriers trapped in barrier states in heterojunction systems such as multi-quantum well structures and heterostructure nanowires. We compare with recent studies in the III-V multi-quantum well and nanowire structures in which high carrier temperatures and long energy relaxation times have been observed.

Acknowledgments: This work was partially supported by TUM Institute for Advanced Study and by the Engineering Research Center Program of the National Science Foundation and the Office of Energy Efficiency and Renewable Energy of the Department of Energy under NSF Cooperative Agreement No. EEC-1041895.

Nodal Points in Weyl Semimetals Survive the Presence of Weak Disorder

Michael Buchhold¹, Sebastian Diehl², and Alexander Altland²

¹ *Department of Physics and Institute for Quantum Information and Matter,
California Institute of Technology, Pasadena, CA 91125, USA*

² *Institute for Theoretical Physics, Universität zu Köln, D-509237 Köln, Germany
buchhold@caltech.edu*

This talk will discuss the physics of individual three-dimensional Weyl nodes subject to a moderate concentration of disorder. Previous analysis indicates the presence of a quantum phase transition below which disorder becomes irrelevant and the integrity of sharp nodal points of vanishing spectral density is preserved in this system. This statement appears to be at variance with the inevitable presence of statistically rare fluctuations which cannot be considered as weak and must have strong influence on the system's spectrum, no matter how small the average concentration. We here reconcile the two pictures by demonstrating that rare fluctuation potentials in the Weyl system generate a peculiar type of resonances which carry spectral density in any neighborhood of zero energy, but never at zero (see Figure). In this way, the vanishing of the density of states for weak disorder survives the inclusion of rare events. We demonstrate this feature by considering three different models of disorder, each emphasizing specific aspects of the problem: a simplistic box potential model, a model with Gaussian distributed disorder, and one with a finite number of s-wave scatterers mimicking isolated impurities. We will address both, the conceptual meaning of the result and consequences regarding the numerical and experimental investigation of disordered Weyl nodes.

[1] M. Buchhold et al., arXiv:1809.04615 (2018), M. Buchhold et al., arXiv:1805.00018

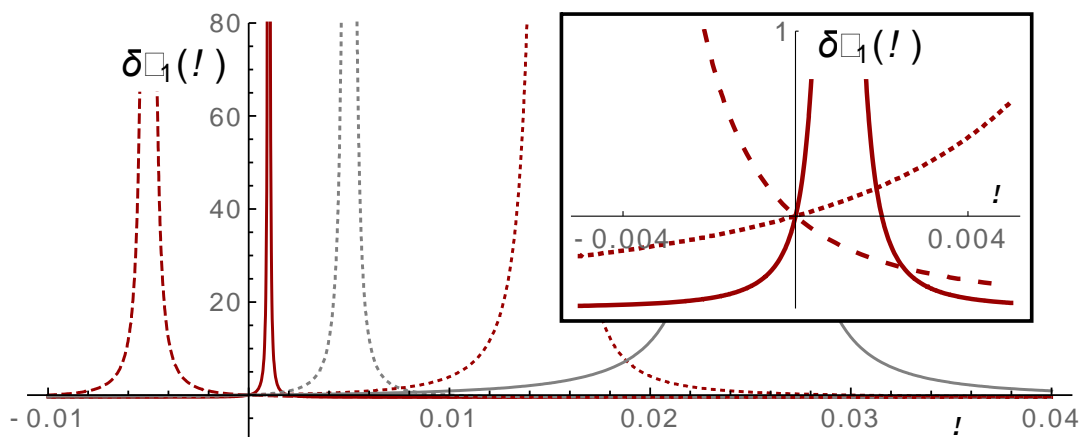


Fig.1: Density of states of a Weyl cone subject to impurity potentials of varying spatial width and depths. The spectral density is carried by isolated resonances whose width shrinks upon approaching zero. No matter what the system parameters, the density of states at zero is pinned to zero.

Quantum Oscillations in Inhomogeneous Weyl Semimetals

Dmitry Pikulin¹

¹*University of California Santa Barbara, CA 93106-6105, USA*

dmpikuli@microsoft.com

Spatially inhomogeneous Weyl semimetals behave as if they were put in external magnetic or electric fields of opposite signs for Weyl nodes of opposite chirality. These fields are akin to axial fields in high-energy physics. The advantage of the condensed matter setting is that it allows us to probe the axial field directly using the well-known quantum oscillations. I will present our results on quantum oscillations due to the axial fields both in purely bulk and in bulk-boundary settings. I will argue that our proposal is promising for the experimental observation of the axial fields in the near future.

Electron Interference in a Double-Dopant Potential Structure

Josef Weinbub¹, Mauro Ballicchia^{2,3}, and Mihail Nedjalkov²

¹*Christian Doppler Laboratory for High Performance TCAD at the*

²*Institute for Microelectronics, TU Wien, Gußhausstraße 27-29, 1040 Vienna, Austria*

³*Department of Information Engineering, Università Politecnica delle Marche,*

Via Brecce Bianche 12, 60131 Ancona, Italy

Josef.Weinbub@TUWien.ac.at

We present an analysis of interference effects as a result of the electron evolution within a coherent transport medium, offering a double-dopant Coulomb potential structure [1]. Injection of coherent electron states into the structure is used to investigate the effects on the current transport behavior within the quantum Wigner phase space picture [2]. Quantum effects are outlined by using classical simulations as a reference frame, a unique feature of Wigner function based transport simulations. In particular, the utilized signed particle approach inherently provides a seamless transition between the classical and quantum domain. Based on this we are able to identify the occurring quantum effects caused by the non-locality of the action of the quantum potential, leading to spatial resonance. Fig. 1 and Fig. 2 show the electron density at 200 fs for all absorbing boundary conditions (i.e. open system) in the classical and in the quantum case, respectively. In the classical case, Fig. 1, no interference pattern materializes beyond the dopants as the action of the force is local. In the quantum case, Fig. 2, the non-locality action of the quantum potential of the dopants affects the injected electrons already right after injection and establishes two transport channels below the dopants. Beyond the dopants (i.e. $y > 30$ nm), interference effects manifest which are highly sensitive to changes of the dopants' potential profiles. Fig. 3 and Fig. 4 compare the cumulative density of the classical and quantum cases at various y positions, clearly depicting the manifesting interference pattern for the quantum case. The results bear a resemblance to the diffraction patterns manifesting over time in double-slit experiments [3,4] and depict the use of dopants to design transport channels as well as specific interference patterns within an open system, all of which are very interesting for novel applications in the area of entangletronics [5].

[1] J. Weinbub et al., Phys. Status Solidi RRL **12**, 1800111 (2018)

[2] J. Weinbub et al., Appl. Phys. Rev. **5**, 041104 (2018)

[3] A. Tonomura et al., Am. J. Phys. **57**, 117 (1989)

[4] R. Bach et al., New J. Phys. **15**, 033018 (2013)

[5] P. Ellinghaus et al., Phys. Status Solidi RRL **11**, 1700102 (2017)

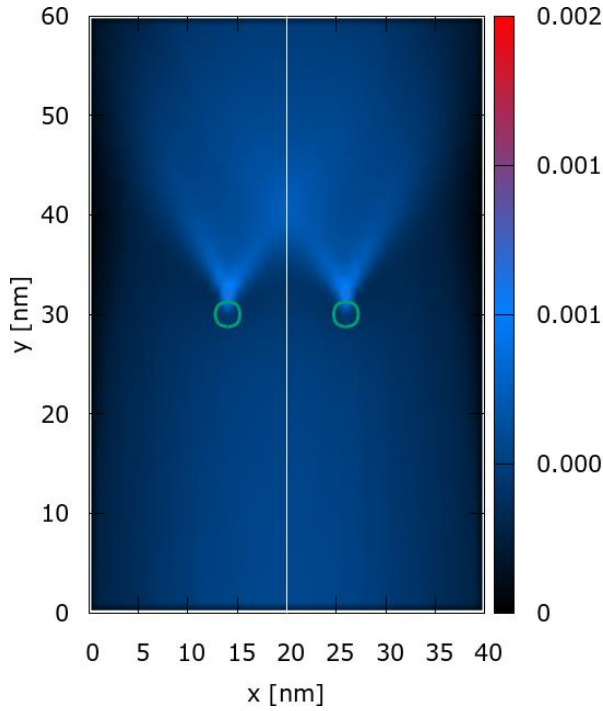


Fig.1: Classical electron density ([a.u.]) after 200 fs of the initial minimum uncertainty condition (absorbing boundary conditions). The green circles are isolines at 0.175 eV of the Coulomb potentials modeling the dopants.

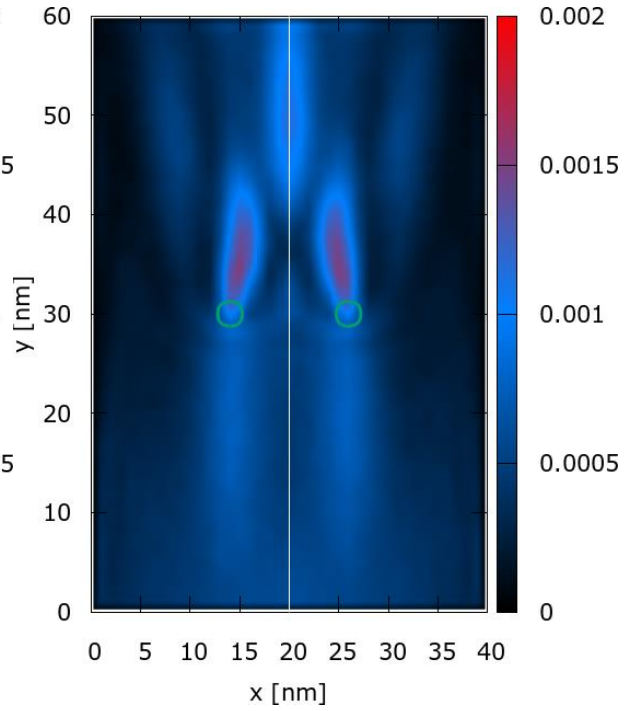


Fig.2: Quantum electron density ([a.u.]) after 200 fs of the initial minimum uncertainty condition (absorbing boundary conditions). The green circles are isolines at 0.175 eV of the Coulomb potentials modeling the dopants.

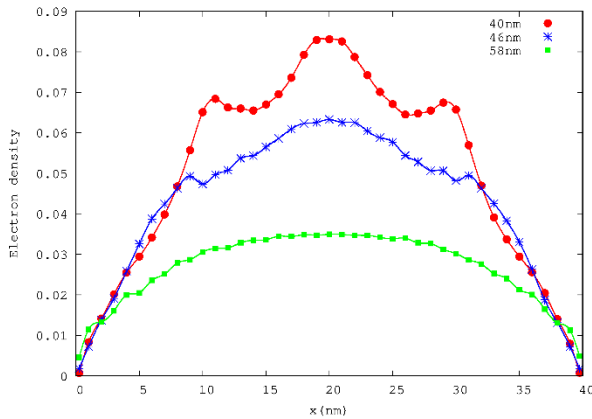


Fig.3: Classical screens show the cumulative density ([a.u.]) recorded at three different y positions.

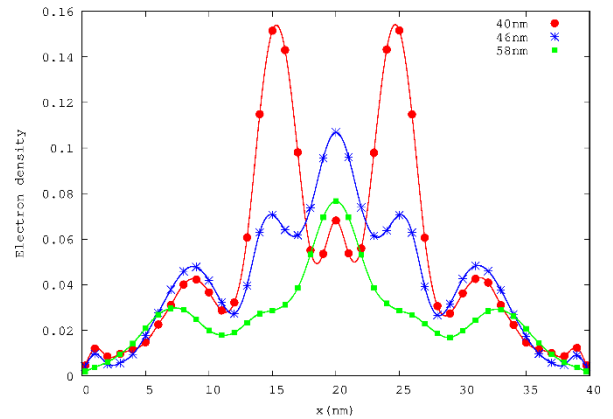


Fig.4: Quantum screens show the cumulative density ([a.u.]) recorded at three different y positions.

Acknowledgments: The financial support by the Austrian Science Fund (FWF) project FWF-P29406-N30, the Austrian Federal Ministry of Science, Research and Economy, and the National Foundation for Research, Technology and Development is gratefully acknowledged. The computational results presented have been achieved using the Vienna Scientific Cluster (VSC).

Neuromorphic Semi-Organic Devices on Flexible Substrates

Mohammad Al-Mamun¹, Muhammad Altaf¹, Ahmad Edrees¹, and Marius Orlowski¹

¹*The Bradley Department of Electrical and Computer Engineering, Virginia Tech,
Blacksburg, Virginia 24061, USA
m.orlowski@vt.edu*

Memristor devices hold the promise of a realization of neuro-inspired computing with neuromorphic functionality implemented on truly neuromorphic hardware. Due to the advantages of good scalability, flexibility, low cost, ease of processing, 3D stacking capability, and large capacity for data storage, polymer-based memristors on flexible substrates look highly attractive, e.g. as wearable electronics. Here, we report on progress of realization of such devices starting with a benchmark, inorganic memristor manufactured on Si substrate and well-characterized [1]. Such filamentary and phase-transition memristors on Si have been successfully modeled [2] according to Chua's theory [3] in terms of electric flux ϕ and total charge q only ($q=q(\phi)$), independent of any specific current or voltage driving input.

Here we report on manufacturing and characterization of such semi-organic devices starting with a well characterized Metal-Insulator-Metal structure (Cu/TaO_x/Pt/on Si) manufactured on a Si substrate and step by step replacing the switching layer (TaO_x) and the substrate by organic polymers. The four derivative devices manufactured are: Cu/O-AA/Al/on Si, Cu/O-AA/Pt/on Si, Cu/O-AA/Pt/Flex, and Cu/P3HT(GNP)/Au/on Si whose cross-sections are shown in Fig. 1. Here O-AA stands for polymer o-anthranilic acid, Flex for flexible substrate, P3HT for 3-hexylthiophene polymer, GNP for graphene nanoplatelets powder suspended in P3HT. We found that: a) conductivity of O-AA increases with increasing concentration of anthranilic acid, b) concentration of graphene nanoplatelets in P3HT modifies conduction properties of the active switching layer from insulator to metallic conductivity. Those technology parameters may help tune the neuromorphic properties of the respective devices.

All derivative semi-organic devices display characteristic current-voltage pinched hysteretic loop under periodic voltage excitation, very similar to the benchmark device Cu/TaO_x/Pt/on Si, demonstrating that the replacement of inorganic by organic materials has successfully preserved the basic memristive properties. Fig. 2 shows a general I-V characteristics for all devices with the threshold voltages, V_{set} , and V_{reset} . Fig. 3 shows I-V for Cu/O-AA/Al/onSi and Cu/O-AA/Pt/onSi. Fig. 4 shows the same I-V for Cu/O-AA/Pt/Flex. In case of the P3HT device, in addition, to the I-V hysteresis, Fig. 5, we observe quantized conductance at no magnetic field and at 300K with integer multiples of $G_0 = 2e^2/h$ ($=12.91 \text{ k}\Omega^{-1}$), and in some devices with partially quantized, $(n/7) \times G_0$ as shown in Fig. 6 [4].

- [1] T. Liu et al., Appl. Phys. Lett, **101**, 073510 (2012)
- [2] M. Orlowski et al., IEEE J. Em. Sel. Top. Circ. Sys., **5**, 143 (2015)
- [3] L. Chua, Appl. Phys. A, **102**, 765 (2011)
- [4] Y. Kang et al., Nanoscale Res. Lett. **11**, 179 (2016)

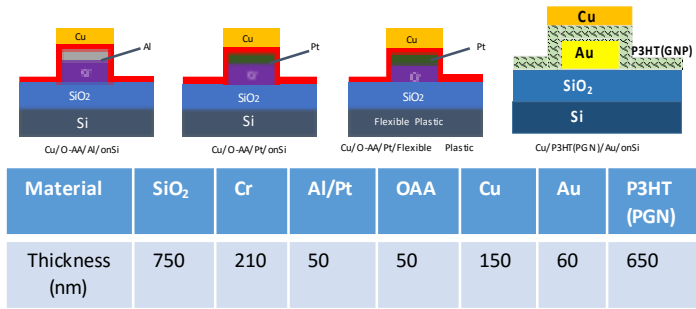


Fig.1: Cross-sections of four semi-organic devices derived from the inorganic Cu/TaOx/Pt device. All devices have an organic active switching layer. Three such devices have been manufactured successfully on a flexible substrate. The last device has organic switching layer of P3HT polymer with suspended graphene nanoplatelets. This device displays integer and partial quantized conductivity, see Fig. 6.. Thicknesses of the respective layers are given in the inserted table.

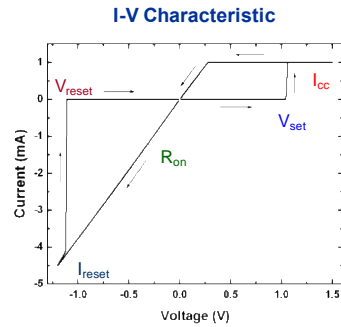


Fig.2: General I-V characteristics for the well characterized Cu/TaOx/Pt device in this work with switching threshold voltages V_{set} and V_{reset} .

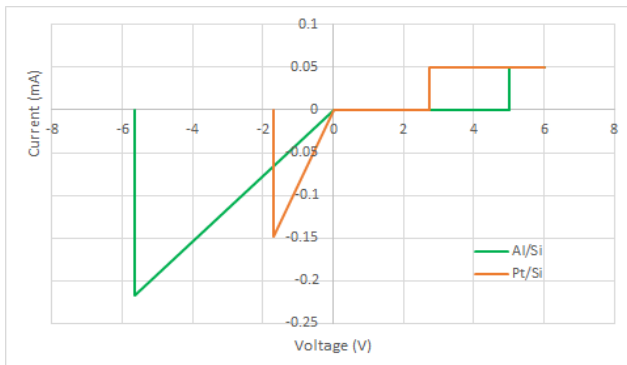


Fig.3: I-V characteristics for devices with polymer switching layer O-AA on Si substrate: Cu/O-AA/Al/onSi and Cu/O-AA/Pt/onSi

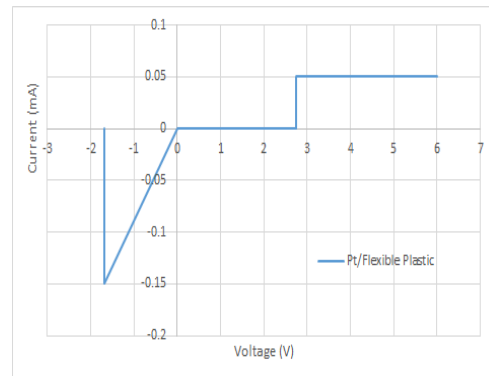


Fig.4 I-V characteristic for Cu/O-AA/Pt/Flex device with polymer switching layer O-AA and flexible polymer substrate.

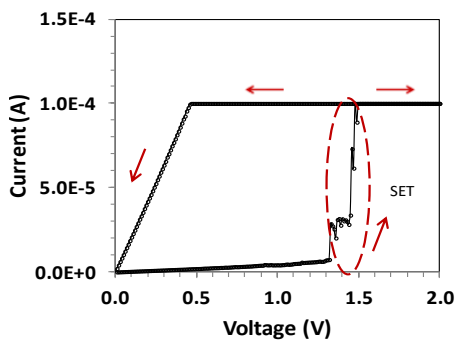


Fig.5: I-V characteristics of a Cu/P3HT(PGN)/Cu/onSi with P3HT polymer merged with graphene nanoplatelets (GNP conc.: 0.1 mg/ml) with a $I_{cc} = 0.1$ mA;

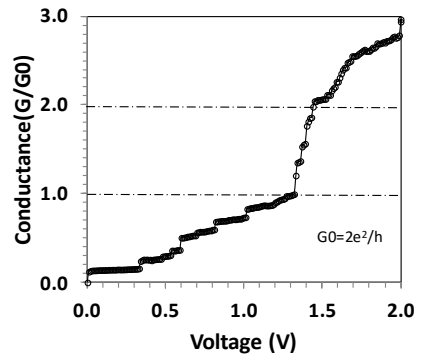


Fig.6: Conductance of the set operation as function of voltage for the device Cu/P3HT(PGN)/Cu/onSi. Integer and partial quantization of the conductance is observed.

Few-Hole Quantum Dots

Andrew Sachrajda¹

¹*Security and Disruptive Technology Division, National Research Council of Canada,
Ottawa K1A 0R6, Canada
andy.sachrajda@nrc.ca*

Holes in quantum dots, defined in 2D systems are predicted to experience a reduced hyperfine interaction, compared to electrons, due to the p-type symmetry of the valence band and to a large light-heavy hole gap. This would mitigate the major source of qubit decoherence in III-V materials which have the advantage of having a direct band-gap for linking to photonic flying qubits (DiVincenzo criteria 6 and 7). Additionally, the hole p-type character generates a strong spin-orbit interaction which can be harnessed to electrically manipulate the spin qubits without the requirement of an oscillating magnetic field (micromagnets) coupled to the device.

In this talk I will review the current status of our experiments [1,2,3] on single and two hole devices defined electrostatically in a GaAs heterostructure¹. The strong spin-orbit interaction is found to strongly influence the properties of the device. Certain hyperfine related effects observable in GaAs electron devices are found to be absent in the hole devices providing evidence of a reduced hyperfine interaction influence. Recently, [4] we introduced the concept of latching to improve the fidelity of spin readout in qubits. I will demonstrate how in the presence of strong spin-orbit the latching approach can be further modified to allow a slow charge detector (e.g. in the millisecond range) to measure fast spin relaxations (e.g. in the 100 ns range). We have used this new technique to measure the field dependence of the spin relaxation and have identified which spin-orbit mechanism dominates.

¹Fabrication of the device was performed at the Center for Integrated Nanotechnologies, a U.S. DOE, Office of Basic Energy Sciences user facility, and Sandia National Laboratories is a multi-mission laboratory managed and operated by National Technology and Engineering Solutions of Sandia, LLC., a wholly owned subsidiary of Honeywell International, Inc., for the U.S. Department of Energy's National Nuclear Security Administration under contract DE-NA-0003525.

[1] A. Bogan et al., Phys. Rev. Lett. **120**, 207701 (2018)

[2] A. Bogan et al., Phys. Rev. Lett. **118**, 167701 (2017)

[3] A. Bogan et al., submitted

[4] S. Studenikin et al., Appl. Phys. Lett. **101**, 233101 (2012)

Atomic Computational Elements Composed of Silicon Dangling Bonds

Robert Wolkow^{1,2}

¹*Department of Physics, University of Alberta, Edmonton, Alberta, T6G 2J1, Canada*

²*Quantum Silicon, Inc., Edmonton, Alberta, T6G 2M9, Canada*

rwolkow@ualberta.ca

Atomic circuitry composed of silicon surface dangling bonds have the potential to address the shortcomings of CMOS. Single dangling bonds behave as atomic silicon quantum dots, in part because such states (and ensembles of such states) are in the band gap and mix poorly with continuum bulk states. Our circuitry appears to have several attractive properties:

Consumes far less energy than CMOS; extreme clocking/THz; ultra compact, low mass; all dots are identical; all distances among dots in an ensemble are identical (rendering all ensembles identical); simple and “green” processing – in one step all active and passive components printed - no layers or mask alignment; can be merged on same chip with CMOS; can perform classical binary logic (proven), likely can perform quantum operations (modeled, yet to be tested), and perhaps most excitingly, can be deployed in entirely unique ways.

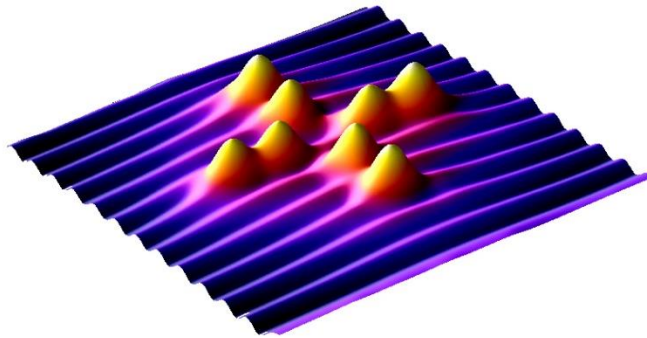
An example of a unique application of the atomic silicon circuitry will be described. Paired dots form a double well potential occupied by one electron. Nearby charges can bias a double well potential to give a preferred occupation of one side of the double well. Multiple pairs and fixed charges have been positioned to create an ensemble that can be viewed as a model – actually a simulator – of a nano-magnet. Such a system is the physical embodiment of an Ising model Hamiltonian. Rather than calculating the properties of such an entity, we merely read them. Because we can read out the state of each bit (the electron position in each atom pair) we can trivially collect a Boltzmann distribution – that is – the fluctuations in energy of this “machine” as it experiences thermal buffeting by the environment.

As we can build an atomic electronic entity that is isomorphous with a neural network, we can foresee ways to more rapidly and accurately achieve unsupervised machine learning. Plans for couplers allowing controlled interaction without physical proximity will be touched upon as will options for exploring quantum behavior. Perfect, atom-defined SETs will enable rapid readout (no microscope will be required).

Lastly, machine learning has been applied to automate our scanned probe fabrication tool: without human supervision, probe errors which occasionally occur are detected and repaired allowing atom-perfect fabrication to proceed, unattended. We now see no barrier to massively parallel, perfect, atom-scale fabrication and therefore to viable, commercial products.

[1] T. Huff et al., arXiv:1706.07427 (2017)

[2] M. Rashidi et al., Phys. Rev. Lett. **121**, 166801 (2018)



A scanning tunneling microscope image of a hydrogen terminated silicon 100 surface on which 8 dangling bonds have been prepared by the removal of 8 hydrogen atoms. These atoms behave as atomic quantum dots and ensembles of dots can be tailored to achieve a wide range of properties. The entity shown here is a "cross", that is, a structure allowing binary signals on two orthogonal lines to pass through one another without interaction. This capability allows truly 2 dimensional circuitry (the avoidance of multilayers and vias between layers) and enhanced connectivity without going out of the plane.

**Formation of Coupled Quantum Dots and
Optically-Operated Conditional Gates with Single-Wall Carbon Nanotubes**

Akira Hida¹ and Koji Ishibashi^{1,2}

¹*Advanced Device Laboratory, RIKEN, Saitama, Japan*

²*RIKEN Center for Emergent Matter Science (CEMS), Saitama, Japan*
kishiba@riken.jp

This abstract is not printed due to the authors' request.

Quantum Control of Silicon Quantum Dot Spin Qubits

Mark A. Eriksson¹

¹*Department of Physics and Wisconsin Institute for Quantum Information,
University of Wisconsin-Madison, Madison, WI 53706, USA
maeriksson@wisc.edu*

One of the remarkable features of spins in the solid state is the enormous range of time-scales over which coherent manipulation is possible. If one considers gate-controlled manipulation of nuclear spins at one extreme, and strongly-interacting multi-electron qubits at the other extreme, coherent control of spins in semiconductors has been demonstrated with over 9 orders of magnitude variation in the manipulation time. Remarkably, confining three electrons in two neighboring quantum dots – a configuration known as the Quantum Dot Hybrid Qubit (QDHQ) – enables all electrical control and measurement of spin dynamics on time scales less than one nanosecond [1-3]. In this talk I will discuss the interesting commonalities and contrasts between the two limiting cases: qubits composed of a single-spin, be it electron or nuclear, where magnetically-driven manipulation is required, and qubits composed of multiple electrons, like the QDHQ, for which case direct electric-field manipulation is possible.

The QDHQ often is formed in quantum dots defined in Si/SiGe heterostructures, where the splitting between the two lowest-lying valley states can be made to define the qubit energy levels. This valley splitting has interesting features that depend on the details of the underlying virtual substrate [4,5]. I will present data demonstrating the importance of materials for these quantum device properties, and I will show recent results demonstrating the first steps towards controlling those properties through the design and modification of the heterostructure growth.

- [1] D. Kim, et al., *Nature* **511**, 70 (2014)
- [2] D. Kim, et al., *npj Quant. Inf.* **1**, 15004 (2015)
- [3] B. Thorgrimsson, et al., *npj Quant. Inf.* **3**, 32 (2017)
- [4] J.C. Abadillo-Uriel, et al., *Phys. Rev. B* **98**, 165438 (2018)
- [5] S.F. Neyens, et al., *Appl. Phys. Lett.* **112**, 243107 (2018)

Integration Technology for Scalable Superconducting Quantum Annealer

Shiro Kawabata¹

¹*Nanoelectronics Research Institute,
National Institute of Advanced Industrial Science and Technology (AIST), Ibaraki 305-8568,
Japan
s-kawabata@aist.go.jp*

Quantum annealing is a promising technique which leverages quantum mechanics to solve hard combinatorial optimization problems [1]. D-Wave Systems Inc. [2] is the first company to commercialize superconducting quantum annealing machine in 2011 and ship a new machine with 2000 qubits in 2017. However, integration of larger number of qubit as well as improvement of qubit coherence are required for practical applications.

In this talk we will overview our technological integration scheme for large-scale superconducting quantum annealer in AIST [3,4]. The scalability is achieved by QUIP (QUbit, Interposer and Package substrate) structure, which is based on our multi-layer fabrication and multi-chip 2.5D packaging technology such as Through Silicon Via (TSV) and flip-chip bonding (Fig. 1). We have also developed an Application Specific Annealing Computing (ASAC) architecture (Fig. 2) in order to increase the available hardware budget and reduces the cost and time for R&D. In addition, we will show a fabricated quantum annealer for prime factoring [4] (Fig. 3) and theoretical activities on quantum annealing [5-7].

Acknowledgments: This presentation is based on results obtained from a project commissioned by the New Energy and Industrial Technology Development Organization (NEDO), Japan.

[1] T. Kadowaki and H. Nishimori, Phys. Rev. E **58**, 5355 (1998)

[2] D-Wave Systems, <https://www.dwavesys.com/>

[3] M. Maezawa et al., arXiv:1712.05561 (2017)

[4] M. Maezawa et al., arXiv:1809.01425 (2018)

[5] V. Karanikolas and S. Kawabata, arXiv:1806.08517 (2018)

[6] K. Imafuku, arXiv:1803.07259 (2018)

[7] K. Imafuku, arXiv:1807.04438 (2018)

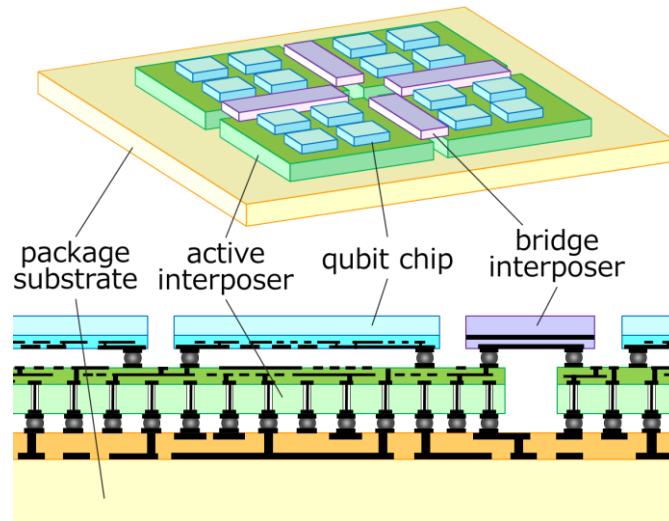


Fig.1: Schematics of scalable superconducting quantum annealer based on 2.5D packaging technology.

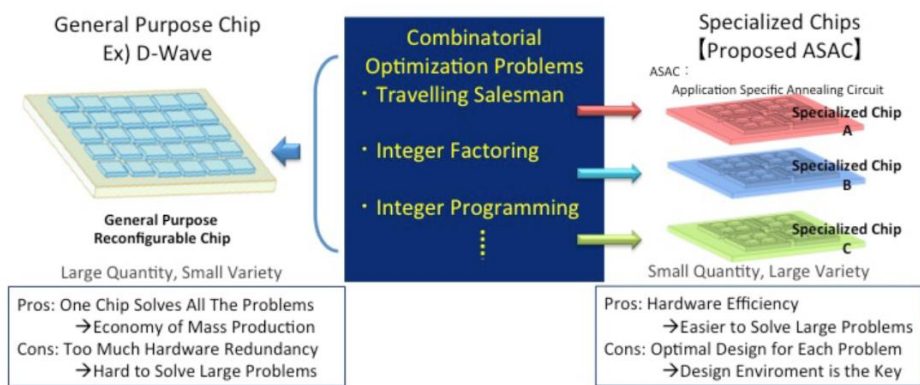


Fig.2: Concept for application specific annealing circuit (ASAC).

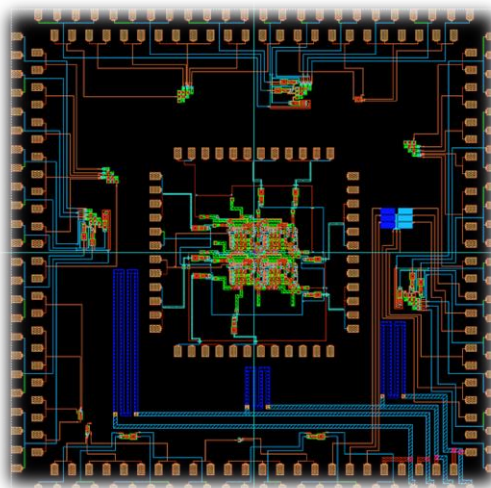


Fig.3: Photo mask for superconducting quantum annealer for prime factoring based on Nb flux qubit.

Magnetotransport in Highly Enriched ^{28}Si for Quantum Information Processing Devices

Aruna N. Ramanayaka^{1,2}, Ke Tang^{1,2}, Joseph A. Haggmann¹, Hyun-Soo Kim^{1,2},
Curt A. Richter¹, and Joshua M. Pomeroy¹

¹*National Institute of Standards & Technology, Gaithersburg, Maryland 20899, USA*

²*Joint Quantum Institute, University of Maryland, College Park, Maryland 20742, USA*

aruna.ramanayaka@nist.gov

Elimination of unpaired nuclear spins can result in low error rates for quantum computation; therefore, isotopically enriched ^{28}Si is regarded as an ideal environment for quantum information processing devices. Using mass selected ion beam deposition technique, we in-situ enrich and deposit epitaxial ^{28}Si achieving better than 99.99998 % ^{28}Si isotope fractions [1]. To explore the electrical properties and optimize the growth conditions of in-situ enriched ^{28}Si , we fabricate top-gated Hall bar devices, and investigate the magnetotransport in this material at magnetic fields as high as 12 T and temperatures ranging from 10 K to 1.2 K. A schematic of the cross-sectional view and an optical micrograph of the fabricated device is shown in Fig.1 (a) and (b), respectively. At a temperature 1.9 K, we measure maximum mobilities of approximately $(1740 \pm 2) \text{ cm}^2/(\text{V} \cdot \text{s})$ and $(6040 \pm 3) \text{ cm}^2/(\text{V} \cdot \text{s})$ at an electron density of $\approx 1.2 \times 10^{12} \text{ cm}^{-2}$ for devices fabricated on ^{28}Si and natural Si, respectively. For magnetic fields $B > 2 \text{ T}$, both types of devices demonstrate well developed Shubnikov-de Haas oscillations on the longitudinal magnetoresistance (see Fig.2 and Fig.3). In contrast to the device on an isotopically enriched ^{28}Si epi-layer, the device on natural Si ($^{\text{nat.}}\text{Si}$) demonstrates spin-splitting for $B > 3 \text{ T}$ (see Fig.2). Furthermore, relative to the device on $^{\text{nat.}}\text{Si}$, the weak localization is stronger for the device fabricated on isotopically enriched ^{28}Si . Based on the T dependence of the Shubnikov-de Haas oscillations and weak localization, the dominant scattering mechanism in these devices appears to be background impurity scattering and/or interface roughness scattering. We believe that the relatively lower mobility and stronger weak-localization observed for the devices fabricated on ^{28}Si may be due to the dilute adventitious C, N and O in deposited ^{28}Si .

[1] K. J. Dwyer et al., J. Phys. D **47**, 345105 (2014)

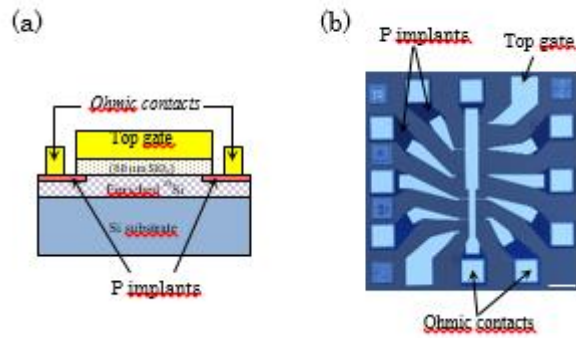


Fig.1: (a) Schematic representations of the gated Hall bar devices fabricated on ^{28}Si and (b) An optical micrograph of a gated multi terminal Hall bar device fabricated on ^{28}Si are shown.

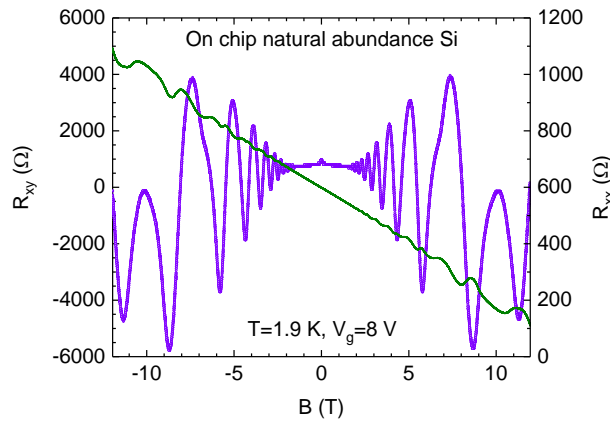


Fig.2: Magnetoresistance R_{xx} (right-axis) and Hall resistance R_{xy} (left-axis) measured for the device fabricated on natural Si substrate are shown. Note that the device on $^{\text{nat}}\text{Si}$ and ^{28}Si are fabricated on the same Si substrate. Therefore, both have the same processing history.

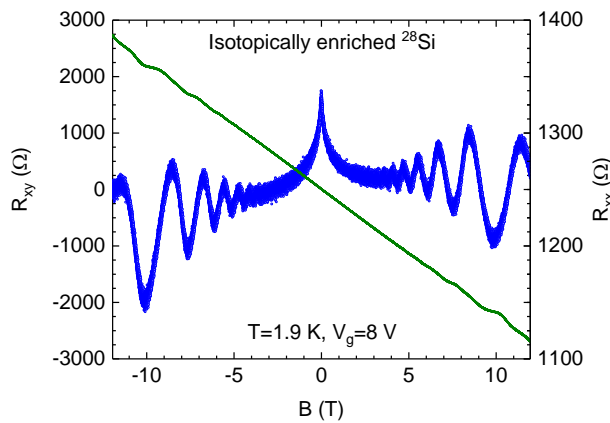


Fig.3: Magnetoresistance R_{xx} (right-axis) and Hall resistance R_{xy} (left-axis) measured for the device fabricated on isotopically enriched ^{28}Si epi-layer are shown.

Terahertz Current-Driven Plasmonic Lasing and Amplification

Deepika Yadav², Stephane Boubanga-Tombet¹, Gen Tamamushi¹, Takayuki Watanabe¹, Akira Satou¹, Alexander Dubinov², Maxim Ryzhii³, Victor Ryzhii¹, and Taiichi Otsuji¹

¹*Research Institute of Electrical Communication, Tohoku University,
Sendai, Miyagi 9808577, Japan*

²*Institute for Physics of Microstructures, Russian Academy of Sciences,
Lobachevsky State University of Nizhny Novgorod, Nizhny Novgorod, Russia*

³*Dept. of Computer Science and Engineering, University of Aizu, Aizu-Wakamatsu, Japan
otsuji@riec.tohoku.ac.jp*

Graphene has attracted considerable attention due to its massless and gapless energy spectrum of Dirac Fermions as well as strong light-matter interactions via plasmon-polaritons. Carrier-injection pumping of graphene can enable negative-dynamic conductivity in the terahertz (THz) range, which may lead to new types of THz lasers [1-4]. The dual-gate graphene channel transistor (DG-GFET) structure serves carrier population inversion in the lateral p-i-n junctions under current-injection pumping, promoting spontaneous incoherent THz light emission [1,2]. We designed and fabricated a distributed feedback (DFB) DG-GFET (Fig. 1) [3], demonstrating a single-mode lasing at 5.2 THz and a broadband 1-8-THz amplified spontaneous emission both at 100K (Fig. 2) [3]. To increase the operating temperature and lasing radiation intensity, further enhancement of the THz gain and the cavity Q factor are mandatory. Current-driven plasmon instabilities in graphene can promote the generation and amplification of THz waves [5-10], leading to intense, room-temperature THz lasing. We fabricated a 100's-nm to micrometer scaled asymmetrically interdigitated dual grating metal gate graphene-channel field effect transistors (ADGG-GFETs) using a high quality exfoliated monolayer graphene encapsulated between the hBN buffer and gate insulation layers (Fig. 3) [10], demonstrating a giant amplification gain up to 9dB over 1-3-THz frequencies at 300K (Figs. 4, 5) [10].

Acknowledgments: This work was supported by JSPS KAKENHI No. 16H06361, 16K14243, and 18H05331, Japan.

- [1] V. Ryzhii et al., J. Appl. Phys. **101**, 083114 (2007)
- [2] M. Ryzhii and V. Ryzhii, Jpn. J. Appl. Phys. **46**, L151 (2007)
- [3] V. Ryzhii et al., J. Appl. Phys. **110**, 094503 (2011)
- [4] D. Yadav et al., Nanophoton. **7**, 741 (2018)
- [5] M. Dyakonov and M. Shur, Phys. Rev. Lett. **71**, 2465 (1993)
- [6] V. Ryzhii et al., Jpn. J. Appl. Phys. **E89-C**, 1012 (2006)

- [7] S. Mikhailov, Phys. Rev. B **58**, 1517 (1998)
- [8] G.R. Aizin et al., Phys. Rev. B **93**, 195315 (2016)
- [9] Y. Koseki et al., Phys. Rev. B **93**, 245408 (2016)
- [10] S. Boubanga-Tombet et al., arXiv:1801.04518 (2018); CLEO Dig., **SW4D.4** (2018)

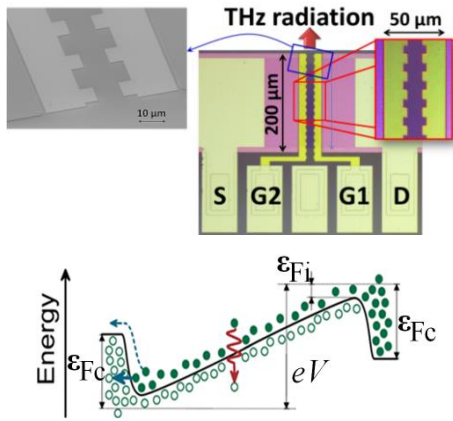


Fig.1: DFB-DG-GFET. Top and bird's view micro-photoimages (top) and its band diagram under population inversion via current-injection pumping (bottom). Complementary gate biasing makes the e-h carrier injection (ϵ_{Fc}) with which drain-source biasing causes the carrier population inversion ($\sim 2\epsilon_{Fi}$).

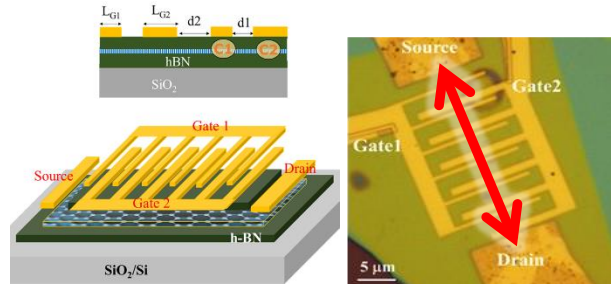


Fig.3: hBN/graphene/hBN FET with an ADGG. Cross-sectional and bird's views (left) and a top view micro-photoimage (right). The red arrow indicates the nominal polarization axis for THz radiation that can excite the graphene plasmons.

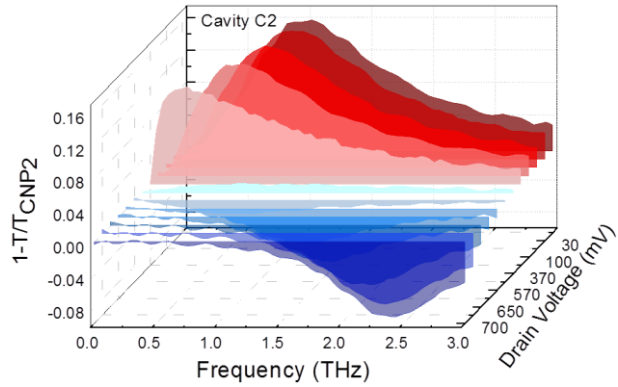
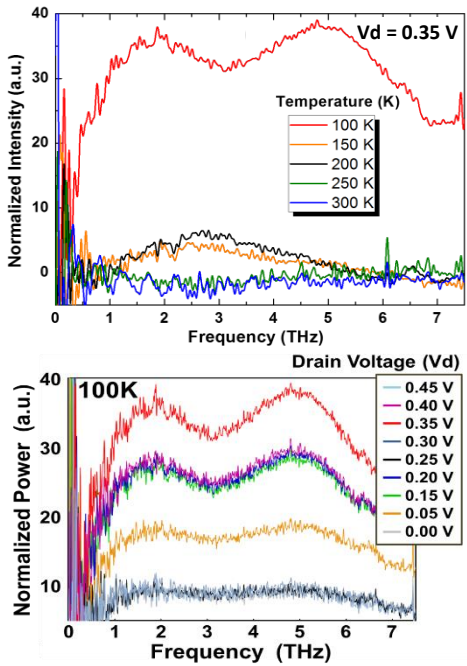
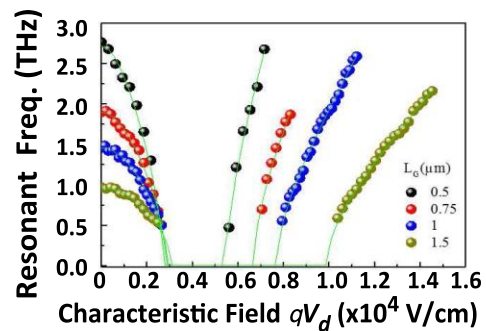


Fig.4: Drain bias dependent extinction spectra measured in cavities C2 of one type of the ADGG-GFET for fixed $V_{g2} = V_{CNP2} = 3 V$ and $V_{g1} = V_{CNP1}$ when varying V_d .



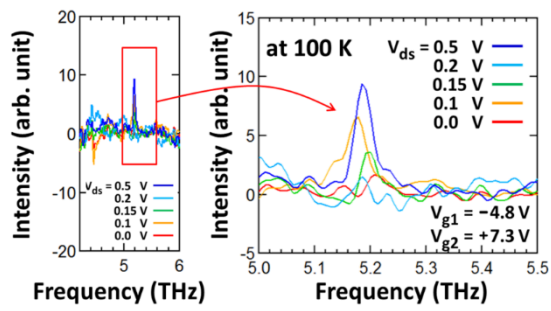


Fig.2: Experimental observation of emission spectra from fabricated DFB-DG-GFET's. Broadband amplified spontaneous THz emission at 100K (upper and middle) and single-mode lasing at 5.2 THz at 100K (lower).

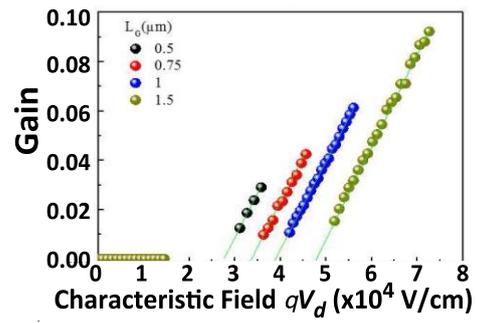


Fig.5: Measured graphene plasmon resonance frequencies (upper) and gain (lower) as a function of characteristic field intensity qV_d ($q = 2\pi/L_{g1,2}$: the plasmon wave vector) and fitting to the dispersion formulae in [7] as solid lines.

Electrically Inert Interface in 2D Heterostructure FETs

Kosuke Nagashio¹

¹*Department of Materials Engineering, The University of Tokyo, 7-3-1,
Hongo, Bunkyo-ku, Tokyo, 113-8656, Japan
nagashio@material.t.u-tokyo.ac.jp*

1. Introduction

To realize the electronic and optical devices, the researchers have tried to passivate the interfaces so far for long time, such as dangling bonds at SiO₂/Si interface and lattice mismatch in GaN/AlN heterointerfaces. Contrary to these conventional cases, 2-dimensional layered heterostructure devices have attracted great attentions because the electrically inert interfaces are “expected” without considering the lattice mismatch due to the ideally dangling bond free surface and van der Waals interface. However, the electrical characterization of 2D interface properties have not been conducted in detail by the capacitance measurement. This is due to the large parasitic capacitance of electrode pad and Si substrate.

In this study, by using the quartz substrate, the parasitic capacitance was completely removed. We focus on interface properties for bilayer graphene, MoS₂ and the heterostructures toward the 2D tunneling electronics. Based on the recent results, the perspective on the 2D electronics will be discussed.

2. Electrically inert h-BN/BLG interface[1]

Bilayer graphene field-effect transistors (BLG-FETs), unlike conventional semiconductors, are greatly sensitive to potential fluctuations due to the charged impurities in high-k gate stacks since the potential difference between two layers induced by the external perpendicular electrical field is the physical origin behind the band gap opening. The assembly of BLG with layered h-BN insulators into van der Waals heterostructure has been widely recognized to achieve the superior electrical transport properties. However, the carrier response properties at the h-BN/BLG heterointerface, which control the device performance, have not yet been revealed due to the inevitably large parasitic capacitance. In this study, the significant reduction of potential fluctuations to ~1 meV is achieved in all-2-dimensional heterostructure BLG-FET on a quartz substrate, which results in the suppression of the off-current to the measurement limit at a small band gap of ~90 meV at 20 K. By capacitance measurement, we demonstrate that the electron trap/detrapping response at such heterointerface is suppressed to undetectable level in the measurement frequency range. The electrically inert van der Waals heterointerface paves the way for the realization of future BLG electronics applications.

3. Energy distribution of D_{it} in MoS₂ FET[2]

Contrary to BLG where the all 2D heterostructure is required, high-k/MoS₂ FET has attracted attentions because large energy gap of ~ 1.8 eV is not largely affected by the potential fluctuation due to high-k oxide. In this study, monolayer MoS₂ FET with ALD-Al₂O₃ top gate was fabricated by the mechanical exfoliation of bulk MoS₂. As for C-V measurement of monolayer MoS₂ FET, the frequency dispersion is much reduced due to the relatively high crystallinity of bulk MoS₂ and the dedicated formation of Y₂O₃ buffer layer for ALD-Al₂O₃. Having confirmed the clear agreement of the experimentally extracted quantum capacitance (C_Q) with the theoretical model, D_{it} is shown as a function of E_F . The measured E_F range is extended to near the conduction band edge by low temperature measurements (75- 300 K). As a result, the band tail-shape of D_{it} is clearly confirmed. This band-tail D_{it} will not be directly related with sulfur vacancies, but explained by the bond bending of Mo d orbital because of the similarity of energy distribution of D_{it} for sp³ Si. The origin for the bond bending of the Mo d orbital might be the strain at the high-k /MoS₂ interface or the surface roughness of SiO₂. Moreover, the important finding realized from this study is that ultra-thin 2D materials is more sensitive to the interface disorder because of reduced DOS, since the effect of interface traps on electrical properties is controlled by the relative magnitude of C_Q and C_{it}.

4. All solid state 2D tunnel FET[3]

2D materials are highly promising for tunnel FETs with low subthreshold swing and high drive current because the shorter tunnel distance and strong gate controllability can be expected from the van der Waals gap distance and the atomically sharp heterointerface formed independently of lattice matching. However, the common problem for 2D-2D TFETs is the lack of highly doped 2D materials with the high process stability as the sources. In this study, we have found that p⁺-WSe₂ doped by charge transfer from a WO_x surface oxide layer can be stabilized by transferring it onto a h-BN substrate. Using this p⁺-WSe₂ as a source, we fabricate all-solid-state 2D-2D heterostructure TFETs with an Al₂O₃ top gate insulator, i.e., type-II p⁺-WSe₂/MoS₂ and type-III p⁺-WSe₂/WSe₂. The band-to-band tunneling and negative differential resistance trends are clearly demonstrated at low temperatures. This work suggests that high doped 2D crystal of the charge transfer type is an excellent choice as sources for TFETs.

Acknowledgments: This research was supported by the JSPS A3 Foresight program, Core-to-Core Program, A. Advanced Research Networks.

[1] K. Kanayama and K. Nagashio, *Sic. Rep.* **5**, 15789 (2015);

T. Uwanno et al., *ACS Appl. Mater. Interfaces* **10**, 28780 (2018)

[2] N. Fang and K. Nagashio, *J. Phys. D* **51**, 065110 (2018);

N. Fang and K. Nagashio, *ACS Appl. Mater. Interfaces* **10**, 32355 (2018)

[3] J. He et al., *Adv. Electron. Mater.* **4**, 1800207 (2018)

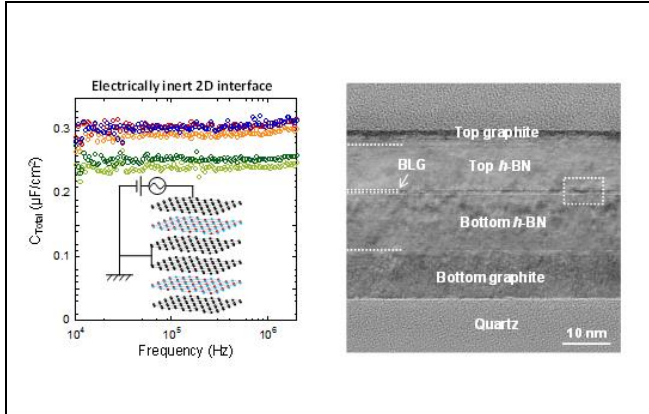


Fig.1: (left) Capacitance between top gate and BLG as a function of frequency. (right) Cross-sectional TEM image of all 2D heterostructure.

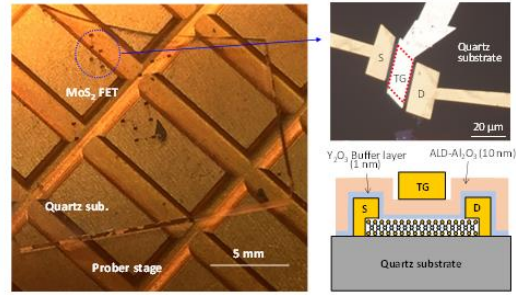


Fig.3: Monolayer MoS2 FET with Al2O3 top gate insulator on quartz substrate.

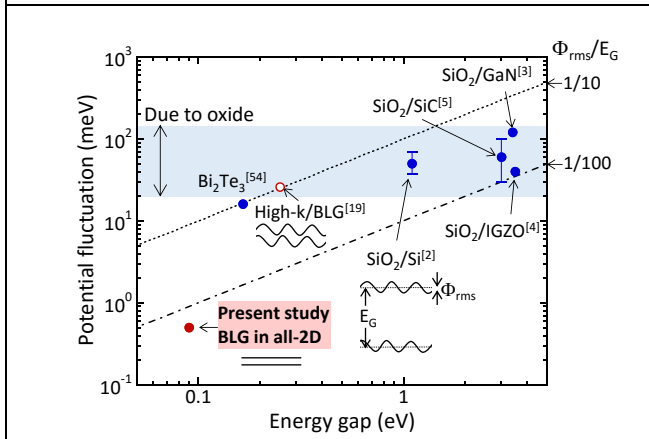


Fig.2: Comparison of potential fluctuations in various semiconductors in different gate stack structures.

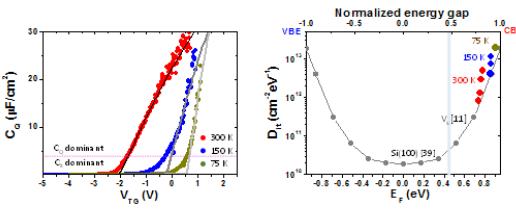


Fig.4: (left) Quantum capacitance as a function of VTG at different temperatures. (right) Dit distribution as a function of EF at different temperatures.

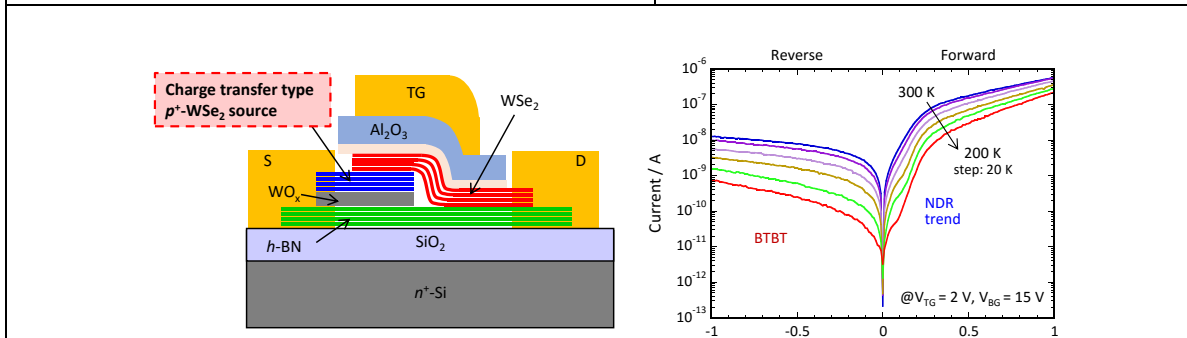


Fig.5: (left) Schematic of all solid state 2D TFET. (right) Diode properties showing BTBT.

Near-Field Hyperspectral Imaging of Hybrid Plasmonics in Twisted Graphene

Slava V. Rotkin¹, Michael Blades², Haomin Wang³, Xiaoji Xu³,
Huy Q. Ta⁴, and Mark H. Rummeli⁴

¹*Materials Research Institute, Department of Engineering Science & Mechanics,
The Pennsylvania State University, University Park, PA 16802, USA*

²*Department of Physics, Lehigh University,
16 Memorial Drive East, Bethlehem, PA 18015, USA*

³*Department of Chemistry, Lehigh University, 6 East Packer Ave, Bethlehem, PA 18015, USA*

⁴*Soochow University, Suzhou 215006, China; Centre of Polymer and Carbon Materials,
Polish Academy of Sciences, M. Curie-Sklodowskiej 34, Zabrze 41-819, Poland
rotkin@psu.edu*

Twisted bilayer (and multilayer) graphene has been in the focus of studies recently¹, due to non-trivial quantum physics as a function of the twist (chiral) angle that manifests itself in transport and optical properties. In fact, tBLG is just an example system from a large family of chiral 2D materials. Here we aim at understanding fundamental physics of hybrid many-body modes in chiral 2D material using an optical tool with subwavelength resolution – scattering Scanning Near-field Optical Microscope (sSNOM). Naturally sSNOM signal is most sensitive to the (evanescent) polaritonic modes of the sample. While, due to the frequency range of our experimental setup (typically between $\sim 1100\text{ cm}^{-1}$ and $\sim 1700\text{ cm}^{-1}$), the polaritonic modes are predominantly based on the graphene plasmons.

It is well known² that graphene plasmons (due to screening nature of 2D layers) can easily hybridize with the optical modes of the substrate, for example phonon-polaritons of SiO₂. Furthermore, due to Dirac bandstructure is sensitive to in-plane deformations, hybrid plasmon-phonon modes could exist even in the MLG in vacuum³. Certainly, the chirality of the tBLG creates a novel spin on plasmon physics in multilayered systems. Given all of the above, it appears interesting to explore whether sSNOM signals will provide new information on any of this many-body physics. Indeed, we show that both sSNOM imaging mode and, especially, sSNOM spectral study give a large volume of experimental information about MLG, tBLG and modes in higher multiplexity layered structures. For example, Fig. 1 shows a typical amplitude map with multiple islands. The contrast allows one to determine the angular mismatch between the top-layer islands and bottom layer grains (Fig.2).

Acknowledgments: Authors acknowledge Dr. Tobias Gokus (Neaspec) for taking some of the sSNOM data and NSF ECCS-1509786 grant that partially supported this research.

- [1] S. Carr et al., Phys. Rev. B **95**, 075420 (2017)
 [2] T. Stauber, J. Phys. Condens. Matt. **26**, 123201 (2014)
 [3] M. Jablan et al., Phys. Rev. B **83**, 161409 (2011)

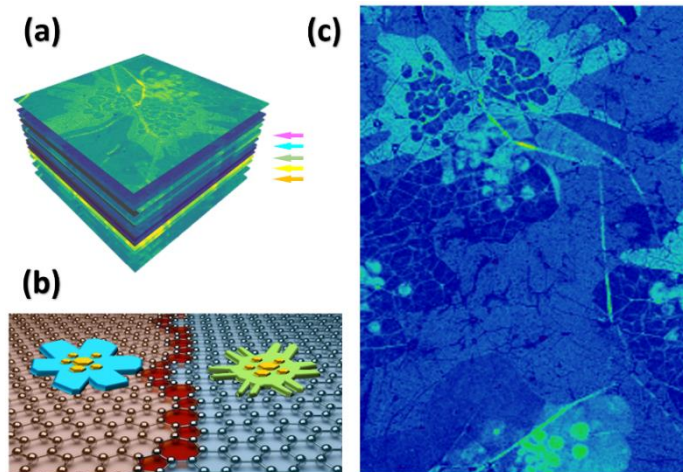


Fig.1: Near-field mapping of multilayered CVD graphene sample: (a) schematics of hyperspectral imaging at different sSNOM excitation wavelengths; (b) cartoon of different shape tBLG islands growing at two sides of the grain boundary of single layer graphene; (c) typical sSNOM amplitude image (6 μm x 9 μm) of the multiple islands (at 1580 cm^{-1}).

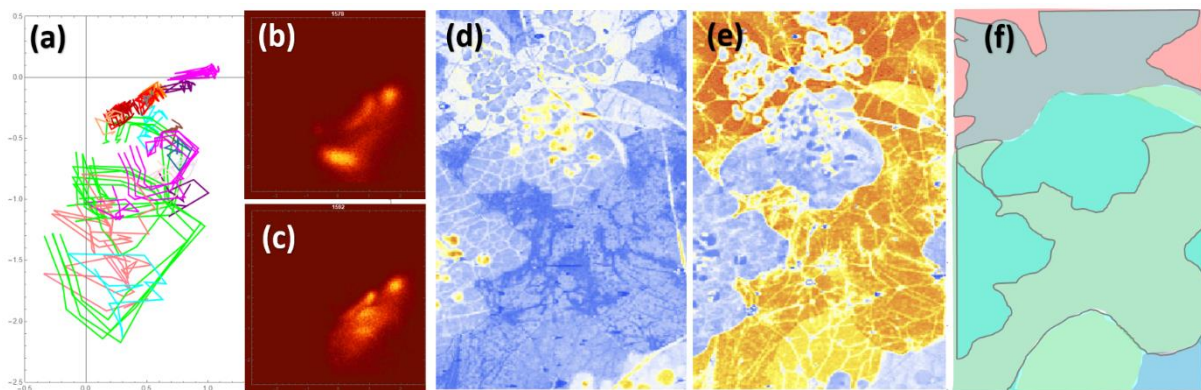


Fig.2: Hyperspectral analysis of sSNOM data: (a) phase maps of average sSNOM signals from specific areas on the sample (for a range of excitation wavelengths); (b-c) statistics of sSNOM amplitude/phase at 1578 cm^{-1} and 1592 cm^{-1} : data from the islands of different chirality clusters in different spots; (d-e) sSNOM amplitude and phase images that show that the sSNOM contrast can be used to distinguish registry between the underlying graphene grains and top layer islands; (f) schematics of top layer islands (highlighted with gray boundaries) and grains in the bottom layer (labeled by color).

Cyclotron Resonance Absorption of Mid-Infrared Light in Graphene/h-BN van der Waals Heterostructures

Tomoki Machida^{1,2}, Kei Kinoshita¹, Yusai Wakafuji¹, Momoko Onodera¹, Miho Arai¹, Satoru Masubuchi¹, Rai Moriya¹, Kenji Watanabe³, and Takashi Taniguchi³

¹*Institute of Industrial Science, University of Tokyo, Tokyo 153-8505, Japan*

²*CREST, Japan Science and Technology Agency, Tokyo 102-0076, Japan*

³*National Institute for Materials Science, Ibaraki 305-0044, Japan*

tmachida@iis.u-tokyo.ac.jp

Charge carriers in graphene, massless Dirac fermions, form a unique sequence of the Landau levels in high magnetic fields. Thus, the cyclotron resonance (CR) in graphene is distinctly different from that in conventional two-dimensional electron systems based on semiconductors. In this work, we study mid-infrared/THz photoresponse due to CR in graphene/h-BN van der Waals heterostructures, fabricated using the mechanical exfoliation and transfer technique of atomic layers. Magnetotransport measurements were carried out at low temperature and high magnetic fields. We demonstrate photoresponse signals induced by three different mechanisms: bolometric effect, photovoltaic effect, and photo-thermoelectric effect. We discuss CR in monolayer, bilayer, and trilayer graphene. In addition, we present our recent development of an autonomous robotic system for building van der Waals superlattices.

[1] K. Kinoshita et al., *Appl. Phys. Lett.* **113**, 103102 (2018)

[2] S. Masubuchi et al., *Phys. Rev. B* **88**, 121402 (2013)

[3] S. Masubuchi et al., *Nat. Comm.* **9**, 1413 (2018)

[4] Y. Asakawa et al., *Phys. Rev. Lett.* **119**, 186802 (2017)

[5] Y. Sata et al., *Phys. Rev. B* **98**, 035422 (2018)

[6] Y. Hoshi et al., *Phys. Rev. Mat.* **2**, 064003 (2018)

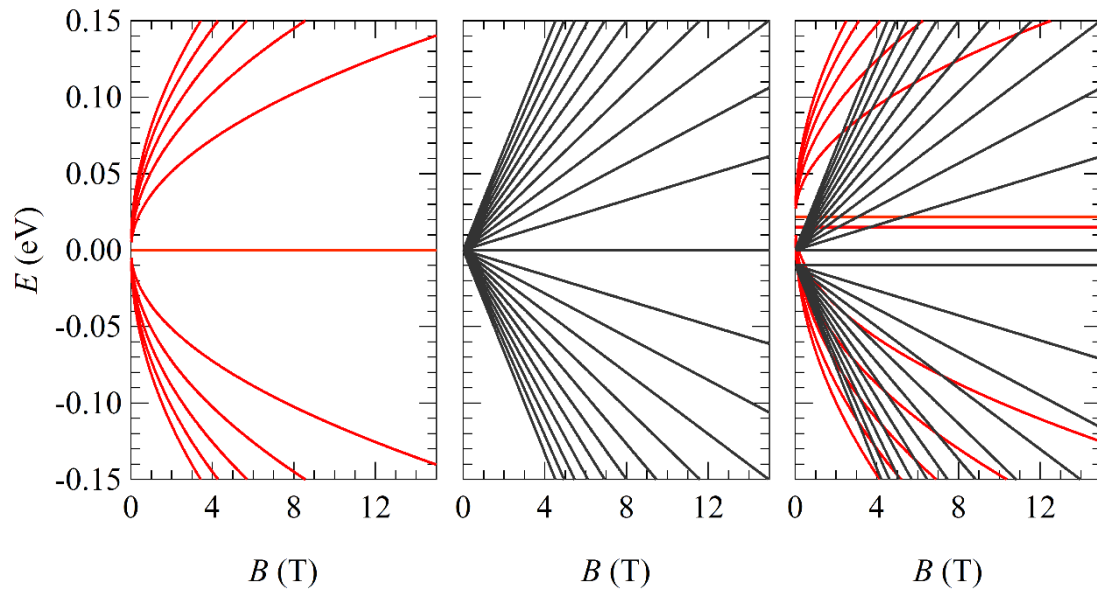


Fig.1: Landau level spectrum of monolayer (left), bilayer (center) and trilayer (right) graphene.

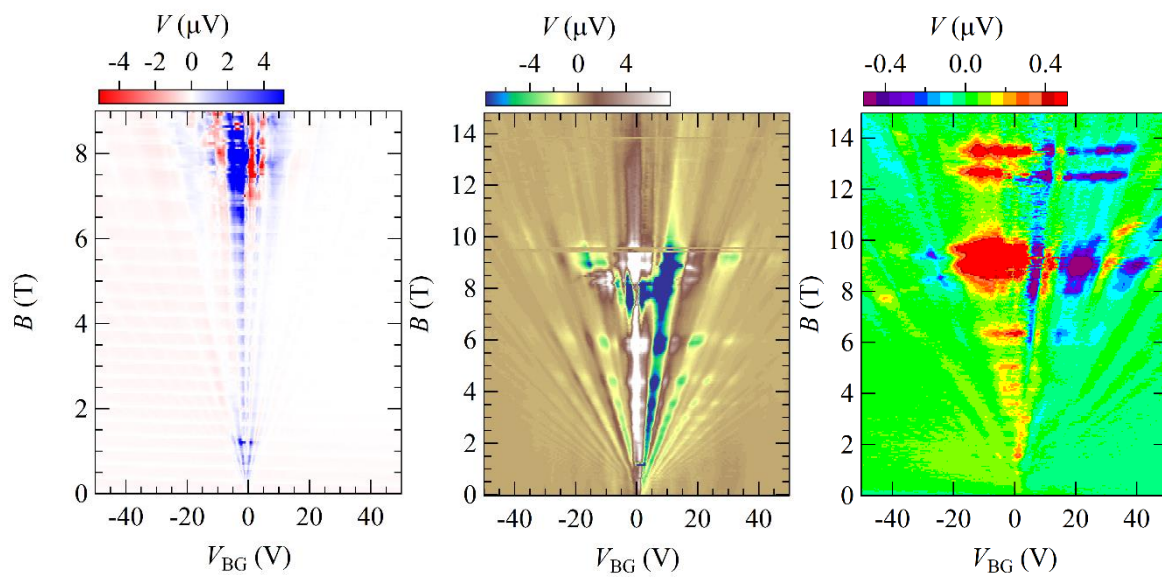


Fig.2: Color-scale plot of photo voltage as a function of back gate voltage and magnetic field in monolayer (left), bilayer (center) and trilayer (right) graphene.

Mobility and 1/f Noise in MoS₂ and MoSe₂ Field-Effect Transistors – Understanding the Intrinsic Device

Jiseok Kwon¹, Suprem Das², Collin J. Delker³, Charles T. Harris³,
Brian Swartzentruber³, and David B. Janes¹

¹*School of Electrical and Computer Engineering and Birck Nanotechnology Center, Purdue University, W. Lafayette, IN, 47906, USA*

²*Department of Industrial & Manufacturing Systems Engineering and Department of Electrical & Computer Engineering, Kansas State University, Manhattan, KS, 66506, USA*

³*Sandia National Laboratories, Albuquerque, NM 87185, USA*
janes@purdue.edu

Two-Dimensional Transition Metal Dichalcogenides (2D-TMDCs), including MoS₂ and MoSe₂, are being widely explored as channel materials in Field Effect Transistor (FETs). For typical FET structures utilizing Schottky-barrier contacts, the dependences of channel mobility on channel thickness and contact work function have been attributed to interfacial scattering and contact/interlayer coupling resistances[1]. While low-frequency (1/f) noise has been reported for various devices with TMDC channels, the overall effects of contact and interlayer coupling resistances have not been considered in detail. The current study focuses on the current-voltage characteristics and voltage-dependent 1/f noise behavior of MoS₂ and MoSe₂ FET devices with various layer thicknesses and various contact metals [2]. In order to understand the effects of contacts and interlayer coupling resistance on the noise properties as well as to correlate to the mobility behavior, the contributions of channel region and series resistance effects are determined versus gate voltage. Consideration of the intrinsic (channel) and extrinsic (total device) noise and resistance behavior allows clear identification of channel-dominated voltage regimes, which allows determination of the associated mechanism responsible for the channel noise, as well as material-dependent variations in the contact contributions. In general, the measured noise amplitude shows a crossover from channel- to contact-dominated noise as the gate voltage is increased. The voltage dependence of noise can be quantitatively modelled using a channel noise contribution described by a mobility-fluctuation (Hooge) noise model, and noise/resistance contributions associated with the contact and interlayer resistances. The figure of merit (Hooge parameter) initially improves (decreases) with increasing channel thickness, indicative of reduced effects of interfacial states, and reaches a minimum for channel thicknesses ~ 15 layers. The results of various channel materials, layer thicknesses and channel length can be used to develop a generalized picture of noise behavior of these devices.

Acknowledgments: This work was supported, in part, by National Science Foundation under grant ECCS – 1408346 and performed, in part, at the Center for Integrated Nanotechnologies, an Office of Science User Facility operated for the U.S. Department of Energy Office of Science. Sandia National Laboratories is a multi-mission laboratory managed and operated by National Technology and Engineering Solutions of Sandia, LLC., a wholly owned subsidiary of Honeywell International, Inc., for the U.S. DOE’s National Nuclear Security Administration under contract DE-NA-0003525. The views expressed in the article do not necessarily represent the views of the U.S. DOE or the United States Government. SAND2018-9837 A.

[1] S. Das and J. Appenzeller, Phys. Status Solidi RRL **7**, 268 (2013)
 [2] S. R. Das et al., Appl. Phys. Lett. **106**, 083507 (2015)

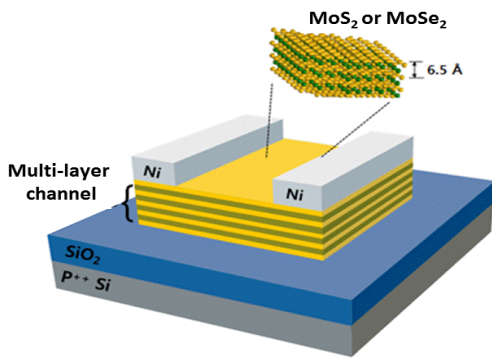


Fig.1: Device schematic for MoS₂ and MoSe₂ devices. Device is back-gated via a 90-100 nm thick SiO₂ layer. Various contact metals were studied (Ni shown in schematic).

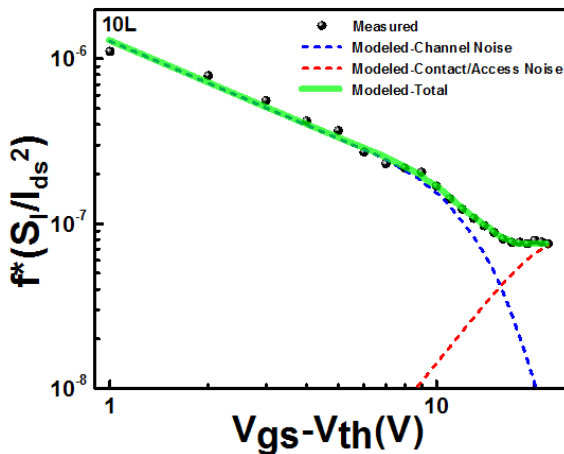


Fig.2: Measured and modeled noise amplitude versus overdrive voltage for 10 layer MoSe₂ FET. Model employs Hooge noise model for channel and resistance/noise parameters for series resistance (contact and interlayer coupling).

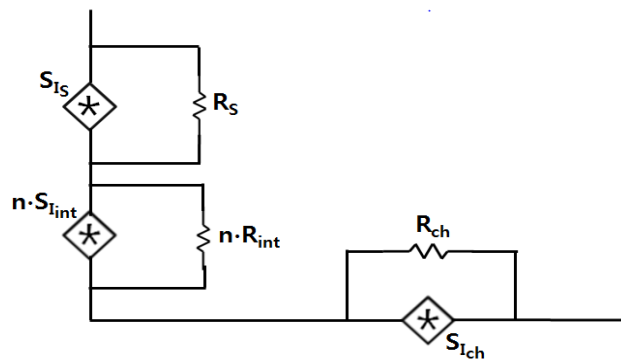


Fig.4: Noise model for intrinsic channel (resistance, R_{ch} and noise current spectral density, S_{1ch}) and elements related to contact resistance (R_s, S_{1s}) and interlayer coupling resistance for n layers (n·R_{int}, n·S_{1int}).

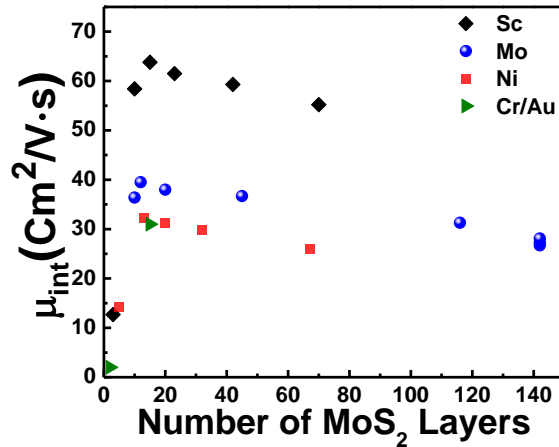


Fig.5 Intrinsic carrier mobility versus number of layers in MoS₂ FETs with indicated contact metal. Decrease at small thicknesses is attributed to interface scattering; increase in peak value with reduced work function is associated with reduced contact barrier.

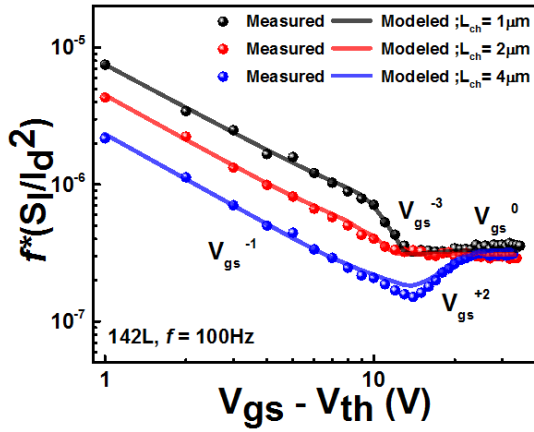


Fig.3: Measured and modeled noise amplitude versus overdrive voltage for 142 layer MoS₂ FETs. Amplitude is inversely proportional to length, indicating constant Hooge parameter. Various voltage dependences of transition regions are due to different voltages at which resistance or noise enter contact-dominated regime (large V_{gs}).

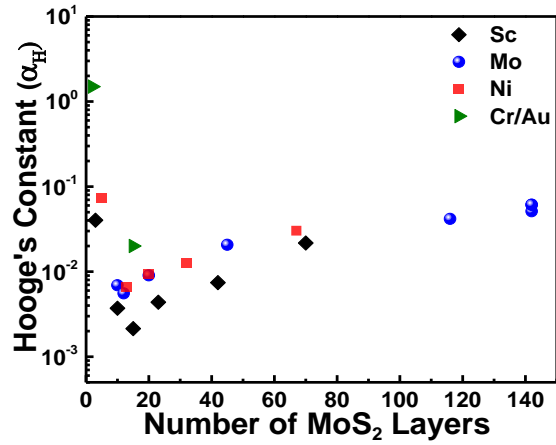


Fig.6: Measured Hooge parameter versus number of layers for MoS₂ transistors with indicated contact metal. Higher values at small layer thickness are attributed to increased effects of interfacial states. Optimum layer thickness is ~ 15 layers for Sc, Mo and Ni contacts.

Novel Optical and Electrical Responses in Topological Materials

Joel E. Moore^{1,2}

¹*Department of Physics, University of California, Berkeley CA 94720 USA*

²*Materials Sciences Division, Lawrence Berkeley National Laboratory,*

Berkeley CA 94720 USA

jemoore@berkeley.edu

Several new classes of topological materials have been confirmed to exist in experiments over the past decade. Many of these materials support unique electromagnetic properties that affect transport and optical responses in potentially useful ways. For example, topological insulators support a particular electromagnetic coupling known as “axion electrodynamics”, and understanding this leads to an improved understanding of magnetoelectricity in all materials. The main focus of this talk is on how topological Weyl and Dirac semimetals can show unique electromagnetic responses; we argue that in linear response the main observable property solves an old problem about optical rotation via the orbital moment of Bloch electrons [1]. Nonlinear optical response (second-harmonic generation) is already known to be remarkably strong in existing Weyl materials [2], and may show an unexpected strength and quantization in Weyl materials without mirror symmetries [3]. Some applications of these effects are mentioned in closing.

[1] S. Zhong et al., Phys. Rev. Lett. **116**, 077201 (2016)

[2] L. Wu et al., Nat. Phys. **13**, 350 (2017)

[3] F. de Juan et al., Nat. Comm. **8**, 15995 (2017)

Induced Superconductivity in Topological-Insulator BiSbTeSe₂ Nanoribbons

Morteza Kayyalha¹, Aleksandr Kazakov², Ireneusz Miotkowski²,
Sergei Khlebnikov², Mehdi Kargarian³, Victor M. Galitski³, Victor M. Yakovenko³,
Leonid P. Rokhinson^{1,2}, and Yong P. Chen^{1,2}

¹*Department of Electrical Engineering, Purdue University, West Lafayette, Indiana, USA*

²*Department of Physics and Astronomy, Purdue University, West Lafayette, Indiana, USA*

³*Department of Physics, Condensed Matter Theory Center and Joint Quantum Institute,
University of Maryland, College Park, MD 20742, USA*

leonid@purdue.edu

We present experimental study of Josephson junctions fabricated from topological insulator BiSbTeSe₂ with superconducting Nb electrodes. In nanoribbon (TINR) devices we observe anomalous enhancement of the critical current at low temperatures. In contrast to conventional junctions, as a function of the decreasing temperature T , the increasing critical current I_c exhibits a sharp upturn at a temperature T^* around 20% of the junction critical temperatures for several different samples and various gate voltages. The I_c vs. T demonstrates a short junction behavior for $T > T^*$ but crosses over to a long-junction behavior for $T < T^*$ with an exponential T -dependence. We attribute the long-junction behavior to low-energy Andreev bound states (ABS) arising from winding of the electronic wavefunction around the circumference of the topological insulator nanoribbon (TINR).

M. Kayyalha et al., arXiv:1712.02748 (2017)

Impact of Thermal Fluctuations on Transport in Antiferromagnetic Topological Dirac Semimetals

Youngseok Kim^{1,2} and Matthew J. Gilbert^{1,2,3}

¹*Department of Electrical and Computer Engineering, University of Illinois – Urbana-Champaign, Urbana, IL 61801, USA*

²*Micro and Nanotechnology Laboratory, University of Illinois – Urbana-Champaign, Urbana, IL 61801, USA*

³*Department of Electrical Engineering, Stanford University, Stanford, CA 94305, USA*
mjgilber@stanford.edu

Recent demonstrations on manipulating antiferromagnetic (AF) order have triggered a growing interest in antiferromagnetic metal, and potential high-density spintronic applications [1] demand further improvements in the anisotropic magnetoresistance (AMR). The antiferromagnetic semimetals (AFS) are newly discovered materials that possess massless Dirac fermions that are protected by the crystalline symmetries. In this material, a reorientation of the AF order may break the underlying symmetries and induce a finite energy gap. As such, the possible phase transition from the semimetallic to insulating phase gives us a choice for a wide range of resistance, ensuring a large AMR. To further understand the robustness of the phase transition, we study thermal fluctuations of the AF order in AFS at a finite temperature. For macroscopic samples, we find that the thermal fluctuations effectively decrease the magnitude of the AF order by renormalizing the effective Hamiltonian. Our finding suggests that the insulating phase exhibits a gap narrowing at elevated temperatures, which leads to a substantial decrease in AMR. We also examine spatially correlated thermal fluctuations for microscopic samples by solving the microscopic Landau-Lifshitz-Gilbert equation, finding a quantitative difference in the gap narrowing effect from that of the macroscopic sample. For both cases, the semimetallic phase shows a minimal change in its transmission spectrum, illustrating the robustness of the symmetry-protected states in AFS [2]. Our finding may serve as a guideline for estimating and maximizing AMR of the AFS samples at elevated temperatures.

[1] Y. Kim et al., Phys. Rev. B, **97**, 134415 (2018)

[2] Y. Kim et al., Phys. Rev. B, **98**, 024409 (2018)

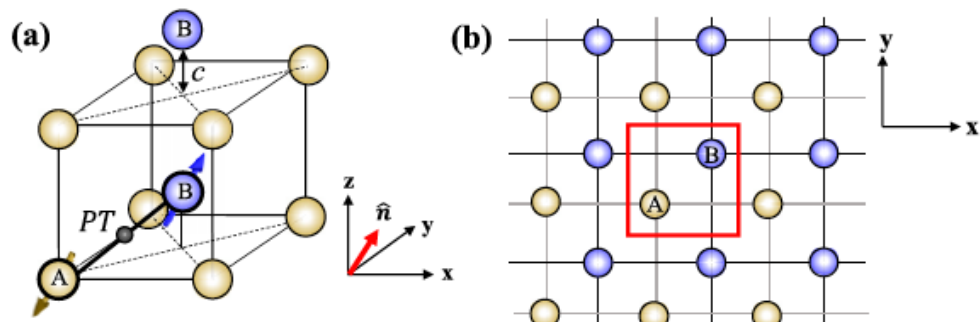


Fig. 1: (a) The lattice structure of the antiferromagnetic Dirac semimetal consists of two sublattice atoms. The constituent subatoms are indicated as A and B that have an opposite spin configuration along the Neel vector, \hat{n} (AF order) enforced by the exchange coupling. (b) The lattice structure has non-symmorphic symmetry G_x (glide symmetry along the x-direction) for \hat{n} parallel to $[100]$ and G_y parallel to the $[010]$.

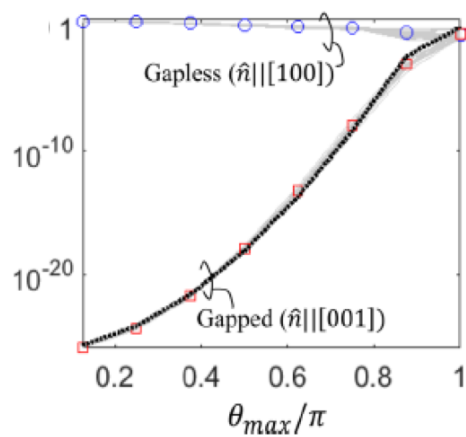


Fig. 2: (a) Plot of transmission as a function of the maximum Neel vector fluctuation for both the gapless and gapped phase orientations at an energy of $E = -40$ meV. Here we observe that the gapped system behaves as gapless once the thermal fluctuations are sufficiently large.

Topology of the Non-Hermitian Chern Insulator

Mark Hirsbrunner¹, Timothy M. Philip², and Matthew J. Gilbert^{2,3}

¹*Department of Physics, University of Illinois at Urbana-Champaign, Urbana, IL 61801, USA*

²*Department of Electrical and Computer Engineering, University of Illinois at Urbana-Champaign, Urbana, IL 61801, USA*

³*Department of Electrical Engineering, Stanford University, Stanford, California 94305, USA*
mjgilber@stanford.edu

Topological band theory has recently been extended from closed systems to open systems, such as mesoscopic devices and gain/loss matched photonic crystals, that are described by non-Hermitian Hamiltonians. While many topological invariants have been constructed for the bands of non-Hermitian Hamiltonians, such as the non-Hermitian generalization of the Chern number [1], the relationship between these invariants and the topological quantization of observables remains unclear. By applying the Ishikawa-Matsuyama formula [2,3], we show that no such relationship exists between the Chern number of non-Hermitian bands and the quantization of the Hall conductivity. Therefore, the Chern number does not provide a physically meaningful classification of non-Hermitian Hamiltonians. As a concrete example, we analytically show that the Hall conductivity of a non-Hermitian Chern insulator is not quantized, exemplifying the disconnect between topological invariants of bands and the physics of non-Hermitian Hamiltonians.

[1] H. Shen et al., Phys. Rev. Lett. **120**, 146402 (2018)

[2] K. Ishikawa and T. Matsuyama, Z. Phys. C **33**, 41 (1986)

[3] Z. Wang et al., Phys. Rev. Lett. **105**, 1 (2010)

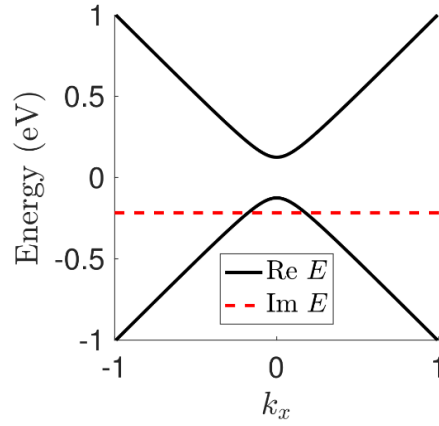


Fig.1: The band structure of a non-Hermitian Chern insulator $H = -i\Gamma_0\sigma_0 + (k_y\sigma_x - k_x\sigma_y) - M\sigma_z$, where $\Gamma_0 = 0.2$ eV and $M = 0.125$ eV. The real part of the spectrum is gapped by the mass term and the non-Hermitian contribution shifts the eigenvalues in the complex plane. Since the bands are separable, meaning that the eigenvalues at each momentum do not coincide in the complex plane, the bands retain their Chern number classification

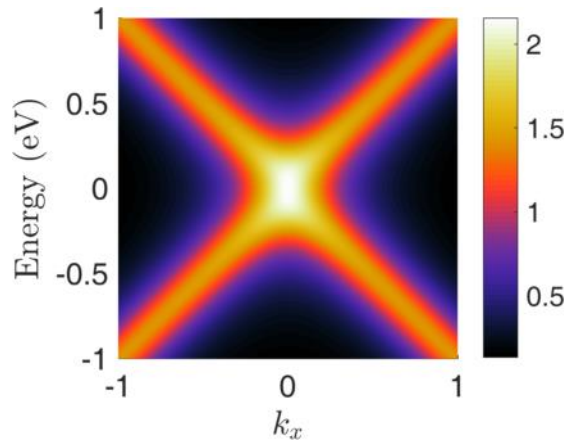


Fig.2: The spectral function of the non-Hermitian Chern insulator with the same parameters as Fig.1. The non-Hermitian part of the Hamiltonian causes the spectral density to broaden, resulting in a gapless spectrum. As such, there is not a clear distinction between the two separable bands, obscuring the connection between the Hall conductivity and the Chern numbers of the bands.

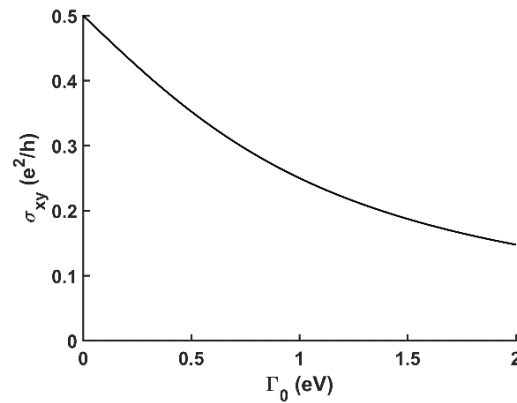


Fig.3: The Hall conductivity of the non-Hermitian Chern insulator with $M = 1$ eV as a function of the broadening, Γ_0 , calculated via the Ishikawa-Matsuyama formula. Although the bands retain their Chern number classification, non-zero broadening causes the loss of topological quantization of the Hall conductivity. This exemplifies the breakdown of the relationship between topological invariants of bands and transport observables.

High-Temperature Magnetic Order in Topological Insulator - Ferromagnetic Insulator Heterostructures

Valeria Lauter¹, Ferhat Katmis^{2,3}, Don Heiman⁴, and Jagadeesh S. Moodera^{2,3}

¹*Neutron sciences Directorate, ORNL, One Bethel Valley Road, Oak Ridge TN 37831, USA*

²*Department of Physics, Massachusetts Institute of Technology, Cambridge, MA 02139, USA*

³*F. Bitter Magnet Lab, Massachusetts Institute of Technology, Cambridge, MA 02139, USA*

⁴*Department of Physics, Northeastern University, Boston, MA 02115, USA*

lauterv@ornl.gov

Generating proximity-induced magnetism on a topological insulator (TI) surface with a ferromagnetic insulator (FMI) provides a clean approach for realizing potential device applications exhibiting novel quantum functionality. Here we demonstrate a fundamental step towards realization of high-temperature magnetization in a TI-FMI heterostructure. We have induced uniform long-range ferromagnetic order onto the surface of epitaxial Bi₂Se₃ films through strong exchange coupling between TI and FMI. Polarized Neutron Reflectometry enables us to discriminate the magnetism at the surface of TI from that in the FMI layer, yielding simultaneous depth-dependent measurement of the chemical structure and magnetism with high precision. This unique tool provides direct evidence that Bi₂Se₃-EuS heterostructures exhibit proximity-induced interfacial magnetism in the top 2 QL (~2 nm) layers of Bi₂Se₃ by short-range exchange, and found to persist up to room temperature, above the Curie point of EuS. The enhanced magnetic ordering temperature results from the large spin-orbit interaction and spin-momentum locking property of the TI surface. Due to the short-range nature of the ferromagnetic exchange, the time-reversal symmetry is broken only near the surface of the TI, leaving its bulk states unaffected [1]. The TI ferromagnetism is observed in a variety of bi-layer structures, providing a controlling mechanism. These findings of locally-induced ferromagnetic order on the TI surface extending over macroscopic areas without impurity doping opens the door for an efficient topological control for future spin-based technologies.

Acknowledgments: Work supported by the Scientific User Facilities Division, Office of BES, US DOE, NSF-ECCS-1402738, MRSEC Program of the NS award DMR-0819762, NSF (DMR-1207469), ONR (N00014-16-1-2657), STC Center for Integrated Quantum Materials NSF grant DMR-1231319, Division of Material Sciences and Engineering DE-SC0006418.

[1] F. Katmis et al., Nature **533**, 513 (2016)

Superconducting “Glue” in Cuprates: Disappearance of Superconductivity Due to Diminishing Coupling in Overdoped $\text{Bi}_2\text{Sr}_2\text{CaCu}_2\text{O}_{8+\delta}$

Tonica Valla¹, Ilya K. Drozdov¹, Genda Gu¹, and Ivan Bozovic¹

¹*Condensed Matter Physics and Materials Science Department,
Brookhaven National Laboratory, Upton, NY 11973, USA
valla@bnl.gov*

In high-temperature cuprate superconductors, superconductivity is accompanied by a “plethora of orders” and phenomena that may compete, or cooperate with superconductivity, but which certainly complicate our understanding of origins of superconductivity in cuprates. While especially prominent in the underdoped regime, these orders are known to significantly weaken or completely disappear on the overdoped side. Here, we approach the superconductivity from this highly overdoped and more conventional side. We present angle-resolved photoemission studies of $\text{Bi}_2\text{Sr}_2\text{CaCu}_2\text{O}_{8+\delta}$ single crystals cleaved and annealed in ozone to increase the doping from the initial value corresponding to $T_c = 91$ K all the way to the metallic, non-superconducting phase on the overdoped side. We show that the mass renormalization in the antinodal region of the Fermi surface, associated with the structure in the quasiparticle self-energy and possibly reflecting the “glue” that couples electrons into pairs is found to monotonically weaken with doping and completely disappearing in the non-superconducting samples. This is the most direct evidence so far that in the overdoped regime, superconductivity disappears due to diminishing coupling. In the highly overdoped but superconducting regime, superconducting gap is found to have the mean-field value of $2\Delta_0 \sim 4k_B T_c$.

Honeycomb Semiconductors and their Artificial Analogues

Daniel Vanmaekelbergh¹, Marlou Slot¹, Thomas Gardenier¹, Saoirse Freeney¹, Ingmar Swart¹, Sander Kempkes¹, Jette van den Broeke¹, Cristiane Morais Smith¹, and Christophe Delerue²

¹*Debye Institute for Nanomaterials Science, University of Utrecht, Netherlands;*

Institute for Theoretical Physics, University of Utrecht, Netherlands

²*IEMN, Lille, France*

d.vanmaekelbergh@uu.nl

Geometric semiconductors: When a nanoscale periodicity is superimposed on a 2-D semiconductor system, the band structure can be deeply influenced. The honeycomb geometry is most prominent in this respect: the band gap of the semiconductor remains comparable to that of a quantum well, but the highest valence and lowest conduction bands show a linear dispersion around the K-points (as for graphene). As a consequence, such honeycomb semiconductors are constituted to host massless electrons and holes by doping or optical excitation. 2-D semiconductors with a honeycomb geometry have been prepared in two ways: by bottom-up self-assembly of nanocrystals, or by top-down lithography. □ In this lecture, I will show the progress that we made on the self-assembly and lithographic pathways. The Dirac-type band structure and the first spectroscopic results will be discussed as well. In this field, the progress is steady but slow, as honeycomb semiconductors show several types of structural disorder.

Artificial systems as model quantum simulators: Meanwhile, artificial systems can be built atom-by-atom in an STM and the relation between the 2-D potential landscape and band structure can be investigated for nearly any 2-D geometry. We used the surface electrons of a Cu (111) surface, and forced them into a Lieb- or honeycomb geometry by positioning repulsive CO in an appropriate geometry. In fact, we engineer artificial atomic sites positioned in a lattice, and control the quantum coupling between these sites. The electronic band structure can be probed by measurement of the local density of states (DOS). The results are understood in the framework of muffin tin and tight-binding calculations.

Artificial Lieb Lattice: The Lieb lattice is a square depleted lattice, with corner sites and edge sites. When only coupling between the nearest neighbor sites is accounted for, the lowest bands form a Dirac cone, crossed by a flat-band. This band structure is due to coupling of the S-type orbitals of the artificial sites. Our experimental results show that also next-to-nearest neighbor coupling must be taken into account. Moreover, at higher energy we find bands due to coupling of the on-site p-orbitals.

Artificial Honeycomb Lattice: From wave function mapping and measurement of the local DOS we find that the two lowest bands are due to coupling of the on-site S-orbitals in bonding and anti-bonding configurations, forming a Dirac cone. Second we observe a strong signature of a flat band due to interference of the P-orbitals. This is followed by another P-band with Dirac-like properties. Our experimental results are corroborated by detailed muffin-tin and tight-binding calculations.

[1] K.K. Gomes et al., *Nature* **483**, 306 (2012)

[2] R. Drost et al., *Nat. Phys.* **13**, 668 (2017)

[3] D. Bercioux and S. Otte, *Nat. Phys.* **13**, 628 (2017)

Relevant publications from us: 3

[4] M.P. Boneschanscher et al., *Science* **344**, 1377 (2014)

[5] J.J. Geuchies et al., *Nat. Mater.* **15**, 1248 (2016)

[6] M.R. Slot et al., *Nat. Phys.* **13**, 672 (2017)

[7] S.N. Kempkes et al., *Nat. Phys.* (2018), in print.

Electron Transport in Quasi-1D ZrTe₃ van der Waals Nanoribbons: Extraordinary High Current Density and Unique Noise Characteristics

Adane Geremew¹, Sergey Rumyantsev^{1,2}, Tina T. Salguero³, and Alexander A. Balandin¹

¹*Nano-Device Laboratory (NDL), Department of Electrical and Computer Engineering, University of California, Riverside, California 92521, USA*

²*Ioffe Physical-Technical Institute, St. Petersburg 194021, Russia*

³*Department of Chemistry, University of Georgia, Athens, Georgia 30602, USA*
balandin@ece.ucr.edu

As scaling in the CMOS technology continues, there is a growing need for new materials that can be used for nanometer-scale local interconnects and device channels. The current density sustained by Cu interconnects in the state-of-the-art CMOS technology is $\sim 2 \text{ MA/cm}^2$. We have recently proposed that quasi-one-dimensional (1D) van der Waals materials, namely transition metal trichalcogenides (TMTs) MX_3 (where $\text{M} = \text{Mo, Ta, W, Zr}$ and $\text{X} = \text{S, Se, Te}$), may have properties attractive for applications in nm-scale electronics [1-2]. Similar to transition metal dichalcogenides (TMDs), which exfoliate into 2D layers, TMTs exfoliate into quasi-1D atomic chains or threads [1-2]. Such quasi-1D materials can be made, in principle, into ultimately downscaled nanowires with a cross-section of $\sim 1 \text{ nm} \times 1 \text{ nm}$, which corresponds to an individual atomic chain. We discovered that several quasi-1D nanowires reveal an exceptionally high current density. The quasi-1D metallic TaSe₃ nanowires have the breakdown current density exceeding $J_B \sim 10 \text{ MA/cm}^2$ [1]. We demonstrated that ZrTe₃ nanoribbons can sustain a record high current density $J_B \sim 100 \text{ MA/cm}^2$ [3]. The fact that ZrTe₃ can exhibit both metallic and semiconducting properties makes our results even more important for future downscaled electronics. We also have found that quasi-1D ZrTe₃ reveal unusual low-frequency noise characteristics, which have to be taken into account in electronic designs.

Acknowledgments: This work was supported, in part, by the Semiconductor Research Corporation (SRC) contract 2018-NM-2796: 1D van-der-Waals Metals: Ultimately-Downscaled Interconnects with Exceptional Current-Carrying Capacity, and by the National Science Foundation (NSF) through the Emerging Frontiers of Research Initiative (EFRI) 2-DARE project: Novel Switching Phenomena in Atomic Heterostructures for Multifunctional Applications (NSF EFRI-1433395).

[1] M.A. Stolyarov et al., *Nanoscale* **8**, 15774 (2016)

[2] G. Liu et al., *Nano Lett.* **17**, 377 (2017)

[3] A. Geremew et al., *IEEE Electron Device Lett.* **39**, 735 (2018)

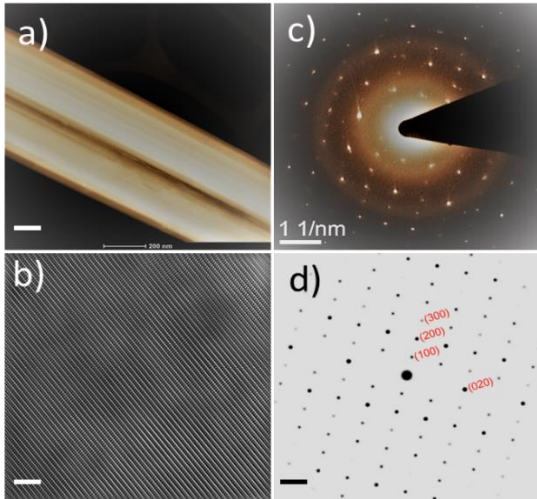


Fig.1: Transmission electron microscopy analysis of ZrTe₃ crystals. (a) A bundle of nanowires on copper grid. (b) A HR-TEM image of a ZrTe₃ crystal. (c) A diffraction pattern. (d) Indexed planes for ZrTe₃. Scale bars in (a), (b) and (d) are 90 nm, 5 nm and 1 nm⁻¹, respectively.

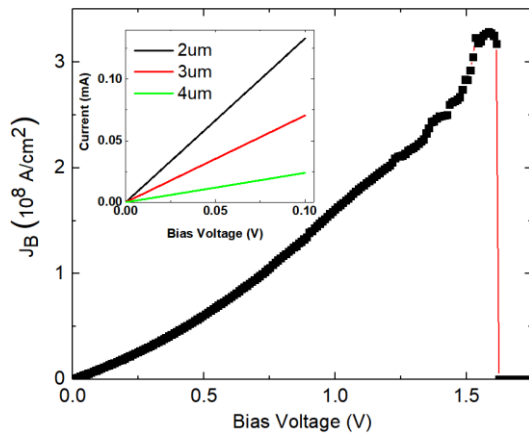


Fig.3: High field I-V characteristics of the best quasi-1D ZrTe₃ nanoribbon device. The apparent breakdown current density, calculated with the AFM measured thickness and SEM measured width, corresponds to $\sim 3 \times 10^8$ A/cm², reached at the voltage bias of ~ 1.6 V. The current shows some signs of instability at $V \approx 1.2$ V indicating that some atomic threads started to break. The inset shows low-field I-V characteristics of quasi-1D ZrTe₃ devices with different channel lengths used for the contact resistance extraction. The data indicate the Ohmic nature of the contacts and channel.

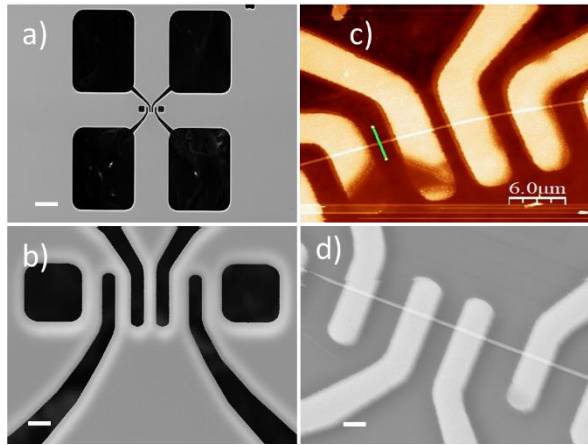


Fig.2: (a) SEM image of a shadow mask with TLM structure patterned on 500-μm thick Si/SiO₂ wafer. (b) Top-view SEM image of the TLM pattern. (c) AFM image of the quasi-1D ZrTe₃ nanoribbon device (~ 33 -nm thick) fabricated using the shadow mask. (d) SEM image of another quasi-1D ZrTe₃ nanowire device with a different cross-sectional area. The scale bars in (a) (b) and (d) are 50 μm, 1 μm and 1 μm.

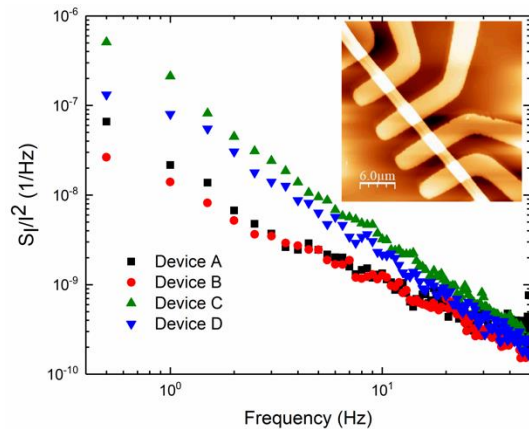


Fig.4: Normalized noise spectrum density as a function of frequency for ZrTe₃ nanoribbon devices with various cross-sections. The inset shows AFM image of the fabricated structure with the devices.

Tunneling-Assisted Relaxation in Hybrid Graphene Quantum-Dot Photodetectors

Cody Hayashi¹, Drew Buzzell², Saptarshi Das²,
Tyler Yamauchi¹, Carlos Torres Jr.¹, and Richard Ordonez¹

¹Space and Naval Warfare Systems Center Pacific, Pearl City, HI and ³ San Diego, CA, USA

²Dept of Engineering Science and Mechanics, Pennsylvania State University,

University Park, USA

cody.hayashi@navy.mil

We investigate different back-gate dielectrics to improve the traditionally slow response time of high-responsivity graphene quantum-dot photodetectors. The combination of high-mobility graphene with photo-active semiconductor quantum dots produces size-tunable optical detectors with a photoresponsivity as high as 10^8 A/W [1]. However, these responses are typically limited to response times greater than a second due to charge traps at the graphene quantum-dot interface and large quantum-dot relaxation times [2]. We show that a graphene quantum-dot device fabricated on a 50nm aluminum oxide (Al_2O_3) dielectric achieves response times lower than 600 milliseconds, and is considerably faster than a similar device on 300nm silicon dioxide (SiO_2) that possesses a response time greater than 5 seconds.

Two similar graphene quantum-dot devices are fabricated with different back-gate dielectrics as shown in Figures 1 and 2. After the graphene deposition and titanium-gold metallization, 1200nm lead sulfide (PbS) quantum dots with ethanedithiol (EDT) ligands are spincoated onto the devices. The devices are illuminated with a 405nm (100pW) laser source and the photocurrent is measured. Figures 4, 5, and 6 show a significant increase in speed when the Al_2O_3 sample reaches -5V. We believe this is due to trap-assisted tunneling occurring in the Al_2O_3 interface. Due to Al_2O_3 's higher dielectric constant compared to SiO_2 ($\epsilon_{\text{Al}_2\text{O}_3} = 9.5$, $\epsilon_{\text{SiO}_2} = 3.9$), it has been shown that the increased polaronic interaction produces a higher number of carrier traps [3]. This phenomenon in addition to the Al_2O_3 's reduced thickness allows the back-gate voltage to induce vertical tunneling through these intermediate traps, and expedite quantum-dot relaxation. This is supported by similar drain-to-source current (I_{ds}) and gate current (I_{g}) responses in the Al_2O_3 sample when subjected to incident light in Figure 3. Further efforts aim to fully characterize the impact different dielectrics have on improving response times of these high-responsivity *devices*.

[1] G. Konstantatos et al., Nat. Nanotechnol. **7**, 363 (2012)

[2] C.H. Liu et al., Nat. Nanotechnol. **9**, 273 (2014)

[3] M. Nugraha et al., ACS Appl. Mater. Interfaces **9**, 4719 (2017)

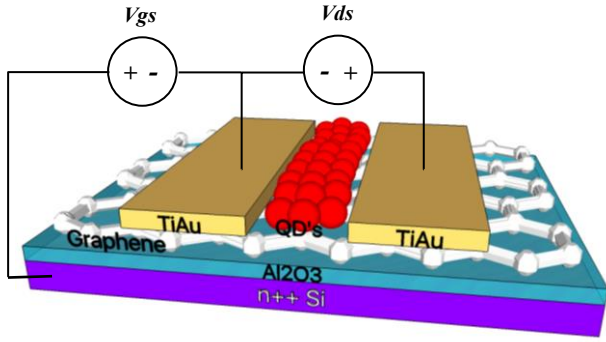


Fig.1: Schematic of Hybrid Graphene – Quantum Dot Photodetector. Back-gated graphene with 50nm aluminum oxide (Al_2O_3) dielectric, titanium-gold electrodes, and spin-coated lead-sulfide (PbS) quantum dots with ethanedithiol (EDT) ligands in the active area

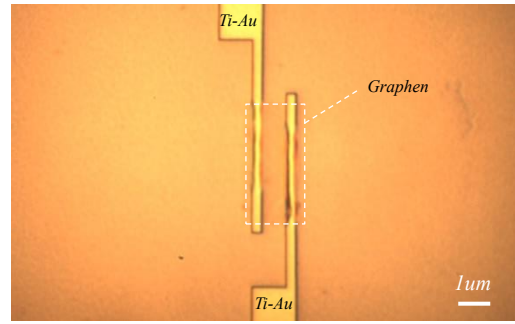


Fig.2: Optical Micrograph Image of Graphene-on- Al_2O_3 Device before 1200nm PbS Quantum-Dot Deposition. W/L = 5 μm /1 μm

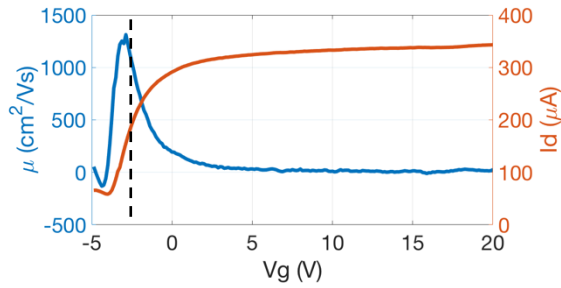


Fig.3: Device Transfer Curve and Carrier Mobility (1,015 cm^2/Vs). Carrier mobility is extracted in the linear regime as indicated by the dashed vertical line

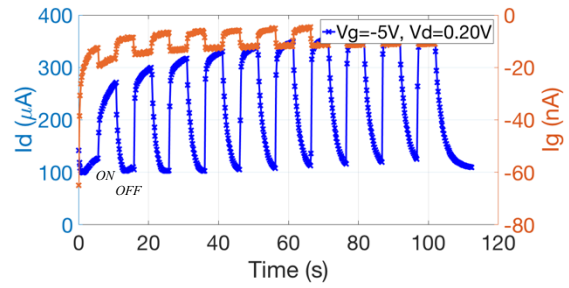


Fig.4: Photoresponse of 50nm Al_2O_3 Dielectric Graphene – Quantum Dot Photodetector to Incident 100pW, 405nm Ultraviolet Source Pulsed at 10s Intervals. The photoresponse is seen through the channel and the gate, which highlights the trap-assisted tunneling experienced across the graphene quantum-dot interface. Responsivity $\sim 10^3 \text{ A/W}$

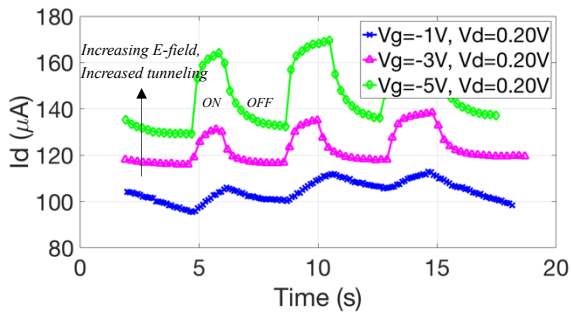


Fig.5: Photoresponse of 50nm Al_2O_3 Dielectric Graphene – Quantum Dot Photodetector with Varying Gate-Voltage Bias. Incident 100pW, 405nm excitation. Response times (t_r) correspond with the gate-voltage bias and signify the overcoming of the oxide's barrier height: [$V_g = -1\text{V}$, $t_r > 5\text{s}$], [$V_g = -3\text{V}$, $t_r = 0.7\text{s}$], [$V_g = -5\text{V}$, $t_r = 0.57\text{s}$]

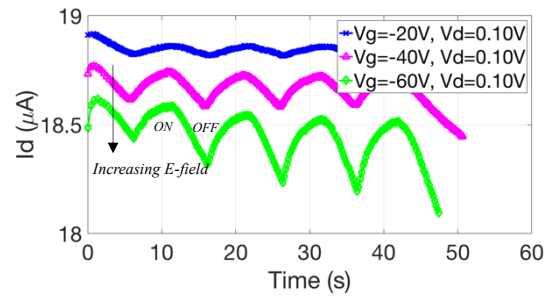


Fig.6: Photoresponse of 300nm SiO_2 Dielectric Graphene – Quantum Dot Photodetector with Varying Gate-Voltage Bias. Incident 100pW, 405nm excitation. Gate-voltage values are scaled up from the Al_2O_3 samples to maintain similar capacitance, and account for the change in dielectric constant and oxide thickness with the SiO_2 samples. Response times illustrate the increased barrier height in comparison to Al_2O_3 : [$V_g = -20\text{V}$, $t_r > 5\text{s}$], [$V_g = -40\text{V}$, $t_r > 5\text{s}$], [$V_g = -60\text{V}$, $t_r > 5\text{s}$]

Optical Studies of Exciton/Biexciton States on a Single Coupled Quantum Dot

Heedae Kim^{1,2}, Jongsu Kim³, and Jindong Song⁴

¹*School of Physics, Northeast Normal University, Changchun, 130024, China*

²*Clarendon Laboratory, Department of Physics, University of Oxford, Oxford, OX1 3PU, UK*

³*Department of Physics, Yeungnam University, Gyeongsan, 712-749, Republic of Korea*

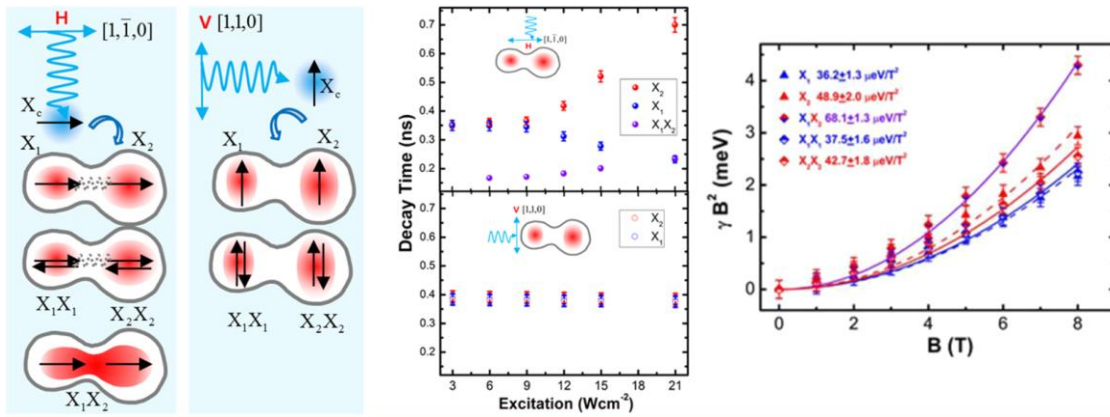
⁴*Nano-Photonics Research Center, KIST, Seoul, 136-791, Republic of Korea*

jinxd371@nenu.edu.cn

Recently, the droplet epitaxy techniques allow us to grow laterally coupled quantum dot (CQD) structure. The vertically CQDs have been intensively investigated in terms of optical coupling and entangling states. When the interdot distance between two quantum dots is short enough ($d < 10\text{nm}$) to result in a wave function overlap between the two quantum dots via the tunneling effect, the optical coupling is controlled by the interdot distance and external DC electric fields along the coupling direction. However, in the case of a laterally CQD, the separation of two quantum dots is not small enough to give rise to a sufficient wave function overlap for tunneling to occur, the exciton dipole-dipole interaction can be used as an alternative method to understand long range optical coupling procedure.

We found that the exciton dipole-dipole interaction in a single laterally CQD structure can be controlled by the linear polarization of a nonresonant optical excitation.[1] The exciton dipole-dipole interaction of a CQD becomes enhanced when the polarization of nonresonant excitation is parallel to the lateral coupling direction. As the excitation intensity is increased with the linearly polarized light parallel to the lateral coupling direction, excitons (X_1 and X_2) and local biexcitons (X_1X_1 and X_2X_2) of the two separate quantum dots (QD_1 and QD_2) show a redshift along with coupled biexciton (X_1X_2), while neither coupled biexcitons nor a redshift are observed when the direction of excitation beam is perpendicular to the coupling direction. The polarized dependence and power dependent redshift are attributed to an optical nonlinearity in the exciton Forster resonant energy transfer interaction (FRET). The FRET interaction becomes dominant with increasing the excitation parallel to the coupling direction, where redshifts, an exciton population transfer, and a coupled biexciton appear. We have also distinguished the coupled biexciton from local biexcitons by the large diamagnetic coefficient. One of the coupled biexciton transition was spectrally overlapped with X_2 .

[1] H. Kim et al., Nano Lett. **16**, 7755 (2016)



Asymmetrically Strained Quantum Dots with Ultrastable Single-Dot Emission Spectra and Subthermal Room-Temperature Linewidths

Young-Shin Park^{1,2}, Jaehoon Lim^{1,3}, and Victor I. Klimov¹

¹*Chemistry Division, Los Alamos National Laboratory, Los Alamos, NM, 87545, USA*

²*Center for High Technology Materials, University of New Mexico,
Albuquerque, NM, 87131, USA*

³*Department of Chemical Engineering & Department of Energy System Research,
Ajou University, Suwon 16499, Republic of Korea*
klimov@lanl.gov

Colloidal semiconductor quantum dots (QDs) have been envisioned as promising materials for application in traditional light-emission devices and prospective single-dot light sources. While QD displays have already entered the market place, realization of single-dot applications still requires overcoming several challenges including elimination of strong spectral fluctuations at the individual-QD level. Recently, there has been considerable progress in suppressing intensity fluctuations by encapsulating an emitting core (usually CdSe) into an extra-thick protective shell (commonly CdS) [1, 2]. Despite nearly “blinking-free” emission intensity, these dots, however, still show considerable fluctuations in both emission energy and linewidth. Here we demonstrate a new class of QDs that overcome these deficiencies. In these dots, the CdSe core is enclosed into a compositionally graded, asymmetrically-strained $\text{Cd}_x\text{Zn}_{1-x}\text{Se}$ shell [3]. As illustrated in Fig. 1, these structures exhibit a highly stable emission energy (~ 0.5 meV standard deviation versus ~ 10 meV in CdSe/CdS QDs) and an unprecedentedly narrow, subthermal room-temperature linewidth (~ 20 meV) [5]. These unusual properties are derived from unique structural features of these QDs, which lead to strong suppression of exciton-phonon coupling and reduction in propensity for random photocharging. The remarkable spectral characteristics along with fast emission rates ($\sim 1/15$ ns⁻¹) and high emission quantum yields (up to $\sim 85\%$) make these novel structures well suited for practical realization of single-dot light sources.

[1] Y. Chen et al., *J. Am. Chem. Soc.* **130**, 5026 (2008)

[2] B. Mahler et al., *Nat. Mater.* **7**, 659 (2008)

[3] J. Lim et al., *Nat. Mater.* **17**, 42 (2018)

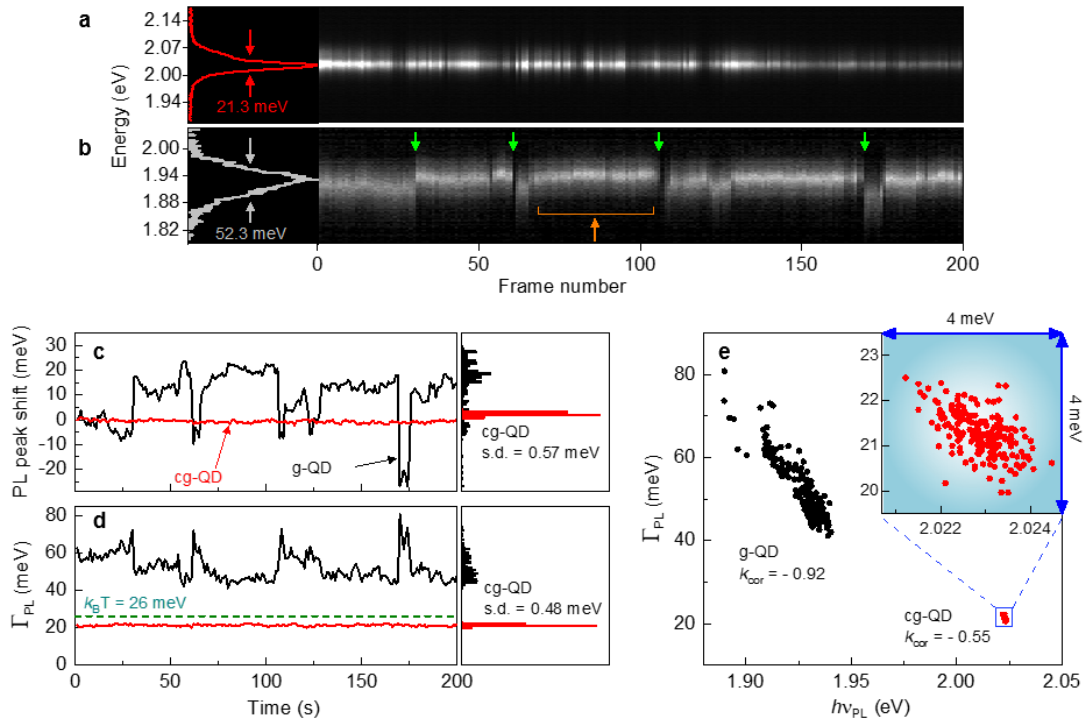


Fig.1: Comparison of single-dot photoluminescence (PL) spectra of CdSe/CdxZn1-xSe compositionally graded QDs (cg-QDs) QDs and reference CdSe/CdS “giant” QDs (g-QDs). a, A single cg-QD PL spectrum (left) averaged over 200 sequential frames and a corresponding spectrally resolved PL intensity trajectory (right). The time per frame is 1 s. b, Same for a single reference “giant” QD. The green arrows mark spectral jumps and the orange bracket shows the period of fast spectral fluctuations (spectral diffusion). c, The PL peak energy as a function of time for the cg-QD (red line; same as in ‘a’) and the g-QD (black line; same as in ‘b’); corresponding histograms are displayed at right. Standard deviation of the PL peak energy is 10 meV for the g-QD and only 0.57 meV for the cg-QD. d, The same analysis but for the single-dot PL linewidth (Γ_{PL}). The cg-QD linewidth exhibits very small, sub-meV fluctuations (s.d. = 0.48 meV) and remains below the room temperature thermal energy ($k_B T = 26$ meV; dashed green line) for the entire duration of the measurements. e, The single-dot PL peak energy versus the linewidth for the cg-QD (red circles) and the g-QD (black circles); these plots are obtained from PL trajectories similar to those in ‘a’ and ‘b’. k_{cor} is a Pearson correlation coefficient. The inset is an expanded view of the region containing the cg-QD data (shown by the blue square).

Acoustic Phonon Spectrum Engineering in Bulk Crystals via Incorporation of the Size-Dissimilar Dopant Atoms

Fariborz Kargar¹, Elias H. Penilla², Ece Aytan¹, Jacob S. Lewis¹, Javier E. Garay²,
and Alexander A. Balandin¹

¹*Phonon Optimized Engineered Materials (POEM) Center, Bourns College of Engineering,
University of California, Riverside, CA 92521, USA*

²*Advanced Materials Processing and Synthesis (AMPS) Laboratory, Department of
Mechanical and Aerospace Engineering, University of California, San Diego, CA 92093, USA
balandin@ece.ucr.edu*

Acoustic phonons make a dominant contribution to thermal transport, affect optical properties, and limit the charge carrier mobility in semiconductors. Recently, there has been a strong increase of interest to the methods of controlling acoustic phonon scattering by tuning the phonon spectrum [1]. Until now, the phonon engineering approach has been associated with the nanostructures, where the phonon dispersion undergoes modification due to the boundary conditions, imposed in addition to the periodicity of the atomic crystal structure. In this method, nanometer dimensions are essential in order to reveal the wave nature of the phonons and induce modification in their spectrum [1]. We discovered a drastically different approach for changing the acoustic phonon spectrum of the materials, which does not rely on nanostructuring. We report results of the Brillouin – Mandelstam spectroscopy of transparent Al₂O₃ crystals with Nd dopants. The ionic radius of Nd atoms is distinctively different from those of the host Al atoms. Our results show that even a small concentration of Nd atoms incorporated into the Al₂O₃ samples produces a profound change in the acoustic phonon spectrum. The velocity of the transverse acoustic phonons decreases by ~600 m/s at the Nd density of only ~0.1 % [2]. From the other side, we proved that the dopants, which have similar atomic radius do not change the phonon spectrum. The obtained results, demonstrating that modification of the acoustic phonon spectrum can be achieved not only by nanostructuring but also by the size-dissimilar doping have important implications for thermoelectric energy conversion and optoelectronic devices.

Acknowledgments: This work was supported, in part, by the Spins and Heat in Nanoscale Electronic Systems (SHINES), an Energy Frontier Research Center (EFRC) funded by the U.S. DOE under Award # SC0012670, and DARPA project W911NF18-1-0041 Phonon Engineered Materials for Fine-Tuning Recombination.

[1] A. A. Balandin and D. L. Nika, Mater. Today **15**, 266 (2012)

[2] F. Kargar et al., Appl. Phys. Lett. **112**, 191902 (2018)

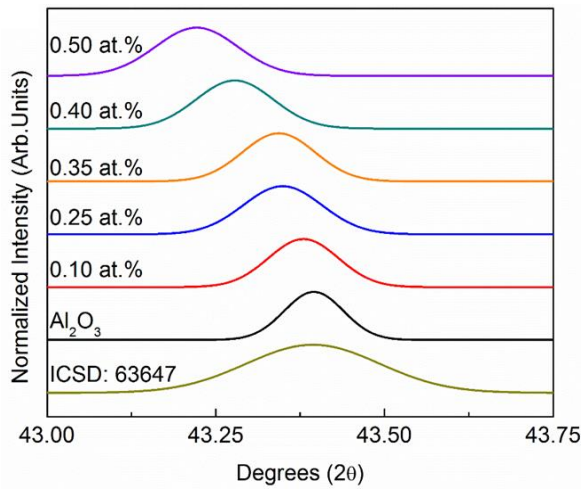


Fig.1: XRD patterns near the (113) plane of the Al_2O_3 and $\text{Nd}:\text{Al}_2\text{O}_3$ samples. Also plotted is an ICSD standard (#63647) for comparison.

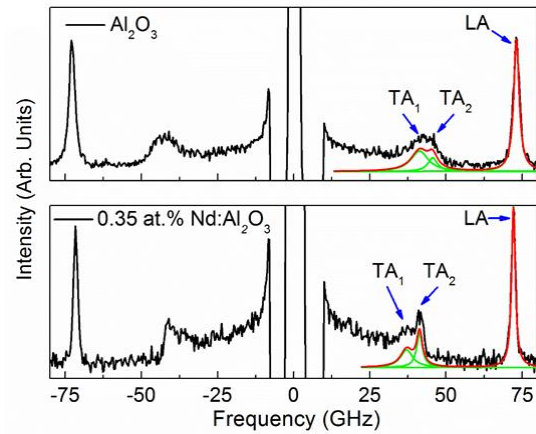


Fig.2: Brillouin-Mandelstam scattering spectra for the pure Al_2O_3 and 0.35 at% $\text{Nd}:\text{Al}_2\text{O}_3$. The experimental data (black curve) has been fitted using individual (green curve) and cumulative (red curve) Lorentzian fittings. The regular longitudinal (LA) and transverse (TA) acoustic phonons are present in both spectra.

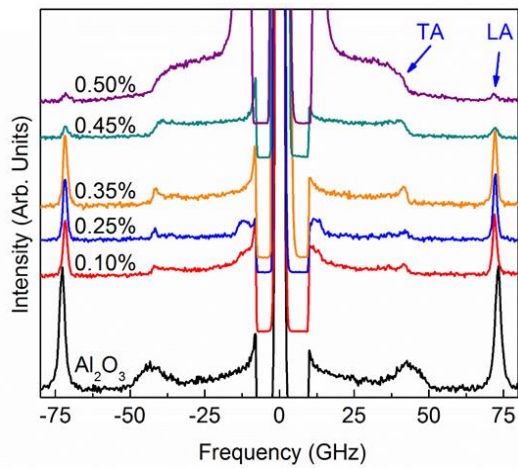


Fig.3: Evolution of the spectrum with increasing the Nd doping level. Note the decrease in frequency of LA and TA phonons of pure Al_2O_3 with increasing the Nd density to 0.1% and more.

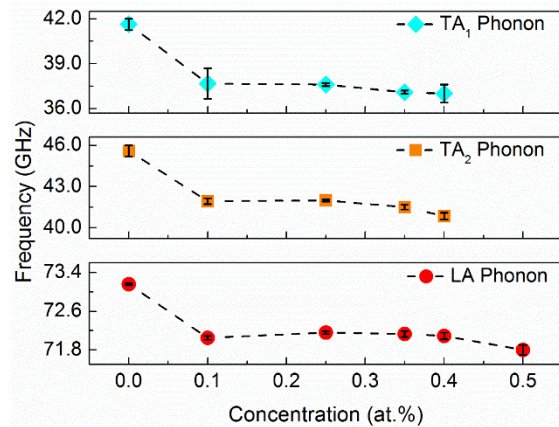


Fig.4: Peak position of LA and TA phonon polarization branches in Brillouin spectra versus Nd density. The frequency of LA and both TA phonon branches decreases with increasing Nd concentration non-monotonically. Note that even the smallest 0.1 at% concentration of Nd results in a noticeable decrease of the phonon frequency, and, correspondingly, group velocity.

Performance Analysis of a 10 nm Phosphorene Double-Gate MOSFET

Gautam Gaddemane¹, Maarten L. Van de Put¹, and Massimo V. Fischetti¹

¹*Department of Materials Science and Engineering,
The University of Texas at Dallas, Richardson, Texas, USA
gautam.gaddemane@utdallas.edu*

Phosphorene, a single or a few-layers film of black phosphorous (bP), has gained considerable attention due to high charge carrier mobility observed in its bulk counterpart [1,2]. In the literature, transport studies have been limited to many layers and thin films of bP, experimentally [3,4], and to free-standing 2D layers of phosphorene theoretically [5,6]. These studies show a large disconnect between the intrinsic mobility of phosphorene ($20 \text{ cm}^2/\text{Vs}$) and bulk bP ($1100 \text{ cm}^2/\text{Vs}$) [1,5]. Given the significant interest in phosphorene for electronic device applications, it is worth assessing the potential performance of phosphorene-based field-effect transistors using advanced simulation methods.

Here we present results obtained from an ab-initio full-band Monte Carlo device simulation for phosphorene-based double-gate n-type MOSFETs. The Monte Carlo simulation is coupled with the Poisson equation and solved self-consistently to obtain steady-state device characteristics. The full electron and phononic dispersions are calculated using density functional theory (DFT), and used directly, rather than using analytical expressions to handle the non-parabolicity and include satellite valleys. In addition, we employ electron-phonon matrix elements calculated from DFT, instead of approximating them from constant deformation potentials. This accounts for the anisotropy of the matrix elements and wavefunction overlaps. We include all inter- and intra-valley scattering processes assisted by all acoustic and optical phonons.

In the figures, we show our results for a 10 nm monolayer-phosphorene double-gate n-MOSFET. We observe an excellent gate control with a sub-threshold slope of 62 mV/dec and negligible short channel effects. Furthermore, we obtain comparable device performance (I_{on} , I_{off}) when compared to FETs with other low-dimensional channels, available in the literature [7]. Results for bilayer phosphorene channels will also be presented at the conference.

Acknowledgments: This work has been supported by Taiwan Semiconductor Manufacturing Company, Ltd (TSMC) and Semiconductor Research Corporation (SRC).

- [1] Y. Akahama et al., J. Phys. Soc. Jpn. **6**, 2148 (1983)
- [2] A. Morita, Appl. Phys. A **39**, 227 (1986)
- [3] F. Xia et al., Nat. Commun. **5**, 4458 (2014)
- [4] L. Li et al., Nat. Nanotechnol. **9**, 372 (2014)

[5] G. Gaddemane et al., Phys. Rev. B **98**, 115416 (2018)

[6] B. Liao et al., Phys. Rev. B **91**, 235419 (2015)

[7] D. Nagy et al., IEEE J. Electron Devi. Soc. **6**, 332 (2018)

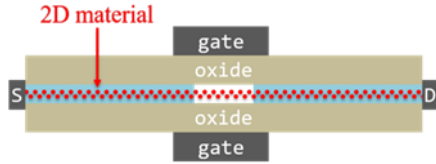


Fig.1: A schematic of the device simulated. The device is n-doped at the source and drain extension with a doping density of $1 \times 10^{13} \text{ cm}^{-2}$. The gate (L_g) and the channel length (L_{channel}) are taken to be 10 and 6 nm respectively. A 2 nm Al_2O_3 oxide (0.7 nm EOT) is used for the oxide layer between the gates and the 2D material.

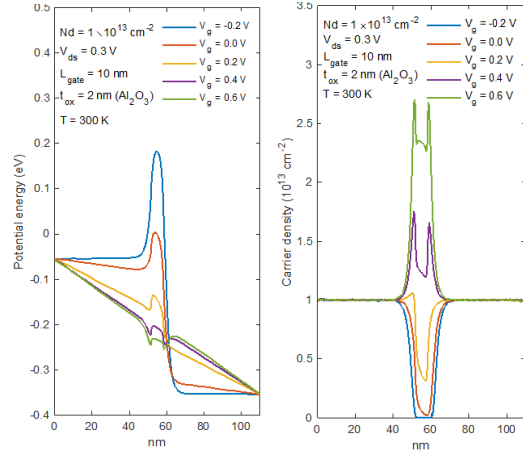


Fig.2: The potential energy profile (left) and charge density (right) along the 2D layer for various V_g at a constant $V_{ds} = 0.3 \text{ V}$.

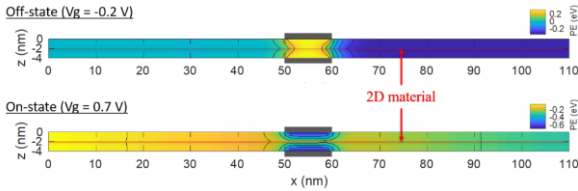


Fig.3: Contour plot of the potential energy for the off- (top) and on-state (bottom) calculated at $V_{ds} = 0.3 \text{ V}$.

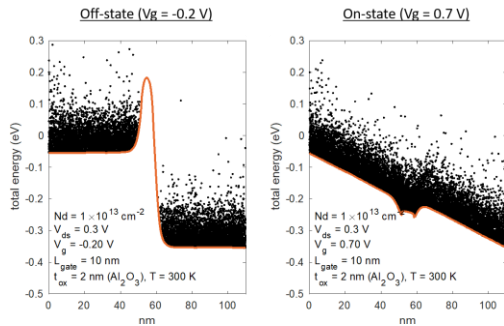


Fig.4: The potential energy and superparticle distribution plot along the 2D layer for the off- (left) and on-state (right).

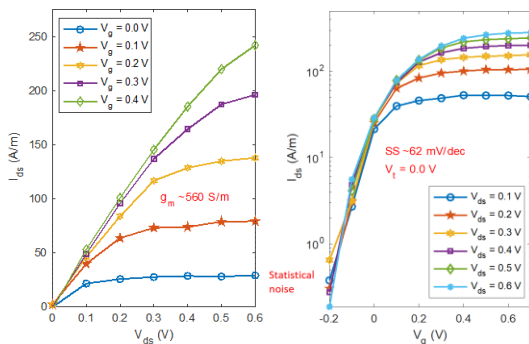


Fig.5: The output (left) and transfer (right) characteristics obtained for our device. Excellent gate control (SS $\sim 62 \text{ mV/dec}$) is observed.

Transient Investigations of Hot-Carrier Transport in BN-Encapsulated Graphene FETs

Jubin Nathawat¹, Miao Zhao^{1,2}, Chun-Pui Kwan³, Harihara Ramamoorthy¹,
Naoki Matsumoto⁴, Masahiro Matsunaga⁴, Nobuyuki Aoki⁴, Gil-Ho Kim², Kenji Watanabe⁵,
Takashi Taniguchi⁵, Jong E. Han³, and Jonathan P. Bird^{1,4}

*¹Department of Electrical Engineering, University at Buffalo,
The State University of New York, Buffalo, NY 14260, USA*

*²High-Frequency High-Voltage Device and Integrated Circuits Center,
Institute of Microelectronics of Chinese Academy of Sciences, 3 Beitucheng West Road,
Chaoyang District, Beijing, PR China*

*³Department of Physics, University at Buffalo, The State University of New York,
Buffalo, NY 14260, USA*

⁴Department of Materials Science, Chiba University, Inage-ku, Chiba 263-8522, Japan

*⁵Advanced Materials Laboratory, National Institute for Materials Science,
Tsukuba 305-0044, Japan
jbird@buffalo.edu*

Graphene is a material with remarkable electrical characteristics, including room-temperature mobility that is unparalleled among semiconductors, electrical conductivity that is better than that of silver, and a current carrying capacity that exceeds 10^8 A/cm². Nonetheless, it is also known that the electrical properties of graphene are typically strongly degraded by the interaction of its carriers with a substrate. With graphene on SiO₂, common issues are carrier trapping by interface states, and by deep levels within the oxide, and current degradation due to Joule heating of the substrate [1,2]. The latter process typically degrades the maximum saturation velocity to which carriers may be accelerated and, thus, the current-carrying capacity of the device [1,2]. A potential strategy that should allow these issues to be alleviated is that of encapsulating the graphene in high-quality BN. This should allow the graphene to be isolated from the influence of defects in the underlying oxide, and to also minimize transient heating effects. In our presentation, we describe the results of experiments that we have performed to investigate transient transport in such encapsulated graphene devices. Our results reveal a transition from current saturation to linear conductance as the charge neutrality point is approached from either the conduction or valence bands. We also identify the influence of Joule heating and charge trapping in these devices.

[1] H. Ramamoorthy et al., Nano Lett. **16**, 399 (2016)

[2] H. Ramamoorthy et al., Semicond. Sci. Technol. **32**, 084005 (2017)

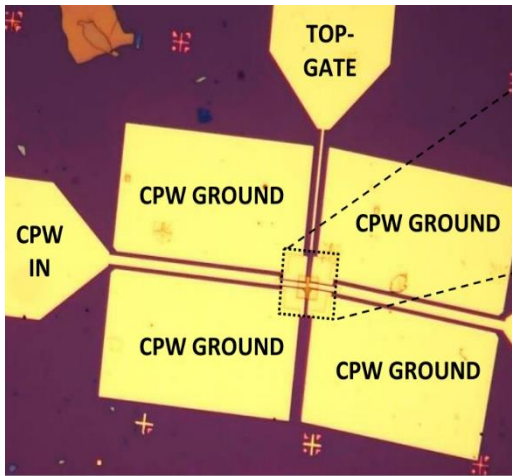


Fig.1: Coplanar waveguides for pulse measurements.

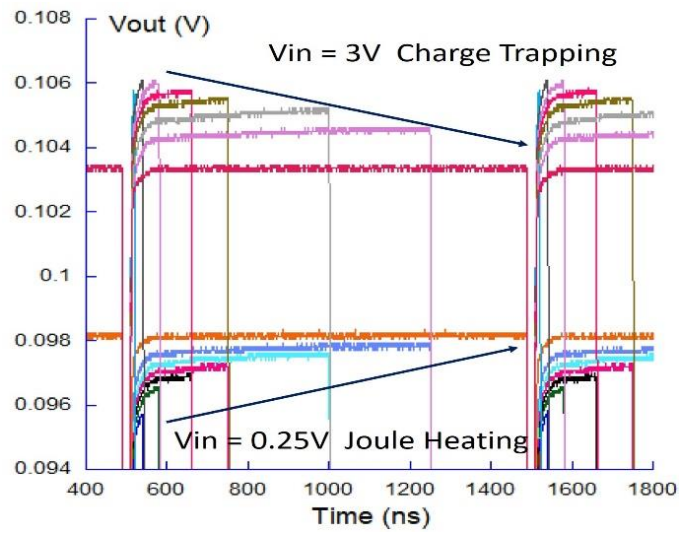


Fig.2: Joule heating and Charge trapping in Bilayer Graphene at different fields.

Realizing Asymmetric Boundary Conditions for Plasmonic THz Wave Generation in HEMTs

Bilal Barut¹, Gregory R. Aizin², Erik Einarsson³, Josep M. Jornet³, Takeyoshi Sugaya⁴,
and Jonathan P. Bird³

¹*Department of Physics, University at Buffalo, Buffalo, USA*

²*Department of Physical Sciences, Kingsborough Community College, New York City, USA*

³*Department of Electrical Engineering, University at Buffalo, Buffalo, USA*

⁴*National Institute of Advanced Industrial Science and Technology (AIST), Tsukuba, Japan*
bilalbar@buffalo.edu

Devices utilizing plasma wave generation are promising candidates for the realization of compact solid-state sources, capable of operating efficiently at THz frequencies. Plasma wave generation can occur when the current flowing through a device exceeds a threshold value, allowing initial plasma excitation produced by ambient noise to be amplified after reflection from the edges of a statically-biased gate. In order to observe such amplification, however, the impedance at the ends of the cavity should be highly asymmetric, i.e. low at the source and high at the drain [1]. While significant experimental effort has focused on implementing plasmonic THz devices, the power radiated into free space has proven to be too weak for practical use. One of the main reasons for this problem is the difficulty in creating asymmetric cavity boundaries. To address this issue, in this work, we show that etching a constriction near (~100 nm away from) the gated region of a HEMT can yield the high impedance required on the drain side of the cavity, thus yielding the conditions needed to trigger plasma-wave amplification. Our devices (Fig.1) are fabricated on an InP based InGaAs/InAlAs heterostructure chip, in which the constriction is defined by wet etching. The onset of plasma-wave amplification is manifested in transport measurements, as an additional dissipation channel that causes a small but sudden drop in the DC current through the channel (Figs. 2 & 3). The significance of the boundary conditions manifests itself when the current direction is reversed (thereby reversing the cavity boundary conditions). In this case, the current instability of Figs 2 & 3 is no longer observed. Our work, realizing reliable asymmetric boundaries required for plasma wave amplification, therefore provides an important step to the realization of compact solid-state THz plasmonic transmitters.

[1] M. Dyakonov and M. Shur, Phys. Rev. Lett. **71**, 2465 (1993)

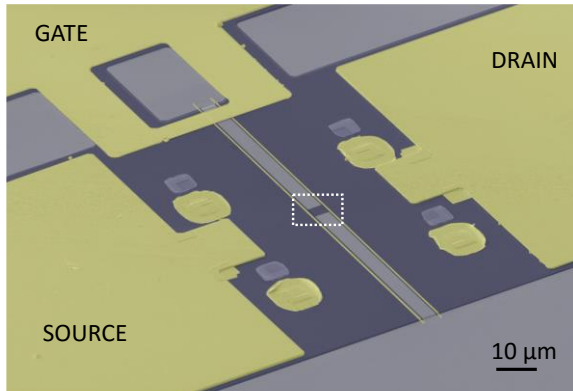


Fig.1a: Fabricated InGaAs/InAlAs FET with plasmonic cavity and asymmetric source/drain conditions. The figure is a global view of the device, showing source, drain and gate contacts.

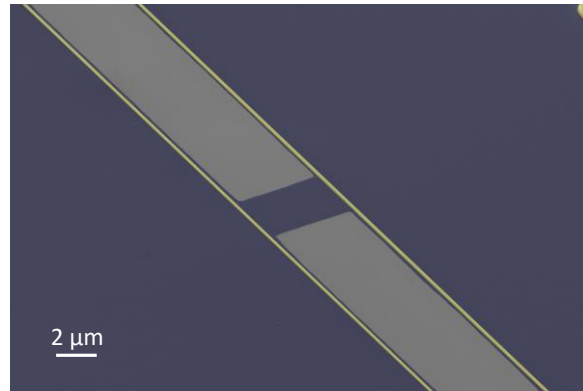


Fig.1b: The figure on the right is an expanded view of the section enclosed by the white dotted line on the Fig. 1a. This expanded view shows the narrow (150-nm wide) metal gates that define the plasmonic cavity on either side of the constriction (the two lighter, rectangular regions correspond to etched regions of the heterostructure).

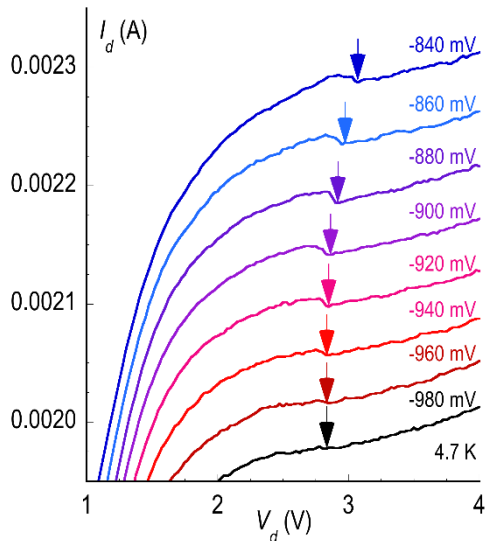


Fig.2: Electrical characteristics of a fabricated InGaAs/InAlAs FET with plasmonic cavity and asymmetric source/drain conditions (at 4.2 K). The figure shows the I-V characteristics obtained with various voltages (indicated) applied to the gate of the device. Arrows denote the presence of a current instability that shifts systematically with variation of the gate voltage.

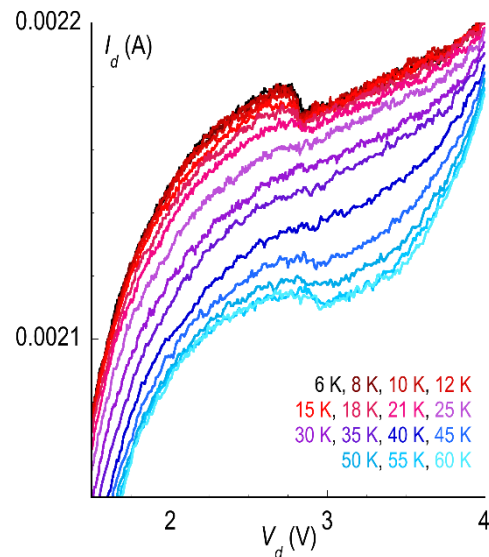


Fig.3: Temperature dependence of the instability, demonstrating its survival to temperatures approaching those of liquid nitrogen, is shown.

DFT Hamiltonian Based Simulation of GaSb UTB-FET with Spin Orbit Coupling Effect

Seong Hyeok Jeon¹, Yun Hee Chang¹, Junbeom Seo¹, and Mincheol Shin¹

*¹School of Electrical Engineering, Korea Advanced Institute of Science and Technology,
Daejeon 34141, South Korea
mshin@kaist.ac.kr*

In this work, we have verified the effect of spin-orbit (SO) coupling on GaSb ultra-thin body field effect transistor (UTB FET) with density functional theory (DFT) Hamiltonian based quantum transport simulations.

The DFT calculations were carried out by using the SIESTA tool [1], which was followed by the DFT-1/2 scheme to adjust the band gap (E_g) [2]. For the DFT-1/2 step, the pseudopotential was optimized for bulk GaSb and the cut off radius was chosen to give correct bulk E_g . Next, the GaSb slab structure was formed and fully passivated with pseudo-hydrogen atoms. A single point DFT calculation with the DFT-1/2 pseudopotential and SO coupling was performed to obtain band structure and non-orthogonal DFT Hamiltonian matrices were extracted. Finally, the Hamiltonian matrices were imported to our in-house transport tool [3], where the transport equations given by the non-equilibrium Green's function formalism were self-consistently solved with Poisson's equation. See Fig. 1 for the simulation flow.

With the SO coupling and DFT-1/2 correction, we were able to obtain bulk GaSb band structure that agrees reasonably well with experiments. Fig. 2 shows the band structure where E_g and the split-off energy are 0.58 eV and of 0.66 eV, respectively, which are comparable to the reported experimental values of 0.726 eV and 0.8 eV. The SO coupling effect is crucial to obtain correct bulk band structure as seen in Fig. 2.

As for a slab with confinement in the z-direction, we have found that the effect of SO is not as pronounced. Fig. 3 compares the slab band structures with DFT-1/2 correction only and with both DFT-1/2 correction and SO coupling. The SO coupling effect is to deform the band structure slightly but the overall shape does not seem to change much.

The transport calculations were performed for the ultra-thin-body structure shown in Fig. 4. Our results show that regardless of the presence of the SO coupling, the transport characteristics give almost identical SS (61 mV/dec) and ON-state current (1700 A/m). Only the threshold voltages differ by 0.08 V. See Fig. 5. We, therefore, conclude that, as long as the device performance is concerned, simulations without SO coupling with lower computational cost are sufficient.

- [1] J.M. Soler et al., J. Phys. Condens. Matt. **14**, 2745 (2002)
 [2] L.G. Ferreira et al., Phys. Rev. B **78**, 125116 (2008)
 [3] M. Shin et al., J. Appl. Phys. **119**, 154505 (2016)

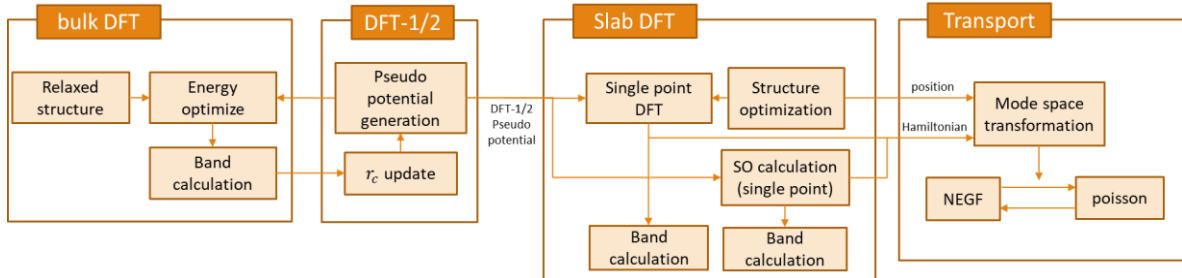


Fig.1: Flow chart of simulation.

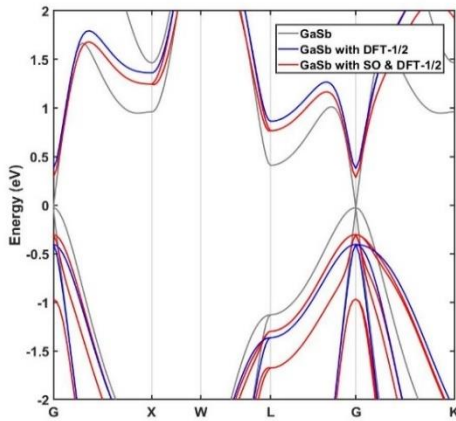


Fig.2: Band structure calculation results for bulk GaSb, with the ordinary GGA-PBE functional (gray lines), with DFT-1/2 correction (blue lines), and with both the DFT-1/2 correction and the SO coupling (red lines).

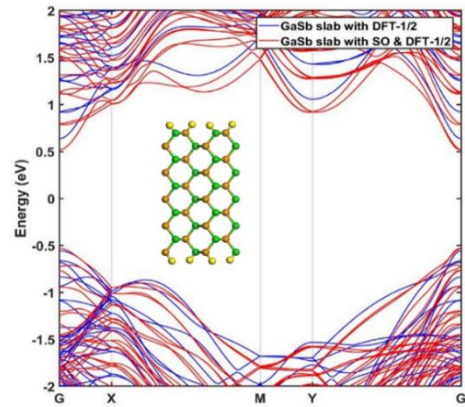


Fig.3: Band structure of GaSb(110) slab: blue lines for band structure with the DFT-1/2 correction only, and red lines for band structure with both the DFT-1/2 correction and SO coupling. Inset shows the slab structure used for the calculation: green for Ga, brown for Sb, and yellow for H.

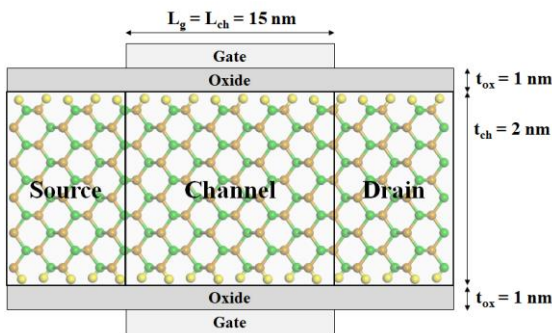


Fig.4: Schematic structure of simulated GaSb UTBFET. $L_g = L_{ch} = 15$ nm, $t_{ch} = 2$ nm, $t_{ox} = 1$ nm, the dielectric constants of oxide and GaSb are 3.9 and 15.7 respectively. Source and drain regions are doped with 1×10^{20} cm⁻³ and the drain voltage is set to 0.5 V.

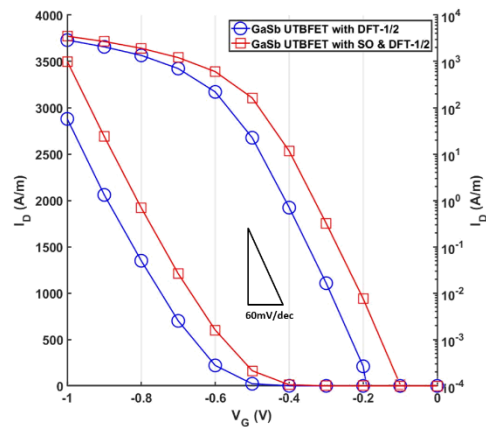


Fig.5: Transport characteristics of GaSb(110) UTBFET with and without the SO coupling: blue circled lines for IV curve with DFT-1/2 correction only, and red squared lines for IV curve with DFT-1/2 correction and SO coupling.

GaAsSb/InGaAs Double Gate Tunnel FET Operating Below 60 mV/Decade and Temperature Dependence of Band-Edge Decay Parameters

Yasuyuki Miyamoto¹, Nobukazu Kise¹, and Ryosuke Aonuma¹

¹*Department of Electrical and Electronic Engineering, Tokyo Institute of Technology,
2-12-1-S9-2, O-okayama, Meguro-ku, Tokyo 152-8550, Japan
miya@ee.e.titech.ac.jp*

Tunnel FETs (TFETs) can achieve steeper subthreshold slopes (SS) and are promising as elements for the next-generation low-power-consumption circuits [1]. Main problem in the SS improvement of TFETs is the interface state density (D_{it}) at MOS. However, even D_{it} is zero, bandgap states close to the source valence band edge induces degradation of SS [2]. One of the causes of bandgap states is impurity band in heavily doped source layer [3]. As impurity band is inherent characteristics, limitation of SS is expected. Recently, we obtained SS below 60 mV/dec by GaAsSb/InGaAs double gate tunnel FET [4]. In this study, we measured temperature dependence of band-edge decay parameters [2] of improved TFETs.

The fabrication processes were reported in ref. 4. The epitaxial structure for the devices consists of p^{++} -GaAsSb ($8 \times 10^{19} \text{ cm}^{-3}$) / i -InGaAs (50 nm) / n^{+} -InGaAs (40 nm: $8 \times 10^{18} \text{ cm}^{-3}$). Schematic of fabricated FET is shown in Fig.1. A sub-10-nm-wide body is confirmed by TEM image [4]. SS- I_{DS} characteristics are shown in Fig. 2. When insulator was changed from Al_2O_3 -1nm/ HfO_2 -3.5nm (1.1 nm as EOT) to Al_2O_3 -1nm/ ZrO_2 -3.5nm (0.9 nm as EOT), improvement of SS was confirmed. The minimum SS was 56 mV/dec at $V_{DS} = 0.2$ V. At low-temperature measurements, the SS_{MIN} was reduced to 47 mV/dec with $\text{Al}_2\text{O}_3/\text{ZrO}_2$ as shown in Fig. 3.

To evaluate temperature dependence of band-edge decay parameters E_0 , negative differential resistance (NDR) region, i.e., combination of negative drain voltage and positive gate bias, was used [2] as shown in Fig. 4. The reduction in E_0 by the gate insulator was observed as shown in Fig. 4. The calculated SS was 35 mV/dec at room temperature using $E_0 = 38$ mV when D_{it} is zero. In ref.2, observed E_0 does not show temperature dependence and is about 50-60 meV. However, in our measurement, E_0 shows temperature dependence and changes with fabrication process even from the same substrate. As our minimum E_0 was lower than that of ref. 2 although doping level is higher than them ($\sim 10^{19} \text{ cm}^{-3}$), we still have a room to improvement on SS.

[1] A.M. Ionescu et al., Nature **479**, 329 (2011)

[2] E. Memisevic et al., IEEE Electron Dev. Lett. **38**, 1661 (2017)

[3] J.I. Pankove, Phys. Rev. **140**, A2059 (1965)

[4] R. Aonuma et al., Proc. SSDM (2018)

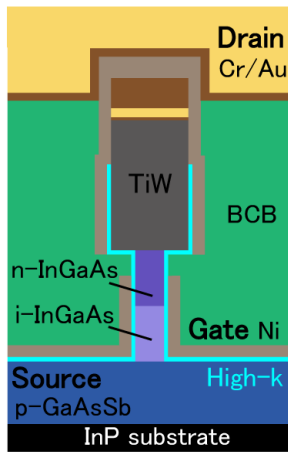


Fig.1: Schematic of double-gate tunnel FET.

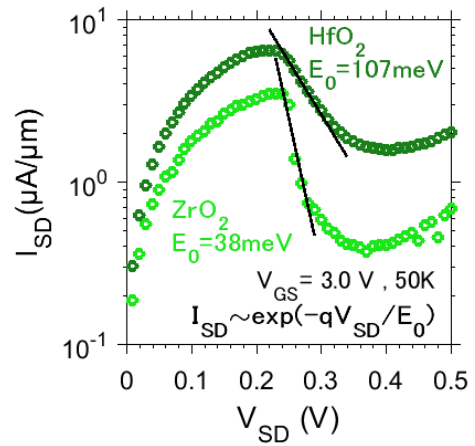


Fig.4: I-V characteristics with differentiated negative resistance.

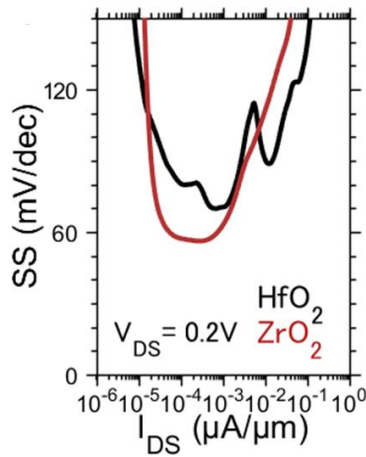


Fig.2: SS-I_{DS} characteristics of TFETs with Al₂O₃/HfO₂ and Al₂O₃/ZrO₂ using thermal evaporated gate electrode.

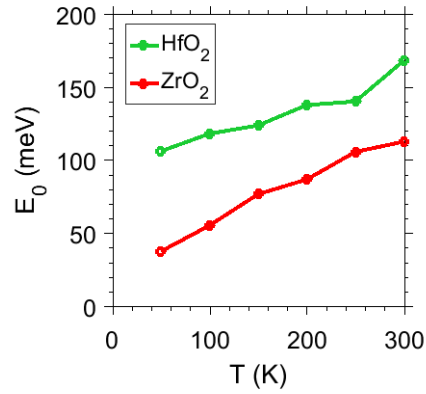


Fig.5: Temperature dependences of I-V characteristics with differentiated negative resistance.

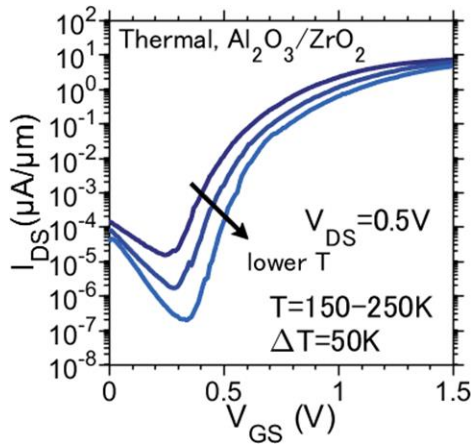


Fig.3: I_{DS}-V_{GS} characteristics at low temperature with Al₂O₃/ZrO₂ insulator.

Electrical Characterization of Thin, Quasi-1D Titanium Trisulfide (TiS₃) Field Effect Transistors

Michael D. Randle¹, Alexey Lipatov², Avinash Kumar¹, Keke He¹, Chun-Pui Kwan¹,
Jubin Nathawat¹, Ripudaman Dixit¹, Shenchu Yin¹, Nargess Arabchigavkani¹,
Peter A. Dowben³, Uttam Singiseti¹, Alexander Sinitskii², and Jonathan P. Bird¹

¹*Department of Electrical Engineering, School of Engineering and Applied Sciences,
University at Buffalo, Buffalo, New York 14150, USA*

²*Department of Chemistry, University of Nebraska-Lincoln, Lincoln,
Nebraska 68588-0304, USA*

³*Department of Physics and Astronomy, University of Nebraska-Lincoln, Lincoln,
Nebraska 68588-0304, USA*
jbird@buffalo.edu

Titanium trisulfide (TiS₃) is an n-type 2D transition metal trichalcogenide that exhibits highly anisotropic, quasi-1D carrier transport. We report extensive electrical characterization of this nanomaterial as a field-effect transistor (FET) when it is exfoliated onto and gated through a SiO₂/Si substrate. The transfer curves of this material, measured at temperatures below 100 K, reveal mesoscopic conductance fluctuations in its disordered conductor state that are modulated by both gate-voltage and temperature in a non-monotonic manner; this unusual temperature-dependent behavior is very different to that normally expected for nanomaterials, and may possibly be related to the formation of a novel charge-density-wave state (Fig. 1). In this regime, the low-temperature transport behavior of TiS₃ can be understood in the context of variable range hopping. Additionally, the emergence of a well-established metal-insulator transition in TiS₃ is demonstrated here to be gate-voltage dependent. Through our observations over a wide temperature range (3-500K), we extract a gate-voltage dependent mobility based on a modified square-law model, obtaining values as large as 20 cm²/Vs at room temperature and ON/OFF ratios as large as 10⁴. Transistor measurements far from the FET cutoff region reveal marked nonlinear behavior at low applied source-drain voltages, which may again be related to the aforementioned charge-density-wave state. With increasing temperature, this behavior becomes less pronounced, and disappears entirely near room temperature. Calculations of the transfer- and transistor-curves for these devices, utilizing standard transistor models and semiclassical Boltzmann transport theory, give further insight into the microscopic origins of these results. The results not only demonstrate that TiS₃ is a testbed for a variety of interesting physics, but show its viability as a channel-replacement material for use in scaled transistors in future technology generations.

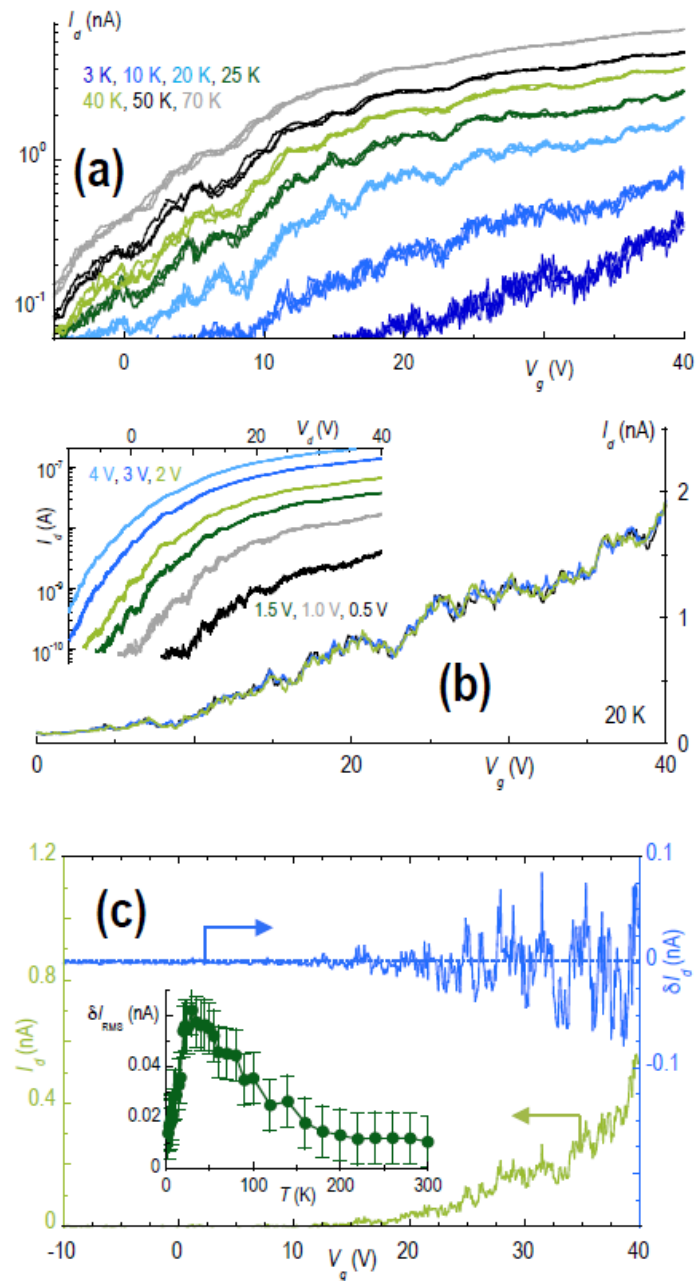


Fig. 1: (a) Mesoscopic fluctuations present in TiS3's insulating state. (b) Results of three successive measurements, demonstrating the reproducibility of the fluctuations. (c) Non-monotonic dependence of the fluctuation magnitude on temperature.

Solution Processed Indium Zinc Oxide Thin-Film Transistors with Nanoscale Multi Stacking Channel Layer

Zi-Tong Ao¹, Fei Shan¹, Han-Sang Kim¹, Hong-Bo Guo¹, Jae-Yun Lee¹, and Sung-Jin Kim¹

¹*College of Electrical and Computer Engineering, Chungbuk National University,
Cheongju 28644, Korea
cugatech@gmail.com*

Transparent oxide semiconductors (TOS) have advanced rapidly in the late years [1-3]. TOS have advantages of high optical transmittance, high electron mobility, and compatibility with low-temperature flexible substrates, and they are considered as the alternative product of amorphous silicon and polycrystalline silicon thin-film transistors, which is essentially a kind of wide bandgap semiconductor with high mobility.

In this work, the thin-film transistors (TFTs) of the nanoscale multi stacking indium zinc oxide (IZO) channel layer are prepared by using a heavily doped-type (n++) silicon substrate, so as to investigate the effect of the multi stacking process of the channel layer on the electrical characteristics of the TFTs. The experimental results of electrical properties show that the TFTs of the three-layer stacking IZO channel layers have the clear switching response, excellent voltage gain and best electrical characteristics.

[1] K. Nomura et al., Nature **432**, 488 (2004)

[2] P. K. Nayak et al., Sci. Rep. **4**, 4672 (2014)

[3] K. Yim et al., npj Comput. Mater. **4**, 17 (2018)

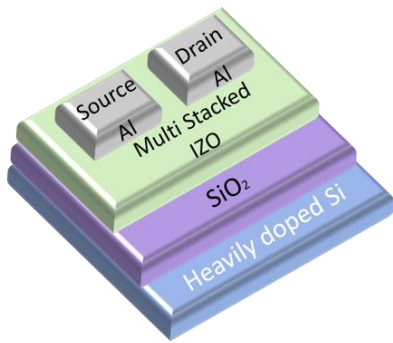


Fig.1: Schematic diagram of nanoscale multi stacking IZO TFTs structure.

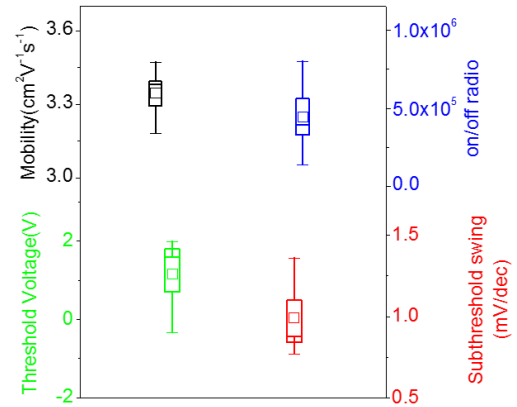


Fig.3: Current as a function of Θ , for $p=1$, $\Gamma_N/\Gamma_F = 10$, $\omega_L/\Gamma_F = 1$, $\Gamma_F T_1 = 10$, and several values of T_2/T_1 .

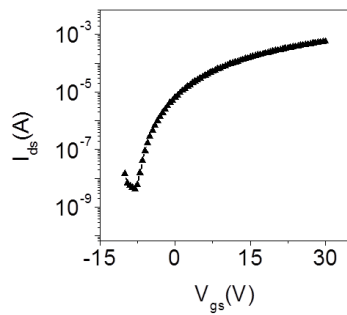


Fig.2: Transfer characteristics curve nanoscale multi stacking IZO TFTs.

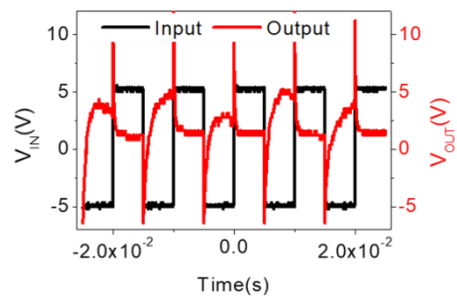


Fig.4: Dynamic response of n-channel inverter under different voltage impulses when the value of the load resistor is 1 MΩ. The value of voltage impulses is 100Hz.

Enhanced Electrical Properties of TiO_x-Based Oxide Thin-Film Transistors by a Femtosecond Laser Irradiation

Fei Shan¹, Zi-Tong Ao¹, Han-Sang Kim¹, Hong-Bo Guo¹, Jae-Yun Lee¹, and Sung-Jin Kim¹

¹*College of Electrical and Computer Engineering, Chungbuk National University,
Cheongju 28644, Korea
cugatech@gmail.com*

Oxide thin-film transistors (TFTs) have received a great deal of attention as potential alternatives as a backplane technology for next-generation displays [1]. Especially titanium-metal cation oxides, such as titanium oxide (TiO_x) [2–3], have recently attracted a lot of attention as an active channel in TFTs because TiO_x exhibits excellent comprehensive properties, including a high refractive index, high permittivity, decent biocompatibility, and long-term stability against photo corrosion and chemical corrosion.

In this work, we first investigate the operation of the ALD equipment for the deposition of TiO_x thin films in detail. Then, the electrical characteristics of TiO_x channel-based TFTs fabricated with a femtosecond laser pre-annealing process at various radiation times were analyzed. We analyze the changes in nanostructure and electrical performance of the TiO_x-based oxide TFT by ALD at temperatures as low as 200 °C for at least 10 h, and femtosecond laser pre-annealing with different laser heat treatment times (0 s, 5 s, 25 s, and 50 s) at 3 W.

[1] K. Nomura et al., *Nature* **432**, 488 (2004)

[2] S.K. Kim et al., *J. Appl. Phys. Lett.* **85**, 4112 (2004)

[3] B. Choi et al., *J. Appl. Phys.* **98**, 033715 (2005)

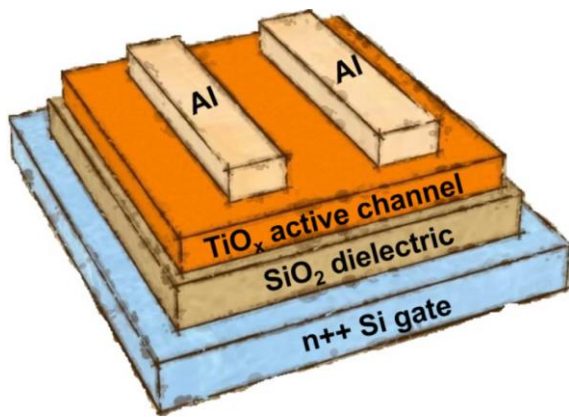


Fig.1: Schematic representation of the TiOx-based TFT structure.

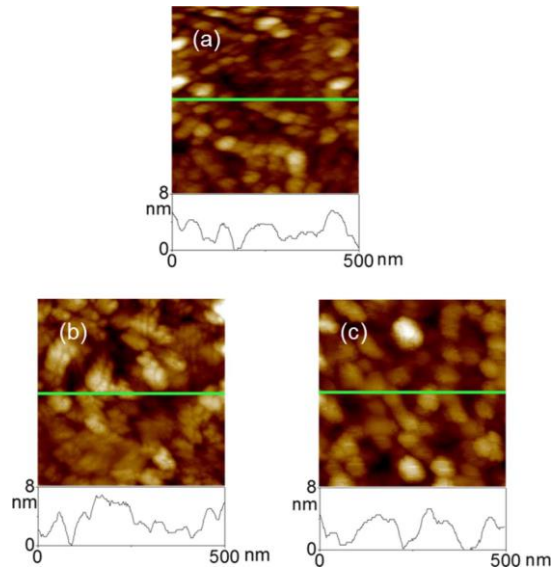


Fig.2: AFM topographies and cross sections by femtosecond laser preannealing at (a) 0 s, (b) 25 s, and (c) 50 s.

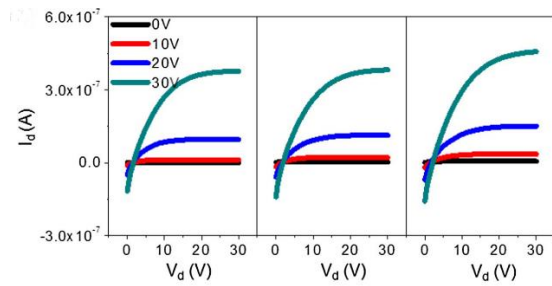


Fig.3: Output characteristics obtained from TiOx-based TFTs.

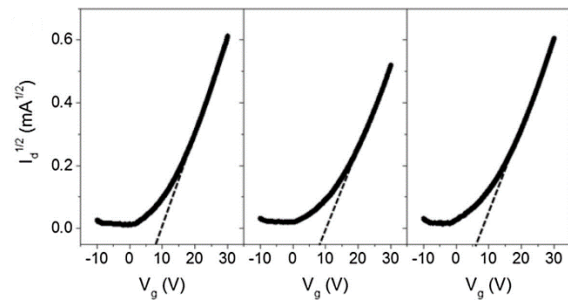


Fig.4: Transfer curve characteristics obtained from TiOx-based TFTs.

Impact of Lattice Matching Condition on the Simulation of Band-to-Band Tunneling in MoS₂/Ge van der Waals Heterojunctions

Futo Hashimoto¹ and Nobuya Mori¹

¹Graduate School of Engineering, Osaka University,
2-1 Yamada-oka, Suita, Osaka 565-0871, Japan
{hashimoto, mori}@si.eei.eng.osaka-u.ac.jp

Recently, tunnel field-effect transistors utilizing band-to-band (BTB) tunneling in van der Waals (vdW) heterojunctions were fabricated, showing excellent device characteristics [1]. Here we study impact of lattice matching condition on the simulation of BTB tunneling in MoS₂/Ge heterojunctions by using the non-equilibrium Green function (NEGF) method combined with a tight-bind (TB) approximation.

We consider a MoS₂/Ge vdW heterojunction whose schematic diagram is given in Fig. 1. The channel of length L consists of a mono-layer MoS₂ on an N -layer Ge. The channel width is considered to be infinite with a periodic boundary condition. Semi-infinite electrodes are attached to the both ends of the channel. We use the NEGF method and calculate integrated transmission functions $\tau(E)$. The band-structures are described by the 11-band TB model [2] for MoS₂ and the sp^3s^* TB model [3] for Ge. We assume that electron transfer between MoS₂ and Ge occurs only in the channel region. The inter-layer transfer integrals are extracted from a density functional theory (see Fig. 2). The lattice constants of MoS₂ and Ge are $a_{\text{MoS}_2} = 3.16 \text{ \AA}$ [2] and $a_{\text{Ge}} = 5.65 \text{ \AA}$ [3], respectively, which gives an irrational ratio of $\eta_{\text{real}} = a_{\text{Ge}} / a_{\text{MoS}_2} = 1.7879\dots$. To apply the periodic boundary condition along the y -direction, we approximate η_{real} as some rational number $\eta = N/M$ with a unit cell of N -period MoS₂ and M -period Ge (see, for example, Figs. 3 (a) and (b) which show the unit cell for $\eta = 2/1 = 2$ and that for $\eta = 3/2 = 1.5$, respectively). Note that we can obtain η infinitely close to η_{real} by using a larger unit cell. Figure 4 shows the band-structures of MoS₂ and Ge along the k_y -direction for $\eta = 2$. The energy-bands are folded in a small first Brillouin zone and the MoS₂ conduction band (CB) bottoms appear at $k_y = \pm\pi/3a_{\text{MoS}_2}$. As a result, MoS₂ CB and Ge valence band (VB) do not overlap each other and tunneling does not take place due to the momentum conservation along the k_y -direction even when the energy-bands energetically overlap each other. On the other hand, for $\eta = 1.5$, MoS₂ CB bottoms appear at $k_y = 0$ (see Fig. 5), leading to finite BTB tunneling in the overlapped energy window. Figure 6 shows $\tau(E)$ for larger unit cells. We find that $\tau(E)$ of larger unit cells are less sensitive to lattice matching condition.

[1] D. Sarkar et al., Nature **526**, 91 (2015)

[2] E. Ridolfi et al., J. Phys. Condens. Matt. **27**, 365501 (2015)

[3] P. Vogl et al., J. Phys. Chem. Solids **44**, 365 (1983)

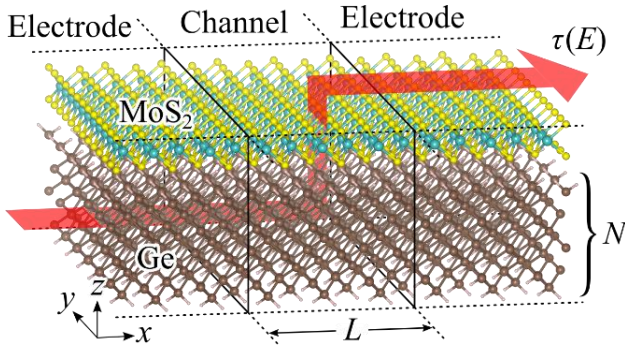


Fig.1: Device model of MoS₂/Ge vdW heterojunction. We set $N = 4$ and $L = 0.56$ nm in the present study.

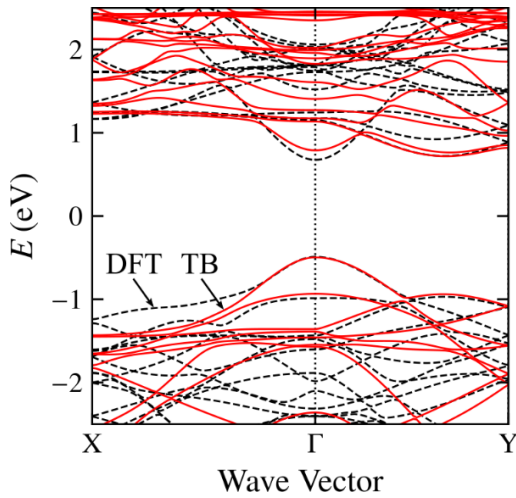


Fig.2: Band-structure of MoS₂/Ge vdW heterojunction calculated by DFT (dashed line) compared with the TB band-structure (solid line).

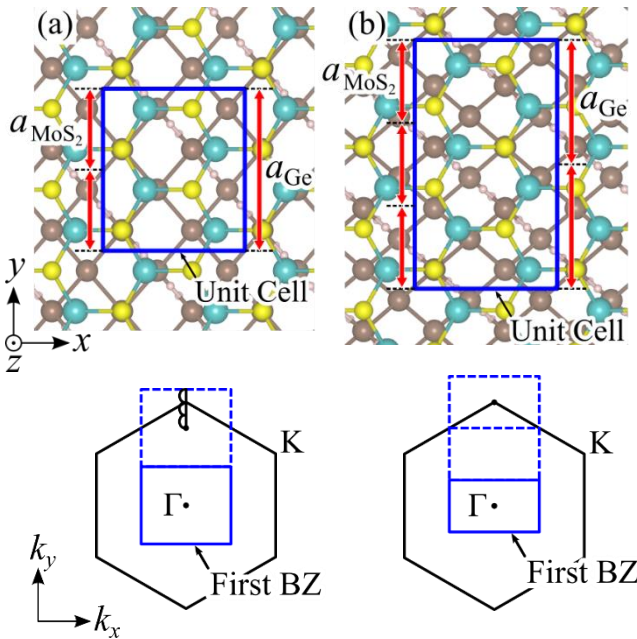


Fig.3: Top view of vdW heterojunction for $\eta = 2$ (a) and $\eta = 1.5$ (b). Bottom figures show the corresponding reciprocal space.

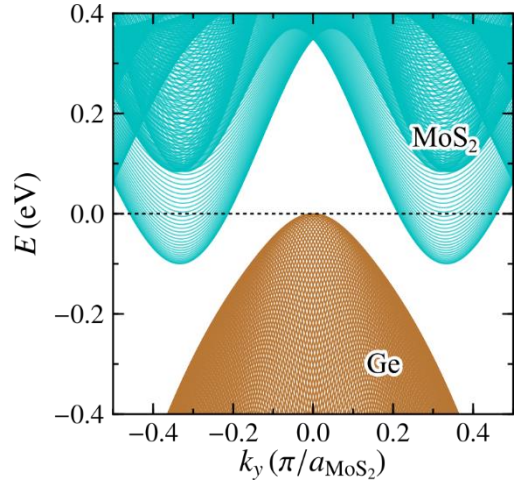


Fig.4: Band-structures of MoS₂ and Ge along k_y -direction for $\eta = 2$.

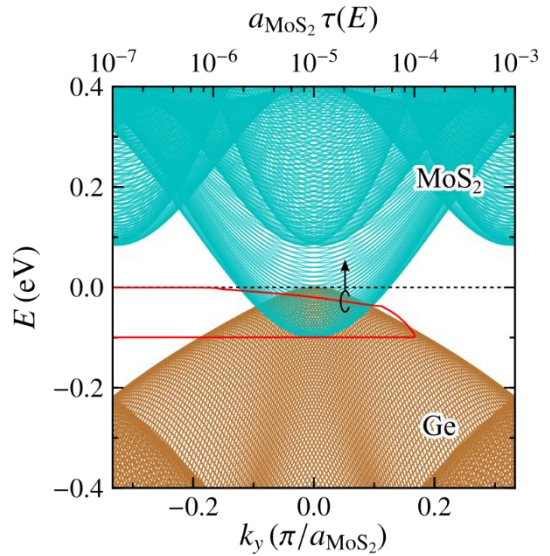


Fig.5: Same as Fig. 4 but for $\eta = 1.5$, together with the integrated transmission function $\tau(E)$ (upper axis).

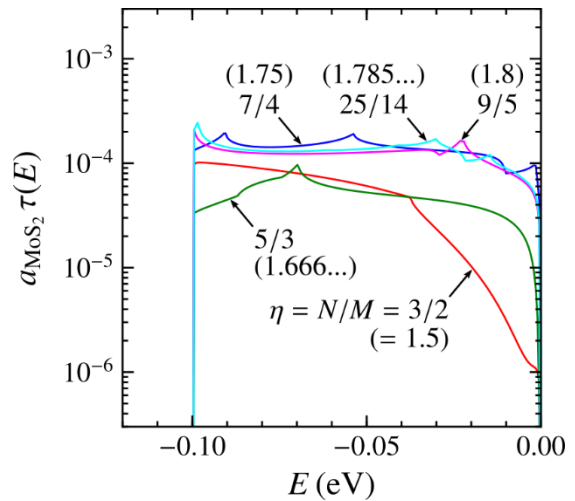


Fig.6: Integrated transmission function $\tau(E)$ for larger unit cells.

Modeling of Inter-Layer Tunneling Between Semiconductor Nanoribbons

Takaya Mishima¹, Futo Hashimoto¹, and Nobuya Mori¹

¹Graduate School of Engineering, Osaka University,
2-1 Yamada-oka, Suita, Osaka 565-0871, Japan
{mishima, hashimoto, mori}@si.eei.eng.osaka-u.ac.jp

Investigations of van der Waals heterojunctions have attracted significant attention for their application in novel electronic devices, such as tunnel field-effect transistors [1]. Inter-layer tunneling between 2D materials is different from the conventional tunneling in the sense that the tunneling direction is perpendicular to the transport direction from the source to drain electrodes. Here we develop a simple model to describe the inter-layer tunneling between narrow 2D materials (or nanoribbons) in the weak inter-layer coupling limit.

We consider a system consisting of two semiconducting nanoribbons of width W whose schematic diagram is given in the inset of Fig. 1. The nanoribbons have a parabolic dispersion $E(k) = \hbar k^2/2m$ with $m = 0.1 m_0$. Electrons can tunnel between the top and bottom nanoribbons only in the channel region of length L . We assume a weak tunneling coupling strength γ between the top and bottom nanoribbons. We calculate transmission functions $T_\alpha(E)$ from the top-left (TL) electrode to the α electrode [$\alpha =$ top-right (TR), bottom-right (BR), or bottom-left (BL)] by using a NEGF method.

Figure 1 shows the transmission functions as a function of the incident electron energy E measured from the bottom of the lowest subband. The tunneling transmission $T_{BR}(E)$ becomes smaller as E increases except for a small onset energy region. It increases as $\propto L^2$ at a fixed E (see Fig. 2). These features are well modeled by considering a semi-classical transit time $t = L/v$ with $v = \sqrt{2E/m}$ and regarding the channel region as a coupled two-state system, and we have $T_{BR}(E) = \sin^2(\gamma t/\hbar)$ and $T_{TR}(E) = \cos^2(\gamma t/\hbar)$. These simple formulae well reproduce the NEGF results except for $E \lesssim \gamma$ or $t \gtrsim L/\sqrt{2\gamma/m}$ (see Figs. 3 and 4). Tunneling conductance G for the non-degenerate case is then approximately given by

$$\frac{G}{G_0} = \beta \int_\gamma^\infty \sin^2\left(\frac{\gamma}{\hbar} L \sqrt{\frac{m}{2E}}\right) e^{-\beta E} dE, \quad (1)$$

which is further reduced to $G/G_0 = \pi(\beta\gamma)^2(L/\lambda_{th})^2 E_1(\beta\gamma)$ as $L \rightarrow 0$ (see Figs. 5 and 6). Here $G_0 = (e^2/2\pi\hbar)n\lambda_{th}$, $\lambda_{th} = (2\pi\hbar^2/mkT)^{1/2}$, $\beta = 1/kT$, n is the electron density, T is the temperature, and $E_1(x)$ is the exponential integral.

[1] D. Sarkar et al., Nature **526**, 91 (2015)

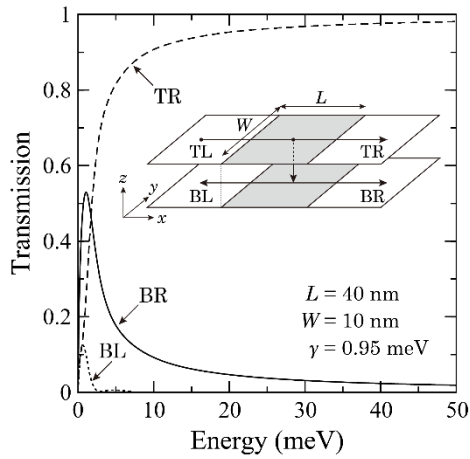


Fig. 1: Transmission functions as a function of the incident electron energy. The inset shows a schematic diagram of the system.

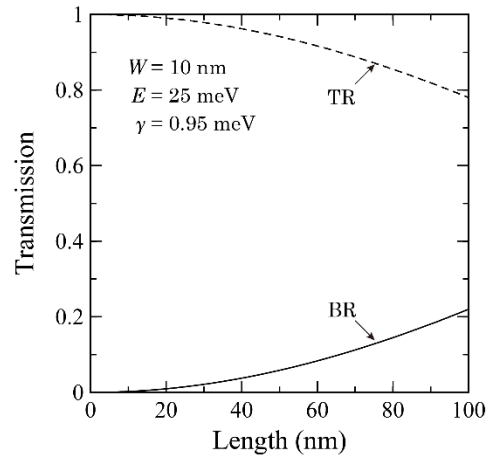


Fig. 2: Transmission functions as a function of the channel length.

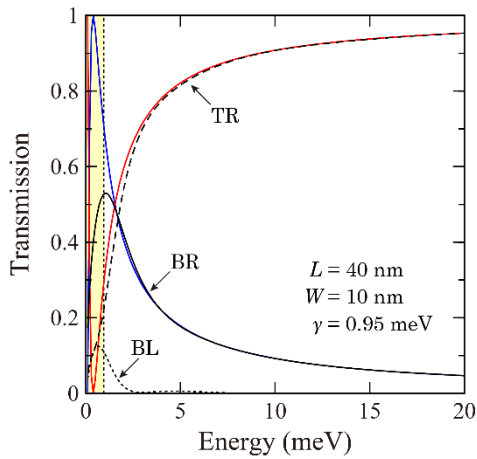


Fig. 3: Transmission functions calculated by the NEGF method (black lines) compared with $\sin^2(\gamma t/\hbar)$ (blue solid line) and $\cos^2(\gamma t/\hbar)$ (red solid line). Yellow region corresponds to $E \leq \gamma$.

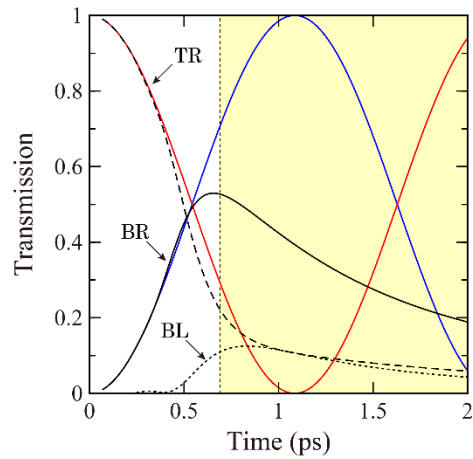


Fig. 4: The same as Fig. 3, but plotted as a function of the transit time $t = L/\sqrt{2E/m}$.

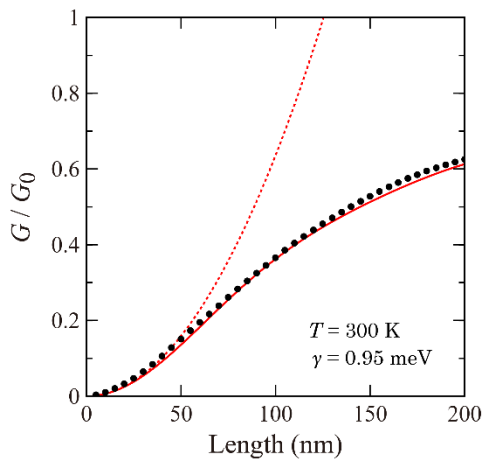


Fig. 5: Tunneling conductance as a function of the channel length for $\gamma = 0.95$ meV. Solid circles show the results calculated by NEGF, solid line by Eq. (1), dotted line by $\pi(\beta\gamma)^2(L/\lambda_{th})^2 E_1(\beta\gamma)$.

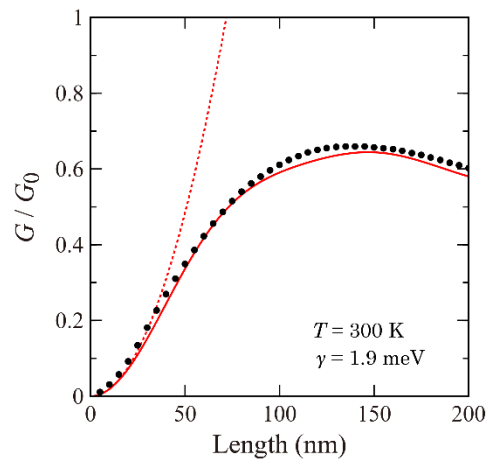


Fig. 6: The same as Fig. 5 but for $\gamma = 1.9$ meV.

Preparation of a Phantom: A Step Toward Application of a Spin-LED for Unstained and Non-Invasive Cancer Detection

Nozomi Nishizawa¹, Kazumasa Takahashi¹, Takahiro Kuchimaru², and Hiro Munekata¹

¹*FIRST, Tokyo Institute of Technology, Japan*

²*Center for Molecular Medicine, Jichi Medical University, Japan*

munekata.h.aa@m.titech.ac.jp and nishizawa.n.ab@m.titech.ac.jp

Polarization of light scattered by tissues contains rich information as to their spatial distribution and temporal change, and has been considered a powerful tool for diagnosis of tumor tissues, especially at pre-cancerous stage [1]. Interesting experiments using an elliptic polarization light have been reported, in which a clear difference in polarization state for backscattered light has been observed between ablated, healthy and tumor tissues [2]. Taking advantage of spin-LEDs that emit nearly pure circular polarization at room temperature [3, 4], we have gotten an idea that unstained and non-invasive, in vivo diagnosis of tumor tissues will be possible if the spin-LEDs and detectors can be integrated with an endoscope (Fig. 1). In view of this goal, however, it is not clear presently the cause and effect between the condition of light scatterers, namely size, shape, and distribution of nuclei, and resultant change in polarization of the scattered light. In the present paper, we report preparation of phantoms that imitate healthy and tumor tissues by semiconductor-based microfabrication process, and optical characterization of those phantoms with a monochromatic, circular polarization (CP) light source.

Phantoms consist of 2D array of 20-nm thick aluminum pads with different diameters d on glass substrates. They were prepared by photo-lithography. Shown in Figs. 2(a) and (b) are micrographs of phantoms that correspond to healthy ($d = 6 \mu\text{m}$) and tumor ($d = 11 \mu\text{m}$) tissues, respectively. Figure 2(c) depicts polarization spectra ($\lambda = 550 - 1200 \text{ nm}$) of scattered light when a CP light beam is impinged with the incident angle of 45° and scattered at the angle -45° . It is clearly seen that the magnitude of CP is reduced for the phantom having larger Al pads. Shown in Fig. 3(b) is polarization states on the Poincaré sphere of the backscattered light beam ($\lambda = 900 \text{ nm}$) obtained from two different spots of a 50- μm thick, liver tissue sample of a mouse affected by colorectal cancer. Its photograph is shown in Fig. 3(a). Values of optical rotation, the longitude on the Poincaré sphere, are close for both healthy and tumor tissues, whereas the value of CP for the tumor tissue tends to be small, near the equator. These results suggest that the size of nuclei affects the scattering process of light, and thus CP value.

- [1] W.S. Bickel et al., Proc. Natl. Acad. Sci. USA **73**, 486 (1976)
- [2] B. Kunnen et al., J. Biophotonics **8**, 317 (2015)
- [3] N. Nishizawa et al., Proc. Natl. Acad. Sci. USA **114**, 1783 (2017)
- [4] N. Nishizawa et al., Appl. Phys. Express **11**, 053003 (2018)

Attaching spin-photonic devices onto tip of flexible endoscope



Fig.1: Schematic illustration of in vivo detection of tumor tissues using a spin-LED, a CP emitter, and a spin-PD, a CP detector. These devices are supposed to be integrated into an endoscope that is shown on left- top side of the figure.

Detected data can be transferred as electric signals through an endoscope

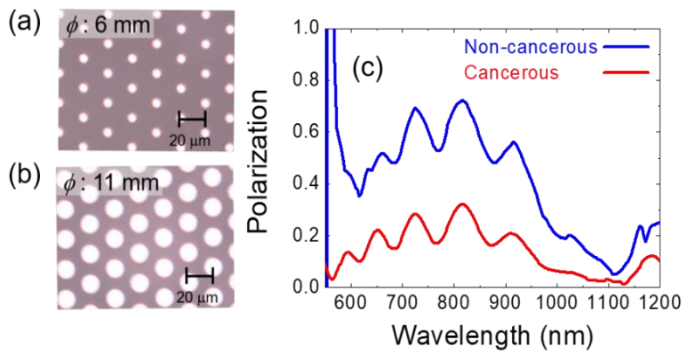


Fig.2: Micrographs of the phantoms for (a) non-cancerous and (b) cancerous tissues. (c) Polarization spectra of scattering light for (blue) non-cancerous and (red) cancerous phantoms, when the left circularly polarized light is impinged on samples

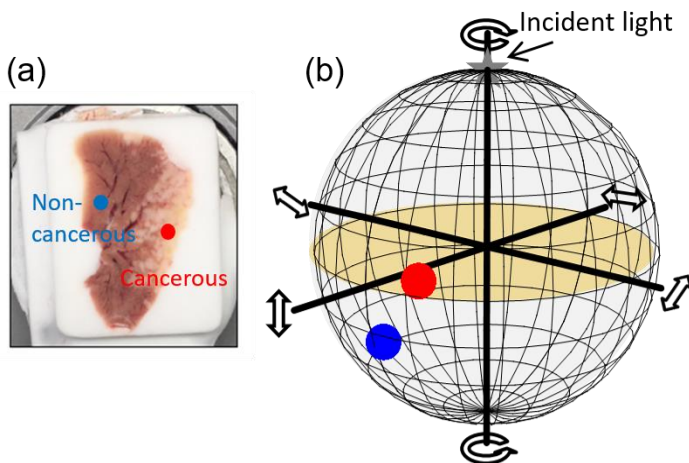


Fig.3: (a) A photograph of a sliced murine tissue of liver metastasis. Blue and red circles show focus points in non-cancerous and cancerous parts, respectively. (b) Polarization plots of scattering light on the Poincaré sphere.

A Variability Study of Ferroelectric Tunnel Junction

Junbeom Seo¹, Seong Hyeok Jeon¹, and Mincheol Shin¹

¹*School of Electrical Engineering, Korea Advanced Institute of Science and Technology,
Daejeon 34141, South Korea
mshin@kaist.ac.kr*

Ferroelectric tunnel junctions (FTJs) have attracted much attention for an emerging non-volatile memory device due to high ON/OFF-current ratio and high reliability [1][2]. A FTJ consists of a thin ferroelectric film sandwiched between metal electrodes (See Fig. 1). The interface properties at metal-ferroelectric junctions are very important for the performance of FTJ. However, the performance variability induced by spatial fluctuations at the interfaces has not been studied yet. In this work, we have performed a variability study of FTJ due to the spatial fluctuations in the band offset (ϕ) and screening length (λ).

The overall simulation flow is shown in Fig. 2. The polarization dynamics of a ferroelectric film is described by Landau-Khalatnikov equation, where the ferroelectric free energy with respect to the polarization is considered by Landau-Devonshire-Ginzburg theory [3][4]. The imperfect screening of the metal electrodes is expressed by the Thomas-Fermi screening model [2][3]. With the potential profile thereby obtained, the current density is calculated by using the non-equilibrium Green's function method [3]. As shown in Fig. 3, the values of ϕ and λ are generated to follow the Gaussian distribution and the standard deviations ($\sigma_{\phi,\lambda}$) of ϕ and λ are varied in a range.

Fig. 4 shows the current-voltage characteristics of FTJs with the spatial fluctuations in ϕ and λ . Although it seems that the memory window is not changed significantly with increasing the magnitude of the variations in both ϕ and λ , ON-current (I_{ON}) is slightly degraded and OFF-current (I_{OFF}) is increased (See Fig. 5). Fig. 6 represents the sensitivity of I_{ON}/I_{OFF} as a function of the standard deviation ($\sigma_{\phi,\lambda}$) in ϕ and λ . As expected, the average ($\bar{\mu}_{ON/OFF}$) of I_{ON}/I_{OFF} is reduced and the standard deviation ($\sigma_{ON/OFF}$) of I_{ON}/I_{OFF} is increased with increasing $\sigma_{\phi,\lambda}$. We found that the degradation of $\bar{\mu}_{ON/OFF}$ is mostly resulted from the band offset variation, while the dispersion of I_{ON}/I_{OFF} is dominantly affected by the spatial fluctuations of the screening length.

- [1] A. Gruverman et al., Nano Lett. **9**, 3539 (2009)
- [2] H. Kohlstedt et al., Phys. Rev. B **72**, 125341 (2005)
- [3] S. C. Chang et al., Phys. Rev. Appl. **7**, 024005 (2017)
- [4] A. K. Saha et al., Proc. IEEE IEDM (2017)

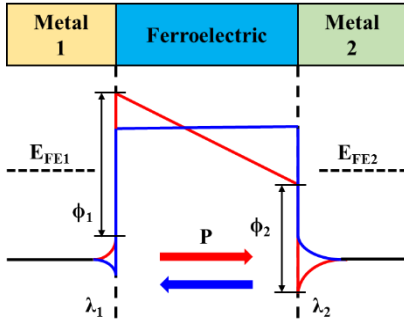


Fig.1: Schematic diagram of ferroelectric tunnel junction. $E_{FE1(2)}$, $\phi_{1(2)}$ and $\lambda_{1(2)}$ represent Fermi level, band offset and effective screening length of metal 1(2), respectively.

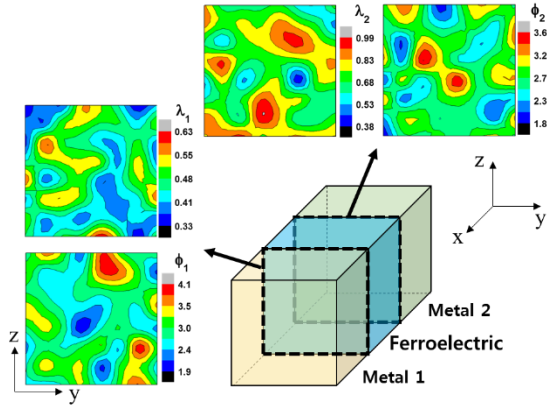


Fig.3: An example of the spatial variations in ϕ and λ . ϕ and λ were generated to follow the Gaussian distribution.

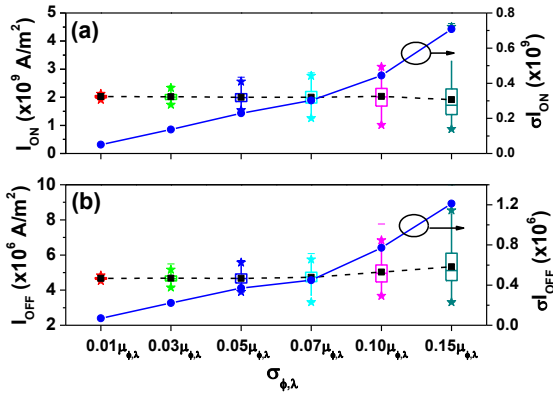


Fig.5: (a) I_{ON} and (b) I_{OFF} as a function of standard deviation ($\sigma_{\phi,\lambda}$). Dashed and solid lines represent the average and the standard deviation of I_{ON} and I_{OFF} , respectively.

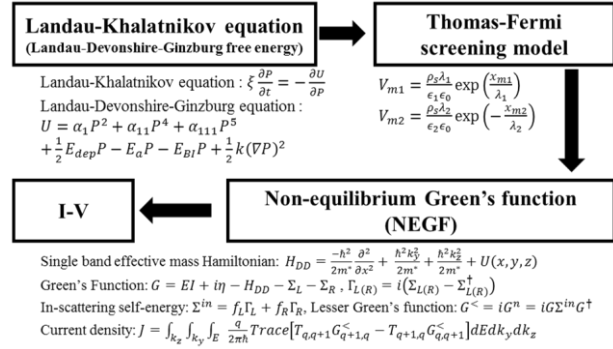


Fig.2: Simulation flow chart. Landau-Khalatnikov equation is solved by Runge-Kutta method and the current density (J) is obtained by the NEGF method.

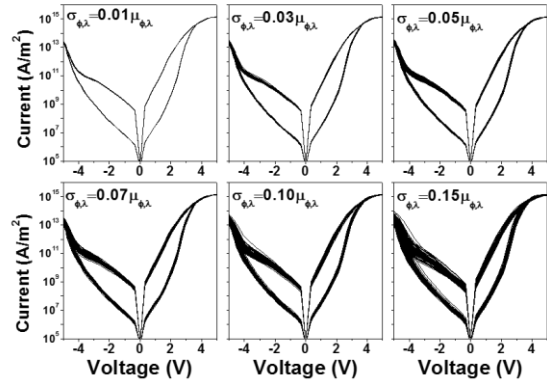


Fig.4: Current-voltage characteristics of FTJs (100 samples) for different standard deviation values ($\sigma_{\phi,\lambda}$).

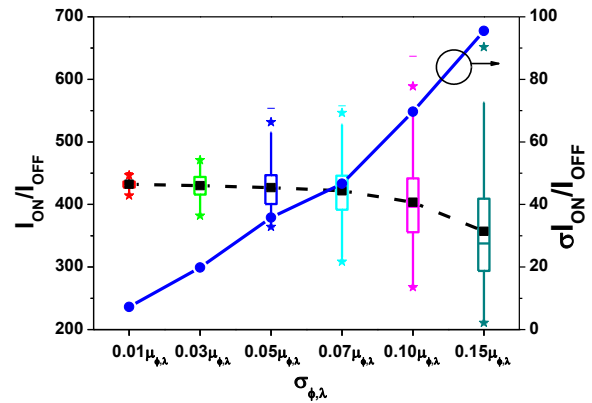


Fig.6: The sensitivity of I_{ON}/I_{OFF} as a function of $\sigma_{\phi,\lambda}$. Dashed and Solid lines represent the average and the standard deviation of I_{ON} and I_{OFF} , respectively.

Fast, Reliable, and Field-free Perpendicular Magnetization Reversal in Advanced Spin-Orbit Torque MRAM by Two-pulse Switching

Viktor Sverdlov¹, Alexander Makarov², and Siegfried Selberherr²

¹*Christian Doppler Laboratory for Nonvolatile Magnetoresistive Memory and Logic at the*

²*Institute for Microelectronics, TU Wien, Gußhausstraße 27-29, 1040 Vienna, Austria
Selberherr@TUWien.ac.at*

The spin-orbit torque magnetic random access memory (SOT-MRAM) combines non-volatility, high speed, and high endurance. It is suitable for applications in caches to mitigate the increase of dissipated power and to facilitate instant-on architectures. However, its development is still hindered by the need of an external magnetic field for deterministic switching of perpendicular magnetic layers [1]. We demonstrate that the switching scheme by means of two orthogonal current pulses previously suggested for in-plane structures [2] allows achieving deterministic, fast (sub-500ps), and magnetic field-free switching in perpendicular free magnetic layers of rectangular shape [3].

A perpendicularly magnetized free layer of the dimensions $52.5 \times 12.5 \times 2 \text{ nm}^3$ is grown on top of a heavy metal wire NM1 of 3nm thickness (Fig.1). A NM2 wire with a non-complete overlap from the right side of the free layer serves to apply the second perpendicular current pulse and the spin-orbit torque associated with it. First, a 100ps short and $100 \mu\text{A}$ strong current pulse is applied through NM1 (Fig.1). The consecutive perpendicular current pulse of varying strength and duration is applied through NM2. The time dependent magnetization dynamics for 20 realizations is shown in Fig.2. Although the NM2 current is large (1mA), it does not provide a deterministic switching as it only orients the magnetization in-plane. However, when the current is decreased to $200 \mu\text{A}$, the switching becomes deterministic, for all 20 realizations (Fig.3). If the current of the “Write pulse 2” is further reduced to the value of that in the “Write pulse 1”, the switching becomes unreliable (Fig.4). However, if the width of NM2 is reduced to 12.5nm (width of NM1), the switching becomes deterministic again (Fig.5). Fig.6 shows the dependence of the switching time on the NM2 width, for several durations of “Write pulse 2”. Importantly, for NM2 widths around 12nm the switching is not only fast, but also not very sensitive to the width and pulse duration fluctuations.

[1] S. Fukami et al., *Nature Nanotechnol.* **11**, 621 (2016)

[2] A. Makarov et al., *Semicond. Sci. Technol.* **41**, 113006 (2016)

[3] V. Sverdlov et al., *Solid-State Electron.*, submitted (2018)

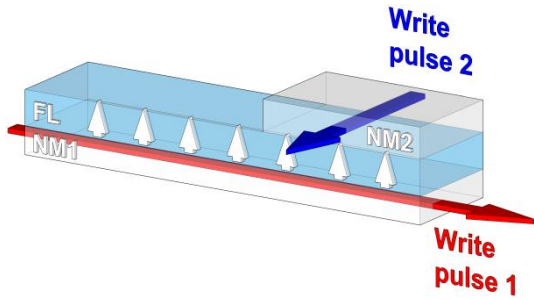


Fig.1: Perpendicular SOT-MRAM memory cell with a $52.5\text{nm} \times 12.5\text{nm} \times 2\text{nm}$ free layer. After the $100\text{ps}/100\mu\text{A}$ current pulse the second perpendicular pulse is applied.

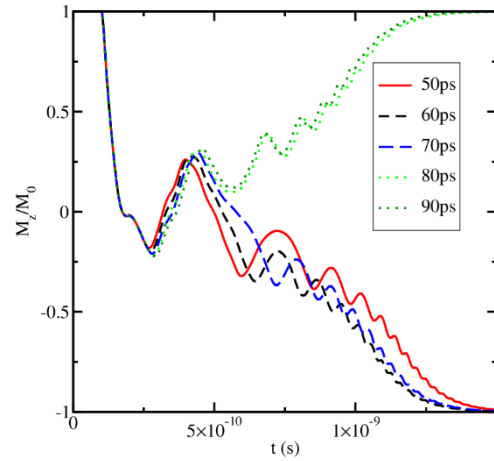


Fig.4: Randomly chosen realizations for a current of $100\mu\text{A}$ in the second pulse, for several pulse durations. Surprisingly, the switching fails for longer pulses. NM2 has a complete overlap with FL.

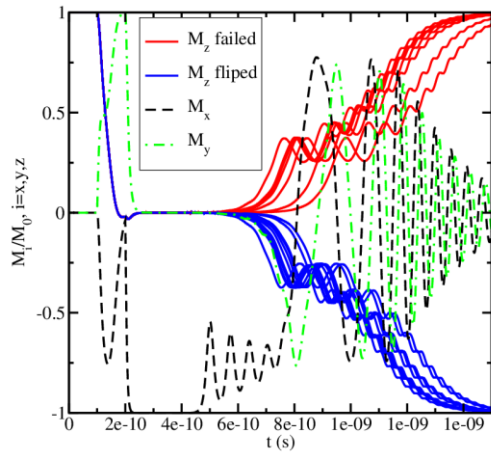


Fig.2: Time evolution of the magnetization in two-pulse switching (second pulse $1\text{mA}/200\text{ps}$). 20 different switching realizations obtained after 100ps initial thermalization are shown.

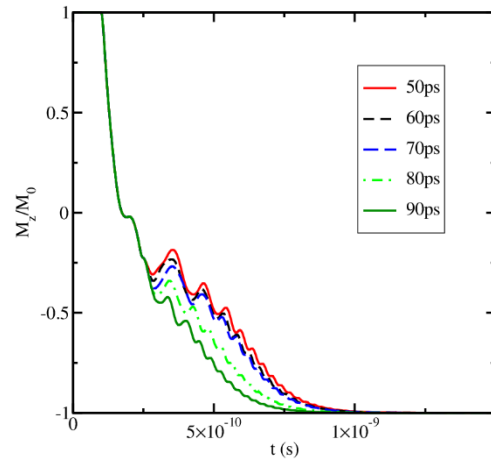


Fig.5: For equal wires NM1 and NM2 (NM2 has a partial overlap) and equal currents of $100\mu\text{A}$ the switching becomes fast and deterministic.

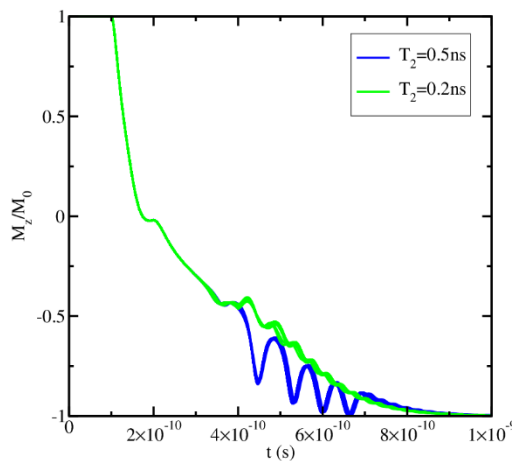


Fig.3: The current in the second pulse is $200\mu\text{A}$. All 20 realizations switch evenly, almost without dispersion. The switching is deterministic. NM2 overlaps fully with FL.

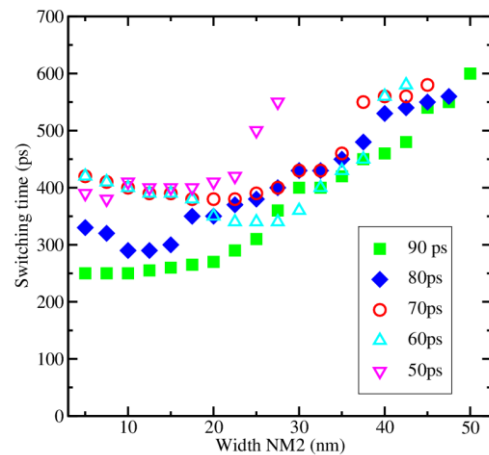


Fig.6: The switching time as a function of the NM2 width. The NM2 width of 12.5nm is optimal as it guarantees fast, robust, and deterministic switching.

Magnetic Anisotropy of KNiF₃ Single Crystals Investigated by Torque Magnetometry

Zhu Diao^{1,2,3}, Kexin Yang⁴, and David G. Cahill¹

¹*Department of Materials Science and Engineering,
Frederick Seitz Materials Research Laboratory, University of Illinois at Urbana-Champaign,
104 South Goodwin, Urbana, Illinois 61801, USA*

²*Department of Physics, Stockholm University, SE-106 91 Stockholm, Sweden*

³*School of Information Technology, Halmstad University, P.O. Box 823,
SE-301 18 Halmstad, Sweden*

⁴*Department of Physics, University of Illinois at Urbana-Champaign,
Urbana, Illinois 61801, USA*

zdiao@illinois.edu

Magnetic properties and magnetization dynamics of antiferromagnets have received renewed interest in light of recent developments in antiferromagnetic spintronics. Perovskite KNiF₃ is a prototypical 3D Heisenberg antiferromagnetic insulator, which largely retains its room-temperature cubic symmetry in the low-temperature antiferromagnetic state. Its weak anisotropy field leads to a low antiferromagnetic resonance (AFMR) frequency of < 100 GHz [1], which ought to be accessible by cutting-edge microwave technology. In order to predict the AFMR response and its evolution with temperature, a precise knowledge of the magnetic anisotropy is required.

In this work, we carry out variable temperature torque magnetometry studies of the magnetic anisotropy of KNiF₃ single crystals. Experiments are performed using the torque magnetometry option of a Quantum Design Physical Property Measurement System with an applied magnetic field up to 9 T. Fourier analysis of the torque curves (Fig.1 and 2) allows us to identify two leading anisotropy terms when the crystals are in the antiferromagnetic state. One is a two-fold symmetry term which is extremely sensitive to the sample mounting method and the thermal history. We find it to be primarily of external origin and associated with the thermal stress between the sample and the torque magnetometer paddle. Another is a four-fold symmetry term which can be related to the inherent magnetocrystalline anisotropy of the crystal and reversible antiferromagnetic domain wall movements under a rotating external field. At 4 K, the magnitudes of both terms are in the order of 40 N·m⁻² under high fields. They decrease with temperature, and disappear at ~250 K, the Néel temperature of KNiF₃.

[1] H. Yamaguchi et al., Phys. Rev. B **59**, 6021 (1999)

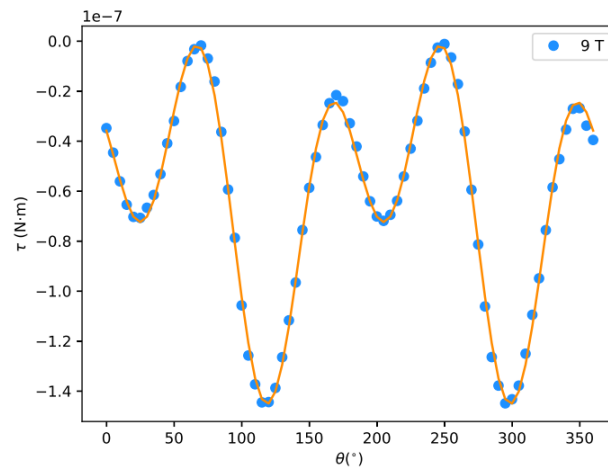


Fig.1: Magnetic torque curve of a 4 mg KNiF₃ single crystal measured at $T = 4$ K under an applied field of 9 T. Filled circles represent the experimental data while the orange curve is the best fit to the data using a two-fold term and a four-fold symmetry term.

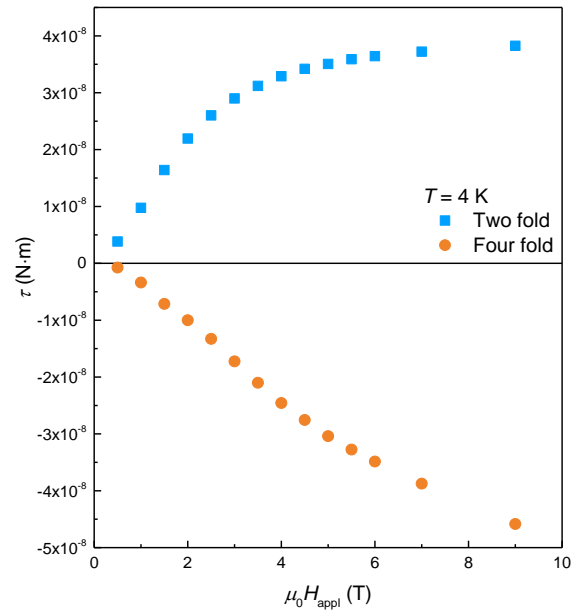


Fig.2: Evolution of the leading Fourier components obtained from fitting the torque curves as a function of applied magnetic field ($T = 4$ K).

Zero-Eigenvalue Method for Solving the Barker-Ferry Equation in One-Dimensional Systems

Shintaro Makihira¹ and Nobuya Mori¹

¹*Division of Electrical, Electronic and Information Engineering,
Graduate School of Engineering, Osaka University,
Suita, Osaka 565-0871, Japan
{makihira, mori}@si.eei.eng.osaka-u.ac.jp*

Widegap semiconductors, such as SiC, GaN, and C, are attractive materials for next generation power devices because of their high breakdown fields, of the order of MV/cm. Under high electric fields, quantum effects, such as intra-collisional field effect (ICFE) and collisional broadening (CB), are expected to play an important role. The Baker-Ferry equation (BFE) [1] can handle such quantum effects, and various attempts have been made to solve BFE, for example, by approximating a term related to the energy conservation law to a simple analytical formula, such as a Lorentzian function [2, 3]. In the present study, we adopt a zero-eigenvalue method and solve BFE in a simple one-dimensional (1D) system.

We consider a 1D system under a constant electric field F . We assume a simple cosine band of the form $E(k) = (\hbar^2/a^2m)(1 - \cos ka)$ with the electron effective mass $m = 0.2m_0$ and the lattice constant $a = 0.5 \text{ \AA}$. We discretize BFE in (k, t) -space with k -space grid size Δk and t -space grid size Δt . When the relation of $\Delta k = (eF/\hbar)\Delta t$ is satisfied, BFE is mapped onto a zero-eigenvalue problem. In the present study, we consider optical-phonon scattering with a constant electron-phonon interaction matrix element and a constant phonon energy $\hbar\omega_0 = 100 \text{ meV}$

Figure 1 shows the distribution function $f(E)$ calculated by BFE compared with that calculated by the Boltzmann transport equation (BTE). For both BFE and BTE, we include CB with a constant electron life time $\tau_T = 10 \text{ fs}$. We find that electrons are more widely distributed over the entire Brillouin zone when we include ICFE, which results in a significant drift-velocity reduction by ICFE (see Figs. 2 and 3 in which we compare drift-velocities calculated with BFE and BTE).

[1] J. R. Barker and D. K. Ferry, Phys. Rev. Lett. **42**, 1779 (1979)

[2] D. K. Ferry and J. R. Barker, J. Phys. Chem. Solids. **41**, 1083 (1980)

[3] L. Reggiani et al., J. Appl. Phys. **64**, 3072 (1988)

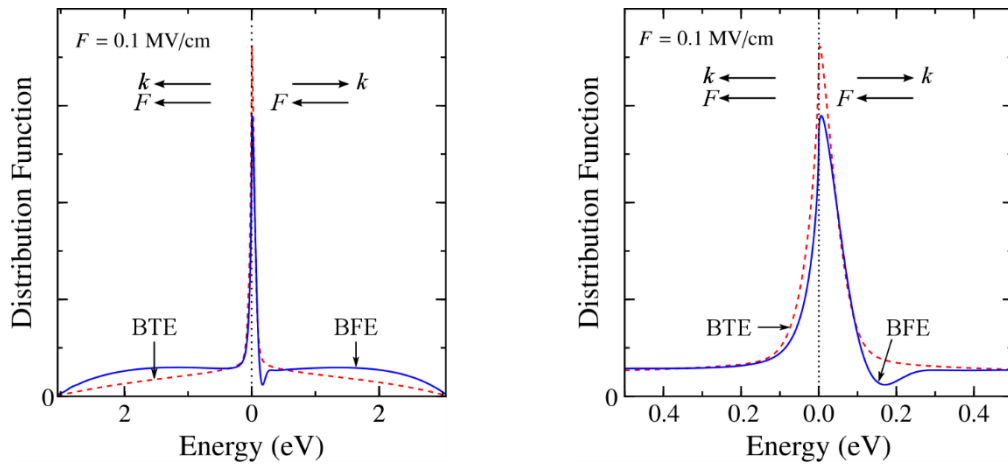


Fig.1: Distribution function $f(E)$ at $F = 0.1$ MV/cm plotted in the entire energy space (left) and a smaller energy region (right) for $\Delta t = (\hbar/eF)\Delta k = 0.04$ fs. Solid line shows $f(E)$ calculated by the Barker-Ferry equation (BFE) with the intra-collisional field effect (ICFE) and dashed line by the Boltzmann transport equation (BTE) without ICFE.

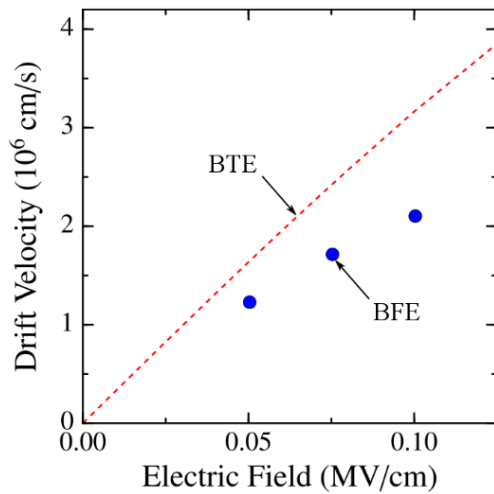


Fig.2: Drift-velocity calculated by BFE (solid circles) compared with that calculated by BTE (dashed line) for $\Delta t = (\hbar/eF)\Delta k = 0.04$ fs.

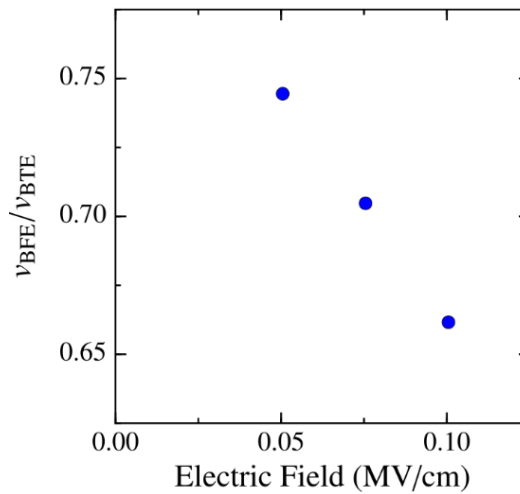


Fig.3: Drift-velocity ratio, $v_{\text{BFE}}/v_{\text{BTE}}$, as a function of electric field F . v_{BFE} (v_{BTE}) is the drift-velocity calculated by BFE (BTE).

Low-Temperature Growth for 3D Integration of 2D Materials

Christopher L. Hinkle¹

*Department of Electrical Engineering,
University of Notre Dame, Notre Dame, IN 46556, USA
chinkle@nd.edu*

The integration of novel logic and memory devices, fabricated from van der Waals materials, into CMOS process flows with a goal of improving system-level Energy-Delay-Product (EDP) for data abundant applications will be discussed. Focusing on materials growth and integration techniques that utilize non-equilibrium, kinetically restricted strategies, coupled with in-situ characterization, enables the realization of atomic configurations and materials that are challenging to make but once attained, display enhanced and unique properties. These strategies become necessary for most future technologies where thermal budgets are constrained and conformal growth over selective areas and 3-dimensional structures are required.

In this work, we demonstrate the high-quality MBE heterostructure growth of various layered 2D materials by van der Waals epitaxy (VDWE). The coupling of different types of van der Waals materials including transition metal dichalcogenide thin films (e.g., WSe₂, WTe₂, HfSe₂), helical Te thin films, and topological insulators (e.g., Bi₂Se₃) allows for the fabrication of novel electronic devices that take advantage of unique quantum confinement and spin-based characteristics. We demonstrate how the van der Waals interactions allow for heteroepitaxy of significantly lattice-mismatched materials without strain or misfit dislocations. Yet, at the same time, the VDW interactions are strong enough to cause rotational alignment between the epi-layer and the substrate, which plays a key role in the formation of grain boundaries. We will discuss TMDs, Te, and TIs grown on atomic layer deposited (ALD) high-k oxides on a Si platform as well as flexible substrates and demonstrate field-effect transistors with back-end-of-line compatible fabrication temperatures (<450 °C). High performance transistors with field-effect mobilities as high as 700 cm²/V-s are demonstrated. The achievement of high-mobility transistor channels at BEOL compatible processing temperatures shows the potential for integrating van der Waals materials into CMOS process flows.

Acknowledgments: This work is supported in part by NEWLIMITS, a center in nCORE, a Semiconductor Research Corporation (SRC) program sponsored by NIST through award number 70NANB17H041. This work is also supported by the National Science Foundation under award 1802166.

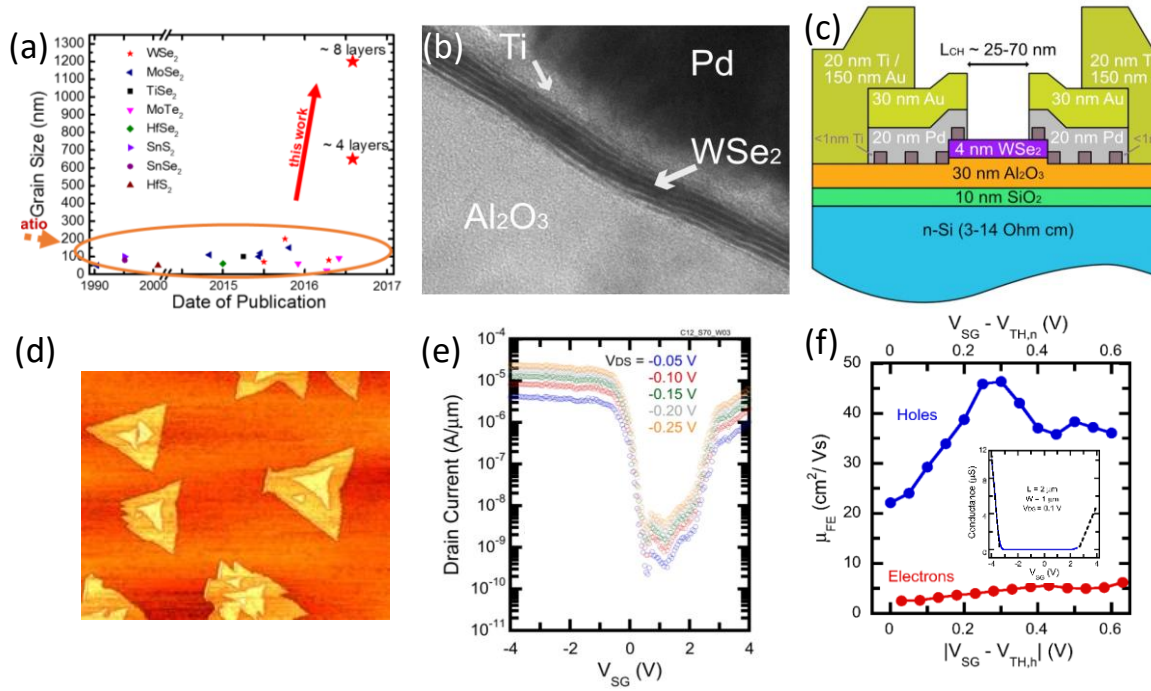


Fig.1: Grain size improvement through low-temperature growth ($\sim 500^\circ\text{C}$), with beam interruption enables the growth on ALD amorphous oxides. Ambipolar transport in WSe_2 grown on ALD Al_2O_3 exhibits excellent hole conduction.

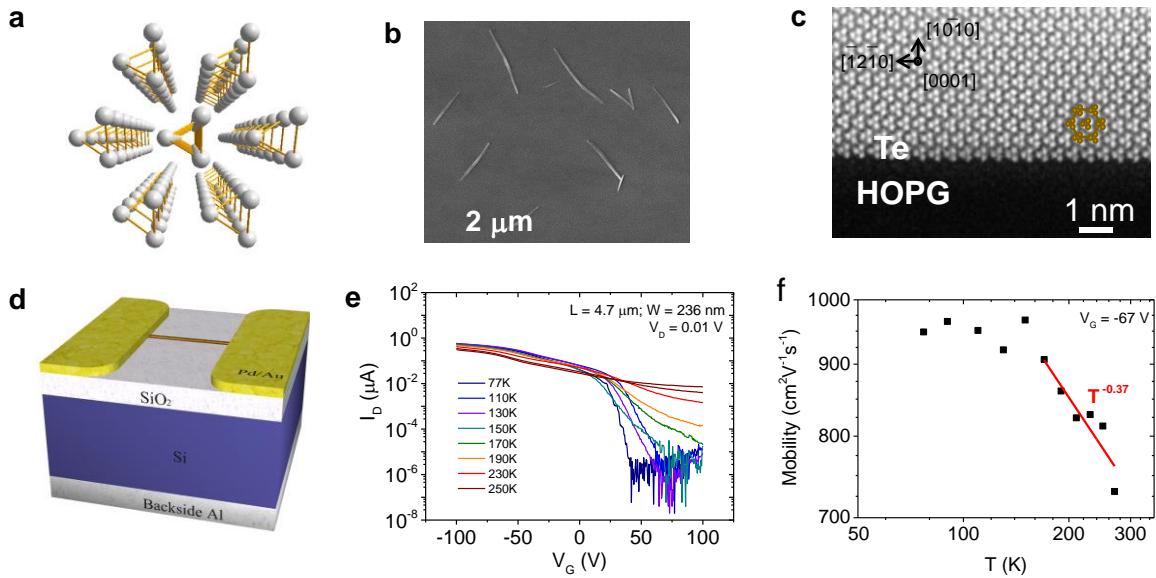


Fig.2: Helical tellurium grown at 120°C on SiO_2 exhibits outstanding room-temperature field-effect mobilities greater than $700\text{ cm}^2/\text{V}\cdot\text{s}$.

Quantum-Limited Monolayer MoS₂ pH and Biosensors

Curt A. Richter¹, Son T. Le^{1,2}, Niranjana D. Amin³, Harish C. Pant³, and Arvind Balijepalli¹

¹*Engineering Physics Division, National Institute of Standards and Technology,
Gaithersburg, MD 20899, USA*

²*Theiss Research, La Jolla, CA 92037, USA*

³*National Institute of Neurological Disorders and Stroke, National Institutes of Health,
Bethesda, MD 20892, USA*

curt.richter@NIST.gov

We have developed sensors based on dual-gated field-effect transistors (FETs) operating at the quantum capacitance limit that allow ultrasensitive pH measurements for biophysics applications. The FETs are fabricated with single-monolayer 2D transition metal dichalcogenide semiconducting films and are top-gated with an ionic-liquid. The high ionic liquid polarizability allows strong coupling between the top gate (ionic liquid) and a back-gate dielectric (substrate oxide) which enables amplification of a voltage applied to the ionic liquid gate by up to 200X. This amplification is limited by the intrinsic quantum capacitance of the single-monolayer MoS₂ semiconducting channel; thus, the devices operate near their theoretical limits. We leveraged the high performance of the devices to enable pH measurements with sensitivities that greatly exceed the Nernst value of 59 mV/pH (at room temperature). The dramatically improved sensitivity allows the detection of pH changes as small as 0.003 which facilitates measurements of activity and kinetics during biological processes such as enzyme catalyzed phosphorylation of substrate proteins.

Accurate and rapid measurements of enzyme activity are critical to the development of therapeutics that target neurological disorders. The super-Nerstian pH measurements enabled by the ionic-liquid gated 2D transistors allow the rapid and quantitative estimation of the kinetics of enzymes that are implicated in Alzheimer's disease. For example, we have demonstrated the ability of ionic-liquid-gated FETs to detect small changes in the solution pH during phosphorylation of the substrate protein, histone H1. We compared these FET measurements against enzyme activity measurements obtained from a radioactively labeled γ -³²P-ATP assay (which involves handling radioactive materials and is slow to perform). The FET-based measurements are in excellent quantitative agreement with this existing technique (Fig. 4), while enabling results in minutes to allow rapid therapeutic screening.

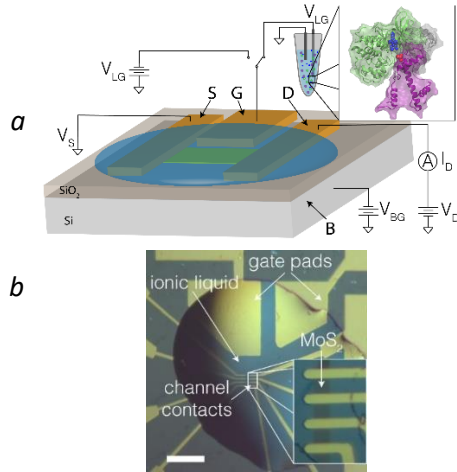


Fig.1: Ionic liquid-gated FETs for biosensing. (a) Device schematic of an ionic liquid-gated FET for biosensing. A channel formed between the source (S) and drain (D) terminals is controlled electrostatically by a voltage applied to the silicon substrate (B) or the ionic liquid top-gate (G). A voltage applied to the ionic liquid-gate (V_{LG}) can be switched between a voltage source for characterization or a biosensing element. (b) An array of ionic liquid dual-gate FETs fabricated using a 2D MoS_2 film on a 300 nm SiO_2 substrate. The scale bar represents 100 μm .

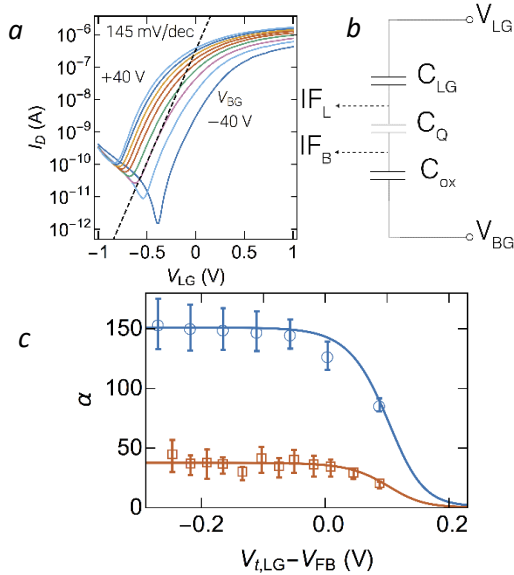


Fig 2: Transfer characteristics show the drain current (I_D) as a function of V_{LG} and varying back-gate voltage (V_{BG}). (b) The dual-gated FET was modeled with three capacitors in series. The quantum capacitance (C_Q) of the 2D channel controls the capacitive coupling between the back (I_{FB}) and liquid (I_{FL}) gate interfaces. (f) A plot of α as a function of V_{LLG} for two devices with back-gate oxide thickness of 300 nm and 70 nm. The solid line shows the theoretical model for quantum capacitance limited device performance. $V_{FB} = -0.82$ V ($d=300$ nm) and $V_{FB} = +0.12$ V ($d=70$ nm) were subtracted from V_{LLG} to allow direct comparison of the devices.

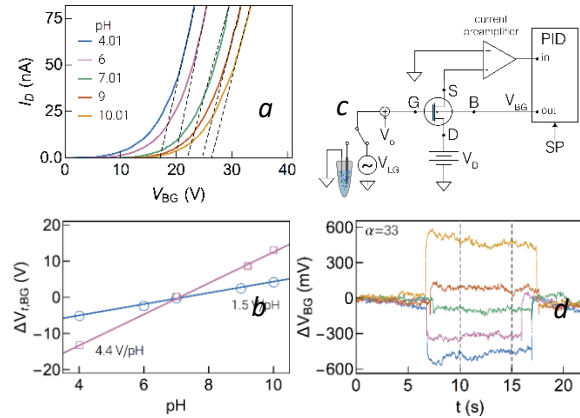


Fig.3: (a) The FETs were used in a constant current mode by using a proportional-integral-derivative (PID) controller. I_D was held constant in response to small changes to V_{LG} . Measurements of pH were performed by connecting the ionic liquid-gate (G) to a sensing element. (b) Shift in the back-gate threshold voltage ($\Delta V_{L,BG}$) as measured when the ionic liquid-gate was used to sense the pH of a buffered electrolyte solution. (c) $\Delta V_{L,BG}$ as a function of the solution pH. (d) Time-series measurements of the back-gate voltage (V_{BG}) response to buffered pH solutions.

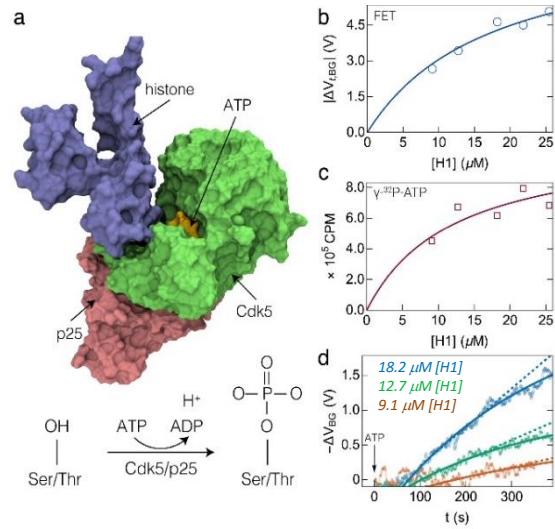


Fig. 4: Ionic liquid-gate FETs for label-free enzyme activity and kinetics measurements. (a) The proline directed kinase Cdk5 catalyzes the phosphorylation of substrate proteins (e.g., histone H1) in the presence of an activator (e.g., p25) and adenosine triphosphate (ATP). The hydrolysis of ATP results in a change in solution pH. (b) Ionic liquid-gate FETs ($\alpha=159$) were used to measure the change in solution pH as a function of the histone H1 concentration ([H1]). (c) The FET measurements are in agreement with an assay that used radioactively labeled γ - ^{32}P -ATP as a reporter of Cdk5 activity. (d) Time-series measurements of enzyme catalyzed phosphorylation as a function of [H1] allow the direct estimation of the reaction dynamics.

Double Indirect Interlayer Exciton in a MoSe₂/WSe₂ van der Waals Heterostructure

Aubrey T. Hanbicki¹, Hsun-Jen Chuang^{1, a}, Matthew R. Rosenberger^{1, b}, C. Stephen Hellberg¹,
Saujan V. Sivaram^{1, c}, Kathleen M. McCreary¹, I.I. Mazin¹, and Berend T. Jonker¹

¹*Materials Science & Technology Division, Naval Research Laboratory,
Washington DC 20375, USA*

^a*Postdoctoral associate at NRL through the American Society for Engineering Education*

^b*Postdoctoral associate at NRL through the National Research Council
berry.jonker@nrl.navy.mil*

An emerging class of semiconductor heterostructures involves stacking discrete monolayers such as the transition metal dichalcogenides (TMDs) to form van der Waals heterostructures. In these structures, it is possible to create interlayer excitons (ILEs), spatially indirect, bound electron-hole pairs with the electron in one TMD layer and the hole in an adjacent layer. We are able to clearly resolve two distinct emission peaks separated by 24 meV from an ILE in a MoSe₂/WSe₂ heterostructure [1] fabricated using state-of-the-art preparation techniques [2]. These peaks have nearly equal intensity, indicating they are of common character, and have opposite circular polarizations when excited with circularly polarized light. Ab initio calculations successfully account for these observations – they show that both emission features originate from excitonic transitions that are indirect in momentum space and are split by spin-orbit coupling. Also, the electron is strongly hybridized between both the MoSe₂ and WSe₂ layers, with significant weight in both layers, contrary to the commonly assumed model. Thus, the transitions are not purely interlayer in character. This work represents a significant advance in our understanding of the static and dynamic properties of TMD heterostructures.

[1] A.T. Hanbicki et al., ACS Nano **12**, 4719 (2018)

[2] M.R. Rosenberger et al., ACS Appl. Mater. Interfaces **10**, 10379 (2018)

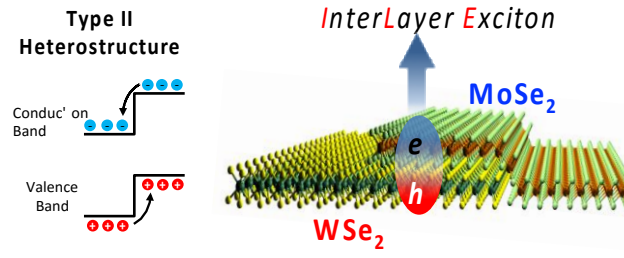


Fig.1: Schematics of band alignments and sample structure showing formation of ILE.

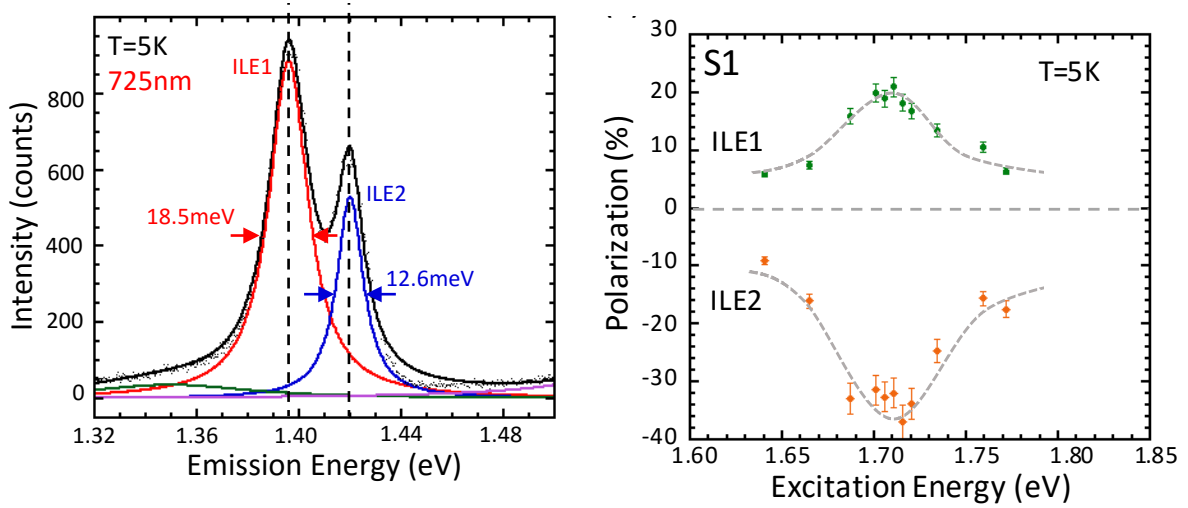


Fig.2: Circularly polarized photoluminescence from ILE, and polarization vs pump energy.

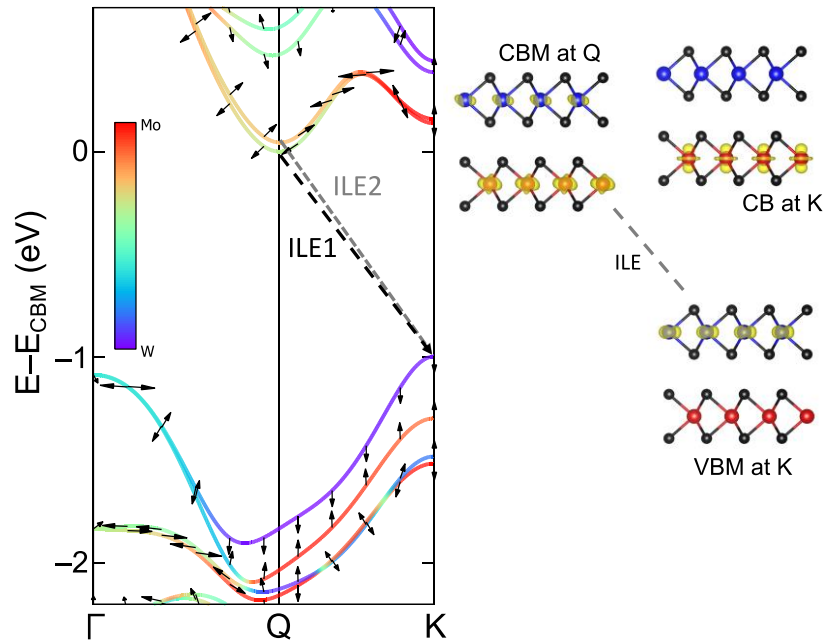


Fig.3: Band structure showing origin of the 2 components of the ILE, and electron hybridization.

Quantum Transport in a Magnetic Semiconductor Oxide

Masashi Kawasaki^{1,2}, Kei. S. Takahashi¹, Kazuki Maruhashi², Mohammad Saeed Baharamy^{1,2}, Hiroaki Ishizuka², Ryosuke Kurihara³, Atsushi Miyake³, Sunao Shimizu¹, Tomoki Murata², Qing Y. Wang¹, Masashi Tokunaga³, Yoshinori Tokura^{1,2}, and Naoto Nagaosa^{1,2}

¹*RIKEN Center for Emergent Matter Science (CMES), Wako, 351-0198, Japan*

²*Department of Applied Physics and Quantum-Phase Electronics Center (QPEC), University of Tokyo, Tokyo, 113-8656, Japan*

³*Institute for Solid State Physics, University of Tokyo, Kashiwa, 277-8581, Japan*
m.kawasaki@riken.jp

EuTiO₃ (ETO) is a magnetic semiconductor, in which 4f⁷ moment on Eu²⁺ site orders in G-type antiferromagnet below 5.5 K and transforms into ferromagnet under a magnetic field above 3T. Electron carriers are readily doped in Ti t_{2g} conduction band by the substitution of Eu²⁺ with La³⁺. A decade ago, we examined the anomalous Hall effect (AHE) in ETO to find that the AHE changes its sign depending on the Fermi level position relative to the band crossing point [1] for low mobility (30 cm²/Vs) films grown by pulsed laser deposition. By developing a metalorganic gas source molecular beam epitaxy (MOMBE) at very high substrate temperature, the quality of oxide films has been dramatically enhanced to materialize the high electron mobility (20,000 cm²/Vs) quantum well system of La-doped SrTiO₃ (STO) that can host quantum Hall effect [2]. We have extended the synthesis to compressively strained EuTiO₃ films (300 cm²/Vs) by MOMBE to observe novel Hall effect arising from magnetic monopole at the Wyle nodes created by crystal-field and Zeeman splittings of Ti 3d bands [3].

We now discuss the transport properties of 100nm thick ETO films grown on lattice-matched STO substrates by the MOMBE. Despite there are two unfavorable conditions compared with STO case, magnetic moment on Eu site and absence of quantum paraelectricity, the electron mobility exceeds 3,000 cm²/Vs at 2 K, Shubnikov–de Haas (SdH) oscillations being clearly observable in high magnetic field. This quantum transport provides opportunities to discuss the detailed band structures with taking into account the Zeeman splitting and exchange coupling between Eu 4f and Ti 3d electrons.

[1] K.S. Takahashi et al., Phys. Rev. Lett. **103**, 057204 (2009)

[2] Y. Matsubara et al., Nat. Commun. **7**, 11631 (2016)

[3] K.S. Takahashi et al., Sci. Adv. **4**, eaar7880 (2018)

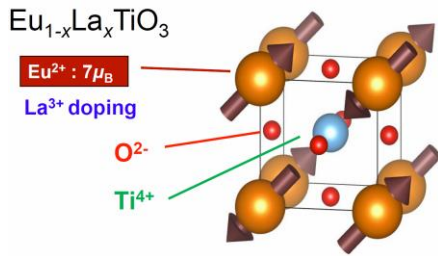


Fig.1: Crystal structure of perovskite EuTiO_3 with antiferromagnetic ordering of Eu 4f moments.

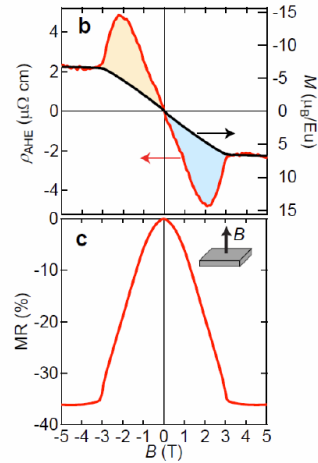


Fig.4: Top: anomalous Hall effect (red) and magnetization (black), and bottom: magnetoresistance [3] for a strained EuTiO_3 film.

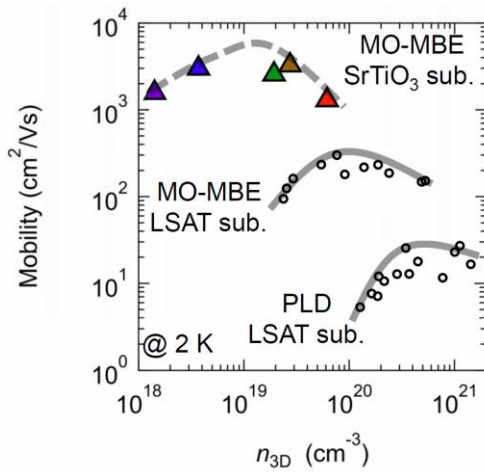


Fig.2: Electron mobility as a function of density for three generations of EuTiO_3 films [1, 3].

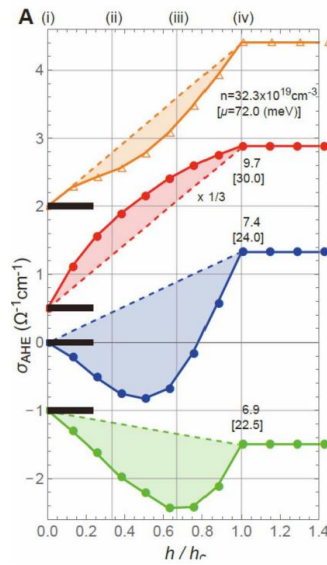


Fig.5: Theoretically revealed anomalous Hall effect as a function of electron density [3].

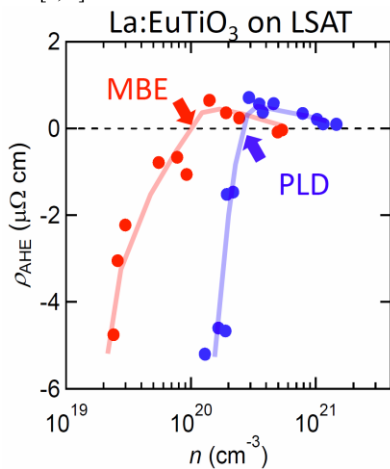


Fig.3: Anomalous Hall effect in strained EuTiO_3 films showing sign reversal at certain electron densities [1, 3].

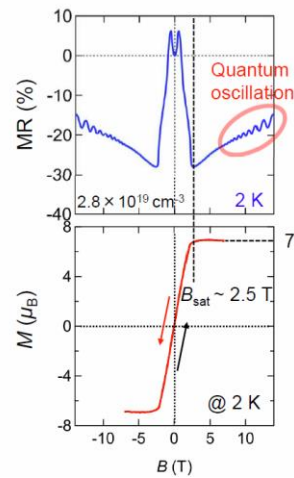


Fig.6: Top: magnetoresistance and bottom: magnetization for an unstrained EuTiO_3 film grown on SrTiO_3 .

Magnetism in Monolayer Transition Metal Dichalcogenides

Manuel Bonilla¹, Paula Coelho Neto¹, Sadhu Kolekar¹, Vijaysankar Kalappattil¹,
Manh-Huong Phan¹, and Matthias Batzill¹

¹*Department of Physics, University of South Florida, Tampa, FL 33620, USA*
mbatzill@usf.edu

Van der Waals heterostructures hold the promise of combining materials with only weak interlayer interaction. This could allow integration of materials with diverse properties and minimize the influences of chemical interface interactions on materials and device properties. Of particular interest would be the integration of magnetic materials in such van der Waals heterostructures. Although it has been recently demonstrated that ferromagnetism may be preserved down to the monolayer limit [1], there exists no known layered van der Waals material with Curie temperatures close to room temperature-- which is a pre-requisite for most applications. Thus there has been excitement by theoretical (DFT) predictions of high Curie temperature ferromagnetism in monolayer materials such as VSe₂ [2], a material that is known to be paramagnetic in bulk-form. In addition, there exist increasing evidence of dilute magnetic semiconductors (DMS) in van der Waals materials. In this presentation, we illustrate direct growth of VSe₂ monolayers on van der Waals substrates (Fig. 1) and demonstrate that these (sub)monolayers indeed exhibit ferromagnetic properties to above room temperature [3] while multilayers exhibit strongly suppressed magnetization (Fig. 2). Recent angle resolved photoemission spectroscopy (ARPES) characterization, however, indicate that VSe₂ monolayers do not exhibit spin-split bands as predicted by DFT. In this talk we discuss possible alternative explanations to the predicted band magnetism for (sub)monolayer VSe₂. Moreover, we show evidence for magnetic coupling between monolayer VSe₂ and a van der Waals substrate, which gives rise to an exchange bias that can be measured by magnetometry (Fig. 3). Finally, we discuss an alternative approach to induce magnetism in 2D materials. Specifically, we show the formation of DMS by incorporation of magnetic impurities by a novel doping mechanism in MoTe₂ (Fig. 4).

[1] C. Gong et al., Nature **546**, 265 (2017); B. Huang et al., Nature **546**, 270 (2017)

[2] Y. Ma et al., ACS Nano **6**, 1695 (2012)

[3] M. Bonilla et al. Nat. Nanotechnol. **13**, 289 (2018)

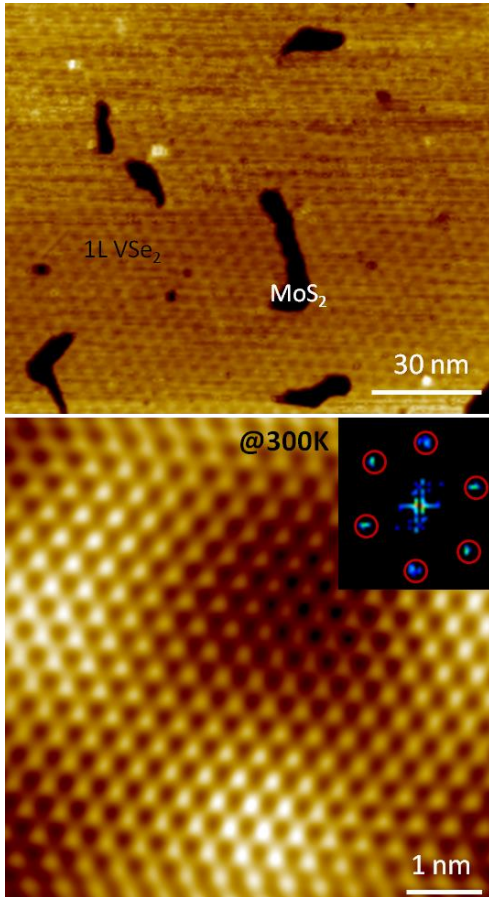


Fig.1: Scanning tunneling microscopy image of almost complete monolayer VSe₂ grown by molecular beam epitaxy on a MoS₂ substrate. A moiré-superstructure is shown in (a) and (b) shows an atomic resolution image.

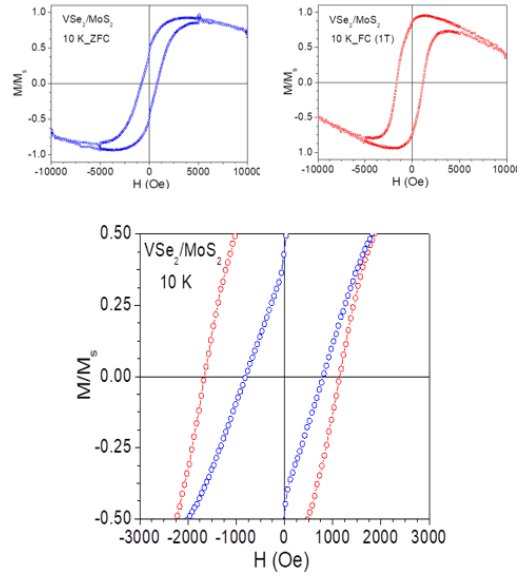


Fig.3: Difference in zero field cooled and field cooled samples shows evidence for exchange bias in monolayer VSe₂ on MoS₂ substrates.

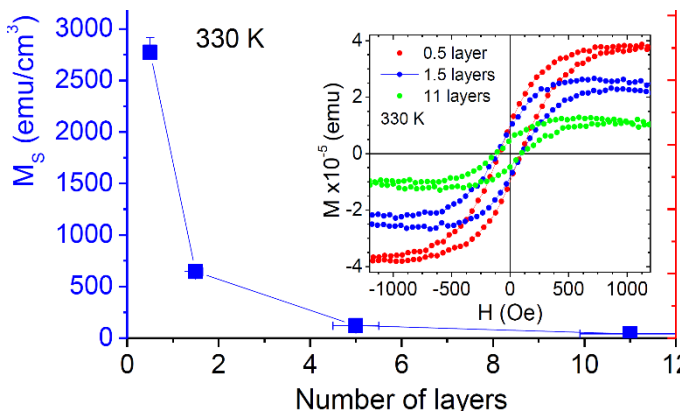


Fig.2: Saturation magnetization of VSe₂ as a function of VSe₂ layers. Only (sub)monolayer VSe₂ exhibits strong magnetization,

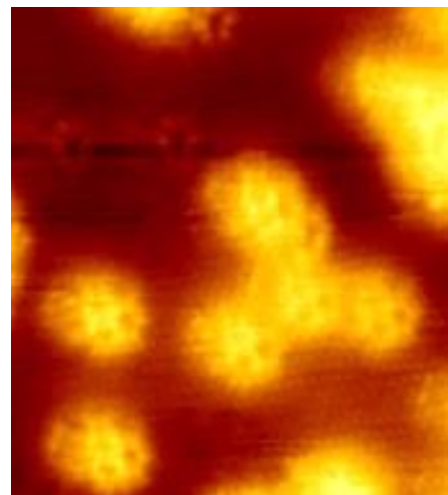


Fig.4: STM images of individual V-dopants in MoTe₂ as the origin for formation of DMS.

Enabling Optically Forbidden Transitions by Extreme Localization of Light

Hayk Harutyunyan¹, Alexander Govorov², Gary Wiederrecht³, and Stephen K. Gray³

¹*Emory University, Department of Physics, Atlanta, GA 30322, USA*

²*Department of Physics and Astronomy, Ohio University, Athens, OH 45701, USA*

³*Center for Nanoscale Materials, Argonne National Laboratory, Lemont, IL 60439, USA*

hayk.harutyunyan@emory.edu

In bulk materials, optical properties and electronic transitions are thought to be fully determined by the electronic band structure. The ability to tune these material properties enables novel functionalities in optical and photonic applications. In the quest to achieve controllable modification of the optical properties of materials, the most widely used approach is the engineering of their electronic structure. This is typically achieved by nanoscale manipulation of material structure and composition which in turn control the electronic transitions and electronic states. Thus our ability to control the optical properties of materials are typically limited by the choice of the constituent materials.

One additional parameter that can affect the nature of photo-assisted electronic transitions is the photon momentum. Typically, the momentum of the free-space photon is negligibly small compared to electron momenta which results in “near-vertical” electronic transitions with no change in momentum [1]. Extreme, nanometer-scale localization of electromagnetic fields can fundamentally change this picture by breaking the translational symmetry. In this talk we will discuss this idea by exploring nanometer-scale light confinement using plasmonic structures. Real-space confinement results in large field wavevectors in the momentum-space leads to the breakdown of the dipole approximation, thus opening up new pathways for plasmon-assisted optical transitions in materials. By effectively creating “large momentum photons” using our plasmonic/dielectric nano-architectures and metamaterials we achieve novel “non-vertical” electronic transitions in materials (Fig. 1). Number of forbidden electronic transitions will be discussed including intraband free carrier absorption in noble metals and interband transitions in Si. We will show that lifting the selection rules that forbid these transitions can lead to novel physical phenomena ranging from efficient hot carrier generation (Fig. 2) to ultrafast femtosecond-scale nonlinear modulation of the optical signal with large amplitudes [2].

[1] H. Harutyunyan et al., *Nature Nanotechnol.* **10**, 770 (2015)

[2] T. Heilpern et al., *Nature Commun.* **9**, 1853 (2018)

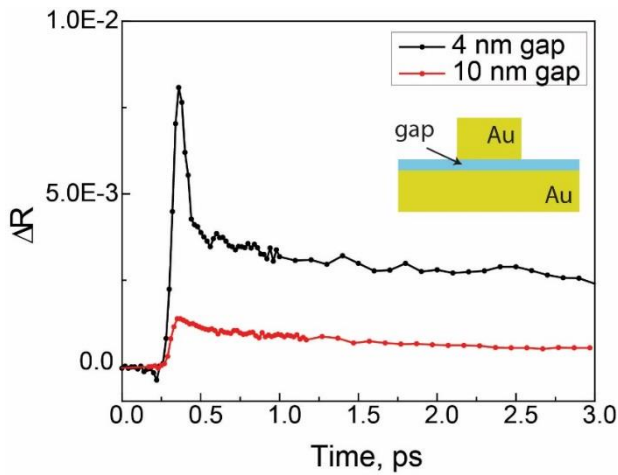


Fig.1: Time dynamics of the plasmon peak with pump at the plasmon resonance. When the mode confinement is strong (black curve), pump-probe signal exhibits fs decay component due to efficiently generated hot electron decay. For large gaps only a ps component is present (red curve) indicating that the excited electrons are close to the Fermi level. Inset: schematics of the plasmonic sample with a nanometric gap.

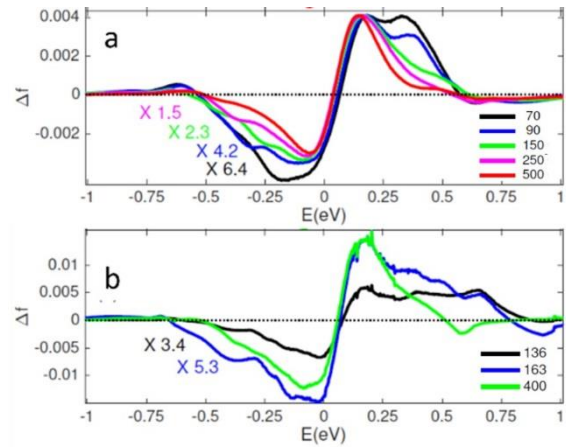


Fig.2: Change in electron occupancy relative to Fermi energy after photoexcitation in a 30 nm Au lm a) at normal incidence, b) at Kretschmann angle. The time delays (fs) for each curve are shown in the insets..

Spintronics Beyond Magnetoresistance: From Spin-LEDs to Spin-Lasers

Igor Žutić¹

¹*Department of Physics, University at Buffalo, State University of New York,
Buffalo, NY 14216, USA
zigor@buffalo.edu*

Practical room-temperature spintronic devices are typically limited to magnetoresistive effects, successfully employed for magnetically storing and sensing information [1]. Injecting spin-polarized carriers into semiconductor LEDs and lasers offers different operating principles: the conservation of angular momentum and spin-orbit coupling leads to the transfer of angular momentum from spin-polarized carriers to emitted circularly polarized light [1-4]. Since electron spin in semiconductors preserves its orientation at times up to ~ns and lengths up to ~ μm , with this carrier-photon spin conversion the spin information can be transferred at much greater distances and sustained over much longer times. While spin-LEDs and spin-lasers have been known for 20 years, breakthroughs in the last few years reveal intriguing opportunities in their nonlinear response. In spin-LEDs pure circularly polarized electroluminescence and electrical switching of helicity was demonstrated at 300 K with Fe-based spin injectors [3], supporting applications from secure optical communication to cancer detection. While spin-lasers usually rely on optical spin injection, advances in ferro- magnets with perpendicular anisotropy suggest paths to robust room temperature electrical spin injection in external cavity lasers [4]. The key opportunity for spin-lasers pertains to their dynamical operation, requiring detailed understanding of their polarization dynamics and optical anisotropy [5,6]. Recent experiments on ultrafast spin-lasers support a novel path to optical communication: they could operate at an order of magnitude higher frequencies than in the state-of-the art conventional lasers, while requiring only about one tenth of their power consumption [7]. Surprisingly, this operation is enabled by short spin relaxation times and large optical anisotropies, typically considered detrimental in spintronics and lasers.

- [1] I. Žutić et al., *Rev. Mod. Phys.* **76**, 323 (2004)
- [2] I. Žutić and P. E. Faria Junior, *Nat. Nanotechnol.* **9**, 750 (2014)
- [3] N. Nishizawa et al., *Proc. Natl. Acad. Sci. USA* **114**, 1783 (2017)
- [4] J. Fougier et al., *Opt. Express* **23**, 229241 (2015)
- [5] M. Alouini et al., *Opt. Express* **26**, 6739 (2018)
- [6] P. E. Faria Junior et al., *Phys. Rev. B* **92**, 075311 (2015)
- [7] M. Lindemann et al., arXiv:1807.02820 (2018)

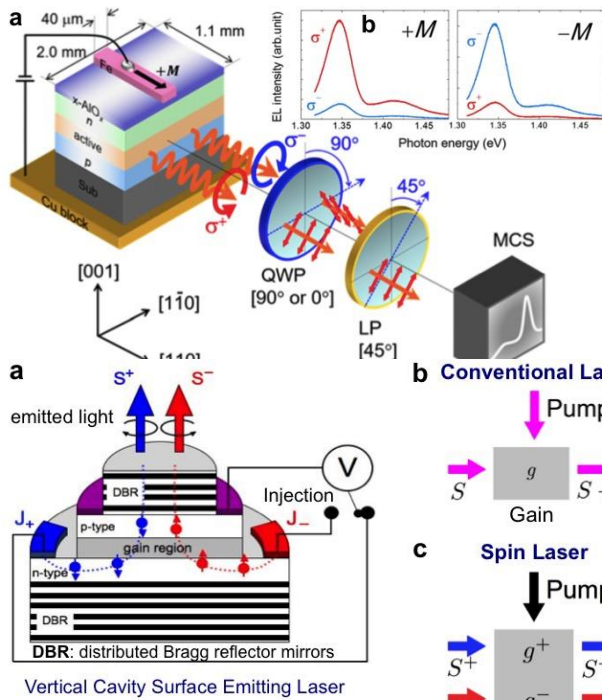


Fig.1: **a** A schematic spin-LED setup for electroluminescence (EL) measurements, ($\lambda/4$) QWP, linear polarizer (LP), and multichannel spectrometer (MCS). EL with right- (σ^+) and left-handed (σ^-) components. Light waves converted into linear polarization by QWP. **b** Helicity-specific EL spectra for remnant magnetization pointing toward QWP (+M, Upper) and against QWP (-M, Lower). From Ref. 2.

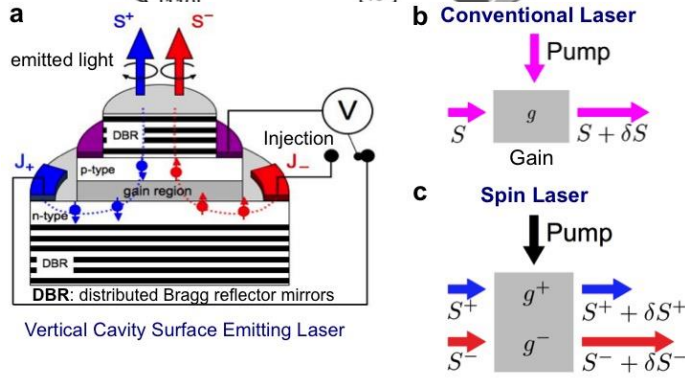


Fig. 2: **a** Spin-laser scheme. The resonant cavity is formed by a pair of distributed Bragg reflectors, the gain region typically consists of quantum wells or dots. Electrical spin injection is realized using two magnetic contacts. Alternatively, spin-polarized carriers are injected using circularly polarized light. Electron-hole recombination leads to the emission of the coherent light of positive (+)/negative (-) helicity (S^+ , S^-). Schematic of the optical gain **b**, **c**. With pumping/injection, a photon density $S=S^++S^-$ increases by δS as it passes across the gain region. In spin-lasers this increase depends on the helicity of the light $\bar{}$. From Ref. 6.

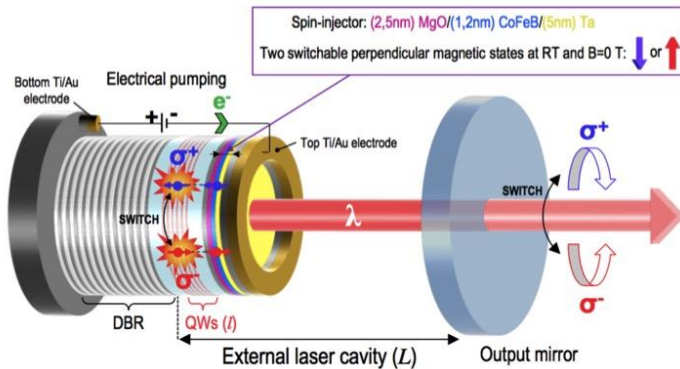


Fig.3: Conceptual illustration of an electrically spin-injected vertical cavity surface emitting lasers (VECSEL) operating at room temperature and magnetic remanence. The external cavity is between the bottom distributed Bragg reflector (DBR) and the output mirror. Spin injector with perpendicular magnetization at magnetic remanence. The active medium is based on multiple quantum wells (QWs). From Ref. 4.

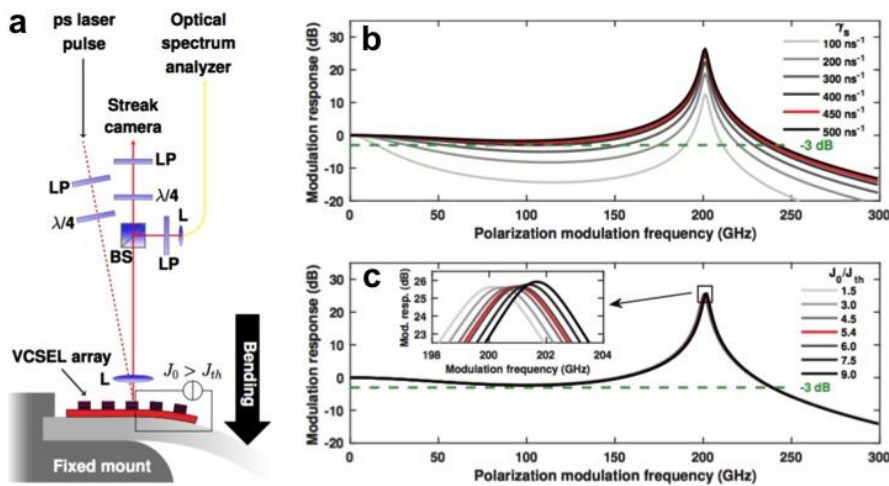


Fig. 4: **a** Schematic of experimental design of highly birefringent laser with linear polarizer (LP), quarter wave plate ($\lambda/4$), lens (L) and beam splitter (BS). The laser is operated with both a pumping current J_0 above threshold J_{th} and pulsed optical spin injection. Influences on modulation bandwidth: **b** of the spin-flip rate γ_s and **c** the of normalized electric bias J_0/J_{th} . The inset shows a nearly pumping-independent resonance frequency. Red traces: VCSEL simulations for the measured birefringence of 200 GHz. From Ref. 7.

Realization of Pure Circular Polarization Electroluminescence at Room Temperature with Spin-LEDs

Hiro Munekata¹ and Nozomi Nishizawa¹

¹*Laboratory for Future Interdisciplinary Research of Science and Technology,
Tokyo Institute of Technology, Japan
munekata.h.aa@m.titech.ac.jp*

Nearly pure circular polarization (CP) electroluminescence (EL) has been achieved at room temperature (RT) with a lateral-type spin-LED composed of a Fe/crystalline-AlO_x spin-injector and a GaAs-based double heterostructure (DH) [Fig. 1(a)] [1]. The maximum CP value is obtained for a laterally emitted EL beam, along the direction of in-plane remanent magnetization of the Fe electrode. For small values of a current density J , circular polarization $Q = (S^+ - S^-)/(S^+ + S^-)$ is $Q < 0.1$, whereas, as J increases, the EL intensity of the minority-helicity S^- component reduces significantly, resulting in the nearly pure CP [Fig. 1(b)]. Electrical helicity switching [Fig. 1(c)] has also been demonstrated at RT [2] using the concept of dual spin-injection electrode [3]. The observed annihilation of the S^- component at relatively high J suggests a mechanism that is different from the occurrence of spin-dependent gain based on the light amplification by stimulated emission of radiation [4].

Let us consider a black box in which a flow of spin-polarized electrons consisting of J^\pm is converted into CP light S^\pm (Fig. 2, bottom left). For a small reduced-current-density J_0 , recombination results in linear relation between J^\pm and S^\pm . Optical selection rule associated with heavy- and light-holes only applies for the low-injection limit. We next assume that, in a relatively high J_0 (case 2), a part of J^- (J^+) contributes to the generation of S^+ (S^-) with a weight given by $\alpha \cdot S^\pm$. Here, α is a non-linear factor that increases with J_0 : e.g., $\alpha = a \cdot J_0 + b$. Shown in Figs. 3 and 4 are calculated S^\pm and Q , respectively, as a function of J_0 with $a = 5 \times 10^{-5}$ and $b = 1 \times 10^{-3}$. These values are selected to yield $\alpha \sim 5 \times 10^{-3}$ near $J_0 \sim 100$. In the insets, S^\pm and Q obtained with $\alpha = 1 \times 10^{-3}$ are shown. It is clearly seen that S^+ and S^- components both increase with J_0 in the low J_0 region, whereas the S^- component saturates and turns reduction with increasing J_0 , and is annihilated at $J_0 \sim 45$ ($Q = 1$). This crude model clearly suggests the validity of non-linearity due to the interplay between J^\pm and S^\pm .

Attempt to recast the black box model with microscopic point of view will be presented using the rate equations composed of spin injection, radiative recombination, and spin flip.

[1] N. Nishizawa et al., Proc. Natl. Acad. Sci. USA **114**, 1783 (2017)

[2] N. Nishizawa et al., Appl. Phys. Express **11**, 053003 (2018)

[3] M. Oestreich et al., Semicond. Sci. Technol. **17**, 285 (2002)

[4] C. Gøthgen et al., Appl. Phys. Lett. **93**, 042513 (2008)

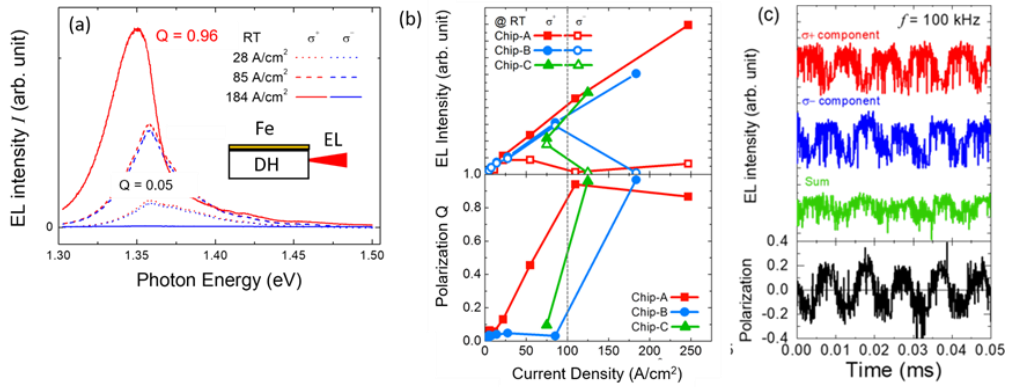


Fig.1: (a) Circular-polarization specific EL spectra for three different current densities. (b) EL intensity and circular polarization Q as a function of current density. (c) Temporal profiles of electrical polarization switching at 100 kHz.

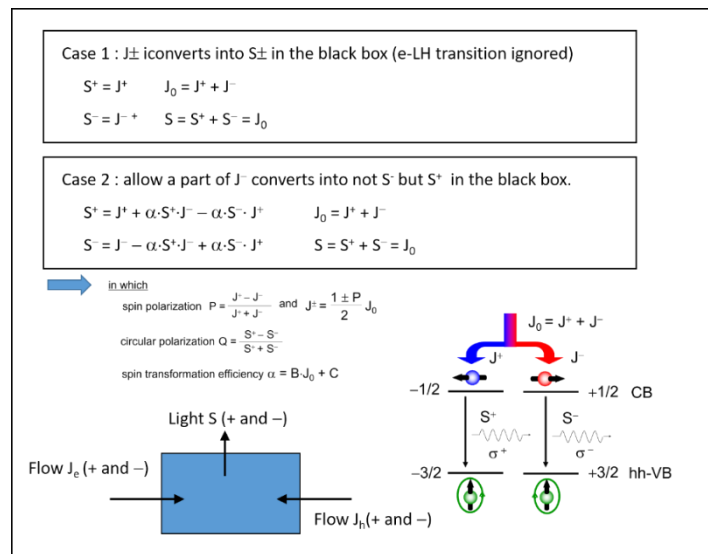


Fig.2: Schematic diagram that summarizes a model incorporating non-linear effect at high J_0 region: a conventional linear behavior (case 1), a behavior considering non-linear effect (case 2), and schematic illustrations of a black box model (left bottom) and simplified radiative recombination (right bottom).

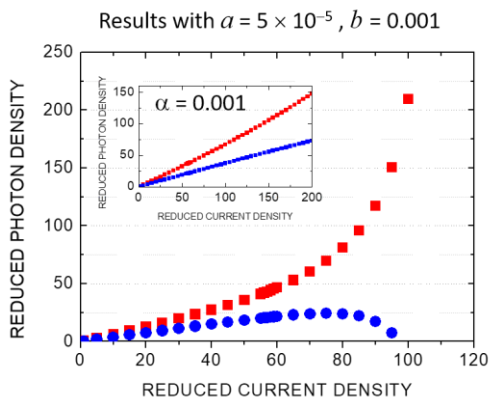


Fig. 3: Calculated S^+ and S^- using a model incorporating current-induced non-linear effect as a function of reduced current density. Here, S^+ and S^- are intensities of right- and left-circular polarization EL, respectively.

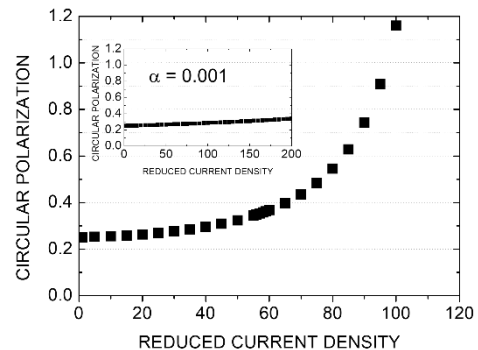


Fig. 4: Calculated Q values as a function of reduced current J_0 on the basis of data shown in Fig. 3.

Modelling Framework for Predicting Polarization Behavior of Spin-Controlled VCSELs and its Experimental Validation

Mehdi Alouini^{1,2}, Alexandre Joly², Julien Frougier³, Ghaya Baili²,
Daniel Dolfi², and Jean-Marie George³

¹*Institut Foton, Université de Rennes 1, CNRS, 35042 Rennes, France*

²*Thales Research & Technology, 1 av. Augustin Fresnel, 91767 Palaiseau Cedex, France*

³*Unité Mixte de Physique CNRS-Thales, 1 av. Augustin Fresnel, 91767 Palaiseau, France*
mehdi.alouini@univ-rennes1.fr

Optimization of spin-lasers relies obviously on the proper design of the active medium in order to enhance the electronic spin induced gain asymmetry [1]. Nevertheless, unlike spin-LEDs, the laser resonator itself plays also a fundamental role in this regard. Indeed, the interplay between gain asymmetry and additional polarimetric effects, either within the active medium or in the resonator, is expected to rule the laser output polarization. Thus a thorough understanding of the laser polarization behavior implies a vectorial description of the transverse electromagnetic field. The VSPIN (Vectorial SPIN) modelling framework that we propose [2] is based on the determination of the laser eigenstates using the Jones formalism in conjunction with the resonant condition of the field, where the electronic spin injection is accounted for as a variable circular gain dichroism. We show the existence of two possible eigenstates which can beat together, lock together or even compete together according to the gain asymmetry strength, leading to various time dependent or steady state polarization behaviors already observed by other groups.

In particular, when switching from a pure left-handed circular polarization to a pure right-handed circular polarization is the intended laser operation, the VSPIN formalism shows that any residual phase anisotropy in the laser has a detrimental role on polarization contrast as well as on possible polarization switching. Such drawback can be experimentally overcome by a fine compensation of the residual phase anisotropy inherent to the cavity and, in a second step, by compensating the linear dichroism inherent to the active medium. Besides, this formalism guided us to the realization of a laser comprising a Faraday rotator so that its two eigenstates become inherently circularly polarized. Owing to the gain competition between the two laser eigenstates, full polarization switching is then predicted and observed despite the very weak spin injection efficiency. Such a leverage effect, which is not present in spin-LEDs, is an additional interesting feature towards the realization of efficient and compact spin-lasers.

[1] I. Žutić et al., *Nature Nanotechnol.* **9**, 750 (2014)

[2] M. Alouini et al., *Opt. Express* **26**, 6739 (2018)

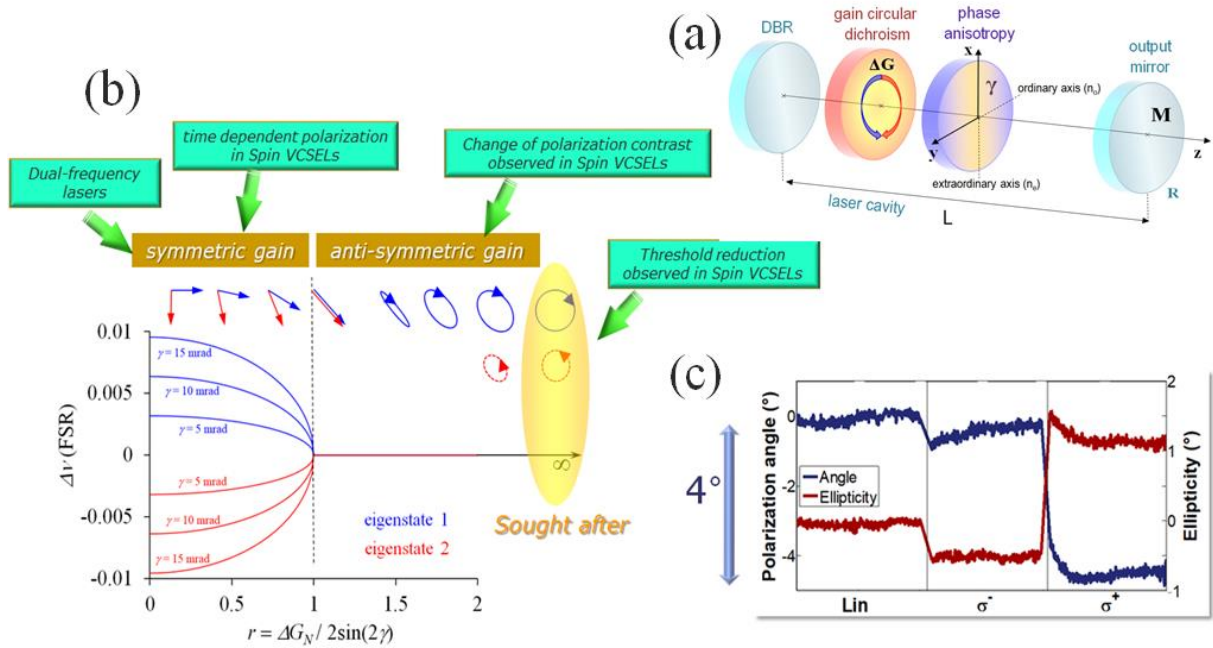


Fig. 1: (a) schematic representation of the laser cavity under consideration. (b) Predicted evolution of the frequency splitting between the two eigenstates and their polarization state as a function of the ratio r between the circular dichroism of gain ΔG_N and the linear birefringence of phase γ . (c) Experimental observation of output polarization orientation and ellipticity when the optical pump is respectively linearly (Lin) and circularly (σ^- , σ^+) polarized. The residual linear birefringence of laser cavity is tentatively compensated in this experiment.

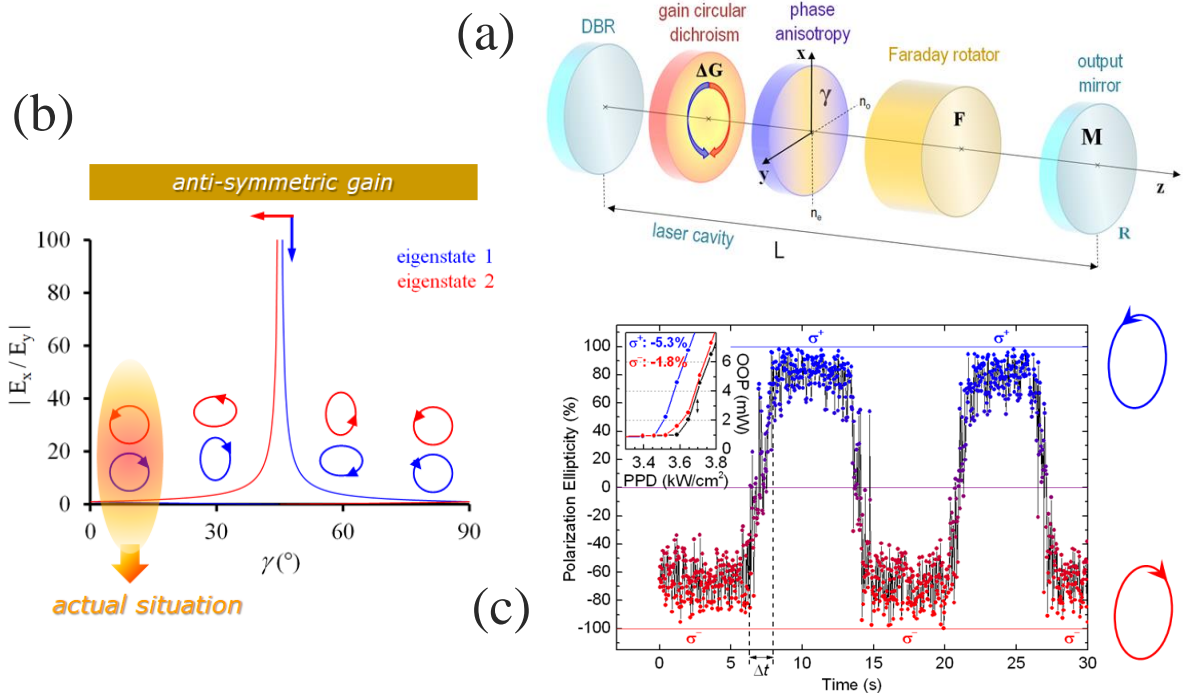


Fig. 2: (a) schematic representation of the laser cavity under consideration. The Faraday rotator enables to match the laser eigenstates with that of the spin injected active medium. (b) Predicted evolution of the polarization of the two eigenstates as a function of the linear birefringence γ . The presence of a Faraday rotator inside the cavity makes the frequency splitting between the two eigenstates null. In this situation the two circular eigenpolarizations are not sensitive to the gain circular dichroism ΔG_N anymore. Nevertheless, ΔG_N plays, as a trigger, on the gain asymmetry of the two eigenstates favoring polarization switching. (c) Experimental observation of polarization ellipticity at the output of the laser when the optical pump is switched from σ^- to σ^+ .

Ultrafast Birefringent Spin-Lasers

Markus Lindemann¹, Tobias Pusch², Gaofeng Xu³, Igor Zutic³, Rainer Michalzik²,
Martin R. Hofmann¹, and Nils Gerhardt¹

¹*Photonics and Terahertz Technology, Ruhr-University Bochum, 44780 Bochum, Germany*

²*Institute of Functional Nanosystems, Ulm University, 89081 Ulm, Germany*

³*Department of Physics, University at Buffalo, State University of New York, Buffalo,*

New York 14260, USA

nils.gerhardt@rub.de

The progress of the global digital revolution is closely tied to the solution of the bandwidth bottleneck to meet the growing demands of high-resolution streaming, cloud computing and the Internet of Things. In particular short-range optical communication systems such as current-driven intensity modulated vertical-cavity surface-emitting lasers (VCSELs) provide the main part of the communication bandwidth. However, the direct modulation bandwidth of these lasers is currently limited to values around 30 GHz [1] and seems to reach a fundamental limit. A very promising approach to overcome these limitations is to use spin and polarization modulation in spin-VCSELs instead of conventional intensity modulation [2]. The dynamics of the coupled spin-carrier-photon system are potentially much faster mainly decoupled from the intensity dynamics, which opens up new opportunities for high-speed transmission by modulating the polarization state [3]. Here we demonstrate experimentally and theoretically that the polarization dynamics in spin-VCSELs can be greatly increased by inducing a large birefringence into the laser cavity (Fig.1) [4]. Resonance frequencies for the spin-carrier-photon system of more than 200 GHz can be achieved (Fig.2). With a generalized spin-flip-model we investigate the influence on the polarization bandwidth. By tuning the resonance frequency via birefringence the bandwidth can be increased to more than 240 GHz enabling digital data transmission of up to 240Gbit/s (Fig.3). A detailed analysis of the limiting factors reveals the huge potential of these novel spin-lasers for future ultrafast optical interconnects with ultralow power consumption [5].

[1] R. Rosales et al., Proc. ESLW, C19 (2017)

[2] N. Gerhardt et al., Appl. Phys. Lett. **99**, 151107 (2011)

[3] I. Zutic and P.E. Faria Jr., Nat. Nanotechnol. **9**, 750 (2014)

[4] M. Lindemann et al., Appl. Phys. Lett. **108**, 042404 (2016)

[5] M. Lindemann et al., arXiv:1807.02820 (2018)

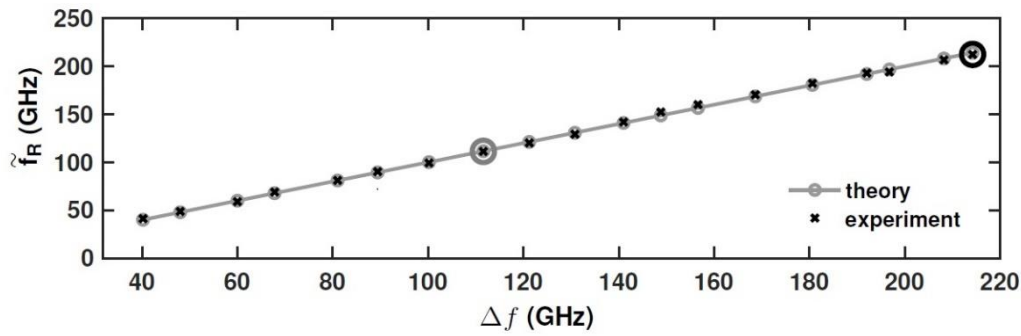


Fig.1: The polarization oscillations are the resonance oscillations of the coupled spin-carrier-photon system in the spin-laser. Their frequency \tilde{f}_R can be enhanced by the amount of birefringence in the cavity via the birefringence-induced mode splitting Δf to values >200 GHz.

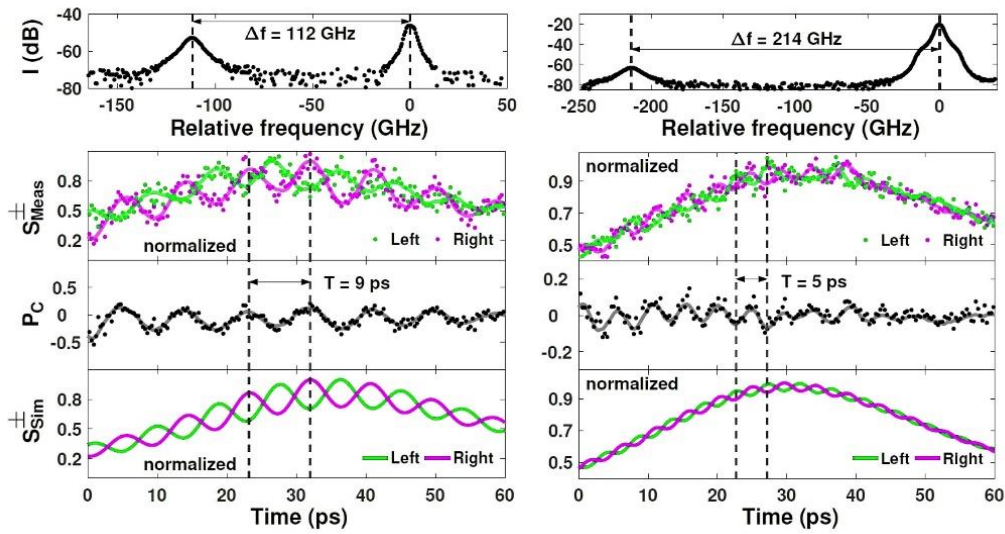


Fig.2: Ultrafast polarization oscillations after pulsed optical spin injection for birefringence-induced frequency splittings of 112 GHz (left) and 214 GHz (right). The optical spectra (top) depict the mode splitting of the orthogonal linearly polarized laser modes. S_{Meas}^{\pm} are the measured transients of the left and right circularly polarized laser modes and P_c the corresponding circular polarization degree. The results are in a very good agreement with simulations performed with a generalized spin-flip model (bottom).

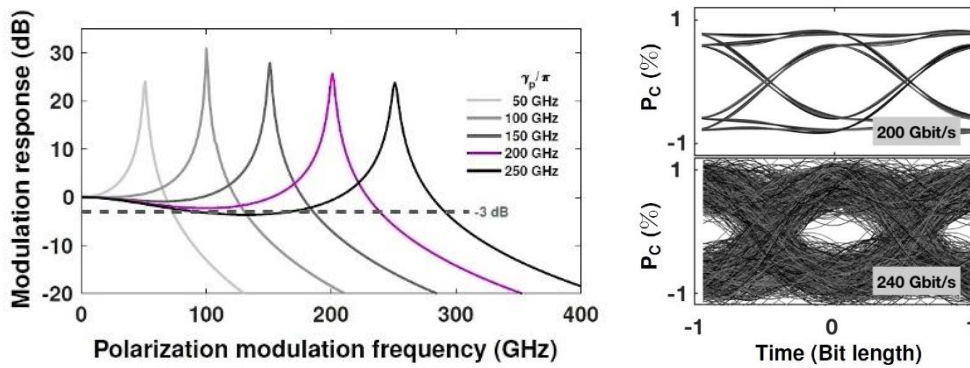


Fig.3: Simulations using the spin-flip model demonstrate that the polarization modulation bandwidth can strongly be enhanced by inducing linear birefringence to the cavity (left). The open eye in the eye diagrams reveals that digital data transmission is possible up to 240 Gbit/s for a birefringence-induced mode splitting of 200 GHz.

